Zinc Oxide Nanorods (ZnO NRs) for photovoltaic applications

Zahra Ishwein

A thesis submitted in partial fulfilment of
the requirements of the University of
Northumbria at Newcastle for the degree of
Doctor of Philosophy

Research undertaken at the Faculty of Engineering
and Environment

April 2019

Abstract

Zinc oxide (ZnO) is a material that has highly attractive cost-effective features and can be grown using different methods leading to a wide range of nanostructured morphologies. In this work, zinc oxide nanorods (ZnO NRs) with various surface distribution density were sensitised using aqueous solutions based on zinc salt at 40°C-85°C. Systematic investigations were carried out on the influences of zinc salt, different ZnO seed layer thickness and growth temperature (T_{growth}). The grown ZnO NRs were used in two different aspects. The first aspect was to grow the NRs on a releasable layer and here Omnicaot was used as a sacrificial layer and SU-8 photoresist as a support structural layer to reach the desired aim. Also, ZnO NRs were grown on polydimethylsiloxane (PDMS). This was used to improve the performance of different types of solar cells by mounting the full structure on top with help of optical gel. The results obtained showed that wet lift-off showed an increasing η from 1.56% to 2.05% when a GaAs solar cell was used, whereas the same solar cell showed an efficiency η increasing to about 2.03% when using dry peel-off nanostructures. CZTSSe ($Cu2ZnSn(S,Se)_4$) solar cells showed an increase in η from 1.3% to (1.79%, 1.65% and 2.15%) for ZnO NRs/SU-8, ZnO NRs/PDMS and flower-like/diluted PDMS, respectively. The second aspect was to fabricate extremely thin absorber solar cells. For lift-off process, the work presented herein provides a cost-effective, simple novel combination of lift-off processing with hydrothermally grown ZnO NRs on SU-8 or PDMS, in a low temperature range T_{growth} from 40°C- 85°C. This study addresses a controllable release/transfer of ZnO NRs when high growth temperature represents a barrier to carrying out an immediate growth on flexible substrates for example wearable electronics applications. The evolution of ZnO NRs with T_{growth} were characterized by scanning electron microscopy (SEM), X-ray diffraction (XRD) and UV-Vis spectroscopy. The ZnO NRs/SU-8 and ZnO NRs/PDMS structures were successfully detached from the glass. The SEM images confirmed that, the ZnO NRs formed different diameters and lengths as T_{growth} increased. Transmitted/scattered light characteristics showed different trends depending on the T_{growth} and structure stack used. The findings of this study offer an easy method of lift-off ZnO NRs (and subsequent stack of layers) using the low-cost facilities and at low temperature. Current-voltage (I-V) and external quantum efficiency (EQE) measurements showed an affective influence of mounting the released ZnO NRs on CZTS and GaAs solar cells. Moreover, a study on ETA cell fabrication using CZTS is presented. The fabricated ETA cell structure was as the following: glass/ITO/ZnO seed/ZnO NRs/CdS/CZTS/P3HT/gold and the aim is for the CdS/CZTS to conformally coat the ZnO NRs, while P3HT acts as a hole transport layer which in turn helps avoiding shunting. ETA cell showed about 0.02% of efficiency (η), 0.05V (Voc), 0.15mA/cm^2 (Jsc), 27.46% (FF) and about 20% EQE in the 300nm-600nm spectra region. These results are clear indication of promising sight for ETA solar cells based on CZTS nanoparticles which can be more improved.

Table of Contents

Abstract ii

Table of Contents iii

Dedications xx

Acknowledgments xxi

Declaration xxii

Chapter 1 Introduction 1

1.1 Research motivation 1

1.2 Thesis Organisation 4

1.3 Contribution 5

Chapter 2 Literature review 6

2.1 Zinc Oxide (ZnO) 8

2.1.1 ZnO Properties 9

2.1.2 ZnO Crystal Structure 12

2.1.3 Zinc Oxide as a semiconductor 14

2.1.4 Zinc Oxide Nanorods (ZnO NRs) 15

2.1.4.1 Synthesis of Zinc Oxide Nanorods 16

2.1.4.2 Zinc Oxide Hydrothermal Synthesis 17

2.2 Solar Cells 18
2.2.1 Types of Solar Cells 19
2.2.1.1 Zinc Oxide Nanorods-Based Solar Cells 21
2.2.2 The Principle of Photovoltaics and Semiconductor 22
2.2.2.1 A Semiconductor 22
2.2.2.2 PN Junction 23
2.2.2.3 The Photovoltaic Theory 24
2.2.3 Light trapping in solar cells 26

2.3 Lift-Off Process 31
2.3.1 The Photoresist 31
2.3.1.1 Support Structural Layer and Sacrificial layer 33
2.3.1.2 SU-8 Photoresist 33
2.3.1.3 Poly(methyl methacrylate) (PMMA) 36
2.3.1.4 Polydimethylsiloxane (PDMS) 39

2.4 Extremely thin absorber (ETA) solar cells 40
2.4.1 The principle of ETA solar cells 42
2.4.2 ETA solar cells ETA Cell Superstrate Configuration using CZTS Nanoparticles 44

2.5 Summary 45

Chapter 3 Experimental setup 46

3.1 Oxide Nanorods (ZnO NRs) hydrothermal Growth 47
3.1.1 Materials and Chemicals 47
3.1.2 ZnO Synthesis Procedure 47
3.1.2.1 Substrate Preparation 47
3.1.2.2 Substrate Pre-cleaning 47
3.1.2.3 ZnO seed deposition 48
3.1.3 Zinc Oxide NRs hydrothermal growth using different growth temperatures (T_{growth}) 49

3.2 Lift-off (dry and wet) processes 50
3.2.1 The final aim of using ZnO NRs/SU-8 and ZnO NRs/ PDMS 52

3.2.2 Poly(methyl methacrylate) (PMMA) as a structural support layer (wet lift-off) 52
3.2.3 SU-8 photoresist as a structural support layer (wet lift-off) 54
3.2.3.1 Process Requirements 54
3.2.3.2 Substrate Preparation .....
3.2.3.3 Spin Coating.....
3.2.3.4 Soft Baking (SB).....
3.2.3.5 UV Light Exposure .....
3.2.3.6 Post-Exposure-Baking (PEB).....
3.2.3.7 Stripping.....
3.2.3.8 Transferring process..... 56
3.2.4 Polydimethylsiloxane PDMS (dry lift-off) 57
3.2.4.1 Materials and experimental method..... 57
3.2.4.2 Spin Coating and Curing..... 58
3.2.4.3 ZnO NRs growth and PDMS peeling off..... 58
3.2.4.4 SU-8 photoresist and PDMS comparison 58

3.3 Extremely Thin Absorber (ETA) Fabrication 60
3.3.1 Hydrothermal ZnO NRs growth..... 61
3.3.2 Chemical bath deposition (CBD)..... 61
3.3.3 Cu2ZnSn(S,Se)4 (CZTS) nanoparticles..... 62
3.3.4 P3HT and gold contact deposition 62

3.4 Characterisation techniques 63
3.4.1 Scanning electron microscope SEM 63
3.4.2 Energy-dispersive X-ray spectroscopy (EDS) 63
3.4.3 Atomic Force Microscopy (AFM) 64
3.4.4 X-Ray diffraction Structural Characteristics (XRD) 64
3.4.5 UV-VIS-NIR transmittance (T%) and Reflectance (R%) analysis..... 64
3.4.6 I-V measurements 64
3.4.7 External Quantum Efficiency (EQE). 65

3.5 Summary 65

Chapter 4 Zinc Oxide nanorods (ZnO NRs) 66

4.1 Results and Discussion 67
4.1.1 Sputtered ZnO seed on ITO-coated glass substrate 67
4.1.2 Electron microscope (SEM) and atomic force microscope (AFM) for Seed layer 68
4.1.3 UV-VIS-NIR for ZnO seed samples 73
4.1.4 Growth of ZnO NRs using zinc nitrate and zinc chloride salts (morphology) 74
4.1.4.1 Seed layer thickness effect 77
4.1.4.2 Growth temperature (T_{growth}) effect 77
4.1.5 X-Ray diffraction Structural Characteristics (XRD) 81
4.1.5.1 Crystal size of ZnO NRs 84
4.1.5.2 Variation of lattice constants of (002) of the grown ZnO NRs 86
4.1.5.3 Intensity of the grown ZnO NRs 87
4.1.5.4 Texture coefficient (TC) 88
4.1.5.5 Preferred orientation (σ) 90
4.1.6 ZnO NRs Optical Properties 91
4.1.6.1 UV-VIS-NIR transmittance analysais 92
4.1.6.2 Haze measurements 95
4.1.6.3 Optical Band Gap calculations of the grown ZnO NRs 98

4.2 Conclusion 100

Chapter 5 Zinc oxide nanostructures using wet and dry lift-off methods

5.1 Results and Discussion 102
5.1.1 Poly(methyl methacrylate) PMMA as a sacrificial layer 102
5.1.1.1 Releasing the Ni thin film 111
5.1.2 Omnicoat/SU-8 structure (wet lift-off) 113
5.1.2.1 Effect of UV light intensity on SU-8 thickness and light transmittance 118
5.1.2.2 Hydrothermal growth of ZnO NRs (wet and dry lift-off) 120
5.1.2.1 UV-VIS spectrometry and haze 124
5.1.2.2 Scanning electron microscopy (SEM) and energy dispersive spectroscopy (EDS) 129

5.1.2.3 XRD for ZnO nanorods/SU-8 under T_{growth} = 40°C, 45°C, 60°C, 65°C and 85°C 131
5.1.3 ZnO NRs/PDMS/glass (dry lift-off)....132
5.1.3.1 Scanning electron microscopy (SEM) and energy dispersive spectroscopy (EDS) for ZnO NRs....132
5.1.3.2 UV-VIS spectrometry....134
5.1.3.3 X-ray diffraction....136
5.1.4 Flower like nanostructure/diluted PDMS....137
5.1.4.1 Scanning electron microscopy (SEM) and energy dispersive spectroscopy (EDS) for ZnO NRs....137
5.1.4.2 X-ray diffraction....138
5.1.5 Mounting the ZnO nanostructures on a complete....140
5.1.6 solar cell for I-V and EQE measurements....140
5.1.6.1 Reflectance measurements with and without NRs on solar cells....141
5.1.6.2 GaAs solar cell with and without NRs (I-V characteristics)....145
5.1.6.3 GaAs solar cell with and without NRs (EQE)....148
5.1.6.4 CZTS solar cell with and without NRs (IV)....152
5.2 Conclusion....158
Chapter 6 Extremely Thin Absorber (ETA) solar cell..... 160
6.1 Results and Discussion....163
6.1.1 CdS deposition on non-annealed ZnO NRs....163
6.1.1.1 Scanning electron microscopy (SEM) and Energy-dispersive X-ray spectroscopy (EDS)....164
6.1.2 The annealed ZnO NRs....166
6.1.2.1 Scanning electron microscopy (SEM)....166
6.1.2.2 Energy-dispersive X-ray spectroscopy (EDS)....167
6.1.2.3 X-ray diffraction analysis....168
6.1.2.4 UV-VIS-NIR spectroscopy....170
6.1.2.5 CdS deposition on annealed ZnO NRs....173
6.1.2.6 Scanning electron microscopy (SEM) and Energy-dispersive X-ray spectroscopy (EDS)....173
6.1.3 I-V characteristics....176
6.1.4 EQE data and discussion....177

6.2 Conclusion 178

Chapter 7 Conclusions and Future Work 180

7.1 Thesis summary 180

7.2 Suggestions for Future Work 182

References 184

List of Figures

Figure 1. Three different main areas of this project. 4

Figure. 2. Electricity generation by using fuel from 1990 to 2040 (trillion kilowatthours per year) 7

Figure 3. Representation of the three different crystal structures of ZnO. A) Represents the rocksalt, b) zinc blende and c) is the Wurtzite structure 13

Figure 4. The ZnO wurtzite structure model with tetrahedral coordination of Zn–O [55] 14

Figure 5. The growth of different nanostructures 16

Figure 6. Two different types of solar cells. (a) Silicon n-based cell, (b) Perovskite solar cell with Al-doped ZnO NRs 20

Figure 7. The fabricated perovskite ZnO based PSCs 21

Figure 8. P-N conventional geometry 24

Figure 9. Illustration of a typical I-V curve in a solar cell device 26

Figure 10. a) Light refraction at the interface of two different mediums having two different refractive indices and b) transmittance and reflection of light in a texture silicon solar cell..... 27

Figure 11. Schematic diagram of light trapping effect within a nanostructure[117]. 28

Figure 12. Light trapping in high-index (n) solar cell. A) without surface texturing and b) with surface texturing 29

Figure 13. Light trapping using random texture, grating structure. a) Trapped light in a textures interface. b) Back reflector with periodic grating on. c) Absorption spectra and waveguide dispersion relation for b structure 29

Figure 14. Lithography of photoresist using Positive Vs Negative Photoresists 32

Figure 15. Molecular structure of SU-8 photoresist..... 35

Figure 16. The lifted SU-8 structure 36

Figure 17. a) SEM image of ZnO NRs/PDMS b) Optical image of flexible ZnO NRs/PDMS.....40

Figure 18. Extremely thin absorber (ETA) solar cell.....42

Figure 19. CZTS solar cell schematic structure.....45

Figure 20.Experimental work accomplished in this project. 46

Figure 21. The hydrothermal growth setup with the sample upside-down facing the growth solution. 49

Figure. 22. Schematic of the structure evolution after each deposition step.....50

Figure. 23. Two targeted structures for the lift-off process. 1) Structure 1 (glass/omnicoat/SU-8/ZnO NRs) and 2) structure 2 (glass/PDMS/ZnO NRs).....51

Figure. 24. ZnO NRs lift-off and transfer processes.....52

Figure 25. PMMA layer preparation.....53

Figure. 26. PMMA/thin film structures before lift-off.....53

Figure. 27. The SU-8 processing steps used in this project. 55

Figure. 28. Omnicoat/SU-8 preparation for the lift-off process.....56

Figure. 29. PDMS preparation process 58

Figure. 30. SU-8 and PDMS processing requirement comparison. 59

Figure 31. ETA Cell fabrication process.....60

Figure 32. ETA solar cell fabrication steps.....61

Figure 33. Evaluation of seed deposition thickness with deposition time 68

Figure 34. Top-view SEM images of ZnO seed layers coated with 3nm Pt. a) 27nm, b) 63nm, c) 70nm and d) 130nm. 69

Figure 35. AFM images for the sputtered ZnO seed layers. a) 27nm seed, 63nm seed, c) 70nm seed and d) 130nm seed. 70

Figure 36. Nanowire growth mechanism using different seed thicknesses [207].....71

Figure 37. XRD patterns of ITO coated glass and seeded samples without the nanostructure 72

Figure 38. UV-VIS-NIR transmittance of the ZnO seed samples deposited on ITO-coated glass. Solid lines represent the total transmitted light and the dotted lines represent the diffused light. 73

Figure 39. Top-view SEM images of the ZnO NRs on ITO-coated substrate with different growth temperatures T_{growth} = (40°C, 45°C, 60°C, 65°C, 85°C). Using zinc nitrate. Inset is cross-section. 75

Figure 40. Top-view SEM images of the ZnO NRs on ITO-coated substrate with different growth temperatures T_{growth} = (40°C, 45°C, 60°C, 65°C, 85°C). Using zinc chloride. Inset is cross-section. 76

Figure 41. Length and diameter vs T_{growth}. a1-a2) for zinc nitrate and b1-b2) for zinc chloride. 78

Figure 42. pH values change before and after the hydrothermal ZnO NRs growth. a) zinc nitrate growth solution and b) zinc chloride growth solution. 80

Figure 43. ZnO NRs XRD patterns grown at five different temperatures T_{growth} using $Zn(NO_3)_2$ at 40°C, 45°C, 60°C, 65°C and 85°C. 82

Figure 44. ZnO NRs XRD patterns grown at five different temperatures T_{growth} using $ZnCl_2$ at 40°C, 45°C, 60°C, 65°C and 85°C. 84

Figure 45. Crystal size vs Tgrowth and ZnO seed thickness. a1), a2) for Zinc nitrate and b1), b2) for zinc chloride. 85

Figure 46. The effect of T_{growth} and seed thickness on the resulted ZnO NRs Intensities. a1, a2) using zinc nitrate and b1, b2) using zinc chloride. 88

Figure 47. Variations of ZnO NRs texture coefficient for (002) peak. a) is Zinc nitrate and b)is zinc chloride. 89

Figure 48. Variations of ZnO NRs preferred orientation. a) Zinc nitrate and b) zinc chloride. 90

Figure 49. UV-VIS-NIR transmittance of the ZnO NRs grown using zinc nitrate. a1) 40°C, a2) 45°C, a3) 60°C, a4) 65°C and a5) 85°C. 93

Figure 50. UV-VIS-NIR transmittance of the ZnO NRs grown using zinc chloride. a1) 40°C, a2) 45°C, a3) 60°C, a4) 65°C and a5) 85°C. 94

Figure 51. Transmittance haze spectra of the ZnO NRs grown using zinc nitrate at (40°C, 45°C, 60°C, 65°C and 85°C). 96

Figure 52. Transmittance haze spectra of the ZnO NRs grown using zinc chloride at (40°C, at 45°C, 60°C, 65°C and 85°C). 97

Figure 53. Tauc`s plots of ZnO of the optical band gap of the grown ZnO NRs under T_{growth} (40°C, 45°C, 60°C, 65°C and 85°C) using zinc nitrate. 99

Figure 54. Tauc`s plots of ZnO of the optical band gap of the grown ZnO NRs under T_{growth} (40°C, 45°C, 60°C, 65°C and 85°C) using zinc chloride. 100

Figure 55. The device structure of Ni on sacrificial layer deposition. 103

Figure 56. a) The thickness of stress represents the results of electrodeposited Ni and b) the evolution of the stress thickness measured in the evaporated Ni 106

Figure 57. (a-f) represent the ZnO disc SEM images form as grown ZnO disc to annealed at 450°C, 550°C, 750°C and 850°C temperatures respectively. g) Band gap variation and stress resulted in ZnO disc by increasing the annealing temperature 107

Figure 58. Different materials stress transition pressure.....108

Figure 59.Representation of intrinsic and thermal stress distribution.....109

Figure 60. Optical images of 360 nm of Ni on both PMMA and SU-8. a) Reference sample, b) 1 PMMA layer and c) 2PMMA layers. 110

Figure 61. Optical images of 200 nm of Ni on PMMA. a) Reference sample, b) 2 PMMA layer, c) 1 PMMA layers. 110

Figure 62.Optical images of 100nm of Ni on PMMA. a) Reference sample, b) 1 PMMA layer, c) 2 PMMA layers. 111

Figure 63. The 100nm of Ni on 2 PMMA layers sample, a) sample soaked in acetone (before lift-off) and b) the lifted-off layer hold by tweezer. 112

Figure 64. Needles used to transfer the layers to new cleaned glass substrates.....113

Figure 65.The Pt/SU-8 structure. a) Before lift-off (on glass), b) during lift-off (in the remover solution) and d) after lift-off (on flexible kapton substrate) 114

Figure 66. ZnO NRs deformation after long time lift-off process. a) And b) are for the same sample at different places.....115

Figure 67. Released SU-8/Pt/kapton structures after using 10min soft baking and post exposure baking at different baking times. a) 1min post exposure baking, b) 5min post

exposure baking, c) 10min post exposure baking and d) 30min post exposure baking. 116

Figure. 68 Exposure energy vs Intensity. 117

Figure 69. The effect of UV light intensity in % on SU-8 thickness. 118

Figure 70. Ultraviolet (UV) light intensity in % on the light transmittance. 119

Figure 71. ZnO NRs/SU-8 (Tgrowth = 85 °C) on (a) bent PET substrate after lift-off bending and (b) the corresponding SEM images of the ZnO NRs (the inset is high SEM magnification). 121

Figure 72. Omnicoat/SU-8/ZnO seed/ZnO NRs structure delamination after the hydrothermal growth process. 121

Figure 73. The Omnicoat/SU-8 structure delamination after 2 h soaking in 40°C DI water. a) Low magnification and b) high magnification 123

Figure 74. UV-VIS-NIR transmittance of a) glass/Omnicoat/SU-8 before and after ZnO seed deposition and b) ZnO NRs grown on glass/Omnicoat/SU-8 structure (before lift-off) using T_{growth} = (40°C- 85°C). Solid lines represent the total transmitted light and the dotted lines represent the diffused light. 125

Figure 75. SEM images for ZnO NRs grown on ITO substrate at different temperatures 95°C-40 °C respectively for 4 hours. (A, C, E, G) is top-view and (B, D, F, H) represent view from 45° [284]. 126

Figure 76. ZnO NRs/SU-8 structure on PET (after lift-off). 127

Figure 77. Transmittance haze spectra as a function of the wavelength for glass/Omnicaot/SU-8/ZnO nanorods under T_{growth} = 40°C, 45°C, 60°C, 65°C and 85°C a) (before lift-off) and b) after lift-off. 128

Figure 78. Scanning electron microscopy (SEM) images of the grown ZnO nanorods/SU-8 under five T_{growth}. a) 40°C, b) 45°C, c) 60°C, d) 65°C and e) 85°C. ... 130

Figure 79. The XRD patterns of ZnO NRs grown on Omnicoat/SU-8 structure before lift-off using T_{growth} = 40°C, 45°C, 60°C, 65°C and 85°C. 131

Figure 80. SEM images of ZnO NRs grown on PDMS using Tgrowth = 40°C, 45°C, 60°C, 65°C and 85°C. 133

Figure 81. The transmittance spectra of a) ZnO/PDMS (before peel-off) and b) after peel off. Solid lines represent the total transmitted light and the dotted lines represent the diffused light. 135

Figure 82. XRD patterns of ZnO NRs grown on PDMS using T_{growth} = 40°C, 45°C, 60°C, 65°C and 85°C. 136

Figure 83. SEM images of ZnO flower-like grown on diluted PDMS using T_{growth} = 40°C, 45°C, 60°C, 65°C and 85°C. 137

Figure 84. XRD patterns of ZnO flower like/diluted PDMS using Tgrowth = 40°C, 45°C, 60°C, 65°C and 85°C. 138

Figure 85. pH value before and after the flower like growth processes. 139

Figure 86. The two used solar cells. a) GaAs solar cell structure and b) CZTS solar cell structure. 141

Figure 87. Reflectance measurement method for CZTS solar cell (before adding the ZnO NRs). 141

Figure 88 Reflectance spectra of a1), a2) for GaAs and b1), b2) for CZTS substrate configuration solar cell with and without ZnO NRs/SU-8 and ZnO NRs/PDMS respectively. 142

Figure 89. CZTS reflectance ripples 143

Figure 90. I-V characteristic for GaAs solar cell using two different ZnO nanostructures. a) ZnO NRs/SU-8 and b) ZnO NRs/PDMS. 145

Figure 91. Improvement of GaAs solar cell performance after the addition of NRs 147

Figure 92. The external quantum efficiency (EQE) for GaAs solar cell with and without NRs using different Tgrowth. a) Using wet lift-off and b) using dry lift-off 149

Figure 93. Integrated Jsc from EQE. 151

Figure 94. I-V characteristic for CZTS solar cell using three different ZnO nanostructures. a) ZnO NRs/SU-8, b) ZnO NRs/PDMS and c) flower like/diluted PDMS. 152

Figure 95. The effect of the three ZnO nanostructures on CZTS solar cell. a) Efficiency and b) resulted improvement in percentage. 155

Figure. 96. The external quantum efficiency (EQE) for CZTS solar cell with and without NRs using different Tgrowth. a) ZnO NRs/SU-8, b) ZnO NRs/PDMS and c) flower like/diluted PDMS. 156

Figure 97. Jsc extracted form EQE for CZTS solar cell. a) ZnO NRs/SU-8, b) ZnO NRs/PDMS and c) flower like/diluted PDMS 156

Figure 98 an example of the fabricated ETA cell structure (ITO/ZnO seed/ZnO NRs/CdS/CZTS/P3HT/gold contact). 162

Figure 99. Top-view of SEM images of CdS deposited on ZnO NRs. a) 27nm seed sample and b) 130nm seed sample. 164

Figure 100. An example of the EDS analysis and the different scanned areas on ZnO NRs/CdS a) 27nm seed sample and b) 130nm seed sample. 165

Figure 101. Top-view and tilted SEM images for ZnO NRs grown at 65C using four different seed thicknesses with 27nm, 63nm, 70nm and 130nm respectively. (a1-d1) before annealing and (a2-d2) after annealing. 167

Figure 103. An example of the EDS analysis and the different scanned areas on a) 27nm seed and b) 70nm seed sample 168

Figure 104 X-ray diffraction patterns of ZnO NRs grown at 65oC with various ZnO seed thicknesses. a) Before annealing and b) after annealing. 169

Figure 105. UV-VIS spectra of ZnO NRs grown at 65°C. a) As deposited NRs and b) after annealing the NRs. 171

Figure 106. Top-view and tilted SEM images of CdS/ZnO NRs. a) 27nm seed sample, b) 63nm seed sample, c) 70nm seed sample and d) 130nm seed sample. 173

Figure 107. Examples of cross-section SEM images for CdS/ZnO a) 27nm seed sample, b) 63nm seed sample and c) 70nm seed sample. 174

Figure 108. EDS obtained from ZnO NRs/CdS. A) 63nm seed sample and b) 130nm seed sample. 175

Figure 109.Current density vs voltage of the fabricated ETA solar cells. 176

Figure 110. EQE for the fabricated ETA cells. 178

List of Tables

Table 1. The reported best efficiencies of different solar cell type 20

Table 2. The main differences of the negative and positive photoresist 33

Table 3. The selected water -soluble polymers used as sacrificial layers 38

Table 4. ZnO seed sputtering parameters 48

Table. 5. ZnO hydrothermal growth parameters 50

Table 6. Variation of lattice constants of (002) of the grown ZnO NRs using zinc nitrate and zinc chloride. 87

Table 7. EDS results for ZnO NRs/SU-8 130

Table 8. EDS results of ZnO NRs/PDMS 134

Table 9. EDS results for ZnO flower like/diluted PDMS 139

Table 10. GaAs solar cell performance with and without mounted ZnO NRs. 146

Table 11. The extracted device parameters from I-V characteristics for GaAs solar cell with and without ZnO NRs as a function of T_{growth}. 148

Table 12. Jsc values extracted from EQE. 150

Table 13. The extracted device parameters from I-V characteristics for CZTS solar cell with and without ZnO NRs as a function of T_{growth}. 153

Table 14. Improvement in CZTS solar cell after the addition of ZnO nanostructures . 154

Table 15. Jsc extracted from EQE 157

Table 16. ZnO NRs/CdS elemental composition 166

Table 17. Chemical composition of as grown ZnO NRs obtained from EDS analysis 168

Table 18. The percentage elemental composition of ZnO NRs/CdS 175

Glossary of Abbreviations

ZnO	Zinc oxide
NRs	Nanorods
PMMA	Poly(methyl methacrylate)
PDMS	Polydimethylsiloxane
ETA	Extremely thin absorber
CZTS	Cu2ZnSn(S,Se)4
GaAs	Gallium arsenide
T_{growth}	Growth temperature
SB	Soft Baking
PEB	Post Exposure Baking
CBD	Chemical bath deposition
SEM	Scanning electron microscope
EDS)	Energy-dispersive X-ray spectroscopy
AFM	Atomic Force Microscopy
XRD	X-Ray diffraction
T% and R%	UV-VIS-NIR transmittance and reflectance
I-V	Current-Voltage
EQE	External Quantum Efficiency

Glossary of Symbols

J	Emission current density
AE	Applied electric field
A	Constant
B	Constant
Φ	Emitter work function
E	Photon energy
h	Planck`s constant
c	Speed of light
λ	Light wavelength
η	Efficiency
P_{max}	Power output
P_{in}	Power input
J_{mp}	Current density
V_{mp}	Voltage at the maximum power point
J_{sc}	Short circuit current density
V_{oc}	Open circuit voltage
FF	Fill factor
n1	Refractive index
n2	Refractive index
θ1	Angle of incident light
θ2	Angle of incident light
$4n^2$	Yablonovitch limit
θ	Emission cone angle
a	Amplitude resonance
ω	Resonance frequency
γ_i	The rate of intrinsic loss
S	Amplitude of incident plane wave
γ_e	Leakage resonance rate
α∘	Coefficient of the material absorption
D	Crystal size

k	Constant
λ	Cu-Kα wavelength
β	Full width of a half maximum
θ	Braggs diffraction angle
a	Lattice constants
c	Lattice constants
T_C	Texture coefficient
$I(h\ k\ l)$	Intensity of XRD
$I_o(h\ k\ l)$	Plane standard intensity
n	Diffraction peaks number
σ	Preferred orientation
H_T	Transmittance haze
T_{diff}	Total diffusion
T_{tot}	Total transmission
α	ZnO absorption coefficient
v	Light frequency
E_g	Bandgap energy
t	Thin film thickness

Dedications

To the most important people in my life, my parents, sisters, brothers, nieces and nephews, Fatma Hamma and Mara Ahmed. Also, to those people who might find this thesis useful.

Acknowledgments

A special thank you goes to my principle supervisor Vincent Barrioz for his advice, support, constant enthusiasm, guidance, throughout this PhD journey. Without his unlimited and constant support, this work would not have been accomplished on time. Thank you so much Vincent.

Besides my advisor, I am highly indebted to Dr Guillaume Zoppi for his valuable support and help. Furthermore, my thanks and appreciation go to Dr Neil Beattie and Dr Yongtao Qu; thanks guys.

I would also like to express my sincere thanks to my colleagues for the valuable support through my PhD journey.

I would like to express my thanks to my sponsor the Libyan government. Without their financial support this PhD journey would not have been possible.

I would especially like to thank Rebecca Payne and Dr Pietro Maiello for their technical support.

Finally, I would like to express my honest apology in case I have unintentionally missed anyone.

Declaration

I declare that this thesis is entirely my own work and I have exercised reasonable care to ensure that my work is original and does not, to the best of my knowledge, breach any copyright law and has not been submitted to support any other degree or qualification.

I declare that the Word Count of this Thesis is 44754 words

Signature:	Zahra Ishwein
Name:	Zahra Ishwein
Date:	30th April 2019

Chapter 1 INTRODUCTION

1.1 Research motivation

"I'd put my money on the sun and solar energy. What a source of power! I hope we don't have to wait until oil and coal run out before we tackle that."— Thomas A. Edison (1847–1931) [1]. Solar energy is a noteworthy sustainable power source with the possibility to address a large number of the difficulties confronting the world. There are numerous motivations to advance its share in the energy market. It is becoming popular since it is a flexible and clean energy source. Rapid global industrial and economic development is expanding demand. In any case, the limited fossil energy cannot meet the needs of growing energy demands. Guaranteeing a sustainable, secure supply of energy is vital for economic and social development of mankind [2]. On the whole, the sources of energy are classified in two groups (renewable and non-renewable) energy sources (RES). For a long time, people have depended on non-renewable energy sources; e.g. petroleum (oil), natural gas and coal [1]. The substantial dependence on non-renewable energy sources such as fossil fuels, given their inescapable depletion and significant negative consequences on the environment, has prompted to intensive scientific investigation to create solutions which will guarantee a sustainable energy supplying by renewable sources. Solar radiation is represented to be available, promising and environment

friendly renewable energy with the possibility to give adequate capacity and to manage energy issues in the long term to the developing human population [1] [3].

It is essential to go for cost effective, everlasting and reliable sustainable energy sources for the arising energy demand in the future [3]. Back in 2007, during the Materials Research Society Meeting in San Francisco, Nate Lewis suggested that six solar cell farms with 10% efficiency and approximately 3.3 TW of energy could be strategically positioned around the world to sufficiently meet the current universal energy requirements. however, this large - scale project could certainly be too expensive because this solar technology would require an average of $ 0.30 per kilowatt – hour [4]. As a result of Smalley and Lewis ' teachings, a lot of researchers around the globe have devoted a great deal of time to investigate ways of making renewable energy sources economically feasible. In 2005 Smalley stated that, nanotechnology innovations and other materials science advances would make our vision of low – cost, abundant energy into reality [5]. Photovoltaic (PV) effect can be simply defined as the basis and direct solar energy conversion into electrical power [6, 7]. Edmund Becquere was the first to observe this physical phenomenon in 1839 [6]. This field has been growing rapidly and a further growth is expected, perhaps at a higher rate [8]. Tackling the energy increasing demand can be obtained if a part of unexploited huge energy is converted into useful energy. The PV field, crystalline silicon cells dominate the PV market, however, fabricating and developing thinner wafers ongoing for less cost and higher efficiency, this might be achieved by nanotechnology [9]. Many countries in the past decade have started to promote research at different national and international levels in order to confirm the contribution of sustainable energy into total energy generation [1]. A wide range materials have been used in fabricating PV different applications which are available worldwide. Also, several new groups of materials are being developed. Among different materials used in fabricating thin-film based solar cells, ZnO is the chosen material of this project.

But, why is ZnO a good candidate for photovoltaic applications? This is because of the diversity and uniqueness of the ZnO nanostructures achieved by the researchers.

Zinc oxide has been extensively studied [10]. Over the past years, an important role has been played by semiconductors in the growth of technology. As a compound semiconductor, ZnO has the feature of direct and wide bandgap of about 3.37 eV. This feature permits and helps devices to be operated at higher temperatures, reducing the thermal noise of when low power devices are used, as well as promises achieving optoelectronic applications at short wavelengths. In contrast to bulk ZnO, the significant changes in ZnO nanostructural properties offer optional for PV [11]. The influence of nanomaterials with nano dimensions is more significant due to surface over bulk interactions. Increasing the surface area to volume ratio shows additional surface phenomena. Light trapping/light scattering structures and transparent contacts are the simplest ZnO-based materials applications in solar cells [12]. For instance, ZnO is used in ZnO-based DSSCs applications and different kinds of solar cells as an electron transport layer [12]. Crystalline ZnO nano-films have also gained attention to be used as a functional materials because of their optical, photonic and electronic properties, whilst the hydrothermal growth method offers a straightforward ZnO crystal morphologies [13]. During this study, the focus was on producing ZnO nanostructures by hydrothermal methods. Another highly attracted feature of ZnO is the possibility of growing it using different methods which are cost-effective such as electrodeposition method [14].

This thesis discusses the importance of ZnO nanostructures in photovoltaic applications. Also, these structures were grown on a releasable layer which known as lift-off process by using Omnicoat as a sacrificial layer for wet lift-off and PDMS as easy peeling off and flexible layer. SU-8 photoresist is widely used in a wide range of applications such as Microelectromechanicalsystems (MEMS), biologicalmicroelectromechanical systems

(BioMEMS) and micro-optoelectromechanical systems (MOEMS). This photoresist plays a pivotal role in pattern transferring as well as can be served and used as a support structural material [15]. Figure 1 shows the main three areas that this project focuses on.

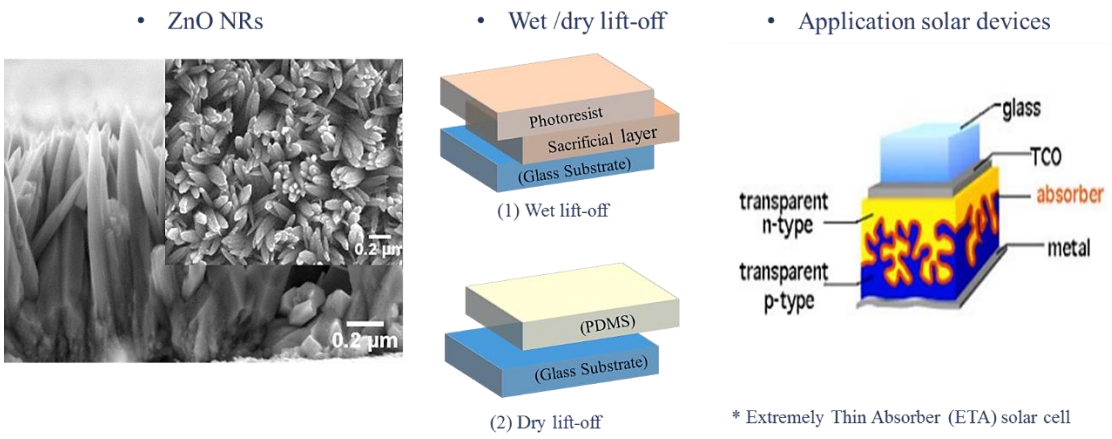

Figure 1. Three different main areas of this project.

A number of approaches can be used by researchers nowadays to enhance the light absorption effect of solar cells. e. g. using the textured surface structure of a transparent polymer. For example, using random-size inverted-pyramid-structured polydimethylsiloxane (RSIPS-PDMS) sticker reported by Hwang et al. [16] reflectance was significantly reduced comparing to bare device (without stickers). In solar cell applications, Polydimethylsiloxane (PDMS) is widely used because it has low refractive index (1.43) and high transmittance [17]. It can be used as an anti-reflective layer as it possesses good adhesion properties [16]. These features make PDMS to be easily attached and detached from different surfaces Tsui et al. [18].

1.2 **Thesis Organisation**

This thesis consists of seven chapters. And the outline of this thesis is as following: Chapter 1 is the introduction. Next Chapter 2 which will provide a review of the literature

to guide the understanding of the coming following chapters. Then experimental set up (methodology) Chapter 3 which is basically focus on the methodology used in this project to growth ZnO nanostructures as well as full details on lift-off process. Chapter 4 will discuss the detailed ZnO nanorods (NRs) fabrication using two different zinc salts and resulted characteristics, optical and structural properties. Chapter 5 will examine the released ZnO nanostructures grown on both Omnicoat/SU-8 photoresist and PDMS layers. Chapter 6 focuses on the extremely thin absorber solar cell and this chapter outlines the results obtained from the fabricated ETA solar cells. All major findings and justifications from this study will then be concluded in Chapter 7.

1.3 Contribution

The following original contributions to the research field were made as the results of the research carried out:

1. Demonstrating an experimental method in growing ZnO NRs grown on a releasable SU-8 photoresist layer.
2. Demonstrating an experimental method in growing flower-like nanostructure have been grown on PDMS layer.
3. Enhancing the performance of GaAs and CZTS solar cells using the lifted-off ZnO NRs and flower-like.
4. Fabricating extremely thin absorber (ETA) solar cells in superstrate configuration using CZTS nanoparticles.

Chapter 2 LITERATURE REVIEW

Renewable and sustainable energy sources are becoming progressively more vital because of increasing green-house gas levels in the atmosphere, the increasing expense of energy and the need to guarantee security of energy supply [19]. Solar energy is attractive since it is the most abundant energy source on earth. In one hour on earth, the sun provides energy which is identical to current yearly consumption [20]. Solar energy is considered to be the most harvestable and abundant renewable energy source [21]. As of late, huge advancements have been made in producing photovoltaics (PV) that can be possibly mass deployed [22]. PV is quickly evidencing to be one of the most powerful competitors for making renewables a typical energy source around the world [23]. It well recognized that, the energy that comes from the sun can be directly converted to electricity by using photovoltaic (PV) solar cells. Significant progress has been achieved to increase PV efficiency to about 34% in multi-junction cells [24]. Figure 2 demonstrates the projected and historic electrical consumption in the United States until 2035. Reliance on oil and coal is predicted to drop, while alternatives, for example, as renewable energy, natural gas and nuclear sources are expected to develop and grow and the energy of solar photovoltaic (PV) is expected to represent 17% of all power produced from renewable

resources by 2040, which is quicker growth than other sustainable energy sources in a similar category [25].

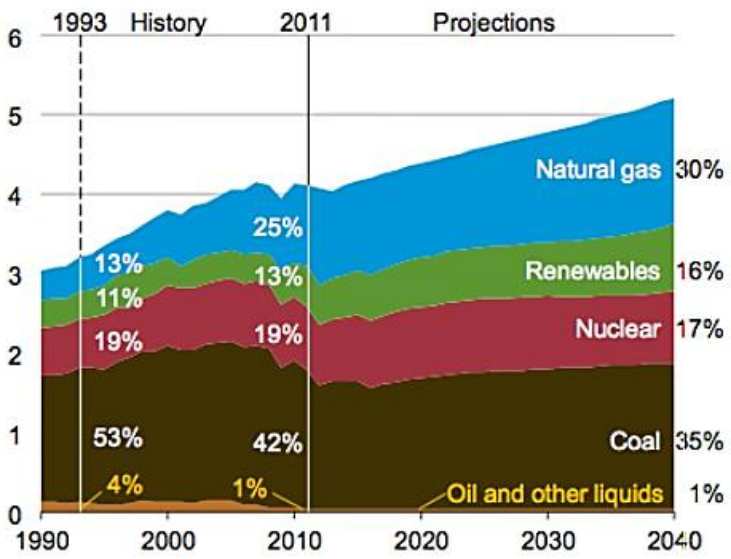

Figure. 2. Electricity generation by using fuel from 1990 to 2040 (trillion kilowatthours per year) [25].

Despite that, the PV solar cells currently contribute small energy portion to the overall world consumption. However there is a large potential of solar energy to meet the needs of energy demand. It was reported that, different solar devices like, solar photovoltaic, solar fuels and solar thermal can technically lead to harvest 600TW of the 10^5 TW of the energy hitting the earth [26]. But high cost is the limiting growth factor for solar cells. Nevertheless ongoing efficiency increase of solar cells will help to reduce cost. Also it worth mentioning that, as the fossil fuels become scarce, the grid electricity cost will increase. Hence, grid parity is the point where the PV electricity becomes less than power grid electricity [27]. Reaching to that point means that, solar cells will economically be more desirable which in turn will make them a primary energy source than the conventional energy source such as fossil fuels and coal [26]. The working principle of photovoltaic cells relies on solar energy exciting the electrons in a semiconductor material [28]. Doping the semiconductor or using n-type and p-type different semiconductors results in forming n and p regions. N-type semiconductor possesses extra valence

electrons while p-type has holes or excess positive charge [29]. Hence the current is generated due to the photons or light hitting the material and exciting the electrons and the current will travel around a circuit. Next, the use of ZnO nanostructures for lift-off processes and for extremely thin absorber (ETA) solar cells will be given.

2.1 **Zinc Oxide (ZnO)**

ZnO is an important photonic and electronic semiconductor material [30] that has a direct wide band gap (E_g ~ 3.3eV) [31, 32]. Wang Zhong claims that exhibiting the properties of piezoelectricity, semiconducting and pyroelectric multiple properties makes ZnO a unique material [33]. Abdulrahman et al. stated that, ZnO has excellent thermal and chemical stability, high transparency [32] and, as the research by Morkoc et al. shows, high exciton binding energy (60meV) will be paving the way for potential future applications [34]. Because of these significant physical properties, compared to other materials ZnO is a promising candidate in the development of excitonic emission applications above room temperature [32]. The feature of wide bandgap for a semiconducting material makes the material effective when it is processed at high power, high temperature and operations that applies large electric fields [35]. ZnO field emission characteristics is another interest for researchers. Comparing to CNT, ZnO nanostructures have threshold-field and turn-on field which are defined as macroscopic fields needed for producing current density of 10 mA/cm^2 and 10mA/cm^2 respectively [36]. The emission current density can be evaluated by the following equation:

$$J = \left(AE^2\beta^2 / \Phi\right) \exp\left(-B\Phi^{\frac{3}{2}} / \beta E\right) \quad (1)$$

Where J (A/cm^2) refers to the emission current density, E (V/cm) represents the macroscopically applied electric field, β refers to the field enhancement factor, A and B are constants. A = 1.56 × 10^{10} (A·V^{-2}·eV) and B = 6.83 ×10^3 (V·eV$^{-3/2}$·μm^{-1}), whereas

Φ is the emitter work function, and for ZnO it is about 5.4 eV [36]. Zinc sulphide is the most important zinc raw material and this type of zinc found as mineral sphalerite [37]. The most used process in producing zinc oxide is known as “French process” [37, 38]. The melting temperature for metallic zinc is about 419.5ºC when a graphite crucible is used, and it evaporates at 907ºC. Zinc oxide is formed by the resulted reaction between the evaporated zinc and oxygen in the air. The resultant agglomerated zinc oxide particles have up to 99% purity and with different sizes in the range of 0.1μm-few microns. The modified French process is referred to as the catalyst free combust-oxidized mesh (CFCOM) process. This process produces acicular zinc oxide nanostructures such as (wires, rods, plates, tetrapods and tripods) [38]. A large and growing body of literature has investigated the importance of metal oxide nanocrystals and their applications. Among different metal oxide nanocrystals, ZnO possesses numerous and noticeable characteristics. Although the literature covers a wide variety of theories this literature review chapter will focus on what appears repeatedly in the literature: the basic background of ZnO as a semiconductor and its utilization in growing different nanostructures. ZnO is one of the most promising materials that can be used to fabricate semiconductor applications such as optoelectronic and electronic devices [39]. The high thermal conductivity, high electron mobility, direct and wide band gap as well as large exciton binding energy lead ZnO to be suitable for several devices including, photodetectors, laser diodes, and thin film transistors[40]. However, as the study by Janotti et al. shows, regardless of the rapid progress made, it is still challenging to control the ZnO electrical conductivity [41].

2.1.1 **ZnO Properties**

The features of photoconductivity and piezoelectricity make this material the preferred candidate when fabricating a wide range of applications such as solar cells, UV optical

devices, biomedical applications and gas sensing [32, 42]. ZnO has diverse structures with rich configurations among any known nanomaterials, including nanotubes [33]. Last but not least, because of its biocompatibility and thermodynamic stability and because it is an environmentally friendly material, considerable interest has been generated in studies of ZnO as a powder, a single crystal structure, a thin film and ZnO nanostructures [42]. In the last, few years there has been a growing interest in using different materials are used to create and form different nanostructures. When the nanostructure is introduced, it tends to change both the intrinsic properties at nano size and the extrinsic properties. For example, it changes the sensitivity of the targeted application. All these changes contribute to a new behaviour of the application. To date, it has been shown in research by Ghosh et al. [43] that reducing the size of the particles has a significant effect on different important properties, for instance the structural parameters that depended on the nanoparticle size. Hence, the most difficult challenge when synthesising a nanocrystal is controlling its size, shape and morphology.

Nanostructures materials are represented to be one of the most facilitating engineering materials due to their morphologies, shapes, promising applications and their highly demanding fields such as electronics, sensing, automotive and biomedical. It is well known that; different materials are used to create and form different nanostructures [44]. When the nanostructure is introduced, it tends to change the intrinsic properties in nano size and extrinsic properties for examples the changing the sensitivity of the targeted application. All these changes contribute in a new behaviour of the application. As target of this project, the investigation of ZnO nanorods will be grown using hydrothermal methods. There is a large volume of published studies describing the multiple use of ZnO nanostructures [45]. These structures are attracting a great attention due to their importance in increasing the efficiency of the many applications. ZnO nanostructure can

be fabricated using different fabrication processes such as vapour phase processes, electrodeposition, chemical bath deposition and sol-gel processes etc. Moreover, different morphologies can be obtained such as spherical particles, wires, hollow tubes, and rods [46]. A brief summary of ZnO properties will be provided. These properties help in rational design when functional devices are targeted, as well as in the development of their potential for the future of nanoscale devices [47]. It is worth noting that shrinking the dimensions of the semiconductor down to a nanoscale will lead to some effects and changes in physical properties. These are known as quantum size effects [47]. ZnO optical properties, (e. g. refractive index) have been extensively investigated for decades due to their unique potential in a variety of practical applications [48]. These properties can be correlated with both intrinsic/extrinsic effects [34] . On the one hand, intrinsic optical transitions occur between the area of holes in the valance band and the electrons in the conducting band [49]. On the other hand, the extrinsic properties are attributed to point defects/ complexes and dopants, that in turn cause the creation of electronic states within the bandgap and hence effect the optical emission and absorption processes [34]. The optical properties of ZnO nanostructures have mainly been studied at room temperature, despite previously reported studies on variable temperature photoluminescence techniques on different ZnO nanostructures [47].

Over the past years, there has been a dramatic increase in the use of ZnO material. Its inherent optical properties and its counterparts such as nanoscale, which have been studied by several groups worldwide [50-52]. Many studies have been carried out for different photonic or optical applications, for example Xu and Wang have reviewed many features of the use of a wet chemicals approach to growing the 1D ZnO nanostructure, as these structures are environmentally friendly and show good optical properties for use in various novel applications [50]. Bousslama et al. have shown that, by using the sol-gel technique, single phase ZnO nanoparticles can be formed with quenched green emission

[53]. This confirms what has been observed of the nanoparticles and the ZnO nanoparticles -that they have fine optical properties with small defects [50]. A study by Shariffudin et al. has shown that the optical properties of the fabricated ZnO thin films have a significant dependency on their thicknesses. Their results showed that, as the film thickness increases, the UV emission intensity of photoluminescence PL spectra decreases [54].

The developments in the field of ZnO material have led to a renewed interest in its properties and its known that ZnO in its bulk form has a Young`s modulus (E) of about 111.2±4.7 GPa and a bulk hardness (H) of about 5.0±0.1 GPa [50]. Various concepts are involved when describing the mechanical properties of any material. For instance, on the one hand Young`s modulus, stiffness, hardness, yield strength and piezoelectric constants, the strain is a physical quantity that describes the deformation of the solids due to an external forces effect. On the other hand, the physical quantity stress can explain the resistance of deformation when an internal mechanical force is applied to the material. Also, it is well known that stress is proportional to strain [51]. ZnO is a rather soft material that has a hardness of approximately 4.5 on the Mohs scales [52]. It has the long optical phonon lifetime [36].

2.1.2 **ZnO Crystal Structure**

ZnO is one of the II-VI compound semiconductors group, but the iconicity of ZnO is on the borderline between ionic and covalent semiconductors [34]. ZnO can crystalize in three different forms: wurtzite, known as hexagonal symmetry, zinc blende and rocksalt, known as cubic symmetry, as shown in figure 3 [34]. However, the crystals of ZnO are

mostly stabilized in the structure of Wurtzite with a hexagonal close packed structure. The rock salt phase results only when high pressures exists about 10 GPa [34].

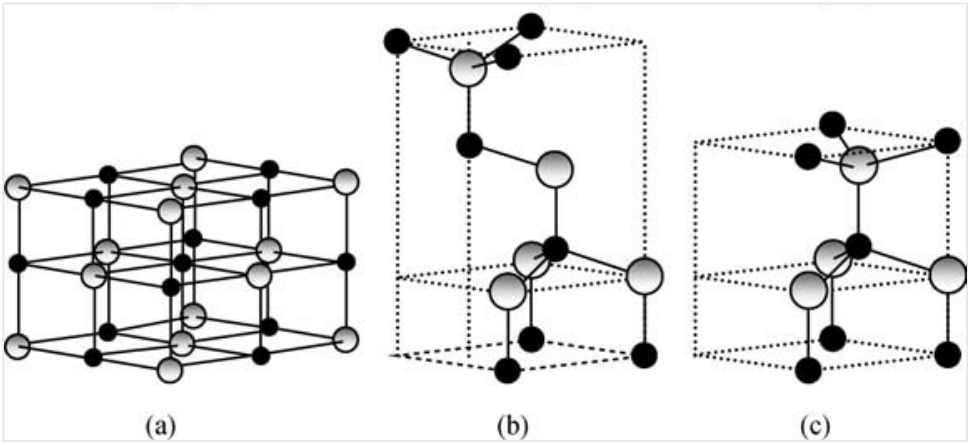

Figure 3. Representation of the three different crystal structures of ZnO. A) Represents the rocksalt, b) zinc blende and c) is the Wurtzite structure [34].

In an ideal wurtzite structure, the hexagonal unit cell and two different lattice parameters referred to as a and c are present in the wurtzite structure and the ratio of these two lattice parameters is approximately c/a=√ (8/3) =1.633[34]. The wurtzite structure consists of two cation (Zn), anion (O) sub-lattices known as interpenetrating hexagonal close packed (hcp), and the cation-anion length within the preferential c-direction causes their displacement. Each (hcp) is comprised of one atom displaced for each other along the threefold c-axis using $u = 3/8 = 0.375$ within the fractional coordinates. The parameter u represents the bond length parallel to the c-axis (the bond length of anion–cation or the closest neighbour distance) divided by the lattice parameter c). α and β represent the bond angle. In such a structure, the four cations surround each anion at the tetrahedron corners and vice versa. The (sp3) covalent tetrahedrals represent the bonding in these materials, however, it was found that other ionic characteristics exist in these materials and can be explored.

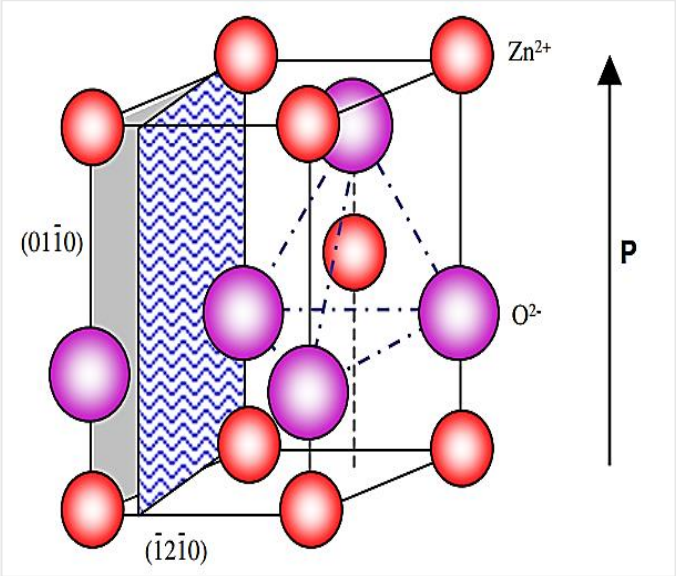

Figure 4. The ZnO wurtzite structure model with tetrahedral coordination of Zn–O [55]

2.1.3 **Zinc Oxide as a semiconductor**

In the past decade, the research on ZnO as a semiconductor has witnessed a revival. When ZnO is initially used as a substrate for GaN and its related alloys, a number of reasons, including its luminescence spectra and the high-quality of the resulting bulk single crystals, have led researchers to switch their focus to its photonic and electronic devices. There is, however, a major issue around the required control of ZnO conductivity and for this reason, it is important to understand the role that native point defects play. Therefore, incorporating impurities is the key to controlling ZnO conductivity [41]. Studies on the properties of ZnO began in the early days of research on semiconductor materials. However, because it was impossible to control its conductivity using ZnO as a semiconductor, particularly in electronics, applications has been hindered [56]. The crystals of ZnO are always n-type a cause of extensive research and debate [41]. It was found that [57] the damage caused by electron irradiation in ZnO is less severe than that found in other semiconductor materials, which makes ZnO of potential use in space applications. However, developing an efficient p-type of ZnO is a challenge, which is

necessary for developing efficient light-emitting devices [57]. Despite ZnO's unique properties in the fabrication of electronic and photonic devices, a number of problems have to be solved prior to producing the most attractive devices in the future [57]. Although Aoki et al. have managed to measure the light emission and diode-like behaviour of p-type ZnO [58], the fabrication of Schottky barriers is, according to Look D C, still a problem [57]. However, experiments by Liu et al. [59] have achieved some success.

2.1.4 **Zinc Oxide Nanorods (ZnO NRs)**

Figure 5 shows the growth of different nanostructures [60]. In the 1960s, research on synthesising ZnO thin film was very active due to its remarkable performance in applications to photonics, optics and electronics. For example we have the work of Baruah et al. [61] and Muchuweni et al. [62]. The study of one-dimensional nanostructures by Baruah et al. found that when size is reduced, novel optical, electrical, chemical and mechanical properties can be introduced into the material from quantum confinements, and increased ZnO conductivity can be achieved by doping [61].The study presented by Iijima [63] in 1991 on the discovery of carbon nanotubes, helped initiate active research into growing and characterizing 1D nanowires to be used for compound and elemental semiconductors such as ZnO [64, 65], Ge [66], GaAs [67], Si [68]and InP [69].

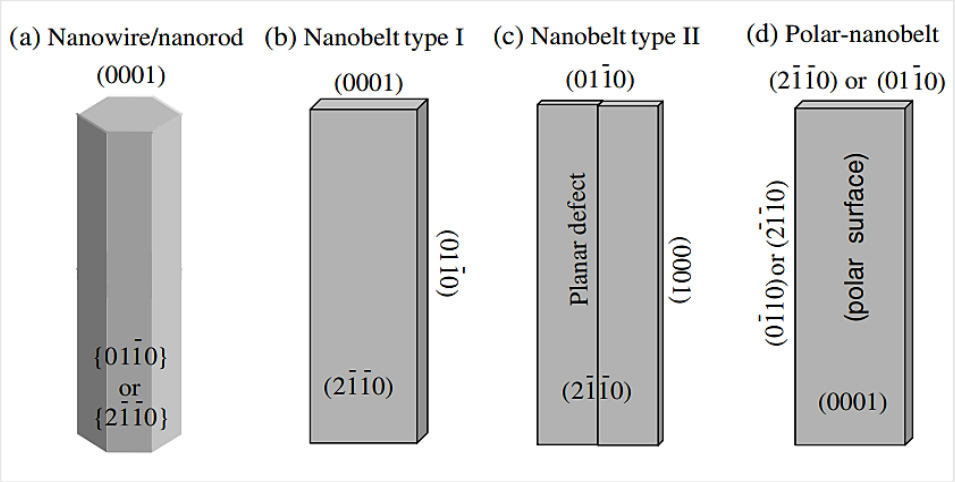

Figure 5. The growth of different nanostructures [60].

2.1.4.1 **Synthesis of Zinc Oxide Nanorods**

Synthesising ZnO semiconductors has attracted the attention of researchers in the past decades, since this material offers several unique characteristics and multifunction properties, which make it a preferred material. Many researchers, for example [47, 70, 71] have studied the growth approach and mechanisms of form of different ZnO and its different nanostructures including nanorods, nanotubes and nanowires [47]. Along with nanotechnology and the development of nanoscience, the synthesis of a nano-scaled ZnO is now a focus for researchers since nano-scales have better optical and electronic characteristics than bulk materials [72]. Two stages used by Idiawati [72] have effectively proved the formation of ZnO nanostructure on the used substrate, either by the liquid or vapour phase approach. Different vapor-phase techniques have been employed, such as chemical vapor deposition [73], metal organic chemical vapor deposition [74] and vapor-liquid-solid [75] However, some of these techniques have drawbacks that make them undesirable in a number of processes because of cost, high energy consumption, the relatively long processing time and relatively high temperature required as stated in [75, 76]**.** The vapour transport method is one of the most common synthesis approaches used to grow ZnO nanostructures. Zhiyong Fan et al. have explained the working principle of

this process as follows: oxygen mixture vapors like Zn and O are brought together hence, and react with each other producing a ZnO nanostructure [47]. Several methods can be used to generate the vapour of Zn and O such as the decomposition method which is a simple and direct approach. However, Kong et al. acknowledges it has the drawback of requiring high temperatures of around 1400°C and that low temperatures cannot be used [77]. Another method, used by Dang demands temperatures ranging between 500-700°C and works by heating ZnO powder in a flow of oxygen [78]. However, as seen in the research of Fan et al. to obtain the desired nanostructure, the ratio between the oxygen pressure and ZnO vapor pressure has to be controlled [47]. As seen in studies by Gautam et al. [70] compared to the above-mentioned technique, the liquid phase technique is more cost-effective and easier when applied to a wide scale range. Researchers such as Kumar and his group [74] are currently investigating different solution-based growth techniques such as hydrothermal, sol-gel, chemical bath deposition and electrodeposition. Of all these methods, the hydrothermal is the preferred choice for many researchers because of its simple and cost-effective method [70]. The hydrothermal approach is used to direct the formation process of several metal oxides as it does not require a complex process, does not require high temperatures and can be applied on a wide scale range [79]. Hence, the hydrothermal growth method has been chosen in this project on ZnO NRs.

2.1.4.2 **Zinc Oxide Hydrothermal Synthesis**

Due to low dimensionality, quantum confinement effects result in one-dimensional nanostructures, and these structures exhibit interesting optical and electronic properties [61]. ZnO was used for years to develop diverse applications [80]. Among the several growth methods, the hydrothermal technique is the most attractive for ZnO due to its tolerable growth conditions, environmental friendliness and simplicity [61]. Sunandan et al. have stated that two methods can be used to grow a nanostructure by either a gaseous

phase, which is more expensive, or a solution-based process, which is carried out in water. When the growth is carried out in aqueous solutions, the growth temperatures used are no higher than the boiling point of water [61]. The classification of the various methods used to grow ZnO nanostructures is as follows:

1. Solution-based method: Here the process is simply carried out in an aqueous solution and thus the process is known as a hydrothermal process. Different processes can be used in this type of growth method such as the sol-gel route [81], template assisted growth [82], spray pyrolysis to grow a thin film [83], and electrophoresis [84].

2. Gas-phase based method: in this approach, a gaseous environment is used when the targeted sample on which the nanostructure is to be grown is placed in a closed chamber where high temperatures ranging from 500-1500 ◦C are used. Different common processes can be used in this type of growth method: a metal organic chemical vapour deposition (MOCVD) [85], vapour liquid solid (VLS)/vapour solid (VS) [86-88], chemical vapour deposition [89], and physical vapour deposition [90].

ZnO NRs that are synthesised in this project are targeted to be used for photovoltaic applications as mentioned in the thesis title. The next section will give an overview on solar cells and light trapping is being enhanced when introducing a texture structure instead of a flat structure.

2.2 **Solar Cells**

Photovoltaic (PV) devices are classified into three different types. Monocrystalline semiconductor silicon which is intrinsically rigid and known as the first generation; thin film PVs which known as the second generation and third generation [91]. Crystalline silicon (Si) is the material that is the most commonly used in solar cells. However, for the

terrestrial application, the cost is the obstacle [92]. Making thin film solar cells on adaptable and flexible polymer substrates or metal foil yet offers many advantages of interest for both terrestrial and space applications [93]. When comparing to a glass substrate, weight savings are significant for flexible substrates due to the possibility of making 5μm solar cell thickness and 5-10μm flexible substrate thickness rather than 3mm thick glass. Despite crystalline Si being the dominant type of solar cells, other solar cells have been produced which can compete in terms of higher efficiencies (III-V compounds based solar cells) or cost reduction from thin film amorphous silicon (a-Si), cadmium telluride (CdTe), or copper indium gallium (di) selenide (CIGS) thin film based solar cells etc. These semiconductors have bandgaps ranging from 1.1 to 1.7 eV, which is close to the ideal energy bandgap of 1.5 eV for PV solar radiation conversion when a single junction solar cell is used.

2.2.1 **Types of Solar Cells**

There are three different types of PV technologies: first generation, referred to as wafer-based, second generation referred to as thin-film [94] and the third generation nanocrystal cells (polymer-based) [95]. For extensive commercial use, the electricity generated from Si solar cells is still too expensive, though it is hoped that its price will fall [96]. However, Kim et al. showed a new technique to design low-cost and high-efficiency monolithic tandem cells based on p-type homojunction Si cells [97]. Some of the best-reported efficiencies are shown in table 1.

Table 1. The reported best efficiencies of different solar cell type [98].

Solar cell Type	Efficiency	Laboratory/institution
Crystalline silicon	24.7	University of new south Wales
Multi-crystalline silicon	20.3	Fraunhofer institute of solar energy system
Amorphous silicon	10.1	Kaneka
HIT cell	23.0	Sanyo Corporation
GaAs	26.1	Radboud University Nijmegen
InP cell	21.9	Spire Corporation
Multi-Junction cell	40.8	National Renewable Energy Laboratory
CdTe	16.5	National Renewable Energy Laboratory
CIGS	19.9	National Renewable Energy Laboratory
$CiInS_2$	12.5	Hahn Meitner Institute
DSSC	11.1	Sharp
Organic Solar cell	6.1	Gwangju Institute of Science and Technology

Crystal silicon shows the highest efficiency level of about 24.7%, whereas the other types of solar cells show less as can be seen in table 1 [98]. III-V group and II-VI group are currently the most common compounds used to fabricate different types of solar cells, and triple junction is used with Ge, GaAs and GaInP layers that can give about 30% efficiency [98]. Figure 6 shows different types of solar cells such as the Si(n)-based cell [99]. and perovskite solar cell with Al-doped ZnO NRs [100].

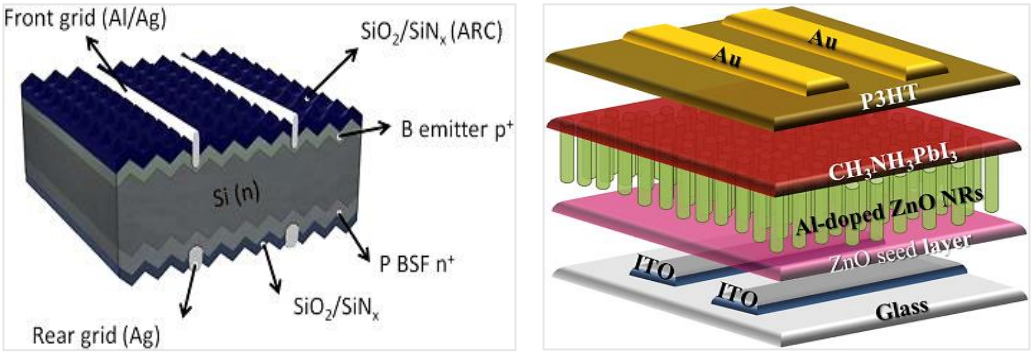

Figure 6. Two different types of solar cells. (a) Silicon n-based cell, (b) Perovskite solar cell with Al-doped ZnO NRs [100].

2.2.1.1 **Zinc Oxide Nanorods-Based Solar Cells**

It is possible to improve the ZnO semiconductor performance if the nanorods length and diameter are optimized and this will cause the surface area to increase and this optimization can be obtained by varying the growth process time [101]. Son et al. showed the effective influence of ZnO NRs when fabricating ZnO NRs based perovskite solar cell and the highest efficiency of 11.13% was achieved as they stated as shown in figure 7 [102]. Relating to the above facts, increasing the electron transport is crucial as it has a significant influence on improving the indicator electrode photosynthesis [101]. According to studies accomplished in 1D nanorods, it was proved that, its morphology has the ability of increasing the electron diffusion on the electrode film and that offering direct conduction pathway. Manorotkul et al. [103] have stated that, the direct pathway within the nanostructure can lead to decreasing the effect of charge recombination that can be happen when the randomly-oriented nanoparticles are exists [103].

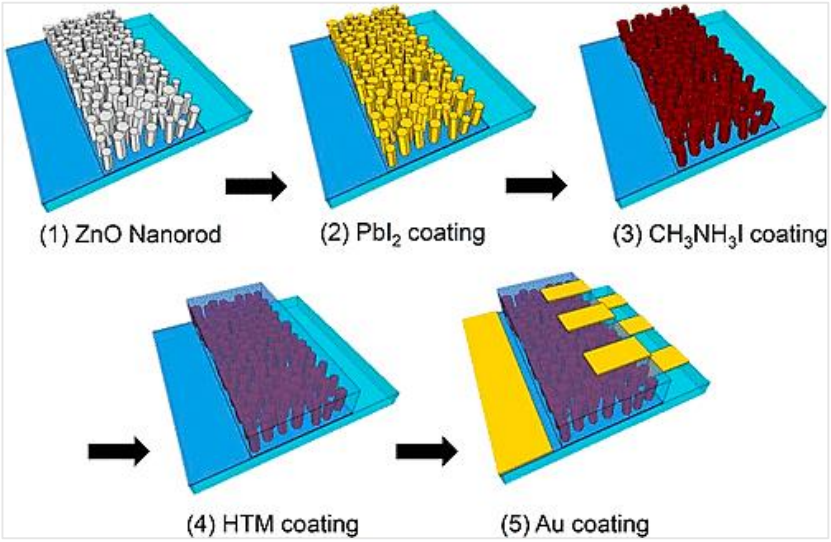

Figure 7. The fabricated perovskite ZnO based PSCs [102].

2.2.2 **The Principle of Photovoltaics and Semiconductor**

2.2.2.1 **A Semiconductor**

In 1782, Alessandro Volta used the term "semiconductor" for the first time [104]. In 1833, Michael Faraday observed the semiconductor effect by noticing the increase of silver sulphide as the temperature changes and this observation was totally different from the one obtained from metals [105]. Certainly semiconductors changed the world e.g. communication and data processing. The rapid progress of physics/electronics semiconductor applications and integrated circuits has led to the provision of increasing amounts of information [101]. New theories, ideas, devices, circuits and models have not only prompted various practical applications but have also provided an opportunity for future and even more significant developments. Working in such a field, though it is not an easy task, inspires and attracts many students and researchers [101]. A number of requirements have to be considered for modern semiconductor devices, such as faster operation while consuming less power, and to achieve that, shrinking/scaling down the size of the device is required [101, 106]. The physics involved to understand semiconductor material performance can be complicated due to dimensions shrinkage and the use of more exotic/complicated materials to fabricate semiconductor devices [101]. Intense research has been carried out for years, and significant efforts have been made to study semiconductor heterojunctions, as this field is an excellent example of the influence and interaction of basic science and nanotechnology and Shockley earlier suggested the utilization of heterojunctions in order to achieve a better performance from the device and he used the celebrated transistor patent [107], whereas Kroemer, two years later, showed the principle of compositionally graded semiconductors [108].

2.2.2.2 **P-n Junction**

When the p-type and n-type of semiconductor materials are brought together, then a p-n junction is formed [109, 110] and it is well-known that, at least one junction is present between the two types in a semiconductor. The operation and characterization of any semiconductor material are intimately correlated to these p-n junctions, and hence researchers are devoting a significant attention to these basics of the devices [109]. According to the Hall Effect theory, first discovered in 1878 by Herbert Hall, there is a deflection of the charge carriers inside the solids and this deflection occurs in a magnetic field. This phenomenon was exploited later by Lukasiak, [105] in studying the different properties of semiconductor materials **.** Eduard [105] has an interesting theory, dating from 1899 that two different charge carriers are present as negative and positive with different mobilities and concentrations. It is essential to understand that the entire semiconductor device is basically a crystal material where acceptor impurity atoms are doped in one region, these dopants are from the p region, and donors are doped to the other region from n type region. Hence the interface separating the two types is known as a metallurgical junction [109]. It is worth mentioning that [111] the absorption process has a strong dependence on the wavelength of the incident light on the device that is related to photon energy expressed as following equation:

$$E = \frac{hc}{\lambda} \qquad (2)$$

Whereas E is photon energy, h represent Planck`s constant, c is the speed of light and λ is light wavelength. In inorganic cells, to dissociate charge carriers, a p-n junction is used. Figure 8 illustrates the conventional geometry of p-n junctions [112]. The diffused electron form n-side to p-side is derived by the concentration gradient that occurs between

the two doped n and p sides. To be precise it crosses the interface from right to left and hence holes are lifted in n-side, while vice versa, holes that will cross to the opposite direction leave electrons in p-side [112]. According to Shockley et al. an equilibrium is reached and the electrical field is the interface by space charge region [113].

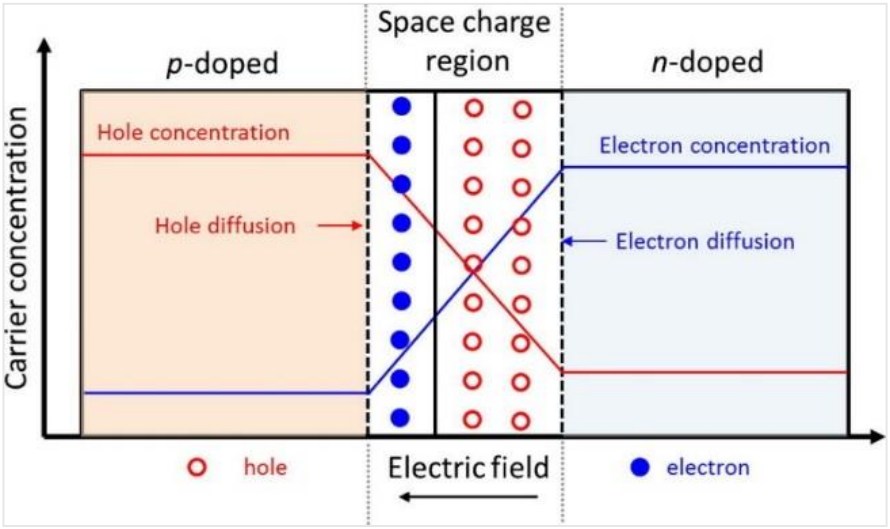

Figure 8. P-N conventional geometry [112].

2.2.2.3 **The Photovoltaic Theory**

In 1883, Charles Fritts managed to construct the first working PV cell with less than 1% efficiency and the constructed cell comprised a metal plate, with a thin selenium layer coated by a thin gold layer [105]. The photovoltaic effect inside solid materials was first discovered by Day and Adams in 1876 as they observed the change in the direction of the current in the presence of light by using a battery connected to selenium [105]. Alexander Edmund Becquerel in 1839 discovered the photovoltaic effect between an electrolyte and a semiconductor within the junction region [114]. Willoughby Smith [103] discovered photoconductivity in 1873. About 25% efficiency can be obtained nowadays from single crystal silicon solar cells that dominate the market at present [112]. However, a number of drawbacks such as indirect bandgap and low light absorption, mean that these single crystal cells require about 200-250 μm to harvest sunlight efficiently [112]. Si solar cells

have been extensively used in building roofs and solar farms, but they are not appropriate for electronic applications that require transparency and flexibility, nor for integrated PVs like facades, widows, and thus thin film solar cells are attracting increasing attention by researchers [112]. The working mechanism of a solar cell can be summarized as follows:

1. Sunlight generates photons, which in turn hit the surface of the solar cells, and get absorbed by the semiconductor material used.
2. An excitation of electrons from the original molecular orbital will result.
3. The excited electron will either be lost as heat or contribute to an electrical field when it reaches the electrode used.
4. The solar cell will convert the sunlight into current. The efficiency of converting sunlight into electrical power can be defined as the follows [112]:

$$\text{Effeciency}(\eta) = \frac{\text{output electricity}}{\text{input sunligh energy}} \tag{3}$$

Where η refers to the power conversion energy. Furthermore, in practice, η of solar cells can be expressed as:

$$\eta = \frac{p_{max}}{p_{in}} = \frac{J_{mp}.V_{mp}}{P_{in}} = \frac{J_{sc}.V_{oc}.FF}{P_{in}} \tag{4}$$

Where, P_{max} , P_{in} , J_{mp}, . V_{mp}, J_{sc}, . V_{oc} FF represent maximum power output, power input, current density, voltage at the maximum power point, short circuit current density, open circuit voltage and fill factor respectively. Figure 9 illustrates the typical I-V curve in a solar cell device [112]. The diagram shows a typical PV cell's current-voltage (I-V) characteristics working under normal conditions. Current and voltage product is the electricity provided by a solar cell. The power curve is obtained for a used radiation level. With the open-circuited solar cell, which is not attached to any load, the current is at its minimum (zero) and the voltage across the cell is at its peak, defined as the open-circuit voltage solar cells, or V_{oc}. Then the curve of the solar cell I-V characteristics ranges from

short circuit current (I_{sc}) at zero output volts to zero output voltage at full open circuit voltage (V_{oc}). In other words, at the open circuit is the peak voltage available from a cell, and at the closed circuit is the maximum current. Naturally, neither of these two conditions produces electrical power, however there must be a point in the solar cell where maximum power is generated.

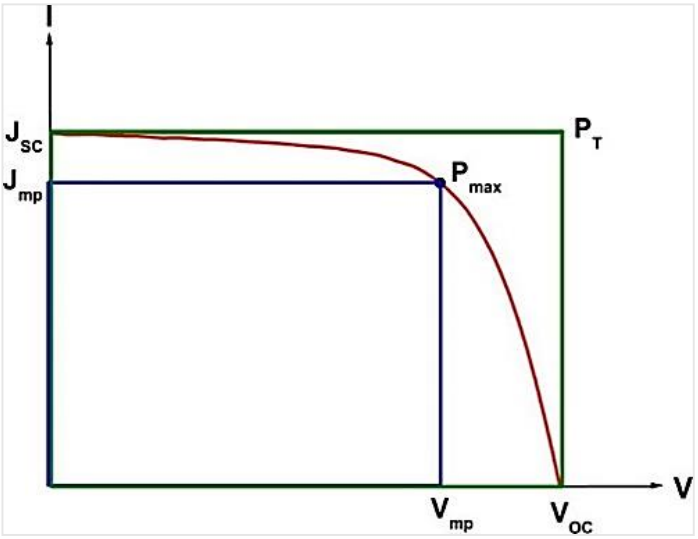

Figure 9. Illustration of a typical I-V curve in a solar cell device [112].

2.2.3 **Light trapping in solar cells**

To improve the efficiency of thin-film solar cells, a major challenge that has to be addressed is the trapped light within the cell [115]. The factors that lead to a decrease in solar cell efficiency are the different wavelength of the absorbed spectrum, and the thickness of the used absorber layer because the band gap plays a pivotal role. In this study, a ZnO nanostructure will be used to enhance light absorption of the solar cell. In addition, we will study the behaviour of the light trapped within the solar cell, because the nanorods have (NRs) has a significant effect on increasing the light scattering effect. NRs will allow the light to be scattering in random directions. The ability for light absorption is considered to be a non-negligible factor when the structure characteristics

are taken into account. When the light is incident on the nanorods, it will multi-reflect between the nanorod structures, increasing the intensity of the absorbed light. In a solar cell, achieving light trapping can be obtained by changing the angle of light travelling in a solar cell by creating an angled/textures surface. This will lead to reduce the light reflection hence trapping the light for longer within the device. The angle of reflection can be expressed by Snell`s law as shown in following equation [116]:

$$n1 \sin \theta 1 = n2 \sin \theta 2 \quad (5)$$

Where $\theta 1$ and $\theta 2$ are the angles of incident light and n1 and n2 are refractive indexes. Figure 10a) and Figure 10b) show the different between the flat surface and textured surface that have a significant effect on the light directions within the material.

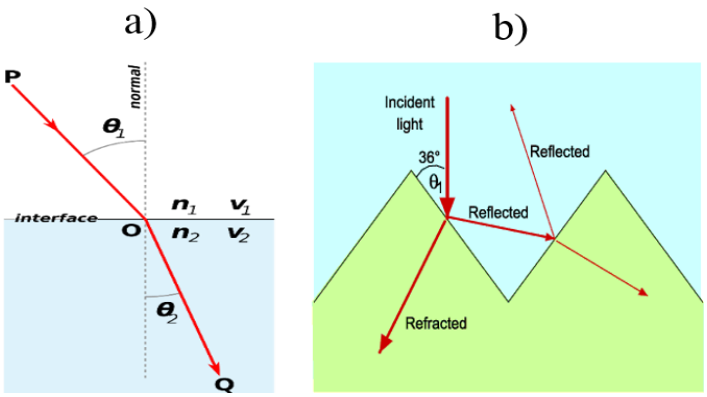

Figure 10. a) Light refraction at the interface of two different mediums having two different refractive indices and b) transmittance and reflection of light in a texture silicon solar cell.

From the figure it can be clearly seen that, in a flat surface interface 10a), when the light is traveling from high refractive index medium to low refractive index medium. The light direction changes and the light is reflected. While adding or creating a texture surface 10b) of a solar cell will enhance the light to be reflected in different directions inside the cell. Therefore, by taking the advantage of total internal reflection, trapping the light can be achieved and the light will distribute randomly. Therefore, light will have multiple passes through the cell which in turn will allow even thin solar cells to sustain high optical

path length. The subwavelength-scale nanostructures for example nanowires and nanoholes have gained a significant attraction due to the induced light trapping when using them. Basically what happens to the light after incident on the mentioned nanostructures can be seen in figure 11 as illustrated by in [117]. They showed that, the photon of incident light will bounce forth and back between the nano-gaps and thus increasing the absorption of light. Inorganic materials such as ZnO and Si are in general more robust comparing to organic material and environmentally friendly [118, 119]. Hence, inorganic materials can be preserved for longer and their manufacturing is easier than the organic ones.

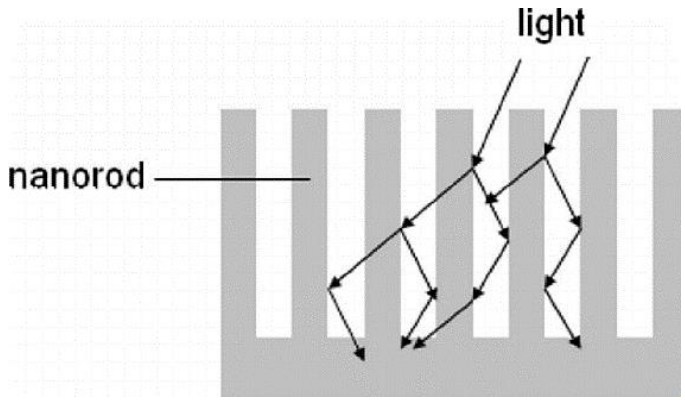

Figure 11. Schematic diagram of light trapping effect within a nanostructure[117].

Another option that is having a great attention is the usage of photonic crystals. Photonic crystals technology can serve as a platform technology for photovoltaic applications [120] as shown in Figure 12. From 12a), significantly, converting large portion of light to photovoltage might not be possible due to the reflectance that occurs at the to-side (front surface) and leakage from the bottom-side (back surface). Increasing the device thickness might yield absorption however it means sacrificing the conversion energy. From 12b), the light is more trapped in the high n and that is due to the textured surface thus light will be converted to photovoltage.

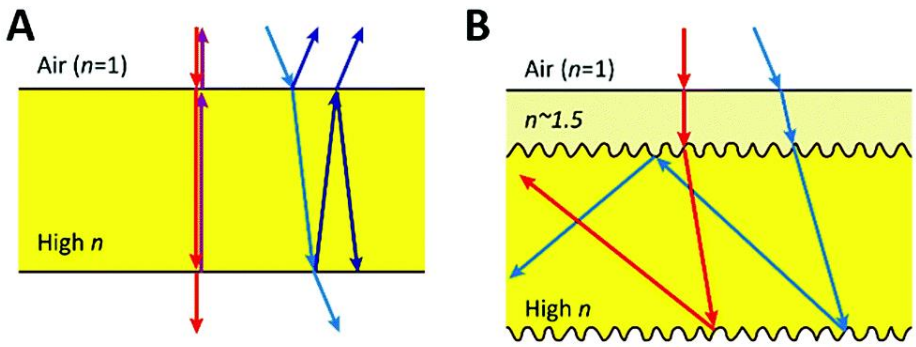

Figure 12. Light trapping in high-index (n) solar cell. A) without surface texturing and b) with surface texturing [120].

Hence, to achieve ultimate success in photovoltaics technologies, advancements in efficiency improvement and material cost reduction are required. These can be obtained simultaneously by using light trapping systems. The process of light trapping has the feature of improving cell efficiency, since better collection of the charge carriers is provided when a thin layer is utilized, and absorbs the incident sunlight through an active layer material that is thinner than the intrinsic materials and Figure 13 shows the trapped light using two different surfaces, a textures surface and a periodic grating placed in the back reflector [106].

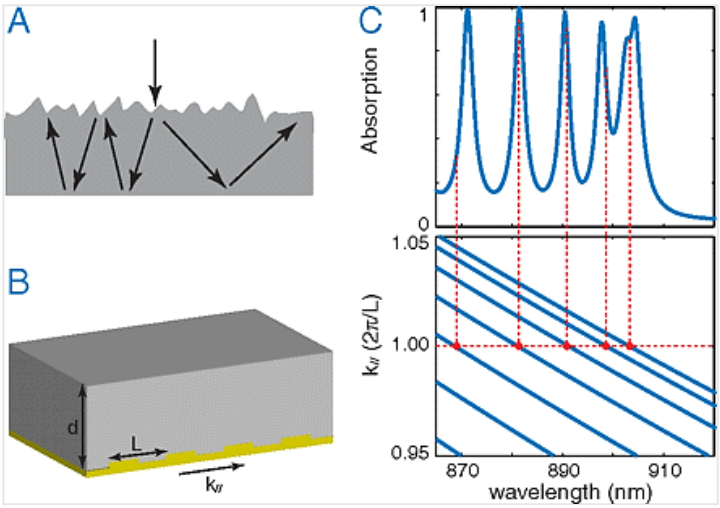

Figure 13. Light trapping using random texture, grating structure. a) Trapped light in a textures interface. b) Back reflector with periodic grating on. c) Absorption spectra and waveguide dispersion relation for b structure [106].

If the light is propagated in random directions inside the material, the effect of total internal reflection will increase, which will result in increasing the propagation distance of the light, and thus achieving essential absorption enhancement. The factor of absorption enhancement has an upper limit known as Yablonovitch or $4n^2$ limit and can be expressed by the following equation [106] :

$$\frac{4n^2}{\sin^2\theta^{2-3}} \tag{6}$$

Where ɵ represents the emission cone angle in the surrounding medium and *n* active layer refractive index. When a single resonant contribution is defined to the total absorption within wide spectrum, the individual resonance can be described by using the equation of temporal coupled mode as:

$$\frac{d}{d}a = \left(j\omega_\circ - \frac{N\gamma_e + \gamma_i}{2}\right)a + j\sqrt{\gamma_e}S \tag{7}$$

Where a is the amplitude resonance, ω resonance frequency, γ_i the rate of intrinsic loss because of the material absorption, S incident plane wave amplitude and γ_e the rate of the leakage resonance to channel with incident waves The rate of the intrinsic decay is related to the coefficient of the material absorption α_0 by the following equation:

$$\gamma_i = \alpha_\circ \frac{c}{n} \tag{8}$$

As ZnO NRs are studied in this project, it is important to consider the light-trapping effect, which represents a major route in achieving the desired target [101]. Two main factors can be considered a major limitation to the fabrication of an efficient solar cell: a thinner absorber layer and long absorption length of the incident photons [101]. One of the solutions to increased light trapping is a textured metal back-reflector**,** so that the light will be scattered in the absorber layer and the optical path length of the incident photons

will gradually increase [101]. Another way of increasing the efficiency of a solar cell is by employing 1D nanostructures, and that will offer a direct pathway to more electron diffusion [107].

2.3 Lift-Off Process

To practically design solar cells, different light trapping techniques have been broadly applied with the intension of achieving near complete absorption of sun energy using small solar cells thickness than the material absorption depth [121]. Different features can be found in using light trapping such as material and solar energy cost reduction. Also, thinner cells (when avoiding sacrificing the absorption ability) can enhance the carrier exaction which in turn will enhance the solar cell efficiency [122]. Likewise, a thinner solar cell device which keeps the thicker device absorption might have a higher voltage. The following section reports the lift-off process used to release the ZnO nanostructure in this project. In this project, the negative photoresist Poly methyl methacrylate (PMMA), SU-8 and Polydimethylsiloxane (PDMS) have been used. More details on each type will be provided. Negative SU-8 is the targeted support structural material in this project, as this material meets the need of the sequence process steps due to its compatibility and wet chemical resistance (for wet lift-off) and PDMS is the used material (for dry lift-off).

2.3.1 The Photoresist

The photoresist can be defined as a light sensitive material that can be exploited to create patterns on a specific surface by both photolithography and photoengraving processes, and this is a crucial step in the electronics industry [123]. The main components of any photoresist are four in total: resin, sensitizer, solvent and other additives. Firstly, the resin

is the binder, which can provide the required adhesion and is known as etc- poly (cis-isoprene) chemical resistance. Secondly, the sensitizer is a photoactive composite like t-butyl benzoic acid, bis (aryl) azide). The third compound is a solvent, which is used to keep the resist in its liquid form. Finally, there are other additives to facilitate and enhance the materials' properties [124].

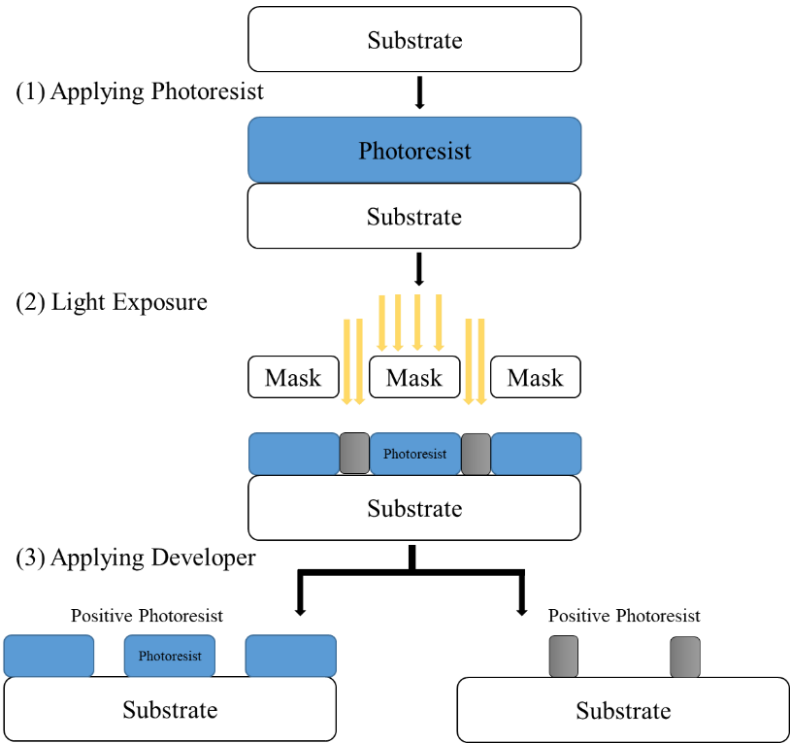

Figure 14. Lithography of photoresist using Positive Vs Negative Photoresists

There are two types of photoresists: negative and positive, as shown in Figure 14. On one hand, the light exposed portion of a positive resist becomes soluble in the development solution and the unexposed portion does not. On the other hand, the exposed area in a negative photoresist is insoluble in the development solution and the developer can dissolve the unexposed portion. The main differences of the two types of photoresist can be seen in table 2.

Table 2. The main differences of the negative and positive photoresist [125]

Characteristic	Positive	Negative
Adhesion to Silicon	Fair	Excellent
Relative cost	More expensive	Less expensive
Developer Base	Aqueous	Organic
Minimum features	0.5 µm	2 µm
Wet Chemical Resistance	Fair	Excellent
Step Coverage	Better	Lower
Solubility in the developer	Exposed region is soluble	Exposed region is insoluble

2.3.1.1 **Support Structural Layer and Sacrificial layer**

The SU-8 photoresist is used here as a support structural layer and Omnicoat as a sacrificial layer. SU-8 is an epoxy-based photoresist that has a high contrast, high sensitivity to ultraviolet (UV) light, and high optical transparency at around 360nm.These properties make SU-8 a suitable material to fabricate high aspect ratio structures [126]. IBM first discovered SU-8 in the late 1980s and its very first applications was as an inexpensive replacement for x-ray lithography in the LIGA process (German acronym for lithography), using near-UV lithography and SU-8 instead [127]. Omnicoat is extensively used as a sacrificial layer under the SU-8 layer.

2.3.1.2 **SU-8 Photoresist**

Due to its unique properties, SU-8 adheres to different substrates and surfaces as shown in table 2, considering the specific processing conditions. This good adhesion makes it the favourite material in permanent structural material. Its other properties make it attractive for structural material in (Micro Electro Mechanical Systems) MEMS applications. Firstly, its processing is simple: different range of thicknesses can be obtained by simply using a spin coating technique [128]. Building up the SU-8 layers can be achieved by spin coating multiple layers until the desired thickness is obtained. Secondly, its optical transparency offers the possibility for SU-8 to be used as a glass

substitute and for pattern alignment in lithography processing. Thirdly, SU-8 when it is cross-linked, has significant chemical resistance to chemicals solutions if used in wet process. The basic process flow of SU-8 photoresist is presented in the experimental chapter. Prior to applying the SU-8 resist on the targeted substrate, proper cleaning and drying must be performed on the substrate in order to achieve the maximum reliability of the process. After that there comes the coating step, followed by the edge bead removal step, soft baking, exposure, development and post baking steps. It is well known that obtaining the optimized SU-8 layer varies according to each different application. Microchem is the manufacturer of the SU-8 resist used in different experiments, and its trade name is EPON™ SU-8 (from Shell Chemicals) [129]. The dissolution of the resist is obtained by using organic solvents such as (cyclopentanone) CP or (gamma-butyrolactone) GBL. The viscosity of the resist can be determined by the added amount of the solvent during formulation which determines the achievable resist thickness. It is worth mentioning that the SU-8 2000 series of the photoresist is used in this project as a support structural layer.

The highly branched EPON™ SU-8 polymer consists of novolac glycidyl ether. Regarding its chemical structure, a single molecule in SU-8 resist has eight epoxy groups, which the number 8 (in SU-8 term) is derived from. Figure 15 shows the SU-8 molecule diagram. SU-8 is formulated from a solution made from mixed resin with triarylsulfonium salt (known as a photo-initiator) and cationic photopolymerization (CP) solvents. As a result of the near-UV exposure effect (365nm), a photochemical reaction is induced because of the photo-initiator and UV light, and hence a strong acid is generated when the resist layer in baking stage. Thus, the polymerization process is facilitated by the photoacid by the action called ring opening cation polymerization. It should be mentioned that only the exposed region of the photoresist will cause photoacid generation. At this step, it is crucial to consider that, as the glass transition temperature is about 55°C, the

temperature required to polymerize the resist must be higher [130]. It is not an easy task to remove a fully cross-linked SU-8 as it has a chemical resistance to many organic solvents, bases and acids. Microchem has recommended that plasma removal, pyrolysis, RIE, piranha etch and laser ablation can be used to strip the resist film [131]. If plasma removal is the selected method, the following process is recommended by Microchem (RIE 200W, 80 sccm O_2, 8 sccm CF_4, 100mTorr, 10°C). Where, sccm is Standard Cubic Centimetre/minute.

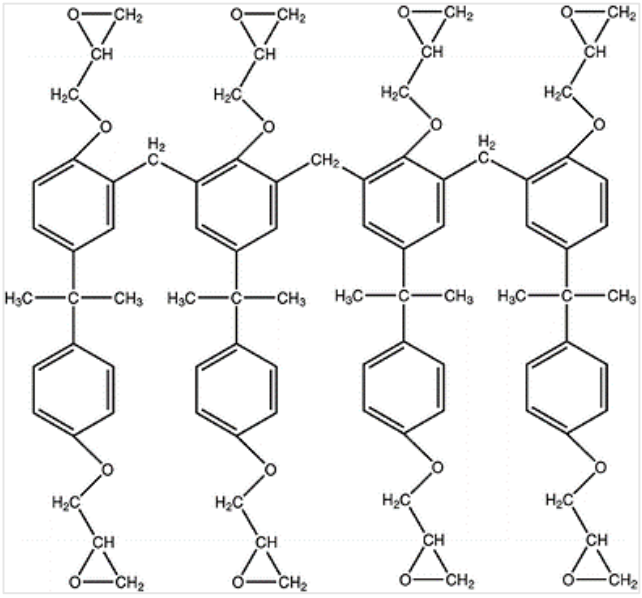

Figure 15. Molecular structure of SU-8 photoresist [132].

SU-8 is used worldwide in itself as a structural material in order to realize a number of applications [127] such as a molding material in (polydimethylsiloxane) PDMS replicating [133] and in microfluidic circuitry [134]. Lorenz et al. in the late 1990s (particularly in 1997) reported the use of a low cost negative SU-8 photoresist that can be used for MEMS applications and they have managed to demonstrate high aspect ratio structures and coils electroplating [128]. In some cases, the photoresist sacrificial layer is removed by thermal degradation or by dissolution in acetone [135]. Luo et al. have successfully developed a new approach (as shown in Figure 16) to lift-off SU-8 structures by applying a dissolved polystyrene in toluene as a sacrificial layer [136]. Their method

represents a good example for MEMS applications fabrication when the SU-8 layer can be used as a support structural layer. The Figure shows the released SU-8 structures from their initial glass substrate with two different thicknesses.

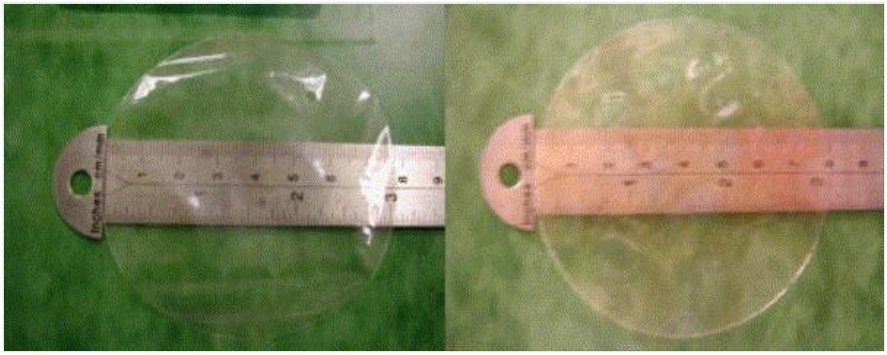

Figure 16. The lifted SU-8 structure [136].

2.3.1.3 **Poly(methyl methacrylate) (PMMA)**

The sacrificial layer has to possess several criteria and characteristics to be chosen. Charles C and Mark A have mentioned that, during processing, the sacrificial layer must provide a planar and stable platform for the consequent machining steps and also, the sacrificial layer has to be removed easily and cleanly in order to release a free standing structure [137]. John Crawford and Rowland Hill are the two British chemists who discovered PMMA in the early 1930s [127]. Also, in 1934, the German chemist, Otto Rohm, managed to achieve the first PMMA application [127]. PMMA is a thermoplastic. PMMA is extensively used as a substitute for inorganic glasses due to a number of unique features such being capable of withstanding favourable processing conditions, being lightweight, having high impact strength and high shatter resistance [138]. Incorporating PMMA with inorganic materials has a pivotal role in nanotechnology because of its flexibility during processing and compatibility as a polymer [133]. PMMA is a group of methacrylates and for several years, effort has been devoted to the study of this photoresist material because of its excellent chemical and physical properties and its utilization in a wide range of applications including protective coatings, adhesive coatings, solar cells

and medical uses etc [136]. PMMA has been also employed as one of the dye sensitised solar cell parts and as a consequence [139], PMMA has attracted researchers' attention in this field [134]. PMMA is also widely used in several optical devices including polymer optical fibres and optical lenses and these devices exhibit an increase in their refractive index upon deep ultra violet irradiation [137]. In advanced radiation microlithography, PMMA has the merit of being the first positive photoresist to be used [140]. The patterning mechanism of PMMA with latent image is a result of the cleaving effect of chemical bonds, bond cleavage results from absorbing high-energy radiation in main chain and side groups, hence decreasing the average molecular weight because of main chain scissions [140].

Leonidas et al. have performed a Raman spectroscopy and lithography study to investigate the characteristics of PMMA [135], when an alcoholic/water mixture is used as the developer solution and they have found that it is powerful and simple method compared to the techniques reported in the literature. And the mixture value 4:1 used to make an ethanol/water solution showed the better development of PMMA resist [135]. To enhance the resolution of scanning electron-beam lithography (SEBL) during the PMMA processing, the key is to consider the following: a simple/cheap process, with cold development below room temperature. Bryan et al. in previous studies investigate a range of temperatures (20 up to 90 °C) to develop PMMA, and the influence of these temperatures on the PMMA resolution when it is used as an electron resist. They found that developing PMMA at a proper temperature, nano-features at sub-10nm can be achieved with SEBL, a difficult resolution to be achieved by conventional development techniques [126]. PMMA emerged as a resist during the 1960s, and ever since its popularity has increased due to the several desired properties that is possesses both as an industrial material and as X-ray and electron beam resist [141]. Patterning PMMA resists can also be achieved using UV-lithography, nevertheless only at 200 – 270 nm exposure

wavelengths (deep UV light). Comparing the two mentioned aspects it was found that, as an industrial material, PMMA is widely available, non-toxic, easily processed, and inexpensive and can be formed in a number of molecular weights. Whereas, as an X-ray or electron beam resist, PMMA has an exceptional high resolution, high sensitivity and moderated resistance to dry and wet etching different processes[141]. PMMA has another significant feature: its high transparency, even more transparent than soda-lime glass substrates [141]. A number of sacrificial layers have been studied in the past few years. Vincent et al. have provided a comparison study on water-soluble sacrificial layers that are used in the process of micromachining, by investigating the advantages and disadvantages for each selected material as shown in Table 3. They have illustrated that, among these layers dextran and (poly acrylic acid) PAA are the promising organic polymers [135]. As shown in the Table 3, different types of polymers showed their solubility in water after lithography. Some of the polymers are showing good solubility in water even after lithography and some of them are not soluble.

Table 3. The selected water -soluble polymers used as sacrificial layers [135].

Polymer	**Film Uniformity**	**Film solubility in water**	**Film solubility in water after photolithography**
Poly(acrylic acid)	Good	Good	Good
Dextran	Good	Good	Good
Poly(methacrylic acid)	Good	Good	Good
Poly(acrylamide)	Good	Good	irreproducible
Poly(vinyl alcohol)	Good	Insoluble	/
Poly(ethylene imine)	Good	only in acidic or alkaline media	/
Poly(ethylene oxide)	Good	good, but also soluble in	/
Sucrose (table sugar)	Not uniform	/	/
Chitosan	Not uniform	/	/
Poly(ethylene oxide), 100 kDa	Not uniform	/	/

Polystyrene [136], polynorbornene, polycarbonate, polymethylmethacrylate (PMMA), organic polymers-poly (imide), and photoresists are also utilized as a sacrificial layer in different surface micromachining processes [135]. The drawbacks of the two mentioned sacrificial materials are fabrication constraints, and for copper its selective deposition, additional fabrication complicity, time consuming removal as the thickness increases as well as the strong acidic etchants required. Whereas, the deposition of SiO_2 requires high temperature [137]. From all above-mentioned sacrificial materials, organic Omnicoat has been chosen as the sacrificial layer in this project to perform the wet releasing of the targeted structures. Omnicoat is basically an adhesion promoter for SU-8 photoresist that can be deposited between SU-8 and the substrate.

2.3.1.4 **Polydimethylsiloxane (PDMS)**

Polydimethylsiloxane (PDMS) is a polymer organosilicon compound in common belongs to a group known as silicones [142]. PDMS is optically transparent and clear down to 230nm [143], non-flammable and non-toxic [144]. PDMS is also the most common used material in flow delivery in microfluidics [145, 146] lab-on-chip applications [147]. PDMS material is the most commonly used organic polymer based on silicon and is especially known for its unusual rheological characteristics and becomes a hydrophobic elastomer after curing, crosslinking process in which can be molded for reproducing several structures up to nanoscale resolution [148, 149]. PDMS is straightforward process. To prepare PDMS, a 1:10 ratio between the curing agent and PDMS elastomer are needed. This ratio can be changed to get softer or harder PDMS. After mixing bubble will result due to the mixing step. Removing the bubbles is an essential process by vacuum pump. Finally the mixture is poured on a mold or coated on the desired substrate. More details on PDMS processing are shown in methodology chapter. In this project

PDMS was used as a flexible substrate to grow ZnO nanostructures. Previously, Chen et el. had successfully grown well-aligned ZnO NRs on PDMS as shown in Figure 17 [150].

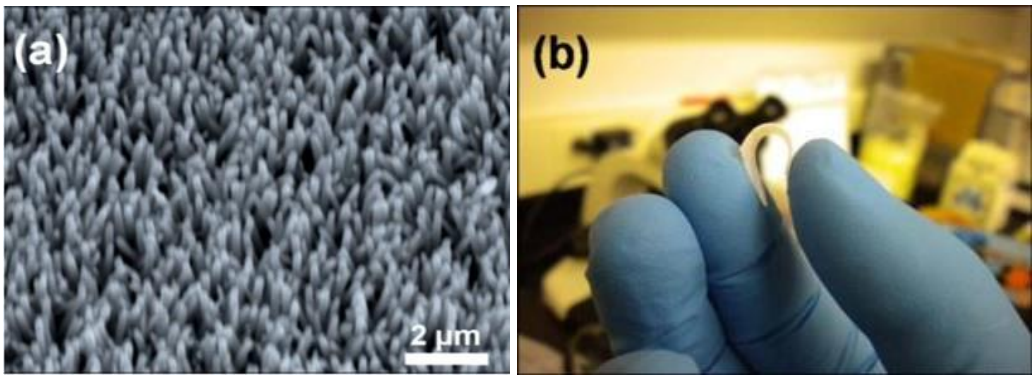

Figure 17. a) SEM image of ZnO NRs/PDMS b) Optical image of flexible ZnO NRs/PDMS [150].

There have been few studies on the growing of finely patterned, density-controllable and vertically aligned ZnO NR arrays using simple hydrothermal method on flexible organic substrates. In addition, to integrate with portable and foldable photoelectronic devices, it is very important to synthesize ZnO nanorods ZnO NR on flexible substrates. Mata et la. showed that, ZnO-NR arrays have been grown in existing literature on organic substrates such as Kapton film, PDMS film and beads of polystyrene [144]. Moreover, due to its transparency to UV, PDMS is also used to encapsulate NRs [151]. Another study showed the synthesis of ZnO NRs on PDMS where they used the hydrothermal method to achieved the NRs structure and the NRs were highly crystalline structures with 200nm in diameter 2.5µm in height [152].

2.4 **Extremely thin absorber (ETA) solar cells**

PV is evidencing to be one of the greatest champions for making renewables energy a typical energy source worldwide [153]. By fabricating extremely thin absorber (ETA) solar cells, low cost fabrication and high efficiency can be achieved using an extremely

thin absorber layer (100's nm) conformally coating a nanostructured substrate [154]. The ideas of ETA cells are that the nanostructure increases the optical path length of the absorbed photons and reduces the required lifetime of the charge carriers, therefore lowering the need for high quality absorber materials [155]. ZnO or TiO_2 micro/nano structures, used as electron conducting layers, are key to the development of ETA solar cells [156], as demonstrated by Kartopu et al. reporting 4% conversion efficiency on a CdTe/CdS/ZnO nanorods (NRs) ETA solar cells [157]. Cu_2ZnSnS_4 (CZTS) is an attractive candidate as a low toxicity absorber with near ideal band gap and due to the Earth abundance of Sn and Zn [158]. Yan et al. have reported over 10% efficiency for planar Cu_2ZnSnS_4 solar cells [159]. Giving an extensive review on ETA solar cells is not the aim of this section but for the purpose of placing this chapter within the research field.

Prior to providing and overview on ETA cells, the question is that, what is an ETA cell and why is it that important nowadays. Simply an ETA cell is an organic cell referred as all-solid-state photovoltaic cell that is fabricate on a substrate with structured electron conducting feature. ZnO or TiO_2 are usually used as n-type semiconductor oxides and $CuAlO_2$, CuSCN, spiro-OMeTAD or poly(3,4-ethylenedioxythiophene) polystyrene sulfonate (PEDOT) are used as a p-type semiconductors [160]. An extremely thin layer with about 5-150nm is sandwiched between the two n-type and p-type materials. This layer is a strong absorbing inorganic semiconductor for example CdS or CdTe [161] or Si:H [162]. Könenkamp et al. are the first researchers who introduced the concept of extremely thin absorber (ETA) cells by using CdTe and indium diselenide $CuInSe_2$ (CIS) as the first candidate materials [163-166]. ETA solar cells are basically a Solid State Solar Cells (SSSC) type [167]. This solar cell type uses a continuous absorber layer in a solid state [168, 169] as opposed to nanocomposite SSSC or quantum-dot SSSC, where the window material or absorbing semiconductor are in the particles form [170-172]. The 2μm thickness of CIS absorber is sufficient for absorbing most of the incident light within

the energy above the bandgap [173] yet the ambition of ETA concept is to reduce the absorber thickness to few hundred nm or even more less [174]. The justification of ETA concept in using low quality materials is that, the diffusion of carriers does not happen over a significant length on the used ETA material [169, 175, 176]. The carrier life impact on the performance of a solar cell is marginal when the diffusion length reaches the absorber thickness [177].

2.4.1 **The principle of ETA solar cells**

The principle of the extremely thin absorber (eta) solar cell design is to completely separate the function of a solid state solar cell into separate materials, with at least one layer being structured to increase the surface area (see Fig. 17). The absorber material is coated onto this structured surface, so that with a local thickness of, 100 nm, an effective optical thickness of >1 µm is created: sufficient to absorb most of the incident light. Briscoe et al. showed the principle of ETA solar cell [154].

Figure 18. Extremely thin absorber (ETA) solar cell [154].

They stated that, a complete separation of solid-state cell function into separate materials is the main ETA principle. This occurs by the existence structured layers in order to increase the surface area as illustrated in Figure 18. The structured surface is coated with the absorber material with <100nm local thickness. A thinner absorber layer relaxes the

material quality requirements, as the diffusion of photogenerated carriers needs to be only a few tens of nanometers in order to reach either the n-type material (electron transport) or p-type material (hole transport). Taretto et al. has provided a theoretical study on ETA cells with about 10% of efficiency. They showed that, the needed carrier life time of an absorber was about 14 times less comparing to thin film cell [176]. Therefore, greater flexibility will be provided by using low quality material in both deposition methods and the type of material. As well as cost-effective chemical synthesis techniques can be used as inherent high defect densities has less significant effect when the low diffusion length are necessary [178, 179]. Principally, choosing the absorber material relies on a couple of factors and properties that relate to superior light absorption, non-complicated deposition as well as an ease optimisation of transport properties of the n-type and p-type material. The ultra-thin solar cells are considered to be attractive type. However, this can be acceptable only when a high photocurrent is obtained. Consequently, a lot of intention has been drawn on the research of light trapping using ultra-layers. Using inorganic semiconductors as sensitizers in solar cells is well recognised. They can replace organic dyes owing to the high absorption coefficient within the visible range [180] and can be concurrently used in fabricating completely organic heterojunction devices [164, 181]. In this project, a study on ETA cell fabrication, using CZTS, is presented with hydrothermally grown ZnO NRs on ITO/glass and more details on the fabrication method and results are provided in this thesis.

2.4.2 **ETA solar cells ETA Cell Superstrate Configuration using CZTS Nanoparticles**

Cu_2ZnSnS_4 (CZTS) is a p-type quaternary semiconductor compound. Due to its inherent properties such as high absorption coefficient more than 10^4 cm^{-1}, optimal direct band gap about 1.4-1.5 eV, and abundant earth components [182], it has attracted great attention throughout the scientific researchers and industrial field lately because it contains non-toxic and earth-abundant materials [183]. CZTS was first produced back in 1966 [184] The synthesis of CZTS is tracked back to 1967 [185] and in 1988 it showed the photovoltaic effect [186]. CZTS solar cells are becoming increasingly popular because of the achieved better efficiencies with different structures and different solar cell types. Friedlmeier et al. has reported 2.3% efficiency in 1997 [187]. By improving the deposition process the efficiency has increased to about 6.7% in 2008 [188]. Recently, conversion efficiency of 6.77% has been reported for CZTS solar cell [189]. The CZTS solar cell schematic structure is shown in Figure 19. Basically the structure consists of glass substrate, 500-700nm of sputtered Mo as a back contact, 1.0-2.0 µm p-type CZTS absorber thin layer deposited on Mo layer, 50-100nm n-type CdS is coated then on the absorber layer in order to form a p-n junction by using chemical bath deposition technique. Then 50-90nm of i-ZnO sputtered on to prevent leakage and prevent the shortage between the two front and back contacts. Finally transparent conducting oxide layer (TCO) is deposited by sputtering technique as front contact, finally, for I-V measurements Ni/Al grid are deposited on Mo and TCO. For CZTS ETA cells, in solar cells field, ZnO is broadly used as a transparent conducting oxide in CZTS and Cu(In, Ga)Se_2 [190]. In this project, ETA Cell fabrication in superstrate configuration using CZTS nanoparticles was carried out and more details on this process results are provided in chapter 6.

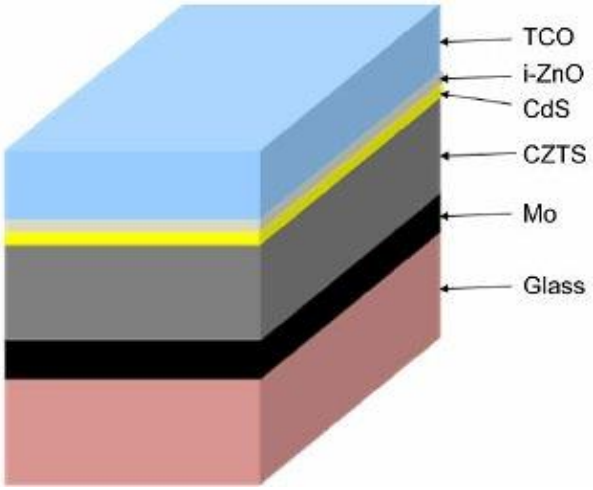

Figure 19. CZTS solar cell schematic structure [191].

2.5 **Summary**

In this chapter, the ZnO material and its different properties, its nanorods structure and applications have been described. An overview of solar cell and their working principle have been were briefly discussed in this chapter as well as light trapping in solar cells. Also an overview on the materials used lift-off process such as PMMA, negative SU-8, Omnicaot, and PDMS. Finally an overview of the ETA solar cell principle and superstrate configuration using CZTS nanoparticles. In general, ZnO have been used in fabricating a large variety of practical applications, such as optoelectronic devices. In this thesis, ZnO NRs are aimed to be used in enhancing the performance of different solar cells. This have been achieved by either fabricating ETA solar cells or mounting a released ZnO NRs/support layer on a complete solar cell.

Chapter 3 EXPERIMENTAL SETUP

This chapter will provide comprehensive details regarding the different experimental work performed in this project. The diagram shown in Figure 20 summarises the lab work accomplished in this project and the aim of each investigation.

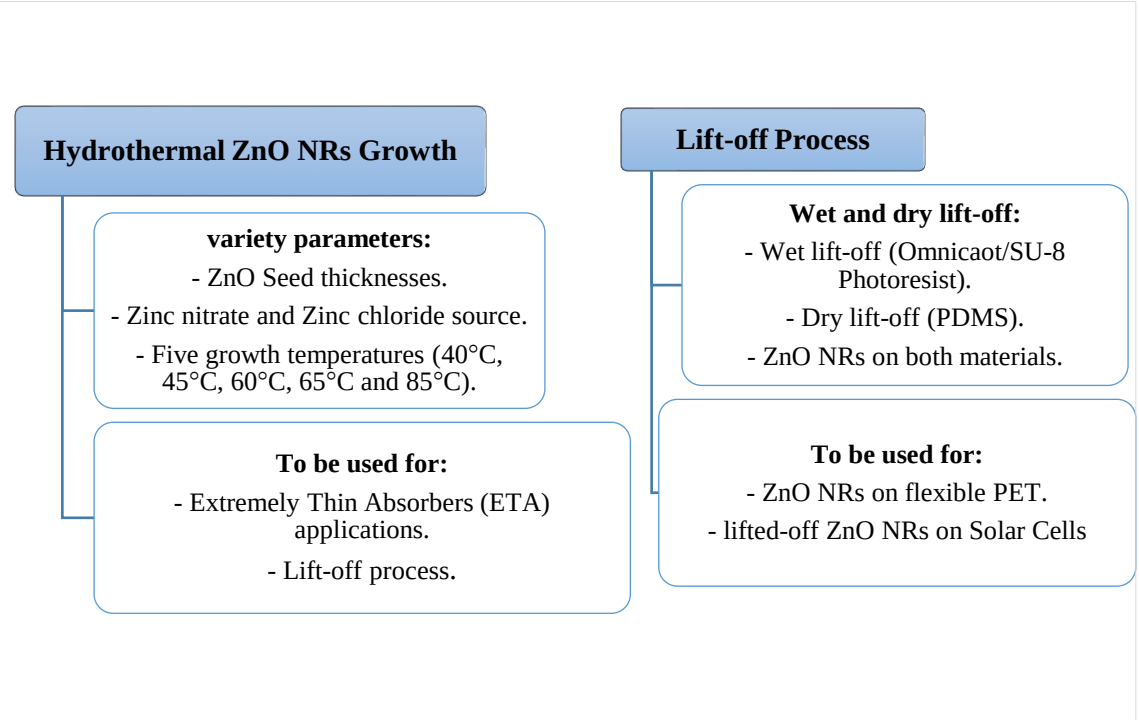

Figure 20.Experimental work accomplished in this project.

3.1 Zinc Oxide Nanorods (ZnO NRs) hydrothermal Growth

3.1.1 Materials and Chemicals

Herein, unless otherwise stated, the chemicals employed for the ZnO NRs growth were purchased from Sigma-Aldrich. No purification steps are added. Two different zinc salts were used as a precursors for the zinc ions; specifically, Zinc nitrate hexahydrate $Zn(NO_3)_2$ and zinc chloride $ZnCl_2$ hydrate. Ammonium NH_4 OH was used as a base precursor for the hydroxide ions.

3.1.2 ZnO Synthesis Procedure

This section of the chapter will introduce the process used to grow the ZnO NRs. Each different step beginning with the pre-treatment of the substrate to the deposition of the ZnO NRs, besides the deposition steps will be described in full detail.

3.1.2.1 Substrate Preparation

Prior to growing the targeted nanostructure, important steps should be followed first to ensure a repeatable surface state upon which ZnO NRs can be grown. These steps can be summarised in two steps: cleaning the substrate and ZnO seed deposition. More details on these crucial steps are shown in the coming sections.

3.1.2.2 Substrate Pre-cleaning

The substrates were ultrasonically cleaned for 15min in (acetone and isopropanol IPA) each and then dried by nitrogen stream to remove any resulting contamination. The role of the primary chemical (acetone) here is to remove the organic impurities and contamination as a good polar solvent can dissolve most organic residues on the surface,

whereas the IPA alcohol rinse agent has an excellent ability in regard to rinsing the contaminated acetone and also removing the existing particles on any surface.

3.1.2.3 **ZnO seed deposition**

At ambient temperature, different thicknesses of ZnO seed layer were deposited on ITO-coated glass using sputtering. In addition, to control the thickness, the ZnO films were deposited by varying the deposition time. More details of the sputtering parameters used are illustrated in Table 4.

Table 4**.** ZnO seed sputtering parameters

Magnetron sputtering parameters for ZnO seed deposition	
Sputtering target	ZnO-mg Dc pulse with low bias
Used substrate	ITO, Omnicoat/SU-8
Sputtering pressure	$9.3*10^{-6}$ mbar
Ar gas flow rate	50 SCCM
O2 gas flow rate	2.0 SCCM
Substrate bias	45/0.09 V/A
Substrate ENI/AE	250/500 Freq/nS
Deposition time	5, 10, 15, 35 mins

ITO-coated glass, Omnicoat/SU-8 and PDMS were used for ZnO seed deposition. More details on Omnicoat/SU-8 ZnO NRs growth will be giving later in this thesis. The process of sputtering ZnO on ITO-coated glass included the following: the source material was a metal Zn target, while the working used gases included argon and oxygen. The deposition processes started when the vacuum of the chamber was approximately 9.3×10^{-6} mbar. The ZnO seed layers were deposited using different deposition times to obtain different thicknesses. In this project, the deposition time was set to four different times: 5min, 10min, 15min and 35min.

3.1.3 Zinc Oxide NRs hydrothermal growth using different growth temperatures (T_{growth})

In this investigation, a solution-based growth method was conducted to hydrothermally grow the nanorods. Figure 21 is an illustration of the experimental setup used to hydrothermally grow the ZnO NRs.

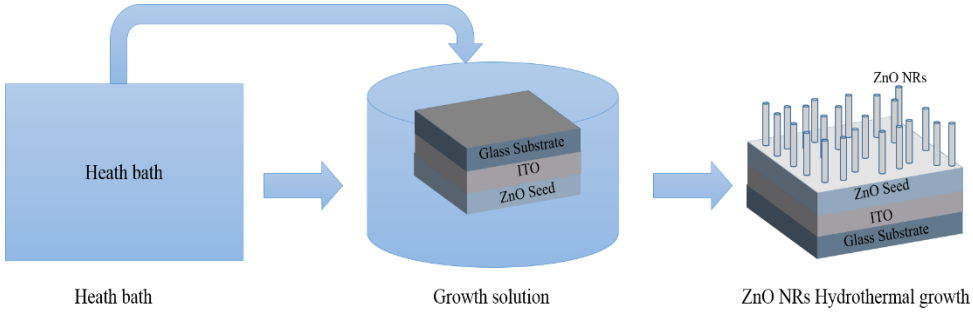

Figure 21. The hydrothermal growth setup with the sample upside-down facing the growth solution.

To achieve the desired ZnO nanostructure in a typical hydrothermal growth process, the growth solution was normally prepared by dissolving and mixing the zinc salt. 25mM of growth solution was used for all experiments. To make 25mM, the amount of zinc nitrate and zinc chloride was dissolved in 150 mL deionized water. In addition, the pH of the growth solution was adjusted and fixed at 10.3 to 10.4 by adding ammonia. Reactants such as ammonia hydroxide (NH_4OH) were then added to the solution. The reason for using ammonium is to provide enough hydroxide ions. This will enhance the process and reactions to take place. Five different temperatures were used to grow the ZnO NRs (T_{growth} = 40°C, 45°C, 60°C, 65°C and 85°C). Four different seed layer thickness were employed. The growth time (t_{growth}), solution concentration and pH value were all kept constant. That is because the goal was to investigate the different zinc source, growth temperature and seed layer effect on the resulting ZnO NRs. Table 5 illustrates the hydrothermal growth parameters used in this investigation.

Table. 5. ZnO hydrothermal growth parameters

Substrate	Seed thickness (nm)	Growth time (h)	T_{growth}
ITO	27	2hrs	40°C,
ITO	63	2hrs	45°C,
ITO	70	2hrs	60°C,
ITO	130	2hrs	65°C and 85°C

The substrates were suspended upside down in the glass bottle containing the prepared solution. When the nanostructure is grown, the immersed substrate is removed from the solution, rinsed with DI water and dried by way of nitrogen stream. Schematic of the structure evolution after each deposition step are shown in Figure 22.

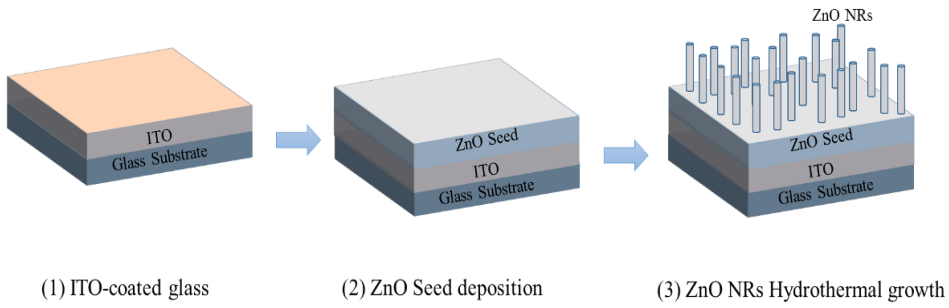

Figure. 22. Schematic of the structure evolution after each deposition step

3.2 Lift-off (dry and wet) processes

The targeted structures are shown in Figure 23. (Omnicoat/SU-8/ ZnO seed/NRs) mentioned as Structure 1 and (PDMS/ZnO seed/NRs) mentioned as structure 2.

(1) (2)

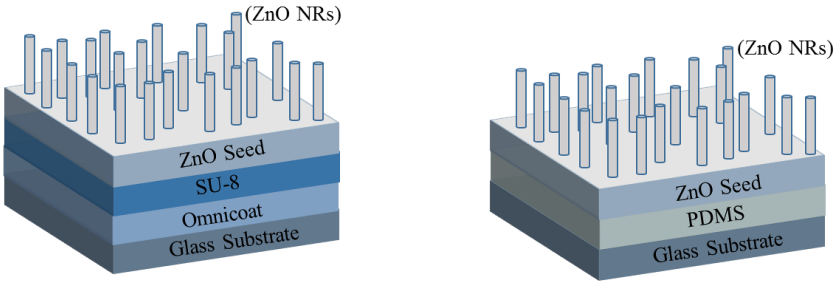

Figure. 23. Two targeted structures for the lift-off process. 1) Structure 1 (glass/omnicoat/SU-8/ZnO NRs) and 2) structure 2 (glass/PDMS/ZnO NRs).

The two structures were chosen in this project in order to achieve the following aims: firstly, structures 1 and 2 are released from the original substrate and mounted on a solar cell device with the aim of investigating the ZnO NRs effect on the device performance, besides studying the light scattering effect. Thus, the aim is to reduce the light reflectance from the device as well as increase its efficiency. Secondly. These structures can be used in different lithography processes where the layer is supposed to be detached as a free standing layer or as a part of a structure that contains several layers.

Two different lift off methods (dry and wet) were used to release the nanorods from the initial substrate into a flexible substrate. The wet lift-off was used as a sacrificial layer. An epoxy-based SU-8 photoresist which is provided in twelve standard viscosities was used in this study. Two different viscosities were utilised (2002 and diluted 2025). Here, SU-8 was used as a permanent support structure due to its highly cross-linking feature (cross-linking means that after SU-8 processing, a stronger layer should be obtained and hard to remove by conventional strippers). Direct removal can be achieved by means of the sacrificial layer (Omnicoat) between the substrate and SU-8, whereas the PDMS layer can be easily peeled off the coated substrate. ZnO NRs/SU-8 and ZnO NRs/PDMS were

successfully released from the glass substrate. Additionally, ZnO NRs/SU-8 was transferred to a flexible kaptone and PET substrates. Details of the preparation of Omnicoat/SU-8 and PDMS layers and lift-off procedure (either wet or dry) used in this project is provided in sections 3.2.3 and 3.2.4 respectively.

3.2.1 The final aim of using ZnO NRs/SU-8 and ZnO NRs/ PDMS

ZnO NRs were grown on different structures, as shown in Figure 24.

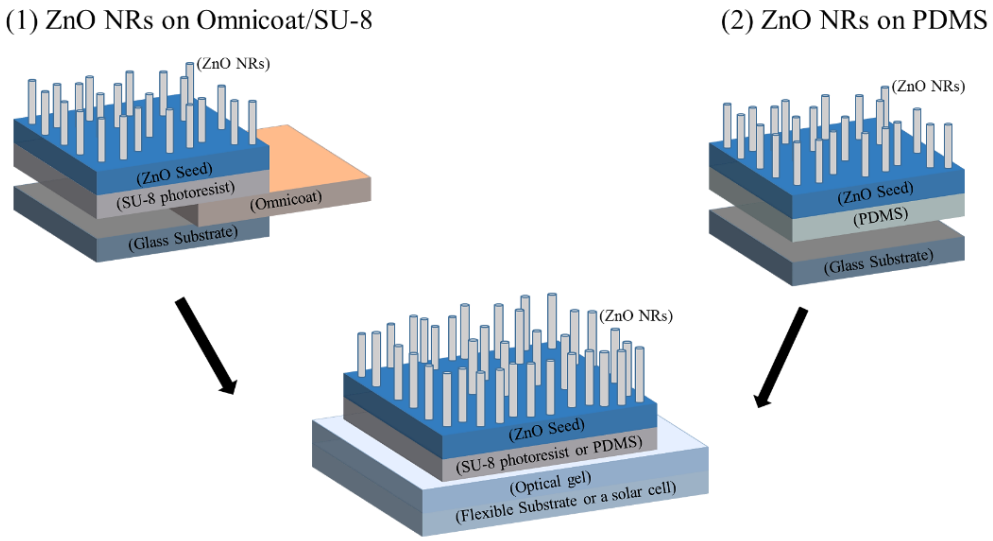

Figure. 24. ZnO NRs lift-off and transfer processes.

3.2.2 Poly (methyl methacrylate) (PMMA) as a structural support layer (wet lift-off)

PMMA was used as a starting point for optimising a support structural layer that can withstand the hydrothermal growth of ZnO NRs. The following procedure was employed to make 20g PMMA solution in the chlorobenzene:

1. 0.2g PMMA powder + 19.8g chlorobenzene.

2. Hot plate was set to 50°C.
3. Solution was left-on a hot plate for 2.5hrs.
4. The solution was fully dissolved after 2.5hrs.
5. PMMA was spin coated on a pre-cleaned glass substrate.
6. Baked at 180°C for 3min.

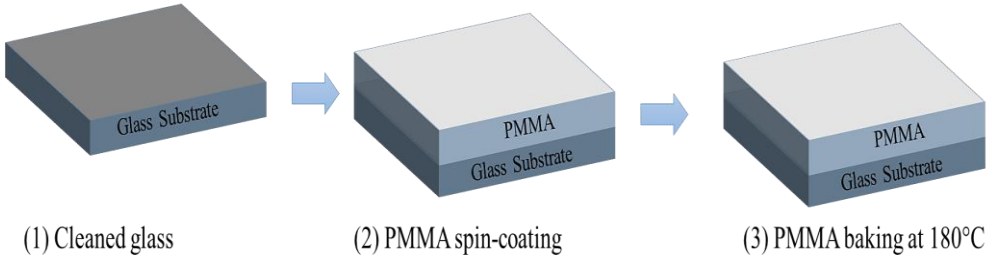

Figure 25. PMMA layer preparation.

Prior to starting the lift-off process, a number of trials were conducted on testing different baking temperatures. To lift-off the PMMA/thin film layers, it was crucial to deposit thin film on the PMMA layer and test the availability of detaching the layer using acetone as a developer.

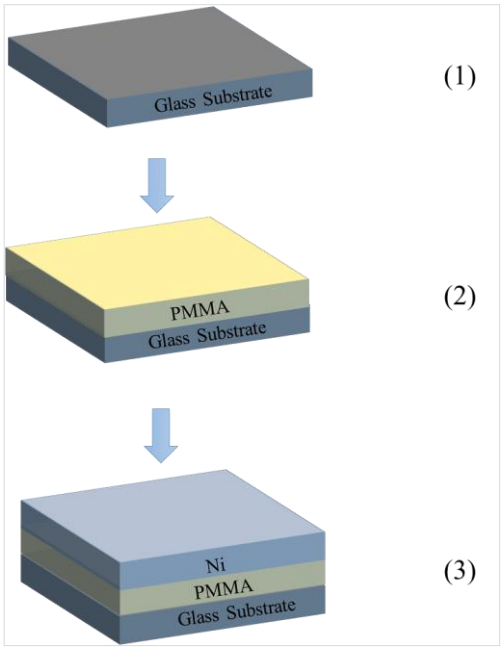

Figure. 26. PMMA/thin film structures before lift-off.

In order to optimise the lift-off process, the PMMA was coated with Ni thin film to carry out the support structural layer/thin film released from the used glass substrate. Initially, Ni was the film chosen in this case. The Ni thin film was deposited on the PMMA layer using an E-beam thermal evaporator. Different thicknesses of Ni were deposited on the PMMA by the technique of e-beam evaporation ranging from 2μm to 100nm. It should be mentioned that the PMMA was not the appropriate layer required to carry out the ZnO NRs growth. Hence, it was exceedingly important to find an alternative that can be successful in growing the ZnO NRs. The route of the investigation was then to focus on SU-8 photoresist as a second choice. Thus, the followed approach was formed in order to release SU-8/ZnO NRs with the assistance of a sacrificial layer which was chosen to be Omnicoat**.** After a series of experiments, starting from using PMMA as a support layer, Omnicoat was selected as a sacrificial layer in the wet lift off process and was coated on glass substrate and then SU8 was coated on top of the Omnicoat.

3.2.3 **SU-8 photoresist as a structural support layer for (wet lift-off)**

3.2.3.1 **Process Requirements**

Omnicoat, Omnicoat developer and remover PG were supplied by MicroChem. Dymax Bluewave LED dx-1000 exposure was used in the exposure step (calibration graph). Spin coating the sacrificial layer and photoresist layer were obtained by using spin coater. 76cm x26cm glass substrates (from Thermo scientific) were utilised in to coat the Omincaot and SU-8 layers. As demonstrated in Figure 27, to process SU-8 photoresist, different steps are generally followed. First, SU-8 was spun coat on a pre-cleaned substrate and then the resist was soft-baked SB (pre-baking) at 95 °C to evaporate the solvents. After pre-baking the resist exposed to UV light where photo acid enhances the

cross-linking of the resist in the last post-exposure-baking (PEB) step. Then the layer was deatched from the substrate using SU-8 PG remover solution.

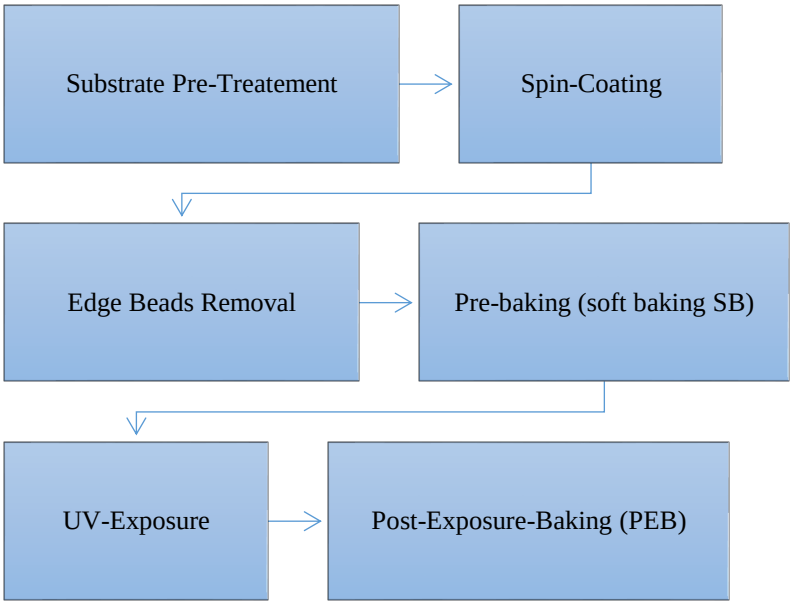

Figure. 27. The SU-8 processing steps used in this project.

A number of experiments were accomplished in order to optimise the Omnicoat/SU-8 coating process and to obtain uniform coated thin films. The process of coating Omnicoat generally includes the following steps:

1. Spin coating. First, the sacrificial layer (Omnicoat) was dispersed at the centre of the cleaned glass substrate. 500rpm for 5 s and final spin speed 1000rpm for 30 s.

2. Baking. 200℃ for 3min on a hot plate.

3. The process of coating SU-8 is as follows:

4. Prior to spin coating, SU-8 must be warmed to room temperature.

5. Spin coating. SU-8 was placed at the centre of the substrate (500rpm for 10 s, 1000rpm for 10 s and 4000rpm for 15 s).

6. Low rotation speed at 100rpm for 10 s was added during disposing the photoresist to the coating programme to ensure full coverage, as recommended by Martinez et al [130].

7. Soft baking (SB) is performed on a hot plate. 95℃ for 5min and 10min. The temperature of the hot plate was gradually reduced in order to cool down the substrate to room temperature, preventing the tension from forming in the thin film and to ensure the evaporation of the solvent.

8. Exposure. Experimental exposures were accomplished at several applied doses and times to optimise the layer that can withstand the ZnO NRs hydrothermal growth (exposure doses). Care must be taken prior to exposing the resist. It is crucial to remove the photoresist ridges (known as edge beads), which is 10 times greater than the main coated thickness as reported [130].

9. Samples were post-baked (PEB) at 95℃ for 5min, 10min, 30min and 60min. The temperature of the hot plate was gradually reduced and samples were cooled down to room temperature to prevent the film thermal shock.

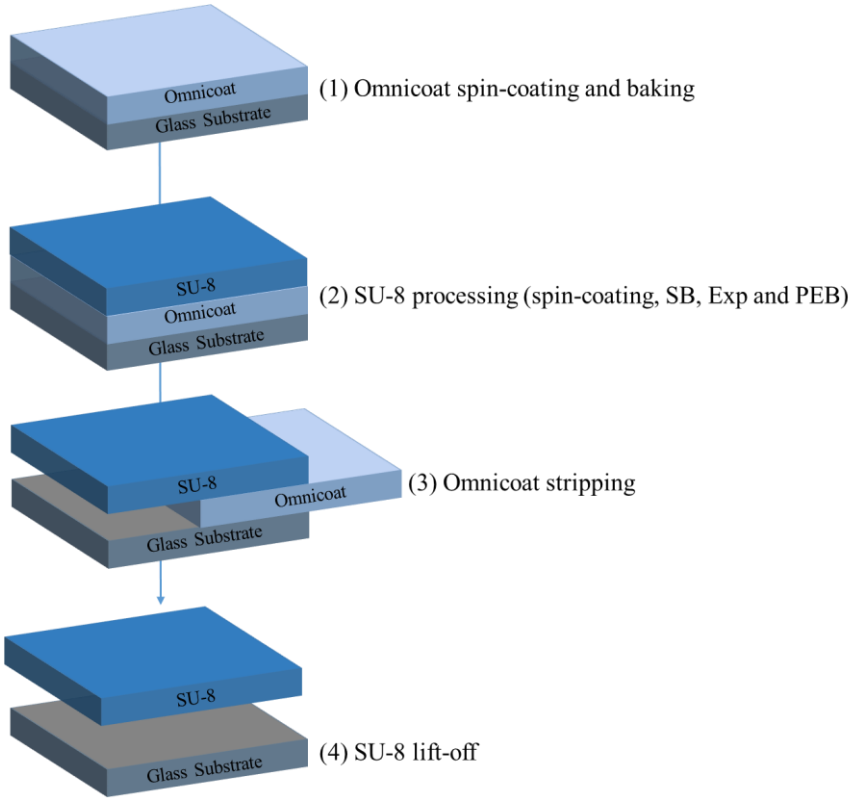

Figure. 28. Omnicoat/SU-8 preparation for the lift-off process.

3.2.4 **Polydimethylsiloxane PDMS (dry lift-off)**

3.2.4.1 **Materials and experimental method**

The viscous PDMS (Sylgard 184) liquid and cross-linking curing agent were purchased from Dow Corning. To allow smooth and easy removal of the flexible PDMS layer, 76cm x 26cm glass substrates (from Thermo scientific) were used for polymer coating. To prepare the desired PDMS layer, a number of steps were followed in the PDMS preparation protocol (see Figure 29). The standard mixing mass ratio is 10:1, mixing 10g of base elastomer with 1g of curing agent. By using this ratio, the desirable mechanical properties could be achieved. The PDMS preparation steps are as follows:

1. Mixing container was placed on the weighting scale
2. 10g of elastomer base was poured and mixed with 1g of curing agent in the container.
3. After reaching the desired amount, the solution was mixed.
4. After stirring, the polymer was left under vacuum pump for almost one-hour to remove the unwanted air bubbles formed during the mixing step.
5. When the produced bubbles were removed, the polymer was spin-coated on a glass substrate. More details on each single step in PDMS preparation were provided in the subsequent sections.

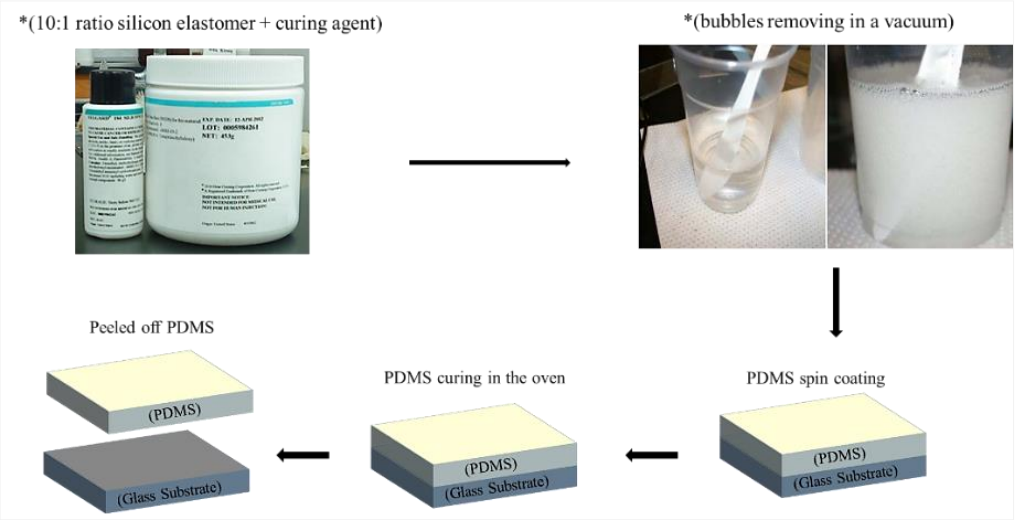

Figure. 29. PDMS preparation process.

3.2.4.2 **Spin Coating and Curing**

A pre-cleaned glass substrate was used for the PDMS coating. The final PDMS thickness strongly depends on the spin speed used as well as the spinning time. In this experiment, the spin-coating used was as follows: 500rpm for 10 s and final spin speed 4000rpm for 90s. The spin-coated PDMS layers were subsequently baked at 80℃ in an oven for 48hrs, following the same recipe provided by Chen et al. [150].

3.2.4.3 **ZnO NRs growth and PDMS peeling off**

To detach the PDMS layer from any substrate, no wet remover was required. PDMS could be peeled-off immediately from the substrate. After depositing the ZnO seed layer, ZnO NRs were grown on PDMS and the whole structure was peeled off the glass substrate.

3.2.4.4 **SU-8 photoresist and PDMS comparison**

In this study, as previously mentioned, two lift-off methods used (dry and wet) lift-off as shown in the comparison in Figure 30. Adding the growth of ZnO NRs on PDMS was an initial step as it illustrates the main differences between the wet and dry lift-off processes. Consequently, the effect of wet/dry released ZnO NRs can be investigated.

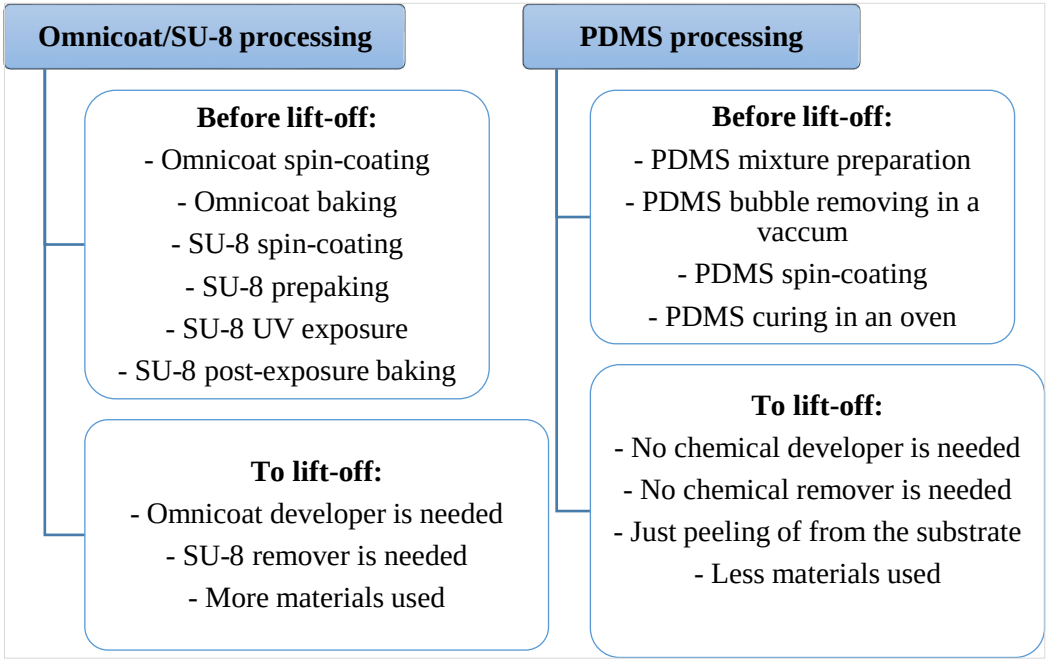

Figure. 30. SU-8 and PDMS processing requirement comparison.

Figure 30 indicates a full comparison of Omnicoat/SU-8 and the PDMS processing steps. Both materials were used successfully to grow ZnO NRs. However, compared to SU-8 photoresist, PDMS was strong enough to withstand the process and not damaged during the wet chemical method. More details will be given in the lift-off result chapter on both structures utilised for hydrothermal ZnO NRs growth.

3.3 Extremely Thin Absorber (ETA) Fabrication

Figure 31 shows the ETA solar cell fabrication process.

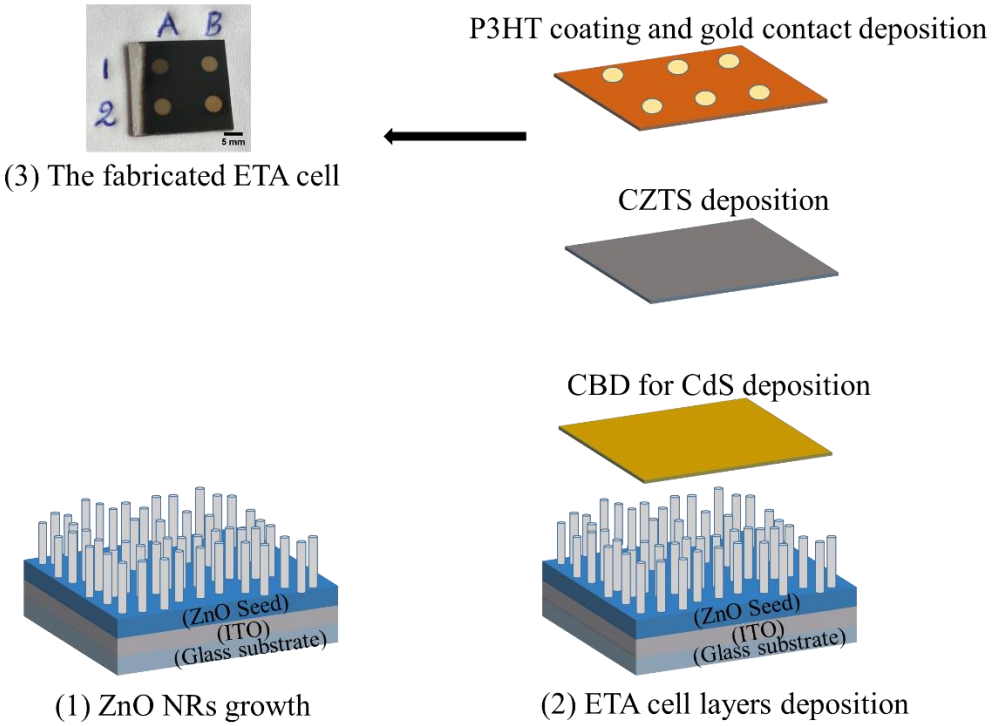

Figure 31. ETA Cell fabrication process

The final structure of the fabricated device is: glass/ITO/ZnO seed/ZnO NRs/CdS/CZTS/P3HT/gold. The steps followed in the fabrication process of the ETA are shown in n. These steps were as follows: The steps followed to fabricate ETA solar cell in this project is shown in Figure 32. The next section will provide full details on each deposition step.

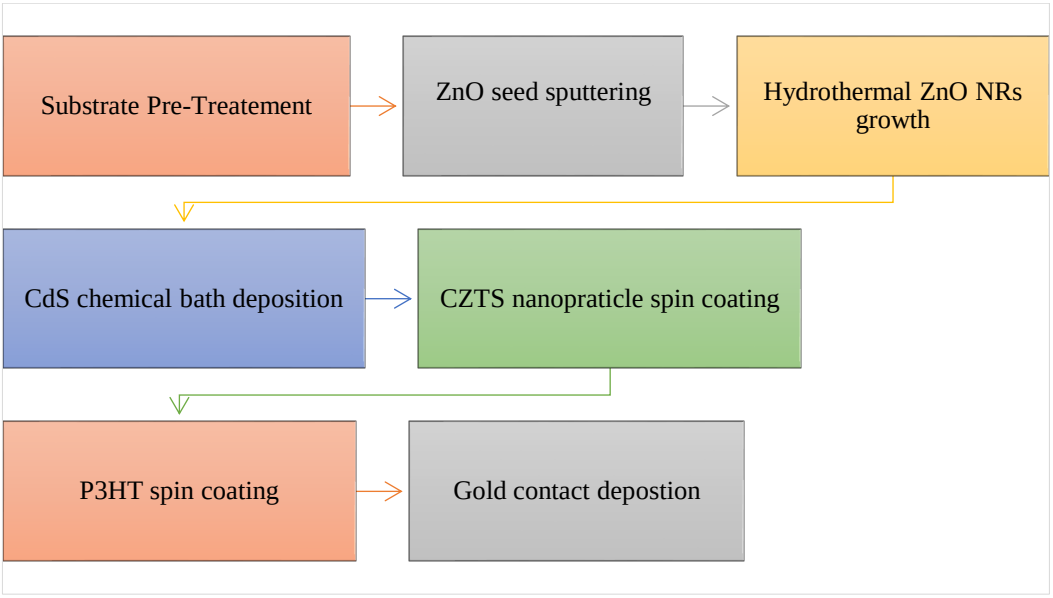

Figure 32. ETA solar cell fabrication steps.

3.3.1 **Hydrothermal ZnO NRs growth**

ZnO seed layer was deposited on the TCO substrate (ITO-coated glass). The ZnO solution was preppared following section 3.1.3. The growth was set to 85°C in the first fabricated device, whereas the growth time was set to two hours.

3.3.2 **Chemical bath deposition (CBD)**

The CdS layer was deposited on ZnO NRs samples by means of the following steps:

1. A vessel chemical bath consisting of the desired chemical precursors and water solution was used.

2. The reaction mixture solution was prepared at 71°C with the help of a water cycling heat bath.

3. To monitor the solution temperature, a thermometer was used.

4. The substrates were mounted on a special holder. Ordinarily, the substrate holder has fewer diameters compared to the beaker used, which allows the substrate attachment holder to move easily in the used chemical bath.

5. The vacuum oven was set to 200°C to anneal the samples.

3.3.3 Cu_2ZnSnS_4 (CZTS) nanoparticles

The CZTS was prepared by the Hot-injection method technique shown in [192]. The CZTS thin film was achieved as follows:

1. The concentrated ink was spun-coat on CdS-coated ZnO NRs at a speed of 1000 rpm for approximately 3-5 sec.

2. Then, the samples were annealed using a hot plate at 150°C and 300°C for 30 sec.

3. The spin-coated step was repeated until the layer looked completely black.

3.3.4 Poly(3-hexylthiophene) (P3HT) and gold contact deposition

1. P3HT was then spin-coated at 4000 rpm for 30 sec as the final layer, seeing as it acts as a complete transport layer which in turn helps to avoid shunting.

2. After spin-coating, the samples were annealed in the oven at 150°C for roughly 20min.

3. Following gold contact deposition.

3.4 Characterisation techniques

The characterisation techniques can be quantified as two different groups. The first group is characterising the material properties, whilst the second group was characterised the performance of the fabricated devices.

The first group includes:

1. Scanning electron microscope (SEM) to study morphology.
2. Energy-dispersive X-ray spectroscopy (EDS) for elemental analysis.
3. Atomic force microscopy (AFM).
4. X-ray diffraction XRD to investigate the crystallinity.
5. UV-VIS-NIR spectroscopy to study the transmittance and the reflectance.
6. The second group comprises:
7. Current-voltage (IV).
8. External Quantum Efficiency (EQE).

3.4.1 Scanning electron microscope SEM and Energy-dispersive X-ray spectroscopy (EDS)

The film composition and morphology were determined using a FEI Quanta 200 scanning electron microscope (SEM) equipped with Oxford Instruments energy dispersive X-ray spectroscopy (EDS). For SEM, top view and cross-section images were taken in order to extract the morphology and (EDS) used in determining material composition using the feature of transmission electron microscopy.

3.4.2 **Atomic Force Microscopy (AFM)**

In this project, AFM was used with the intention of studying the electrophysical and morphological characteristics of ZnO seed layers. AFM was used to measure roughness of ZnO seed samples with a physically contacted solid probe tip to carry out the surface scanning. This achieved by scanning a solid probe tip across the sample surface which in turn leads to a topography map or the height of the scanned surface being created as it scans through. In this system, a laser is focused onto the above mentioned cantilever and reflected onto the photodetector.

3.4.3 **X-Ray diffraction Structural Characteristics (XRD)**

The technique of XRD crystallography was used to study the material structure and gain further information regarding its atomic scale structure. The incident beam on the crystal structure was diffracted into several specific directions. Therefore, a three-dimensional picture was obtained by measuring the intensities and the angles of the diffracted beams.

3.4.4 **UV-VIS-NIR transmittance (T%) and Reflectance (R%) analysis**

The measurements of UV-VIS-NIR were obtained by (Shimadzu SolidSpec 3700 Spectrophotometer). The samples were place in the way that, the surface of NRs was facing the incident beam.

3.4.5 **I-V measurements**

Photo-current (I-V) of the fabricated devices was performed by way of a two two-point probe configuration using under a standard air mass 1.5 solar illumination with an intensity of 100 mW cm^{-2} (Abet Technologies Sun 2000 Solar Simulator).

3.4.6 **External Quantum Efficiency (EQE).**

EQE spectra was achieved by measuring the electrical sensitivity of the device to the light. Since the photon energy is precisely inversely proportional to its wave length, different wavelength range is often used in measuring the EQ with the intention of measuring the device efficiency at all different photon energy range. EQE measurements in this project, (Si) was used in the calibration step. The wave length range was set to 300nm-1100nm.

3.5 **Summary**

In this chapter, a detailed discussion of the different experimental set up used in this project to grown ZnO NRs on either ITO or releasable layer as well as fabricating ETA solar cells. First starting with the ZnO NRs hydrothermal growth. Also ZnO seed layer was then sputtered to initiate the ZnO NRs growth with different thickness using sputtering technique. ZnO NRs were grown using solution based process at a range of T_{growth} for two hours. In this process, two different Zn salts were used. The NRs on ITO were then used in ETA solar cell fabrication. Then explaining the lift-off process step by step from the deposition of Omnicoat until the final step which is optimizing the support structural layer and ZnO NRs growth. This was basically achieved by spin coating the sacrificial layer on glass. Followed by the SU-8 layer. Then, releasing the ZnO NRs from the initial layer was shown by using lift-off process. The method of growing ZnO NRs and flower-like structures on PDMS was also discussed in this chapter.

Chapter 4 ZINC OXIDE NANORODS (ZNO NRS)

Zinc oxide is a material that attracted a great deal of interest specially in the period of end of 1990s [193] hence, great consideration for one-dimensional ZnO nanostructure is due to the remarkable performance and properties that ZnO possess in photonics, optics and electronics [61]. Due to the mentioned properties, ZnO is a good candidate material to be used in different applications including light emitting diodes, sensors, photocatalysts, solar cells and others.[194]. Great effort have been carried out in order to understand the chemical reaction during the growth process, so that optimisation of the synthesis is possible through investigation of the ZnO properties [36]. The aqueous solution method represents one of the most used techniques to grow ZnO NRs [195], as the main requirements for this process are the used zinc salt and a hydroxide source to obtain the targeted nanostructure. The main features of the hydrothermal method is that it is not expensive and the growth can be accomplished at a low temperature. Much effort has been taken in order to optimise the growth process and control the different involved parameters such as (the zinc salt source, the growth temperature, different seed thicknesses etc.). In this chapter, the effect of zinc source was studied and the effect of the growth temperature, ZnO seed thickness were examined. The effect of different processes parameters was studied by analysing the obtained nanostructures.

4.1 Results and Discussion

As an amphoteric oxide, ZnO has an isoelectric point value at about 9.5 which makes ZnO crystalize dissolving the Zn salt in either weak or strong alkalis [36]. For typical aqueous solution of ZnO 1-D nanostructure growth processes, an alkaline growth environment is crucial [196]. Chemical composition such as pH value, zinc nitrate salt, zinc chloride salts, seed layer thickness and growth temperature will be studied in this chapter.

4.1.1 Sputtered ZnO seed on ITO-coated glass substrate

Prior to the ZnO NRs growth, ZnO planar thin films (termed as seed layer) were sputtered on ITO-coated glass substrate. There has been a number of reports on seed layer types such as sol-gel seed layers [197], spin-coated ZnO nanoparticles [198] and RF magnetron sputtered seed layer [199]. In this study seed layers were employed by RF magnetron sputtering. Sputtering techniques are preferentially applied when depositing ZnO thin films due to process scalability when coating large area is required [200]. The sputtered ZnO thin films can be formed and crystallized at room temperature which does not require any substrate heating [200]. The preferred orientation of RF magnetron sputtered ZnO thin films is along <0001> axis [201]. ZnO is hexagonal and in 4 indices notation, the <0001> direction relates to that of the c axis in which the film has that orientation and means the planes are parallel surface. The sputtered ZnO thin films have a tendency of growing with the c-axis to the substrate [202]. At ambient temperature, different thicknesses of ZnO seed layer were deposited on ITO-coated glass using the sputtering process detailed in 3.1.2.3. To control the thickness, the ZnO films were deposited by simply varying the deposition time. The seed layer thicknesses were measured by SEM, the thicknesses were in the range of (27nm, 63nm, 70nm and 130nm) respectively. The

seed layer has been reported [11] to have a significant role to promote the NR growth process in perpendicular orientation, decreases the thermodynamic barriers and it also tends to supply and nucleation centres [203].

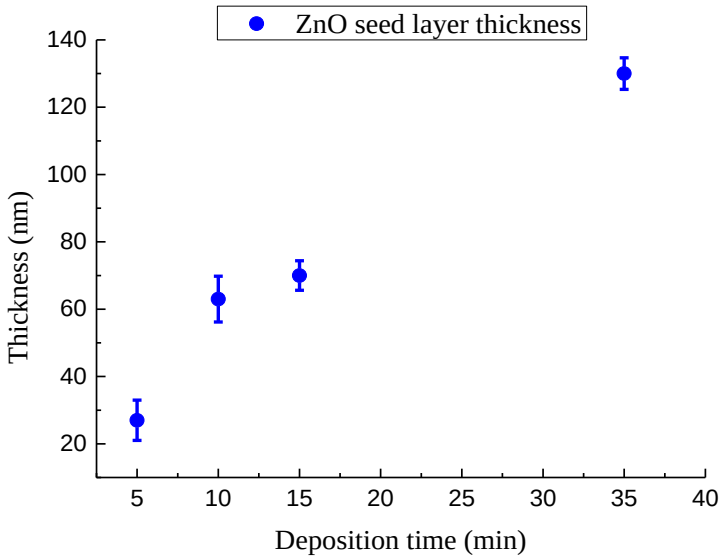

Figure 33. Evaluation of seed deposition thickness with deposition time.

4.1.2 Electron microscope (SEM) and atomic force microscope (AFM) for Seed layer

In this project a study of four different seed layers has been accomplished. The morphological properties of ZnO seed layers have been characterised by SEM and AFM. The micrograph images of SEM are used in evaluating the layer homogeneity over the substrate and AFM to estimate the first film roughness. Before carrying out the morphological SEM, the samples were coated with 3nm platinum (Pt) to avoid electron charging effect. As can be seen that, the distribution of the nanoparticles was almost uniform for all samples.

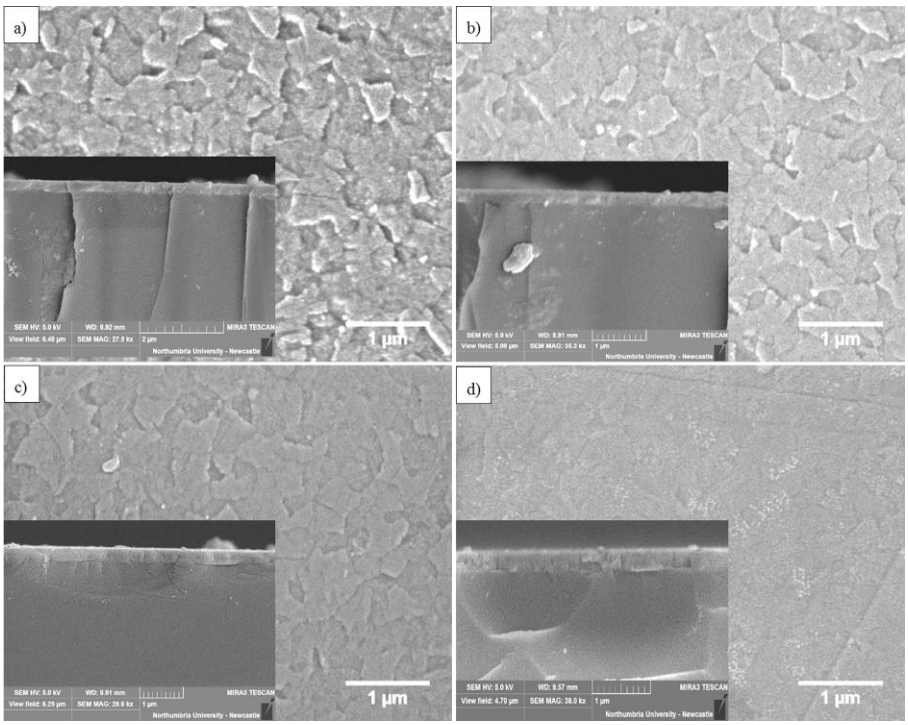

Figure 34. Top-view SEM images of ZnO seed layers coated with 3nm Pt. a) 27nm, b) 63nm, c) 70nm and d) 130nm.

Figure 34 shows the SEM morphology of the deposited ZnO seed layers. Data show that, the samples are ultra-thin films. Distinct closed-packed structure and highly coalesced grain boundaries were observed and continuous coverage of grain of the four different seed thicknesses (27nm, 63nm, 70nm and 130nm) respectively. These variations might be due to either grain boundary movement or evolution of the growth morphology or during the deposition process. It has been reported that, grain-boundaries are more disordered atomic arrangement ZnO NRs may nucleate in that area and growing in [002] plan may tend to grow vertically or obliquely to the substrate [204]. Figure 34a), 34b) and 34c) show in the first three deposition times 5, 10 and 15min almost the same structure and grains (exhibiting rough surface) whereas the 35min sample resulted in smoother surface. However, 35min deposited sample showed smoother surface. The thicker film, the lower is the strain needed to initiate cracks [205]. All of the observed results validate the fact that, the deposition time of seed layer has a significant impact on thickness of the

deposited ZnO seed layers. Thus, it is quite understandable that, the growth of the nanostructures could be influenced due to all observed changes in the seed layers.

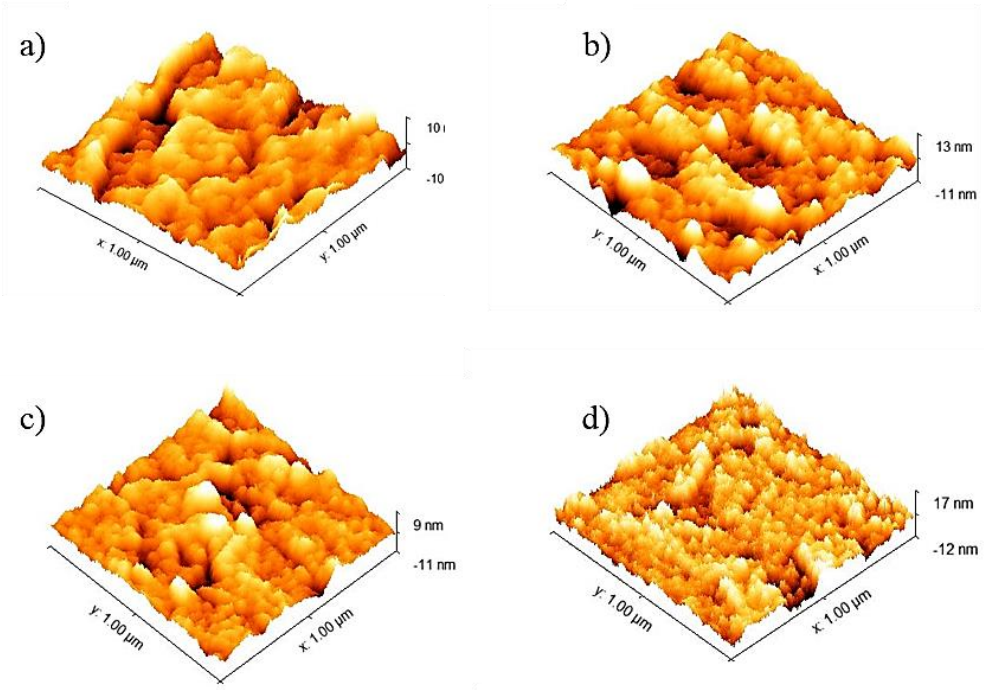

Figure 35. AFM images for the sputtered ZnO seed layers. a) 27nm seed, 63nm seed, c) 70nm seed and d) 130nm seed.

Figure 35 shows AFM images of ZnO seed layers sputtered on ITO-coated glass with average thicknesses of (27nm, 63nm, 70nm and 130nm) respectively. It can be clearly seen that, the surface of the samples are having different roughness. This tendency can be coincides with the seed grain size. Also match the SEM images in Figure 34. It can be mentioned that, the structure mismatch between the substrate and seed layers has played a significant role in the resulted films. For ITO, the Root Mean Square (RMS) of surface value is 3.8nm hence the seed deposition appears slightly to planarize the surface of ITO [206]. An analytical investigation of the surface topography of the deposited ZnO seed layers was obtained by AFM as a complementary analysis for the obtained results from SEM. The SEM images shown in Figure 34 indicated a uniform formation of the seed particles with a various roughness and grain sizes. The AFM image Figure 35 shows that,

the surface of the seeded samples have contained features with different roughness. Ji et al. presented a model that showed that, as the thickness of seed layer increases, the smoothness of the surface increased. And this is what was observed here with the T_{130nm} sample [207]. Figure 36 shows the significant effect of seed layer thickness and its impact on the orientation of top deposited layer. From the figure it can be clearly seen that, the thicker the layer the more vertically aligned NRs.

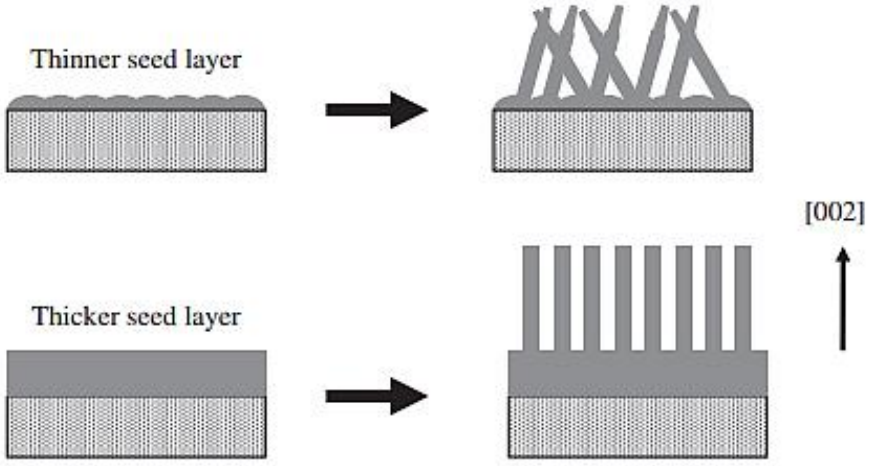

Figure 36. Nanowire growth mechanism using different seed thicknesses [207].

To investigate the crystallinity of seed samples, XRD analysis was performed. XRD spectrum of ZnO seed samples and ITO-coated glass is shown in Figure 37. The data from ITO-coated glass revealed three peaks (222), (400) and (440). These peaks were identical to the JCPDS (No. 06-0419) which correspond to indium oxide. And for seeded samples, three very weak peaks were observed for each sample. The peaks are obtained at the angle of diffraction peaks ($2\theta=30°$, $2\theta=35°$ and $2\theta=50°$) respectively. From the presented XRD results it was hard to observe any ZnO orientation on these samples as the layers are too thin [208]. The main diffraction peak of ZnO is $2\theta=34°$ and which corresponds to (002) plane. Normally for ZnO powder, the (002) peak position is at $2\theta=34.42°$ according to [209], indicating a good c-axis orientation which is perpendicular to the substrate surface [210]. The detected ($2\theta=35.48°$, $2\theta=35.46°$ and $2\theta=35.33°$) might

represent the (002) which showed slight shift from 2θ=34° and these variations were (35.48°, 0°, 35.46° and 35.33°) respectively. The shift towards higher diffraction angles could be due to the internal compressive stress in the resulted seed thin films as reported previously [207].

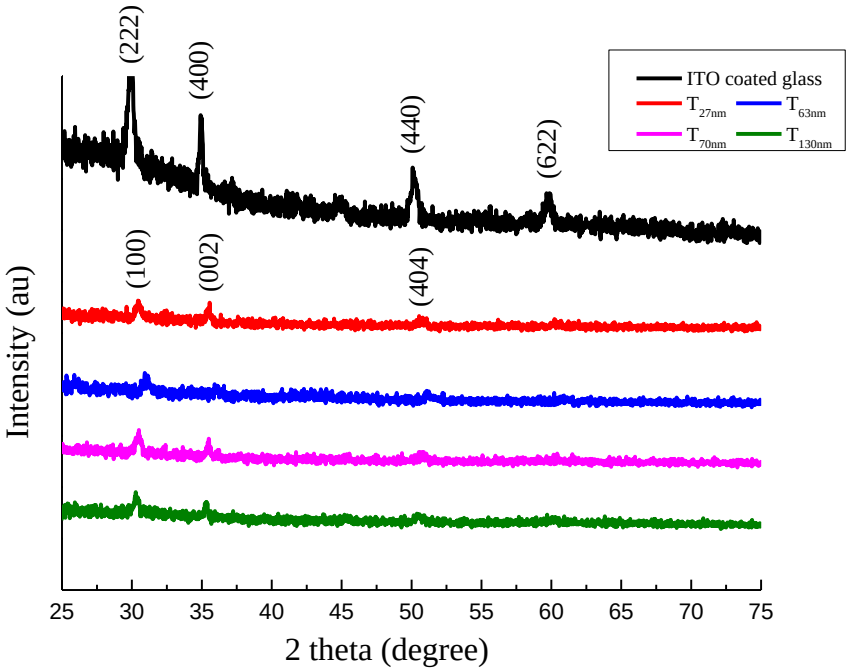

Figure 37. XRD patterns of ITO coated glass and seeded samples without the nanostructure

The four samples showed poor crystallinity features. The poor crystallinity is related to the very thin seed layer which was ranging from 27nm to 130nm, confirming that, the resulted seed layers are having thin layer. As the thickness of seed layer increases, the crystallinity increases [211]. For structural properties, almost same form is shown for all samples, different peaks were observed and the longer deposition time sample (T_{130nm}) which has a slight increase. The increasing intensity can be associated with thickness of the seed layer which was about130nm. The scans of X-ray diffraction revealed that, the full width half maximum (FWHM) value was the same for the observed 2θ=35°peaks at the value of 0.23° for T_{27nm}, T_{70nm} and T_{130nm} deposited samples. Whereas, the T_{63nm} deposition time has no 2θ=35° peak. (FWHM) did not show any significant changed as

the deposition time increases. For the T_{63nm} film, the 2θ=35° was not detected. The smaller FWHM values, the more ZnO films textured along c-axis as smaller FWHM value is an indication of a better crystallization of the thin films. It has been reported that, the particle size was closely related to the FWHM [212]. The ZnO seed samples exhibited almost same particle size. The particle size remains stable as the deposition time increases.

4.1.3 **UV-VIS-NIR for ZnO seed samples**

Figure 38 shows the spectra of the optical transmittance of different ZnO seed/ITO-coated glass substrate and the relative scattered light. High transmittance at around 90% is present in all seed samples with small variations for each sample. The ZnO optical transmittance is affected by film thickness, absorption coefficient and surface roughness [212].

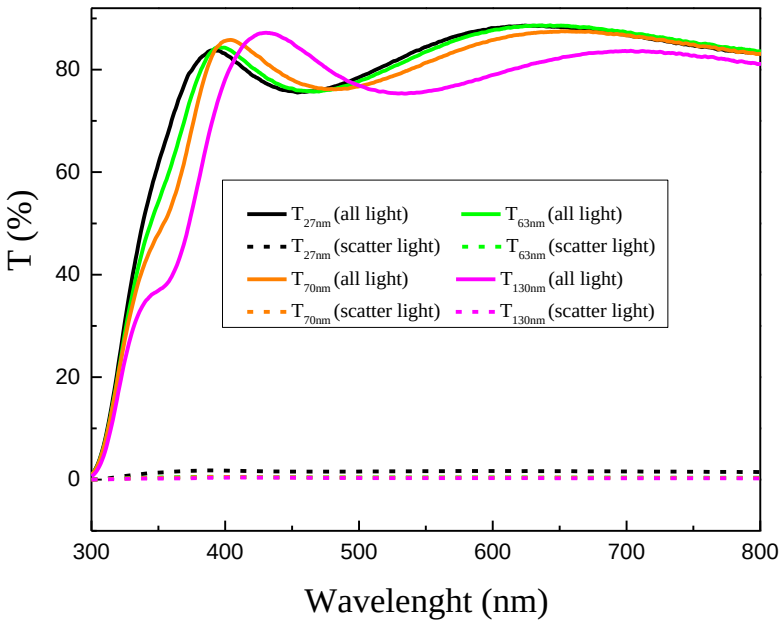

Figure 38. UV-VIS-NIR transmittance of the ZnO seed samples deposited on ITO-coated glass. Solid lines represent the total transmitted light and the dotted lines represent the diffused light.

The transmittance values were high in the visible range data. It was found that, as the thickness of the seed layer increases, the absorption edge was shifting towards the longer wavelengths. This can be attributed to the similar thin film characteristics that allows the light passing through to exhibit the same manner. Although the thicker thickness T_{130nm} showed lower transmittance due to increasing the scattered light. There was almost no scattered light for T_{27nm} T_{63nm} T_{70nm} samples.

4.1.4 Growth of ZnO NRs using zinc nitrate and zinc chloride salts (morphology)

High-density nanostructure have been obtained with different shapes, diameters as well as different orientation. The corresponding morphological features are shown in figure 39 when zinc nitrate is used and 45 when zinc chloride is used. It can be appreciated that, all of the resulted NRs showed hexagonal structure and exhibit different top end. There are two steps that can control the quality of 1D semiconductor nanostructures and these two steps are, nucleation which is the first initiation of 1D nanostructure growth and the second one is the growth temperature which represents a high importance in 1D nanostructure to obtain anisotropic growth with controlled shape, size and orientation [213].. The single crystallinity of ZnO NRs can be evident by their faceted crystal habit and by the XRD characterization. The hexagonal wurtzite ZnO crystal has a typical polar (001) plane and non-polar faces [(100) (101)] planes [214]. Therefore, the growth rate along polar (0001) plane is relatively faster than the non-polar crystal plane, hence c-axis takes faster growth rate than other crystallographic directions [215].

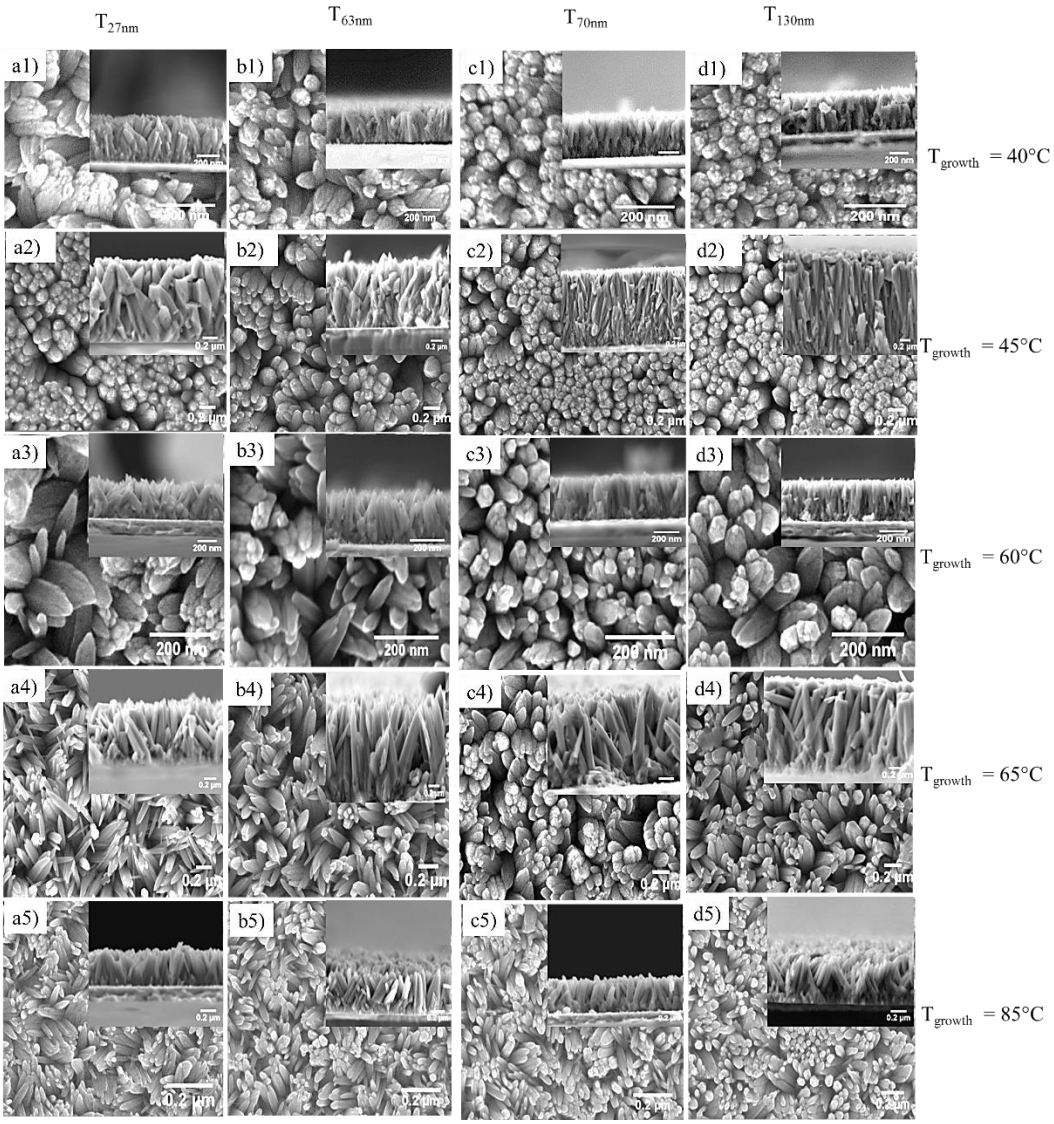

Figure 39. Top-view SEM images of the ZnO NRs on ITO-coated substrate with different growth temperatures T_{growth} = (40°C, 45°C, 60°C, 65°C, 85°C). Using zinc nitrate. Inset is cross-section.

The difference in ZnO seed thickness and T_{growth} showed a significant influence on the grown ZnO NRs as will be shown in the coming sections. It has been reported that, different surface energies (in Gibbsian sense is basically calculated as the excess energy over its bulk counterpart.) and the theoretical studies predicted that, the surface energy of non-polar plane is two-fold lower than one polar which makes the thermodynamic of non-polar planes higher and thus the energetically ZnO crystal are favourable for nano/micro structures formation as they have higher surface energy [37].

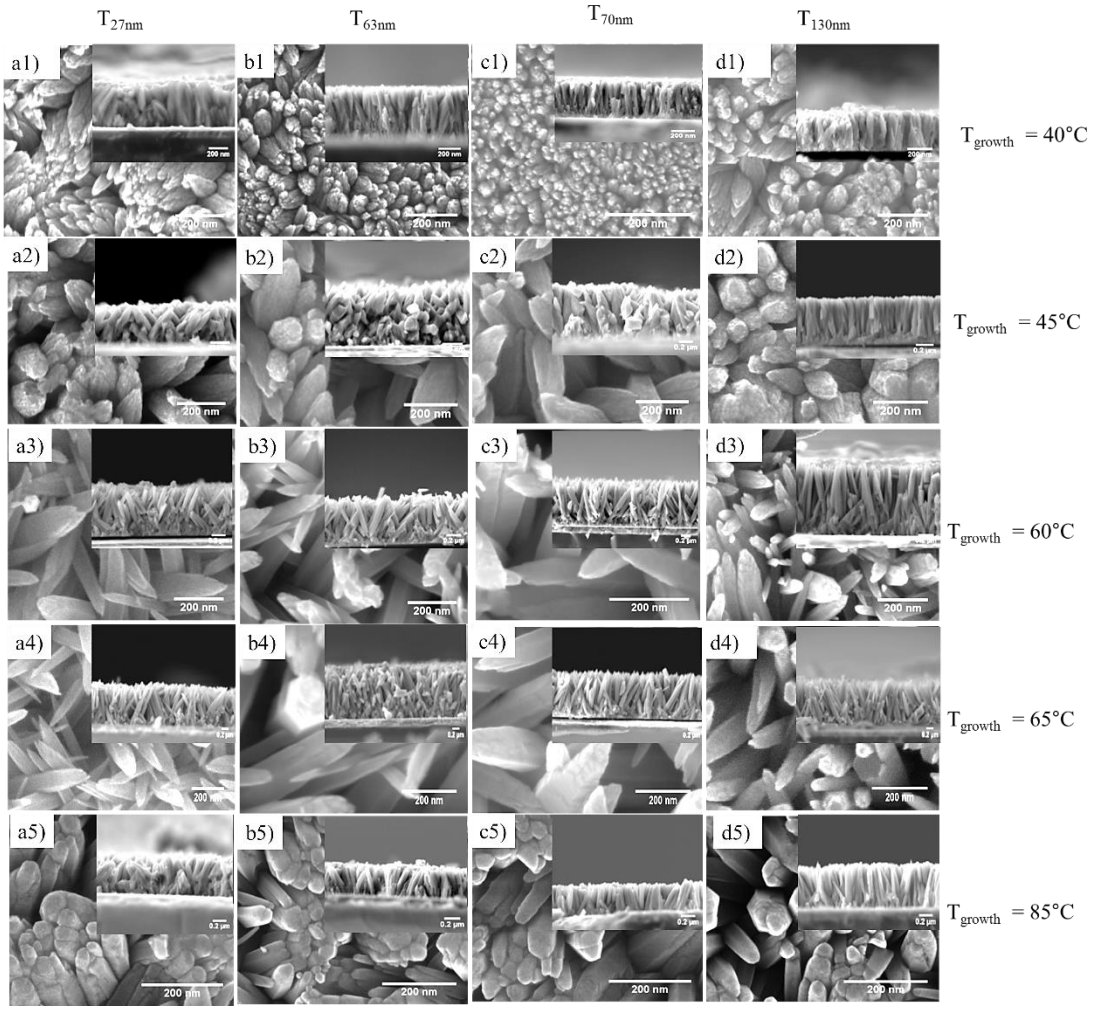

Figure 40. Top-view SEM images of the ZnO NRs on ITO-coated substrate with different growth temperatures T_{growth} = (40°C, 45°C, 60°C, 65°C, 85°C). Using zinc chloride. Inset is cross-section.

From figure 39 and figure 40 it can be clearly seen that, the resulted morphologies had different diameters and lengths. This can be attributed to several factors such as seed layer thickness and growth temperature and Zn salt which are detailed in sections 4.1.4.1 and 4.1.4.2. With zinc nitrate, the NRs are sharper and less dense whereas, zinc chloride showed more packed NRs.

4.1.4.1 **Seed layer thickness effect**

The diversity of morphology is due to different surface morphologies of ZnO seed samples and T_{growth} effect. The seed layer, in hydrothermal growth, is highly important as it provides an enhanced nucleation of the ZnO NRs growth hence, the it is crucial to understand the relationship between them[216]. A number of studies have been accomplished to investigate the growth and nucleation habit of polar ZnO crystal under the hydrothermal method different conditions [215]. More details on the resulted length and diameter are shown in Figure 41.

4.1.4.2 **Growth temperature (T_{growth}) effect**

The temperature effect on the hydrothermal growth of ZnO NRs was investigated by five different growth temperatures (T_{growth} = 40°C, 45°C, 60°C, 65°C and 85°C). From SEM images shown in Figure 39 and Figure 40. Many compact and hexagonal ZnO NRs can be seen on all samples. The resulted NRs are not well-ordered and consist of diagonal and pointed NRs for higher T_{growth}. The grown ZnO NRs are mostly tilted from c-axis the substrate. This tilting from the c-axis does not improve with varying the seed thicknesses and T_{growth}. The different surface morphologies are due to the different growth mechanism and different nucleation mechanism [215]. Moreover, both zin nitrate and zinc chloride salts illustrated that, most NRs grown on different seed thicknesses and different T_{growth} exhibit an obvious variation in the length and diameter. The corresponding length and diameter results are shown in Figure 41. The growth time and reaction temperature have significant effect on the resulted aspect ratio and morphology of ZnO NRs. In the growth of NRs, low temperature is favourable as at high temperature leads to re-evaporation due to high thermal energy. [217]. Hence dense and short ZnO NRs result. When low temperature is used, the energy of the vaporized reactants atoms is not high enough to diffuse through the used substrate, thus the atoms just merge over the surface and sit.

Temperature is represented to be one of the most important key parameters in the solution-based nanostructure growth [36, 217-219].

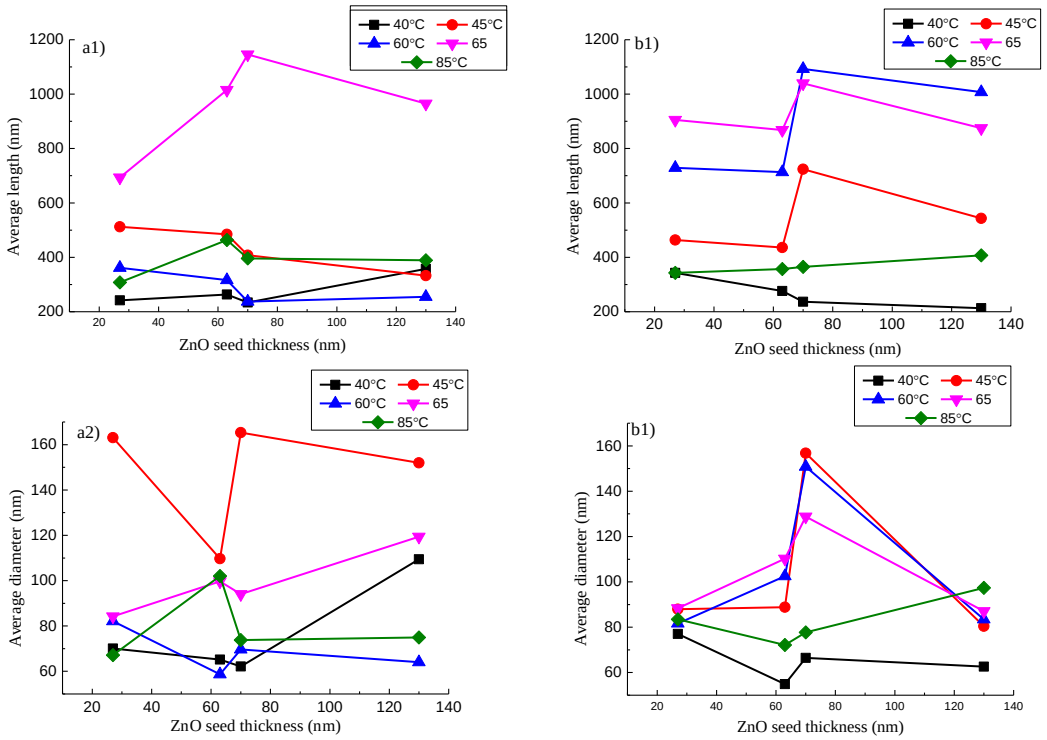

Figure 41. Length and diameter vs T_{growth}. a1-a2) for zinc nitrate and b1-b2) for zinc chloride.

From figure 41 it can be seen that, different T_{growth} exhibited variety of length and diameter from these two growth temperatures it was found that, the nanorods started to form NRs with large diameters when the T_{growth} is low. The morphology of the NRs improved as the T_{grwoth} goes to 60°C, 65°C and 85°C. From all represented figures it can be clearly seen that, T_{grwoth} = 40°C almost had the smallest length and diameter. Shuzi et al. revealed that, at the bottom of every hexagonal ZnO structure, there are a number of small NRs [220]. The phenomenon means that, the ZnO crystallises and amalgamate each other during the latter growth step as the growth along c-axis is faster than other directions [221]. The ZnO NRs growth process is reported to follow an epitaxial growth onto the

seed layer nanoparticles [222, 223]. This was shown in Figure 39 and Figure 40. As a consequence of that, the diameter of the NRs is highly sensitive to the seed layer grain size [199, 224]. Hence, the size of ZnO nanoparticle limits the radial growth during the nucleation step and also the mass transport of chemical precursors during the growth step [222]. Yet, it cannot exclude the coalescence of neighbouring nucleation sites during the second step [224]. It can be seen that, when the seed thickness increased from 27nm to 130nm, the average length of all samples grown at different temperatures showed variation in the resulted values. The length was further increase when the growth temperature increased to higher T_{growth}.

The diameter of ZnO NRs varied from (58 nm to 119nm) and (54nm to 156nm) for zinc nitrate and zinc chloride respectively. Such behaviour can be described by recalling the different seed layer thickness and surface nature. This confirms that, the crystallinity of the samples are different. The NRs in Figure 39 and Figure 40 showed different trend in terms of a decrease in the length of the NRs when the growth temperature was elevated from 40°C to 85°C. These variations in the length are attributed to the effect of seed layer on the growth of ZnO NRs. Many studies indicated that, as the seed layer thickness increases, the length of NRs decreases [225, 226].

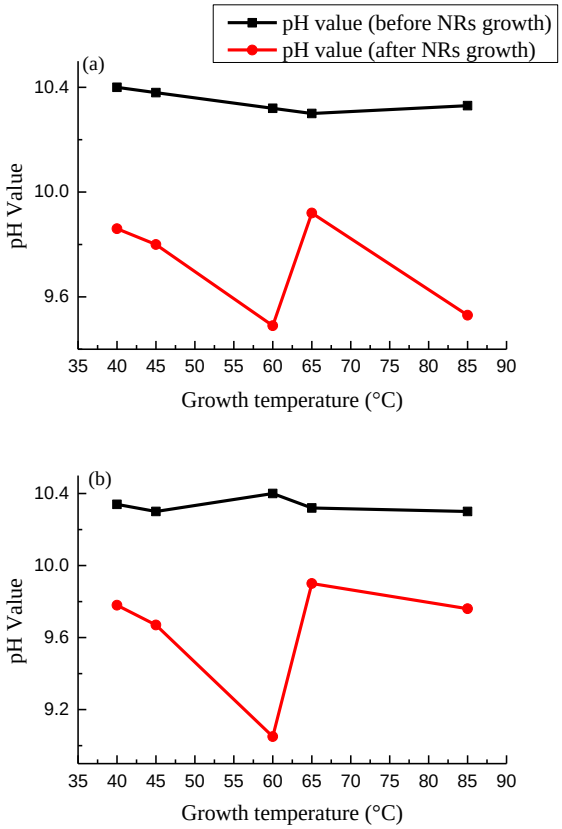

Figure 42. pH values change before and after the hydrothermal ZnO NRs growth. a) zinc nitrate growth solution and b) zinc chloride growth solution.

The value of pH was also monitored before and after the growth process as shown in Figure 42. The $pH_{initial}$ value (before the growth) and the pH_{final} (after the growth) were recorded to study its effect on the resulted NRs. The pH was fixed to 10.3-10.4 for all hydrothermal growth. As shown in Figure 42, the two used zinc salts showed almost similar trend. After two hours growth time, it was found that, at T_{growth} from 40°C to 60°C, the pH_{final} value dropped significantly from 10.02 to 9.05 and 9.4 for zinc nitrate and zinc chloride respectively. And the pH_{final} was increased at T_{growth} = 65°C and slightly dropped at T_{growth} = 85°C. The pH_{final} at 40°C and 45°C illustrates that, the temperature is not high enough to enhance the fast chemical reaction and this can be clearly seen at the colour of the solution which takes a longer time to turn to non-transparent colour. As at the beginning of the growth, the solution colour is transparent and after applying the temperature it starts to change to milky colour when the reaction starts. The pH_{final} at 60°C

started to drop dramatically for zinc nitrate and zinc chloride respectively. This can be interpreted as that, at low growth temperatures, the provided hydroxide ions by ammonia caused the growth reaction to be slow down. Hence, the state of supersaturation is suppressed to for ZnO film. Also, supersaturation might be the reason as it is a key driving force to form ZnO which is influenced by solution concentration and OH^- needed for ZnO growth. OH^- is an important content in the hydrothermal growth solution which plays a pivotal role in achieving proper supersaturation to grow a nanostructure. When ammonia is introduced to solution used in the hydrothermal process, it tends to generate nitrogen atoms which play the key role in the growth of the nanostructure[227]. The crystal growth rate is usually reduced by solution supersaturation. The critical supersaturation point below which a crystal does not form and grow might be correlated to the low growth temperature. Additionally, in solution-based growth, higher degree of supersaturation is favourable to achieve a homogeneous nucleation and that leads the nutrition to be consumed quickly [228]. The resulted nanostructures are about to form a continuous film rather than nanorods like structure.

4.1.5 **X-Ray diffraction Structural Characteristics (XRD)**

In order to investigate the influence of the different zinc salts, different seed thicknesses and different T_{growth}, structural characterization of the as-grown ZnO NRs has been accomplished. Using X`pert HighScore, the XRD patterns of the grown ZnO NRs are displayed in figure 49. It was clearly observed that, a wurtzite hexagonal structure was present for all samples with diffraction intensity peak of (002). The presented results in this work can be indexed to the used standard spectrum in JCPDS (No. 36-1451) and the pattern are shown in Figure 43. The diffracted peak (002) is dominating in these samples. It can be appreciated that, comparing to the standard JCPDS value for (002) (2θ = 34.438◦) for ZnO bulk material.

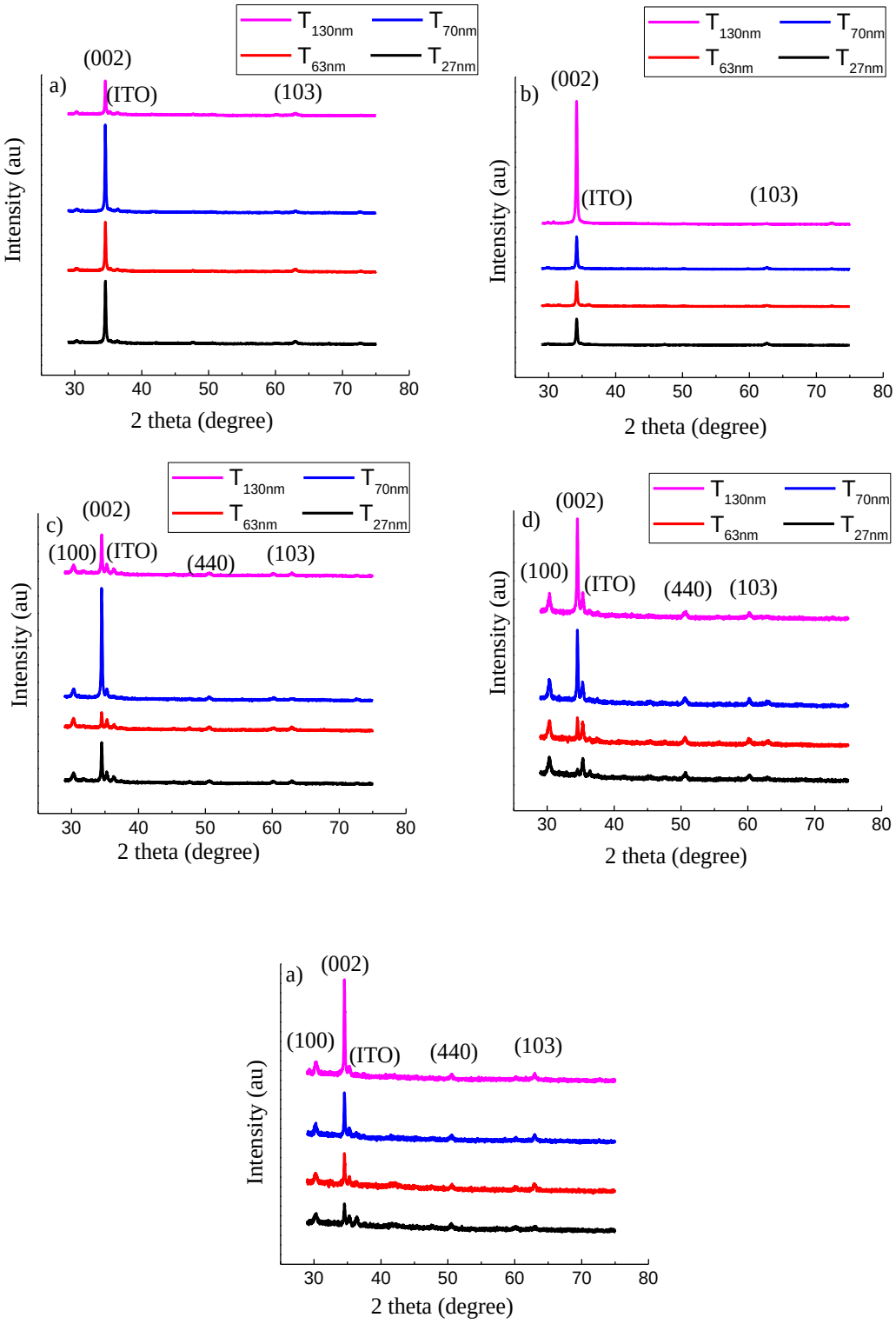

Figure 43. ZnO NRs XRD patterns grown at five different temperatures T_{growth} using $Zn(NO_3)_2$ at 40°C, 45°C, 60°C, 65°C and 85°C.

For zinc nitrate Figure 44, it can be seen that, different diffraction peaks of the resulted hexagonal ZnO NRs were revealed such as (002), and (101), (103) and (004) crystallographic plans are clearly identified. There are some resulted peaks which were not recognised by XRD software analyser. This can be because of some impurities in the sample.

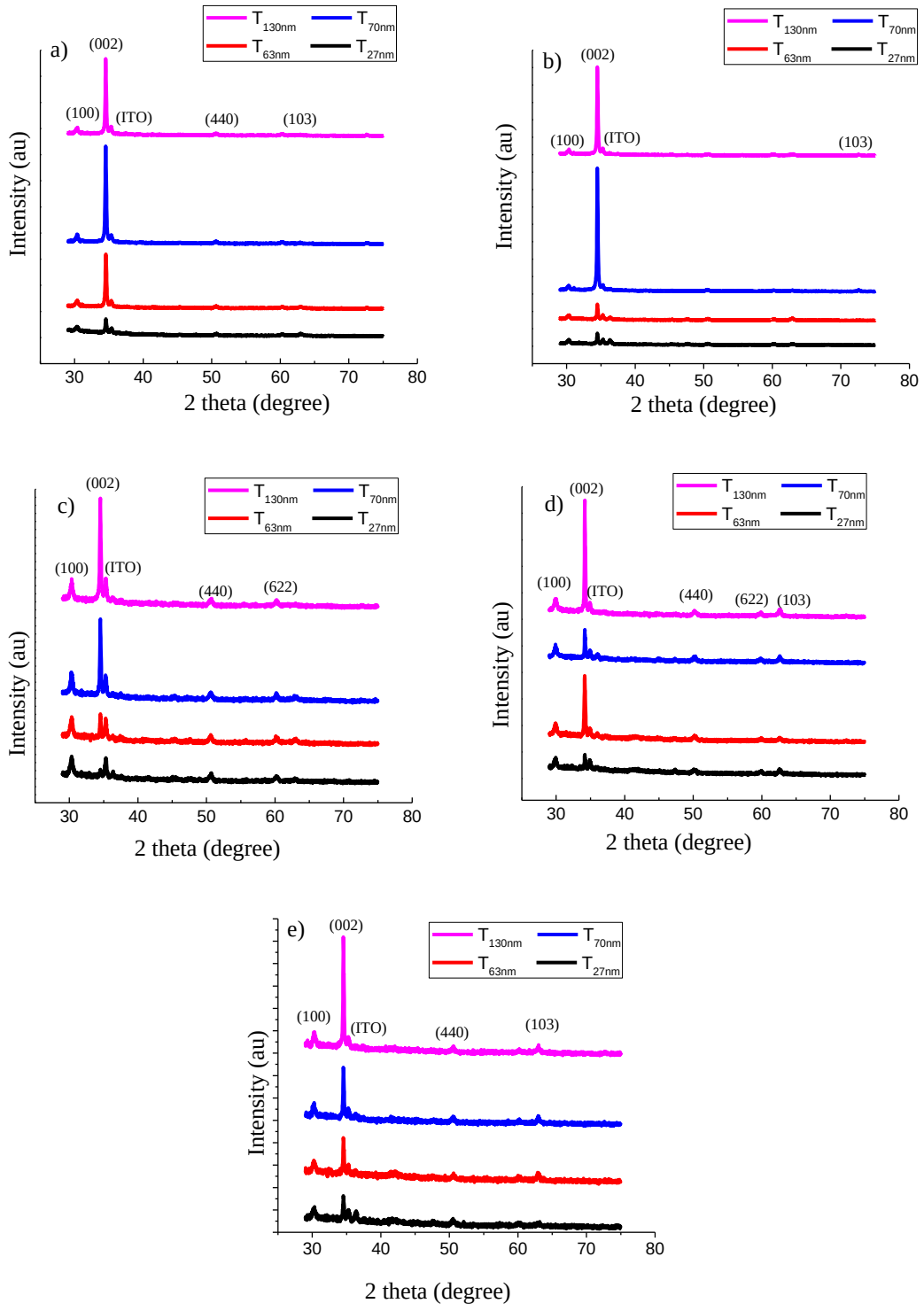

Figure 44. ZnO NRs XRD patterns grown at five different temperatures T_{growth} using $ZnCl_2$ at 40°C, 45°C, 60°C, 65°C and 85°C.

On the other hand, zinc chloride samples figure 44, it can clearly see that, (100), (002), (101) (102), (103) and different peaks are revealed however, the (002) peak dominates in these samples. The rest of the peak are relatively small since they are diffracted from different planes, which reveals that, the NRs are growing in c-axis (the initial orientation owing to nucleation and the final growth orientation on the substrate interface and the sequential growth in the direction perpendicular to the used substrate). Unrecognised peaks were observed which might related to the used ITO-coated glass substrate. From the XRD variations it can be mentioned that, the uniform growth of ZnO NRs and the vertical alignment are strongly affected by the seed layer used. The alignment and the density of the NRs can be improved by providing more nucleation sites [199, 229]. Thicker the seed layer, the smaller nanoparticles (more seeds) over the surface [230]. It means that, although being able to grow high aspect ratio (smaller diameter and longer nanorods) by thicker seed layer, the main criteria to select the suitable seed layer such as best morphology, alignment and texture uniformity are not provided [230].

4.1.5.1 **Crystal size of ZnO NRs**

The crystal size as a function of the seed deposition time and T_{growth} are shown in Figure 45. Different approaches are used with the purpose of estimating the average particle size of the thin films using XRD data. However, the Debye Scherrer size equation is the method that is employed the most and, is used herein to calculate the crystal as the following:

$$D = \frac{k\lambda}{\beta \cos\theta} \qquad (9)$$

Where D is the crystal size, k is a constant = 0.9, λ is the Cu-Kα wavelength, i.e. 1.54056A°, βis the full width of a half maximum of the corresponding peak, θ the angle of corresponding XRD peak (Braggs diffraction angle). As the crystal size can have a significant effect on the grown NRs, it was important to calculate it values. This will enhance understanding the reason behind obtaining different length and diameters. In relation with the crystal size, it has been obtained that, different values were observed. Remarkably, the crystal size was drastically increased for T_{27nm} at T_{growth} = 60°C (see figure 45b1).

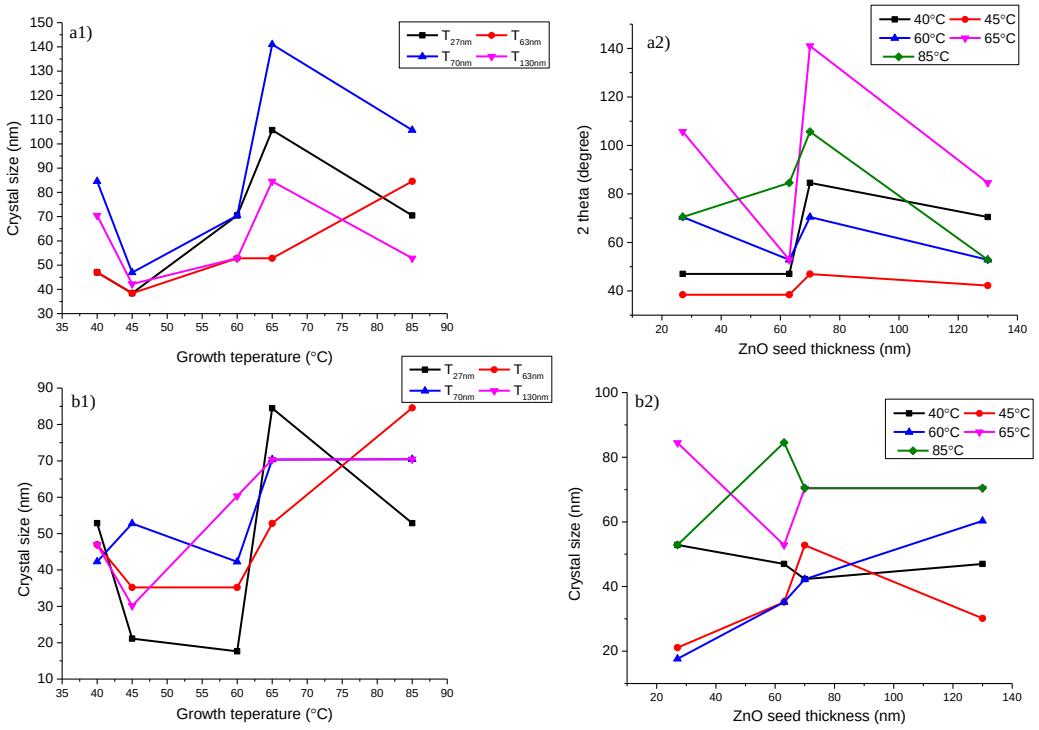

Figure 45. Crystal size vs Tgrowth and ZnO seed thickness. a1), a2) for Zinc nitrate and b1), b2) for zinc chloride.

Introducing the lattice strain occurs during the growth time and this residual strain have a significant effect in tuning the optical and structural properties of the grown nanostructure, hence affecting the performance of the targeted device performance [231]. Herein, by calculating and estimating the strain values, it can be achieved that, whether

the strain have an impact of the grown NRs or not. The lattice strain can be estimated [32, 231].

4.1.5.2 Variation of lattice constants of (002) of the grown ZnO NRs

Different values have been obtained and the existence of these variations can be clearly noticed in the diffracted peaks shown in Figure 43 and Figure 44. The obtained values were relatively close and similar for all samples. The lattice strain ƹc the strain along the c-axis, (c = 5.2038 Å) and (a = 3.2494 Å) are standard lattice constant for the unstrained ZnO NRs. The lattice constants of ZnO wurtzite structure a and c are calculated by using Bragg's law, as following equations [232]. The calculated a and c values are displayed in table 6.

$$a = \frac{\lambda}{\sqrt{3}\sin\theta} \quad (10)$$

$$c = \frac{\lambda}{\sin\theta} \quad (11)$$

Where, λ = 1.54056 A° [32].

Table 6. Variation of lattice constants of (002) of the grown ZnO NRs using zinc nitrate and zinc chloride.

Zinc nitrate								
Seed thickness (nm)	**T_{27nm}**	**T_{27nm}**	**T_{63nm}**	**T_{63nm}**	**T_{70nm}**	**T_{70nm}**	**T_{130nm}**	**T_{130nm}**
T_{growth} (°C)	**a(Å)**	**c(Å)**	**a(Å)**	**c(Å)**	**a(Å)**	**c(Å)**	**a(Å)**	**c(Å)**
40°C	3	5	3	5	3	5	3	5
45°C	3	5	3	5	3	5	3	5
60°C	3	5	3	5	3	5	3	5
65°C	3	5	3	5	3	5	3	5
85°C	3	5	3	5	3	5	3	5
Zinc chloride								
Seed thickness (nm)	**T_{27nm}**	**T_{27nm}**	**T_{63nm}**	**T_{63nm}**	**T_{70nm}**	**T_{70nm}**	**T_{130nm}**	**T_{130nm}**
T_{growth} (°C)	**a(Å)**	**c(Å)**	**a(Å)**	**c(Å)**	**a(Å)**	**c(Å)**	**a(Å)**	**c(Å)**
40°C	3	5	3	5	3	5	3	5
45°C	3	5	3	5	3	5	3	5
60°C	3	5	3	5	3	5	3	5
65°C	3	5	3	5	3	5	3	5
85°C	3	5	3	5	3	5	3	5

4.1.5.3 **XRD peak Intensity of the grown ZnO NRs**

The resulted (002) XRD intensity as a function of T_{growth} and seed thickness is shown in Figure 46. When zinc nitrate was used, Figure 46a1) and Figure 46a2), when the intensity in plotted as a function of T_{growth}, the thicker seed layer T_{130nm} grow at T_{growth} = 45°C showed the massive increase to the highest XRD intensity. And similar trend is observed for the rest of the samples. It has been reported that, the sharper intensity the better crystallinity [233]. However, this was not the case here as low T_{growth} showed almost continues film (NRs with large diameter). On the other hand, for zinc chloride, the thinner seed layer showed the lowest intensity values. As the seed thickness increased, the intensity increased. However, T_{70nm} grown at T_{grwoth} = 40°C showed higher intensity. When then the intensity is plotted as a function of seed thickness it was found that, T_{growth} = 40°C showed different behaviour in contrast to other T_{growth}.

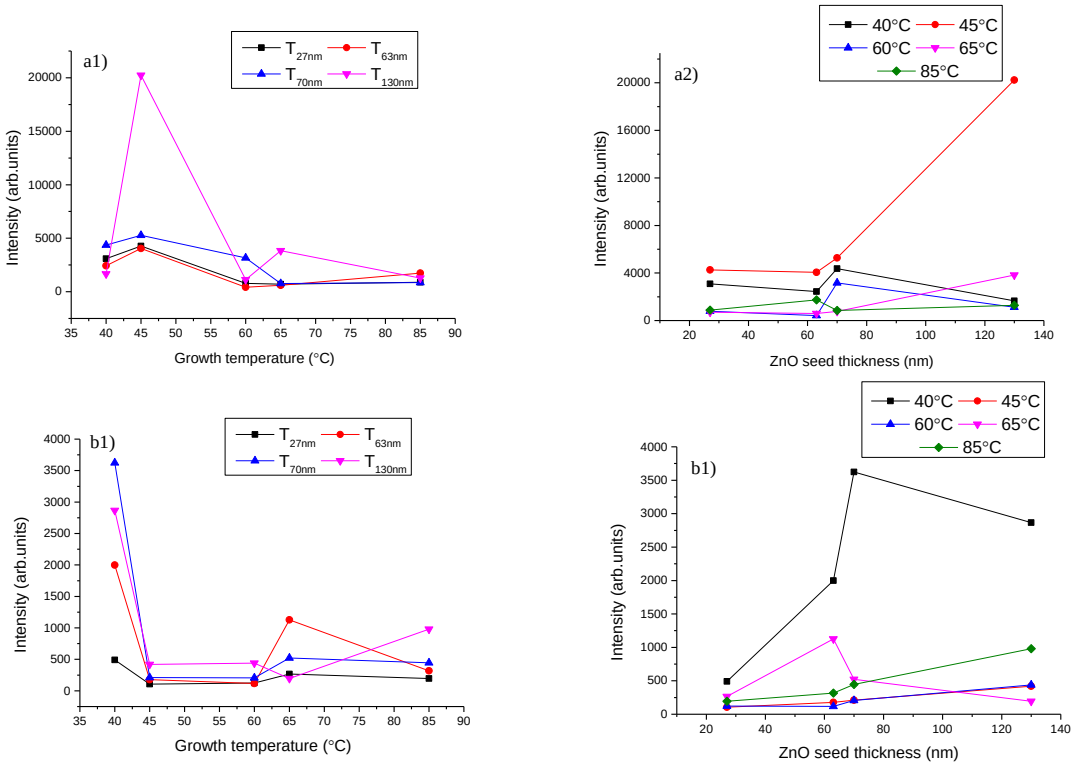

Figure 46. The effect of T_{growth} and seed thickness on the resulted ZnO NRs Intensities. a1, a2) using zinc nitrate and b1, b2) using zinc chloride.

4.1.5.4 **Texture coefficient (TC)**

As can be seen in Figure 47, most TC values were lager than one. For all (002) at different T_{growth} the TC values ranged from (1.1 to 6.7) and (0.2 to 6.5) for zinc nitrate and zinc chloride respectively. The effect of seed thicknesses and T_{growth} can be clearly seen. As increasing the seed thickness and T_{growth} showed different values. A wide variety of the observed textures at varying the growth conditions contributes in providing the detailed information about the grown film and its structural properties. The higher degree of orientation along c axis means a higher TC [234]. The texture coefficient (TC) can quantify the degree of c orientation of the synthesised NRs. Texture coefficient (T_C) was also calculated to extract the quantitative information for the ZnO NRs produced and regarding their preferential crystal orientation. T_C was calculated using the following equation as showed in [235, 236].

$$C_{hkl} = \frac{I_{hkl}}{\frac{1}{n}\sum_n \frac{I_{hkl}}{I_{rhkl}}} \quad (12)$$

$$C_{hkl} = \sqrt{\sum \frac{1}{n}(C_{hkl} - 1)^2} \quad (13)$$

Where T_C (h k l) represents the texture coefficient, I (h k l) signifies the intensity of XRD, n is the diffraction peaks number considered and finally, I_o (h k l) represents the plane standard intensity which is normally taken from JCPDS data, as illustrated in [237, 238].

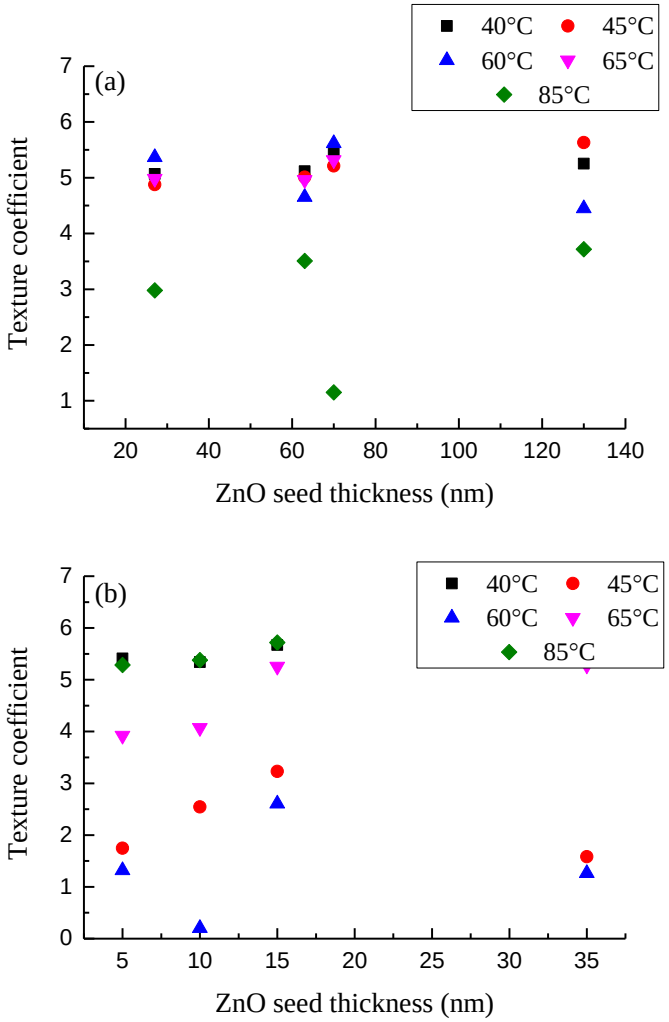

Figure 47. Variations of ZnO NRs texture coefficient for (002) peak. a) is Zinc nitrate and b)is zinc chloride.

Figure 47a) showed that, different TC values were resulted. These observations illustrated that, the growth was suppressed at some point. In the other word, strong ZnO NRs TC can be achieved when the T_{grwoth} is between (40°C - 65°C). When the zinc chloride used, Figure 47b), the highest TC was around 6. Comparing to zinc nitrate, T_{growth} = 85°C showed higher TC values with T_{growth} = 40°C. A clear improvement is observed for 85°C samples as it showed almost linear dependence between the TC and seed thicknesses.

4.1.5.5 **Preferred orientation (σ)**

Form figure 48, it can be concluded that, from Figure 48a) the preferential orientation of the grown ZnO NRs can be achieved when the T_{growth} ranges from 40°C to 65°C. The Highest T_{growth} = 85°C was giving the lowest values over the all used samples. In contrast, Figure 48b) showed TC values range of 0.9 to 2.3. The lowest TC was obtained when the NRs grown at T_{growth} = 45°C using T_{63nm} seed layer.

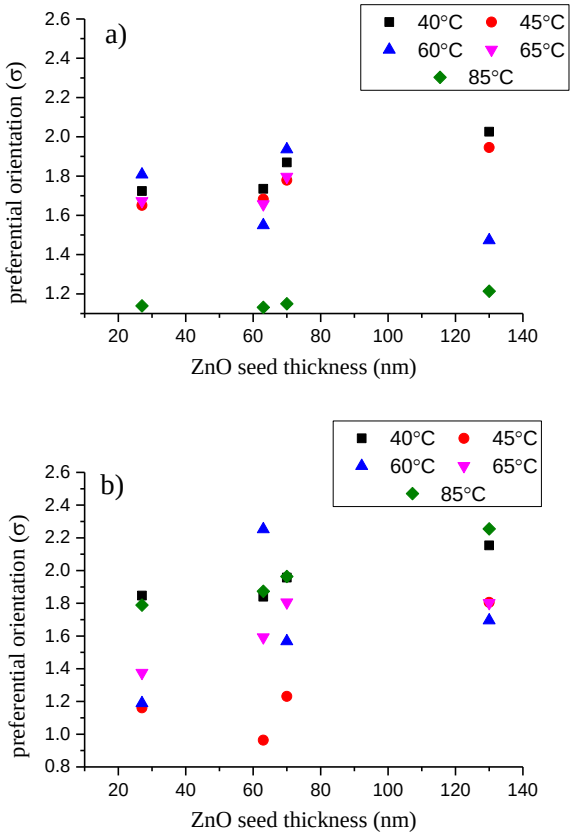

Figure 48. Variations of ZnO NRs preferred orientation. a) Zinc nitrate and b) zinc chloride.

Analysis of the preferred orientation of a film can be achieved by using the standard deviation σ of the values of all C_{hkl} as shown in the following equation.

$$\sigma = \sqrt{\sum \frac{1}{n} (Chkl - 1)^2} \quad (14)$$

Where the values of σ are used in the comparison of degree orientation between different used samples. Hence, the low σ value indicates that the film is more randomly orientated. A large TC value of a diffraction peak is an indication of a preferred orientation along that direction. Form Figure 48, it can be concluded that, from Figure 48a) the preferential orientation of the grown ZnO NRs can be achieved when the T_{growth} ranges from 40°C to 65°C. The Highest T_{growth} = 85°C was giving the lowest values over the all used samples. In contrast, Figure 48b) showed TC values range of 0.9 to 2.3. The lowest TC was obtained when the NRs grown at T_{growth} = 45°C using T_{63nm} seed layer. Hence, it can be concluded that, T_{130nm} at T_{growth} = 40°C is the preferred orientation for zinc nitrate and 10min at T_{growth} = 65°C is the preferred orientation for zinc chloride. $T_{63nm\ and}$ T_{130nm} at (T_{growth} = 60°C and T_{growth} = 85°C) is the preferred orientation as well when using zinc chloride. This high TC value imply that, crystal growth along these plans is promoted. All of the grown ZnO NRs demonstrated an obvious preference to grow along (002). This effect (i. e., preferential growth was more predominate at (002). The increased XRD intensity is always accompanied by the full width half maximum (FWHM) decrease. Such this issue supports the enhancement and the increasing of the order of the material or material's crystallization.

4.1.6 **ZnO NRs Optical Properties**

Achieving a full understanding of multi-layer optical properties is no a trivial task. In particular, when tilted, disordered and randomly oriented nanostructured film that possess range of dimensions in wavelength order that makes the system more complex [239]. The optical properties on ZnO nanorods depend on two main parameters, the morphology and crystal quality of the film [239]. It is illustrated that, to achieve better UV light absorption, smallest ZnO NRs are preferred [240]. The investigation of the ZnO optical properties was carried out and the optical transmittance was observed by using the UV-VIS-NIR spectrophotometer.

4.1.6.1 **UV-VIS-NIR transmittance analysais**

Figure 49 and Figure 50 display the UV-VIS-NIR transmittance of the grown ZnO NRs with variation of growth conditions (zinc salt, temperature and seed layer thickness) in the range of 400-1400nm wavelength. Seed samples without NRs were shown in Figure 43. For both zinc salts, the grown ZnO NRs show almost 60-80% transmission. The effect of introducing a nanostructure over a sample can be clearly seen compared to seed samples. The average transmittance of all grown samples in the visible light is over 70%. Whereas, the scattered light was about 50% in the 400-600nm wavelength range for all samples. Figure 49a1-a5), similar range of transmitted light is observed for T_{growth} = 40°C, 45°C, 65°C and 85°C. However, ZnO NRs grown at 60°C showed lower transmittance at about 60% despite the scattered light being almost at the same range with the other growth temperatures. The lower transmittance can be attributed to reflected light at the interface of air/glass.

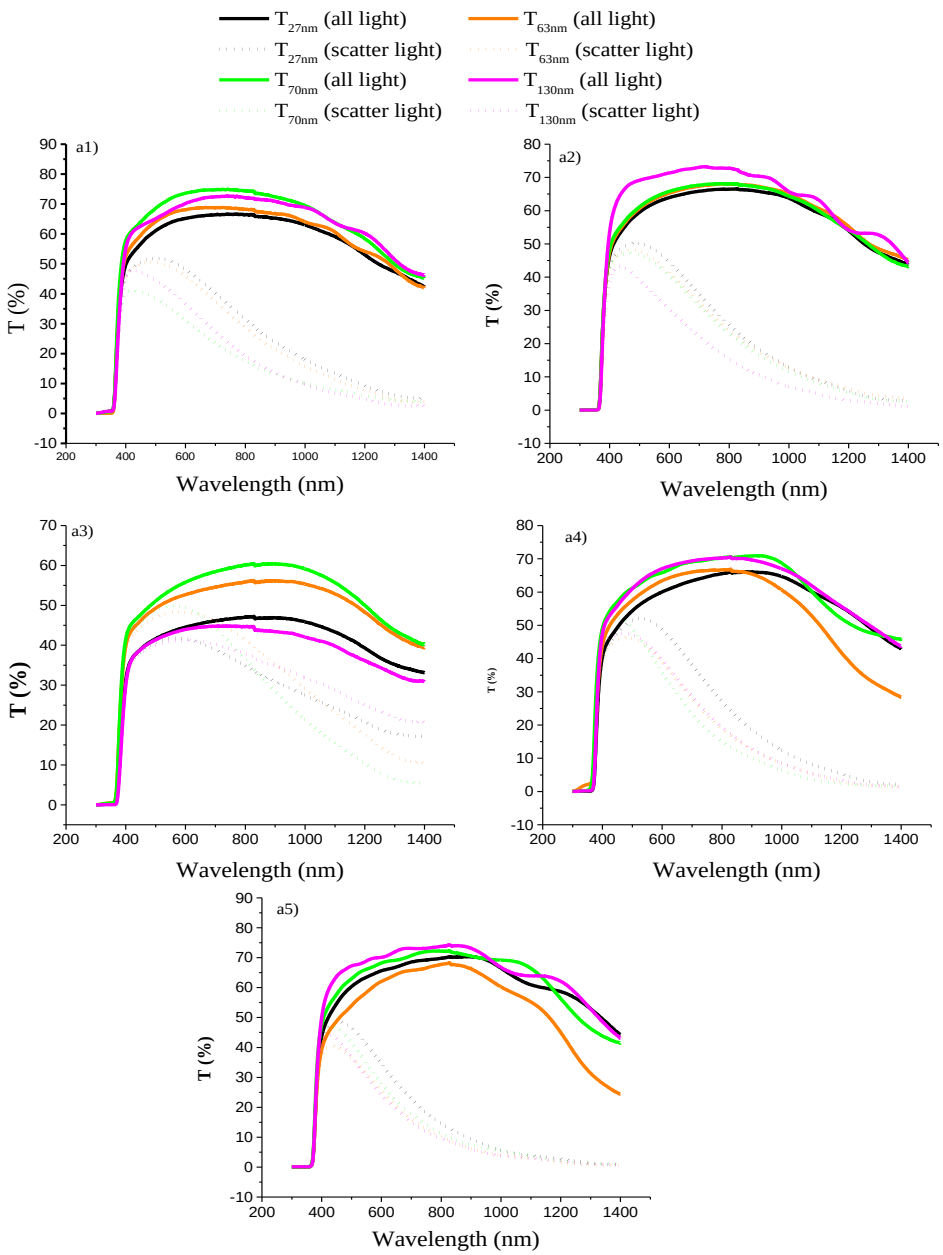

Figure 49. UV-VIS-NIR transmittance of the ZnO NRs grown using zinc nitrate. a1) 40°C, a2) 45°C, a3) 60°C, a4) 65°C and a5) 85°C.

No significant changes were observed except slight transmittance decrease at 60°C. At 60°C (figure 49), the T_{63nm} showed the highest preferred orientation. Only this growth temperature showed different manner regarding the slight shift of the absorption edge for T_{27nm} and T_{130nm} samples. Figure 50b1-b5) showed almost similar values comparing to zinc nitrate samples. When zinc chloride is used, 40°C and 60°C showed variations in all

transmitted light and scattered light. At 60°C (Figure 50), the all transmitted light for T_{70nm} was the highest at about 70% in the 400nm-1000nm wavelength. Whereas, the all transmitted light decreased for the rest of samples.

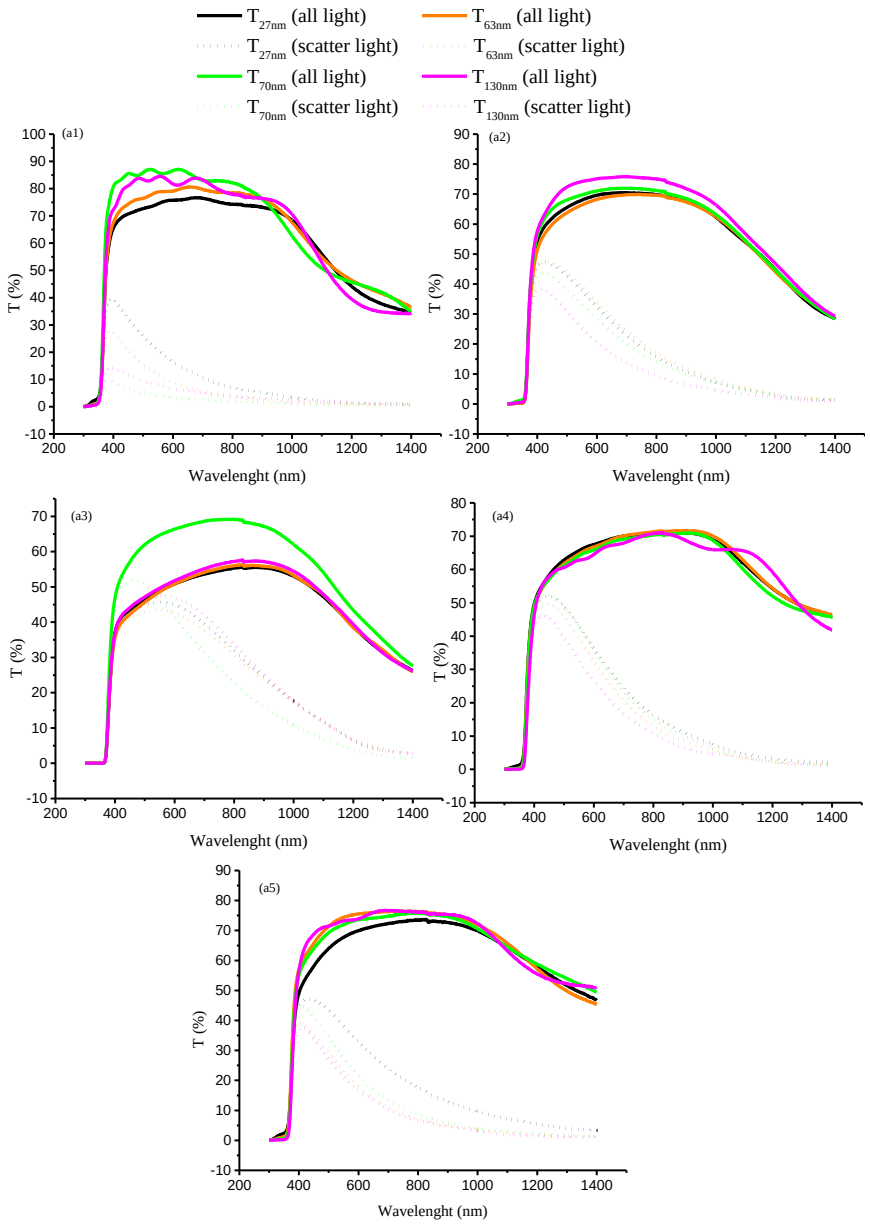

Figure 50. UV-VIS-NIR transmittance of the ZnO NRs grown using zinc chloride. a1) 40°C, a2) 45°C, a3) 60°C, a4) 65°C and a5) 85°C.

Increasing the light scattering is connected to the ZnO film roughness and hence correlating that to obtained morphology [239]. Increasing the diameter of NRs can enhance broadening the light absorption spectra from short wavelength to longer

wavelength [239, 241, 242]. When comparing the tilted NRs to perfectly aligned or perpendicular NRs, more broadening in wavelength range is possible to occur since the optically effective tilted NRs diameter is increased [239, 241, 243]. A number of studies demonstrated that, decreasing the length of the NRs induces an intensity reduction and no effect for wavelength of the scattered light [239, 241, 242].

4.1.6.2 **Haze measurements**

Light management is considered as one of the most important direction in order to achieve high efficiency and low cost in solar cell fabrication due to the importance of scattering light effect. Increasing and extending the light propagation path is receiving a considerable attention from the researchers [244]. Nanostructures are one of the preferential ways to achieve the desired goal since some improvements have been shown for the sunlight absorbers that are used in fabricating solar cells when for example plasmonic nanostructures, photonic crystals and diffraction gratings are used. Moreover, utilizing ZnO NRs could lead to increased light scattering in the visible range [245]. Light scattering effect can be estimated by calculating the transmittance haze, which in turn can be defined as the ratio of light diffusion to total radiation transition [245]. Transmittance haze (H_T) can be expressed as the following:

$$H_T = \left(\frac{T_{diff}}{T_{tot}}\right) \quad (15)$$

Where H_T transmittance haze, T_{diff} total diffusion and T_{tot} total transmission. In addition, the haze ratio can be regarded as an important characteristic value that shows the substrate ability to scatter light at different and random angles [246]. The haze values were extracted using the wavelength range 400nm-1400nm as shown in figures 51 and Figure 52.

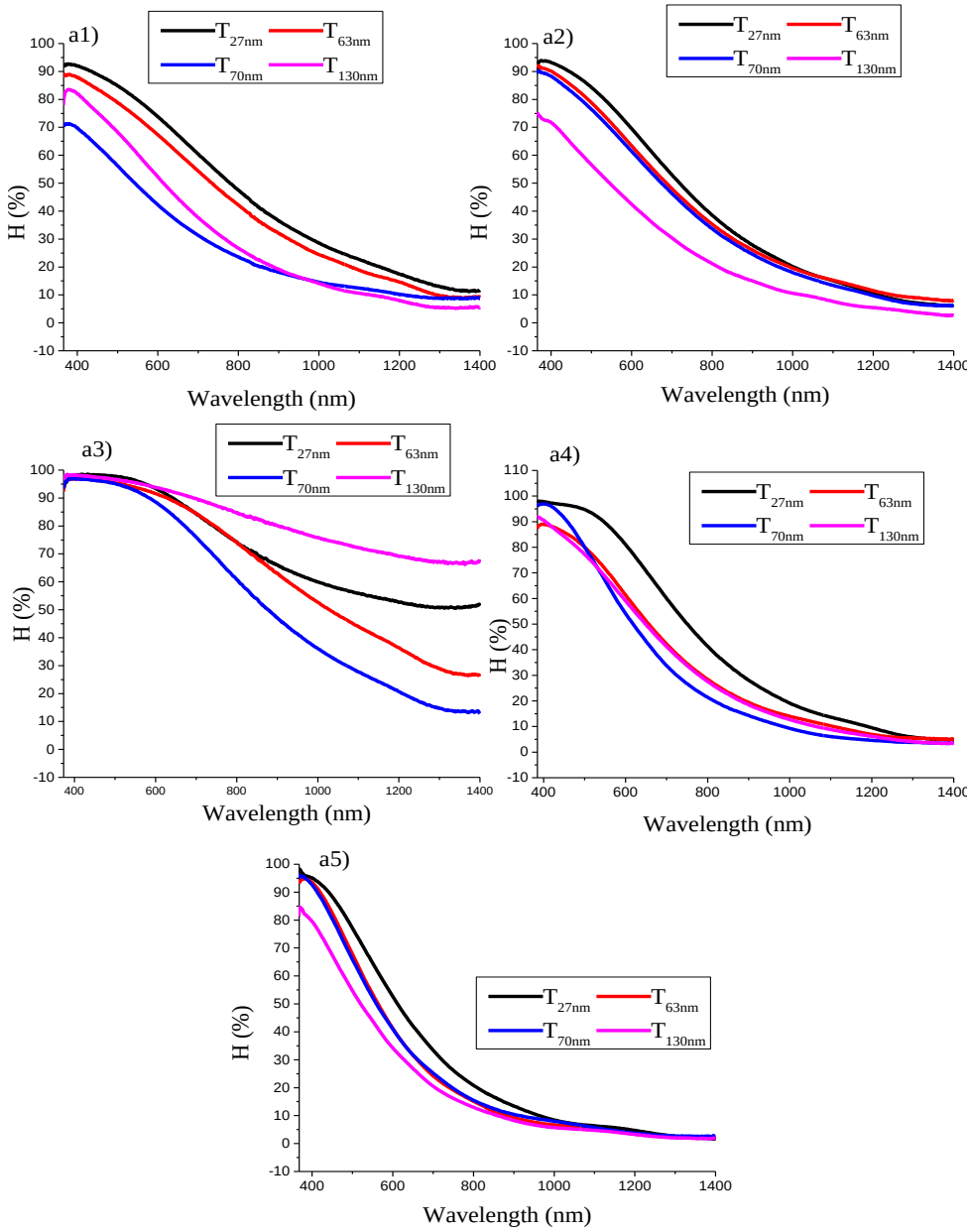

Figure 51. Transmittance haze spectra of the ZnO NRs grown using zinc nitrate at (40°C, 45°C, 60°C, 65°C and 85°C).

From Figures 52 and Figure 53, the highest haze value was reaching over 90 %. All samples had almost similar shape except 60°C Figure 51 a3. Under the 40°C growth temperature, the T_{27nm} and T_{63nm} samples showed a similar shape and light scattering properties having total haze higher than the T_{70nm} and T_{130nm} samples respectively. Either this similarity can be attributed to the shape of the NRs or the behaviour of the penetrated light. The T_{70nm} seed is even much lower reaching a value of 70 % at 400nm. For 45°C

(figure 51), the spectrum for T_{27nm} was much higher reaching a maximum value of about 93 % and minimum haze value at this growth temperature was observed for T_{130nm} at around 70 %. Whereas For 45°C (Figure 52) T_{70nm} sample showed about 97 % haze among the other samples. For 60°C (which showed different shape over the rest of the growth temperatures), form 400-600nm the recorded haze was almost the same for all samples at about 98 %. For 65°C and 85°C (both cases, zinc nitrate and zinc chloride), the resulted spectra for the different seed thicknesses show that, thinner seed layers had the highest values and the thicker seed layer had the lowest haze value.

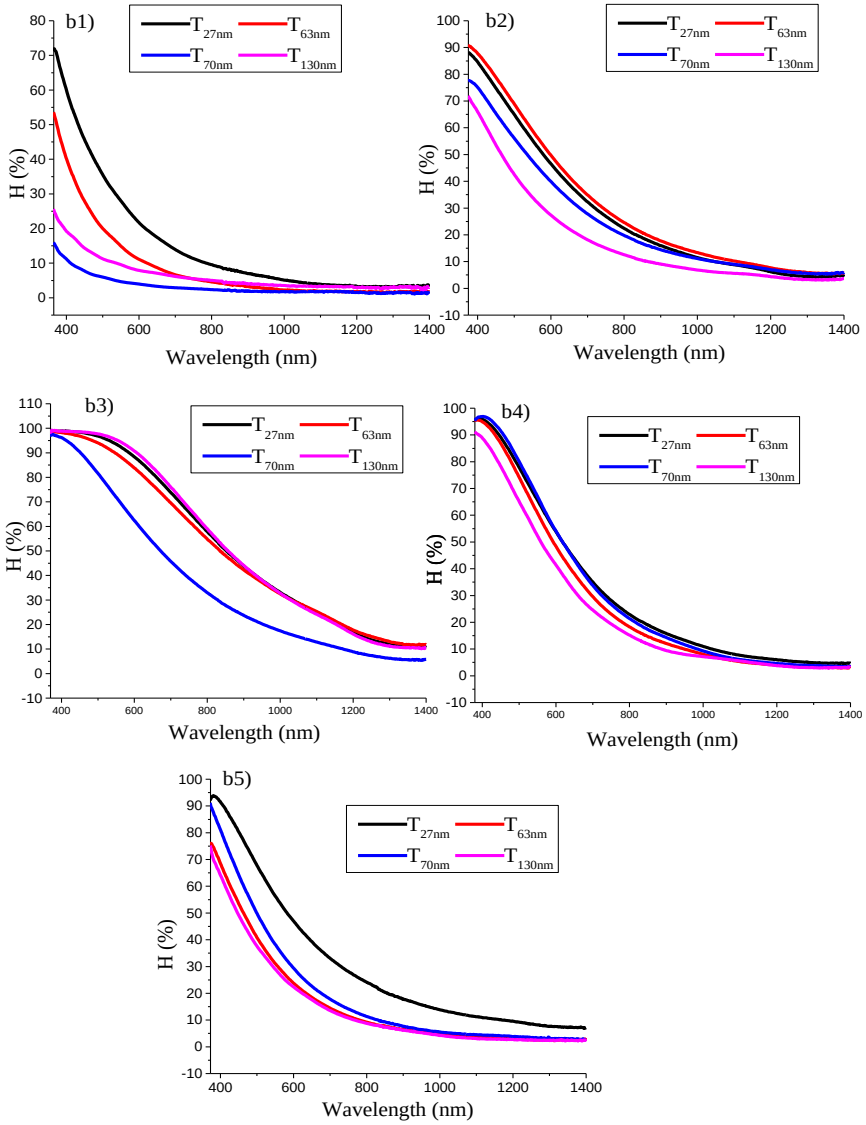

Figure 52. Transmittance haze spectra of the ZnO NRs grown using zinc chloride at (40°C, at 45°C, 60°C, 65°C and 85°C).

When comparing the different growth temperatures, it can be seen that, only 60°C was giving different trend. It can be concluded that, as the ZnO seed increases, the haze value decreases. It was reported that, 70 % is the highest haze value obtained at 400nm [247, 248]. Our results showed higher haze value at above 90 % and this due to the resulted NRs morphology as well as the used substrate and seed layers.

4.1.6.3 **Optical Band Gap calculations of the grown ZnO NRs**

Applications such as solar cells, photocatalysis and H_2 generation, require understanding of a number of important optical parameters of a material used such as the absorption coefficient, bandgap and the refractive index in order to predict the performance of the chosen material. Band bap can promotes more precise usage of the light sources and materials for the chosen application) [249]. In practice, to estimate the bandgap, indirect methods can be used, commonly by using a Tauc`s plot [249]. The estimation of the energy band gap can be achieved by using the following formula:

$$(\alpha hv)^2 = A\,(hv - Eg) \qquad (16)$$

Where: α is the ZnO absorption coefficient, A is a constant, h represents the Planck`s constant, v light frequency and $E_g$ is the bandgap energy. The absorption coefficient can be determined. It known that, the ZnO semiconductor has a direct bandgap. Therefore, drawing the Tauc`s plot can be obtained by plotting $(\alpha hv)^2$ vs hv as shown in figures 53 and Figure 54.

$$\alpha = \frac{1}{t} \ln \left[\frac{(1-R)^2}{T}\right] \qquad (17)$$

Where t is the thickness of the thin film, R represents the reflectance and T represents the transmittance. The evaluation of the optical band energy (E_g) of the ZnO NRs was obtained by using the transmittance spectra. Determination of the value material`s bandgap can be then given by linear part of extrapolation point on the abscissa [250].

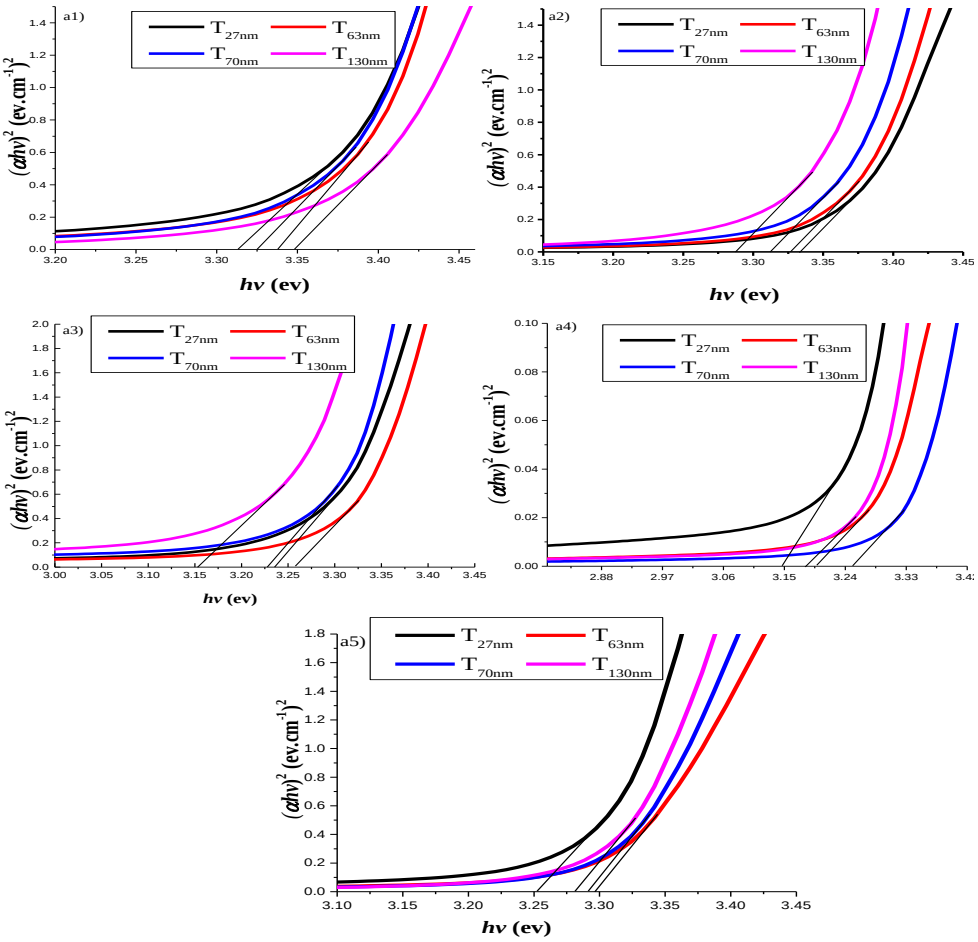

Figure 53. Tauc`s plots of ZnO of the optical band gap of the grown ZnO NRs under T_{growth} (40°C, 45°C, 60°C, 65°C and 85°C) using zinc nitrate.

For both zinc salts, the grown ZnO NRs showed almost similar band gap values as the T_{growth} increased. The interpretation variations in the bandgap energies might be due to the different resulted morphologies. It was reported that, the bandgap energy has strong dependence on the nanostructure morphology (length, diameter and density etc) [250].

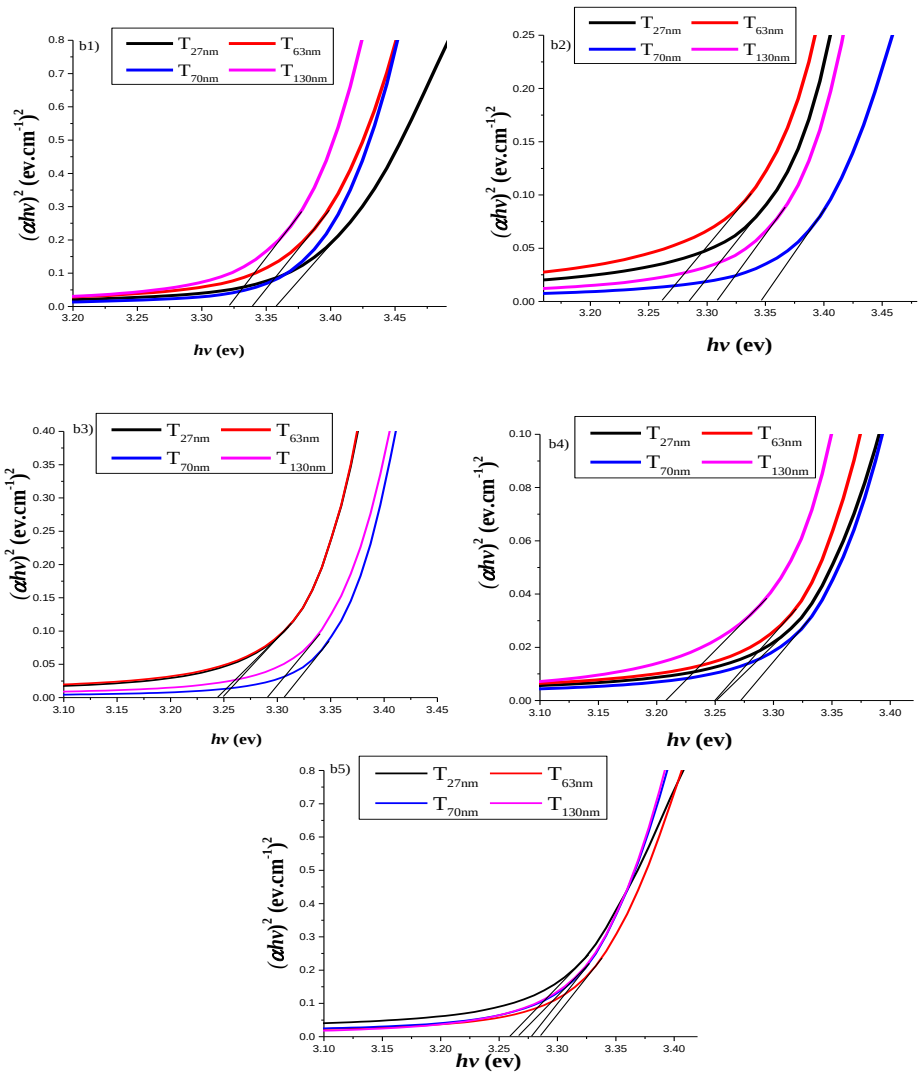

Figure 54. Tauc`s plots of ZnO of the optical band gap of the grown ZnO NRs under T_{growth} (40°C, 45°C, 60°C, 65°C and 85°C) using zinc chloride.

4.2 **Conclusion**

ZnO NRs were grown using two different zinc sources (zinc nitrate and zinc chloride) used to grow ZnO NRs. A solid phase is formed in the used solution. This process includes two main steps, which are nucleation and growth. The nucleation mechanism has an important role in the fabricated nanostructure as the heterogeneous nucleation and homogenous nucleation can be resulted according to the growth conditions. Densely backed NRs were obtained. The optical properties of the NRs were investigated. All samples showed high transmittance at about % and scattering about %. Different length

and diameters were observed. As well the density of the NRs was observed. The crystallinity, particle size, lattice parameters were investigated. The highest preferred orientation was achieved for T_{130nm} at (T_{growth} = 65°C) for zinc nitrate and T_{130nm} at (T_{growth} = 60°C and 85°C) for zinc chloride. The results indicated that, the grown ZnO NRs on different seed thickness and T_{growth} exhibited a range of lengths and diameters. It was observed that, there was no a clear dependence of the density on the seed thickness variation and on different T_{growth} as well. The seed layer thickness has a strong influence on the morphology and corresponding crystal size also when different seed thicknesses are used, different surface area can be provided, which can be attributed to the change that occurs in crystal size due to the seed layer thickness. In terms of crystallinity, the most cases, the (002) was resulted along the c axis. The narrow and strong peaks indicate that, the crystallinity is good; its orientation is preferential along the c-axis and perpendicularity to substrate surface [n]. Controlling the specific morphologies of nanomaterials is not an easy task However, it is important to optimize synthesis conditions in order to obtain nanostructures and morphologies of a particular kind because the behaviour of materials depends on crystal morphologies [3]. A good morphology control is essential for an optimized ZnO NRA performance in thin-film solar cells. Not only do the optical properties strongly depend on the ZnO NRA morphology but also the charge carrier transfer and collection can be critically affected. Controlling the length, diameter and the density of ZnO NRs was one of the challenges in this project. Addressing this issue is highly important in order to grow controlled morphology according to the application requirements.

Chapter 5 ZINC OXIDE NANOSTRUCTURES USING WET AND DRY LIFT-OFF METHODS

In this chapter, results of growing of ZnO NRs grown on a releasable layer is given and the effect of hydrothermal growth conditions ZnO morphology will be shown in detail. Moreover, the effect of these released NRs on the performance on different solar cells will be given.

5.1 Results and Discussion

5.1.1 Poly(methyl methacrylate) PMMA as a sacrificial layer

The starting point of this project was to determine the appropriate material that can be used as a transparent structural support layer in order to grow releasable ZnO NRs. Poly (methyl methacrylate) known as (PMMA) was initially used in this project as the chosen material to achieve successful detaching of the ZnO NRs. PMMA is typically used as a sacrificial layer in different applications, where acetone is commonly used to dissolve it [251]. Hence, after the PMMA spin coating and preparation on the glass substrate, acetone was used as a testing solution in order to achieve the successful removal of

PMMA from the initial rigid glass substrate. It was essential to conduct an initial test to investigate the adhesion suitability between the PMMA and any coated thin film. In this step, Ni was chosen as the first material tested, as shown in Figure 51.

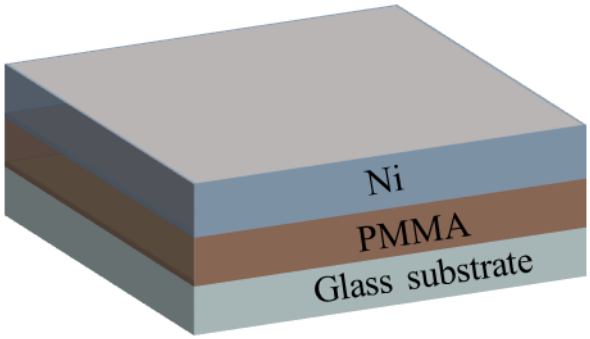

Figure 55. The device structure of Ni on sacrificial layer deposition.

Nickel could be used as an electrode for organic or inorganic flexible solar cell and it seems to attract more attention among the transition metals because of its abundance in nature and low price tag [252]. Ghosh showed that, in order to achieve electrically conductive and transparent electrodes, cost-effective ultrathin Ni capped Cu metallic bilayers have been used. Prior to starting the lift-off process, a number of trials were conducted. Different Ni thicknesses (2µm, 360nm, 200nm and 100nm) were deposited on PMMA by the technique of e-beam evaporation. It was ascertained that the thickness of the deposited Ni on the sacrificial layer has a significant effect on the PMMA/thin film adhesion. Figure 55 illustrates the resultant PMMA/Ni structure on a glass substrate. The inset images represent samples a) and b) after blowing them gently with nitrogen to test the adhesion strength. It can be clearly seen that the 2 µm thick Ni layer coated on one and two PMMA layers had peeled off due to the developed stress. Consequently, most of the Ni film was randomly delaminated subsequent to the deposition and exposure to air, owing to the large tensile residual stress in the thick Ni layer. This action can be explained as the stress created built in to the Ni layer depth.

In many applications of technology, the presence of stress in thin films and is a major concern as the performance can be dramatically affected by excessive residual stress levels, durability and reliability of material components and devices and worst case scenarios result in film cracking in the case of compressive stress for layers subjected to tensile stress or peeling off, buckling, or blistering [253]. The residual stresses in films can significantly affect their physical properties, built up either during or after their deposition and from a reliability and performance point of view, stress in films is an gradually important technological issue [254]. Thermal or intrinsic stress are raised in thin films when using sputtering, evaporating and deposition techniques. The physical properties of the coated film are influenced by those stresses [255]. The technological issue of stress in thin films is increasing from the standpoint of the performance and reliability of the fabricated application. Large stress leads the films to uncontrollably peel off [255]. It should be noted that stress can be either tensile or compressive. Tensile stress is when the film is attempting to contract where the radius of the curvature is positive. Conversely, the compressive stress is explained by the expanded film on the substrate. Its radius of curvature is negative.

Hence, it was important to examine 2µm thinner Ni layers. The thick layer first used was just as starting point to optimise the layer needed for later stage. Thornton et al. [256] presented a review study on the fundamental nature of the resulting internal stress in thin films in both (sputtering and evaporated) coating techniques. They illustrated that in practically all vacuum deposition techniques, the state of stress is present. It is acknowledged that the final residual stress is a combination of intrinsic stress and thermal stress. The former occurs as a result of the built-in accumulating effect of the crystallographic flaws dung the coating, whereas the thermal stress is caused by the difference in the coefficients of the thermal expansion between the substrate and the coated film. The internal stress is relaxed, and their accumulation prevented because of

the bulk diffusion. However, flaws can be caused due to these diffusions; hence, causing the formation of hillocks and holes. In the case of thermal stress, the intrinsic stress will accumulate which in turn will dominate the thermal stress. Hence, stress buckling which refers to a compressive stress in the layer and cracking which refers to a tensile stress in the layer are generally detected [256]. However, thermal stress requires large coefficient of thermal expansion difference and/or large temperature variations. The e-beam here was done at room temperature. Hence, the resultant stress in the PMMA/Ni structure can be due to the several aspects such as film density. The density of a material is well known to depend on the preparation method and subsequent treatment [257]. In general, thin film density could be sensitive to growth rate, vacuum pressure or the film structure. Higher density is attributed to closer stacking molecules [258].

Alagoz et al. were able to reduce film stress by engineering and controlling the film density by more than one order of magnitude comparing with conventional dense films produced at low working gas pressures and film with no cracking was achieved[259]. Freedman. J. F. stated that, three main sources of stress and strain introduced into an evaporated film: (1) a structural contribution resulting from epitaxial misfit, (2) stresses resulting from any impurity or defect distribution resulting from deposition or subsequent thermal annealing, and (3) Stresses resulting from the constraints imposed by the substrate's thermal contraction [260]. Also, might be due to intrinsic and thermal stresses, such as the thermal stresses in which the difference in thermal expansion coefficients between the substrate and the coated film is the main cause of the thermal stress in thin films, as the temperature of the coated substrate will be different both before and after the deposition [256]. The value of tensional or compressive stress can be defined as follows:

$$\sigma = \frac{E}{1-\upsilon}\frac{h^2}{6t}\left(\frac{1}{R_2}-\frac{1}{R_1}\right) \qquad (18)$$

Where, σ mean layer stress (Pa), E Young`s modulus of the used substrate (Pa), υ passion ratio, h thickness of the substrate (µm), t layer thickness (µm),R_1, R_2 are the curvature radius of the substrate before and after coating respectively [261]. These types of stresses are dependent on the deposition conditions [256], where the recovery and recrystallization effects store energy in a thin film by the stress and tend to act as a thermodynamic driving force that causes the stress to relax by several factors, such as (dislocation movement, interstitial, vacancy or relaxes by peeling off). This occurs when the temperature T/T_m range is (0.3-0.5) [256]. T is the substrate temperature and T_m is the melting point of coating material [262].

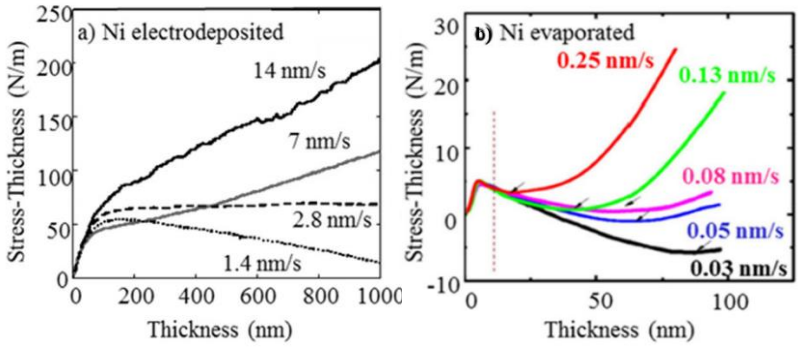

Figure 56. a) The thickness of stress represents the results of electrodeposited Ni and b) the evolution of the stress thickness measured in the evaporated Ni [253].

A further reason can be the influence of deposition conditions where the deposition conditions in a vacuum have a significant effect on coated microstructures and thus, the resulting intrinsic stress. A number of studies have investigated the function of pressure and its effect on the resulting stress in thin films [263]. At some point, every variable in the sputtering process is exhibiting stress reversal. It is significant to identifying the pressure at which the stress reversal materialises is significant. Grégory et al. showed the consequence for the stress thickness of the microstructural evolution as illustrated in Figure 56. where they showed that, in Figure 56 a), the thickness of stress represents the results of electrodeposited Ni that grow at a constant grain size so constant growth rate and grain size result in constant increase in stress, whereas Figure 56 b), shows the effect

of changing grain growth and grainsize is having significant implications for the evolution of the stress thickness measured in the evaporated Ni where the slope changed continuously with changing thickness instead of reaching a constant slope, and a turnaround phenomenon is observed (indicated by arrows) from compressive to tensile incremental stress [253]. Mechanical stress affects not only the mechanical stability of thin film structures regarding adhesion in both thin film technology and microelectronic but it also effect the electrical parameters [264].

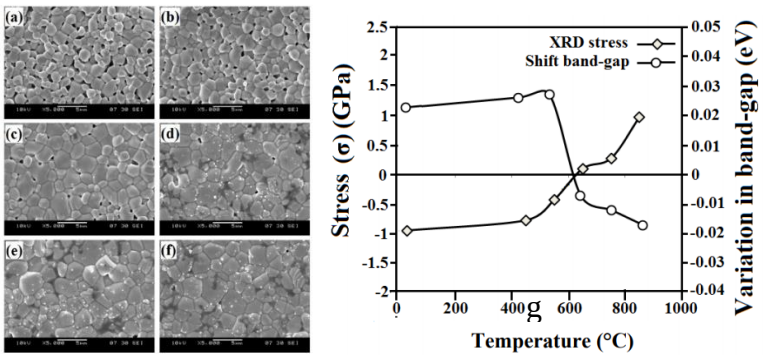

Figure 57. (a-f) represent the ZnO disc SEM images form as grown ZnO disc to annealed at 450°C, 550°C, 750°C and 850°C temperatures respectively. g) Band gap variation and stress resulted in ZnO disc by increasing the annealing temperature [265].

Sendi et al. investigated stress control of ZnO nanoparticle based discs by annealing the samples at different temperatures [265]. They found that, Form the SEM images Figure 57 (a-f) it was found that, increasing annealing temperature led to the concentration of oxygen in the disk and caused a distortion in the form of the grains, indicating the presence of tensile stress in ZnO discs. Whereas, as shown in Figure 65 e), the resulted bandgap and stress are varying. The observed shift from higher to lower in the energy band gap can be attributed back to the conversion of compressive stress to tensile stress as the annealing temperature increases. As well as at higher annealing temperatures, a decrease in the UV emission peak was observed as the compressive stress increased due to the increased grain size. Figure 58 shows that some materials, such as aluminium tends

to produce tensile stress, while other materials, for instance tantalum forms only compressive stress [263].

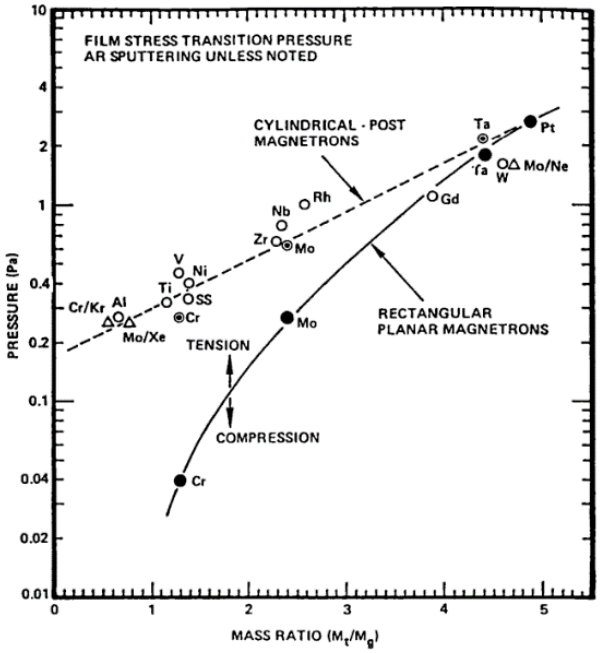

Figure 58. Different materials stress transition pressure [263].

Likewise, the T/T_m influence on internal stress and Figure 59 illustrates the total stress induced in a thin film as a function of T/T_m. It is assumed that the substrate temperature during the measurement (in room temperature) is less than the substrate temperature during the coating process. Thus, the thermal expansion coefficient of the film is greater than that of the used substrate. Consequently, after the substrate is cooled down, depending on the nature of the material a tensile thermal stress can be generated [256].

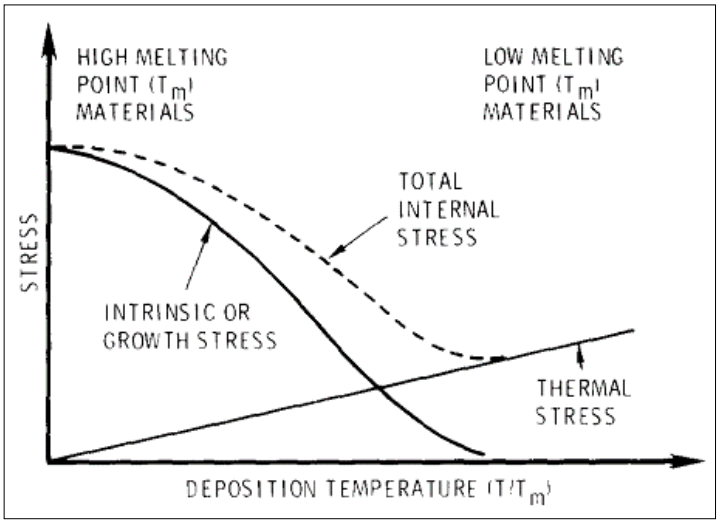

Figure 59.Representation of intrinsic and thermal stress distribution [256].

For sputtered coatings, the coating stress in sputtered thin films can be influenced by a number of parameters, such as the substrate temperature, distance between the source and the substrate, deposition rate, orientation of the surface, coating flux direction, working gas pressure and working gas species, etc. [256]. This project, when Ni is deposited on PMMA the adhesion was weak when the Ni layer was thick. However, the adhesion can be improved by reducing the Ni layer thickness. Based on the results achieved by Roshangias et al. [266], it is suggested that improving the adhesion strength of thin films with reduced thickness is related to higher surface energy due to lower mean grain size and energy dissipation due to thinner film decohesion. Thus, reducing the thickness of the Ni layer is a proposed solution to reduce the stress. Figure 60 a) illustrates the Ni layer deposited on glass substrate to be as reference and 360nm Ni layers used to reduce the resultant defect and to obtain better adhesion. The thinner the Ni layer the better adhesion on PMMA. Hence the Figures 60 and 61 show cracking which would suggest tensile stress in the layer.

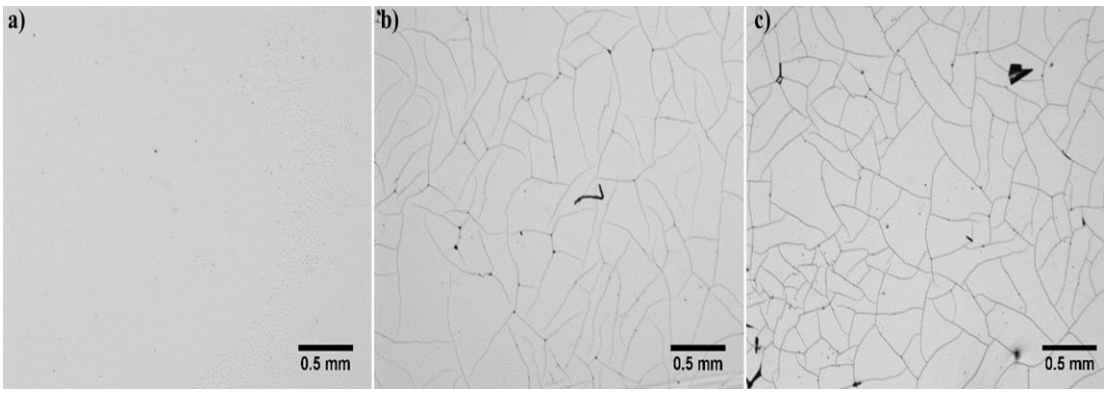

Figure 60. Optical images of 360 nm of Ni on both PMMA and SU-8. a) Reference sample, b) 1 PMMA layer and c) 2PMMA layers.

The figure 61 shows the improvement of the Ni layer after reducing the thickness, although the surface defect and several cracks network were produced and these defects might be due to the particles on the samples during the characterization. This would suggest that in these conditions the deposited Ni film is still too thick.

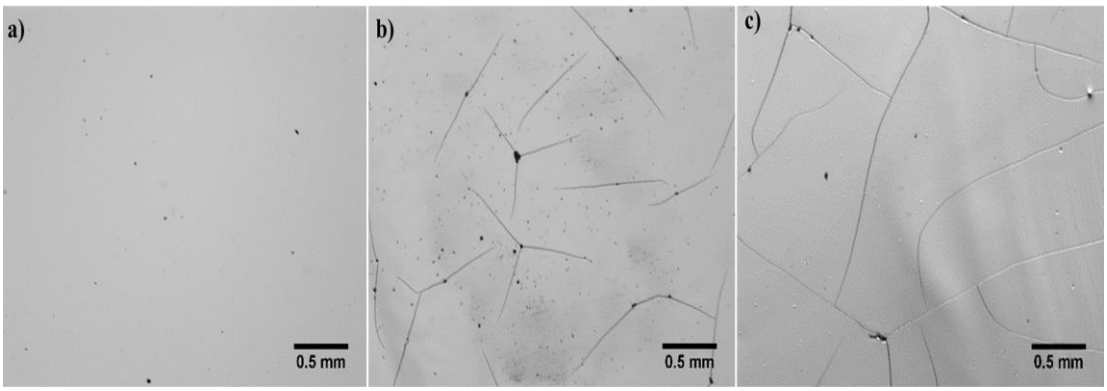

Figure 61. Optical images of 200 nm of Ni on PMMA. a) Reference sample, b) 2 PMMA layer, c) 1 PMMA layers.

Figure 61 a) displays the reference sample, 72b) 1 PMMA layer, 72c) 2 PMMA layers. As the Ni thickness reduces, the PMMA/Ni adhesion improves, and the number of cracks reduces. The observation and analysis of stress shows of the study presented by Baek et al. [267]that there are three stages in the growth of crack in film. The film crack initiates and grows at first stage by the tensile stress of film, buckle formation is the second stage and finally accompanied by buckling of film is the last stage of crack growth. A non-deformed thin film was achieved when 100 nm of Ni was deposited, as shown in Figure

62. Hence, studied thinnest Ni layer showed homogeneous, smooth and crack free film. Form this point it can be concluded that, the Ni thickness had a significant effect on the adhesion and yet resulted cracks.

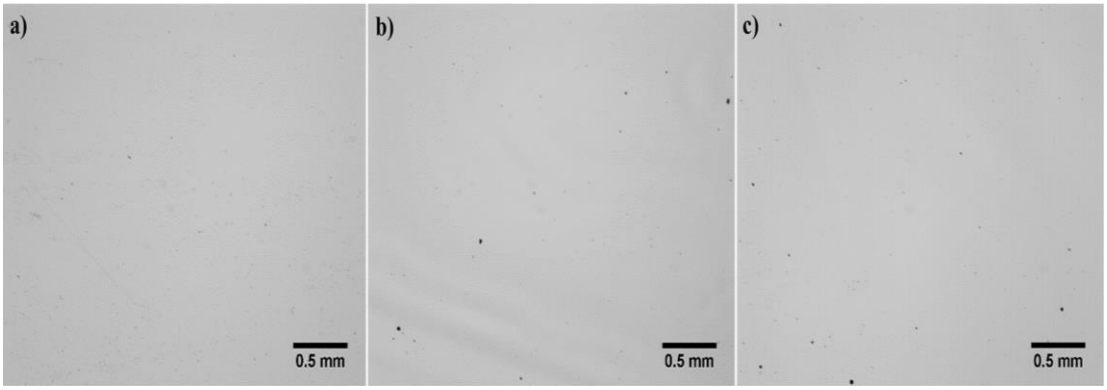

Figure 62.Optical images of 100nm of Ni on PMMA. a) Reference sample, b) 1 PMMA layer, c) 2 PMMA layers.

5.1.1.1 **Releasing the Ni thin film**

After reducing the surface defects and cracks produced by depositing Ni on PMMA, a preliminary study was conducted on releasing the PMMA/Ni structure from the glass substrate. The samples were soaked in acetone for 60s at room temperature. Acetone has been used to remove the PMMA layers [137, 268]. The aim of this step is to retain the PMMA/Ni structure. Retaining the full structure will give a positive insight to use PMMA later for growing ZnO NRs. When soaking the PMMA/Ni samples in acetone, the entire structure was damaged as the acetone is a strong solvent which can impact on the whole structure. The full damage of the structure could be due to the existing cracks on the films, which therefore allows the acetone solvent to penetrate between the 100nm PMMA and Ni layers instead of penetrating between the PMMA layer and the glass substrate.

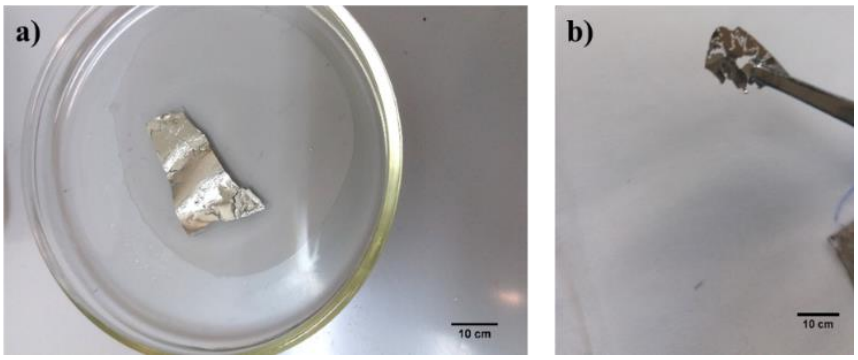

Figure 63. The 100nm of Ni on 2 PMMA layers sample, a) sample soaked in acetone (before lift-off) and b) the lifted-off layer hold by tweezer.

A partial release of PMMA/Ni structure was achieved, although several defects were seen on the Ni layer due to acetone attacking the Ni layer. MichroChem (as supplier) stated that, as a photoresist stripper, acetone is not well-suited. The acetone high vapor pressure causes a rapid drying. It is recommended that isopropyl alcohol must be used to rinse the sample afterwards to remove the resistant-contaminated acetone immediately after the acetone step. Using acetone as striper can lead the PMMA layer to dissolve. This was confirmed by Carlberg et al. [269] where they reported a method of lifting nanoimprint lithography that was achieved using acetone to dissolve the PMMA, a warm acetone bath is used. The lift-off layer is not affected by acetone and remained in place to prevent electrostatic adherence of metal flakes to the silicon substrate. As a result, PMMA as a support structural layer and acetone as the remover are not the preferred materials for lifting off ZnO NRs, as the hydrothermal growth of the NRs will follow, which could bring about other barriers to achieving the aim of this project. Therefore, an investigation on SU-8 photoresist as an alternative to PMMA was carried out. The reason of choosing SU-8 as an alternative of PMMA is that, SU-8 is widely used as support structural layer and releasing is from the substrate can be easily archived by introducing an Omnicaot layer . The following section will provide more details on using Omnicoat as a sacrificial layer and SU-8 photoresist as a support structural layer to be used in the hydrothermal growth of ZnO NRs.

5.1.2 **Omnicoat/SU-8 structure (wet lift-off)**

After unsuccessful PMMA lift-off, the alternative was to use Omnicoat was used as a sacrificial layer. A number of experiments were accomplished in order to optimise the correct lift-off process recipe that can withstand the hydrothermal growth process of ZnO NRs. The Omnicoat layer is typically used to allow easy SU-8 photoresist layer stripping, seeing that it has a significant effect on improving the adhesion between the SU-8 layer and the substrate. The starting point was optimising a strong SU-8 layer, without Omnicoat, that could withstand the wet hydrothermal deposition process. Thus, the first step was to follow the recipe provided by the MichroChem (the supplier). Regarding the removal of the stack of layers, when the stack started to float on the surface of the solution, sewing machine needles were used, as shown in Figure 64 to transfer the layers to the new, cleaned flexible Kapton substrate.

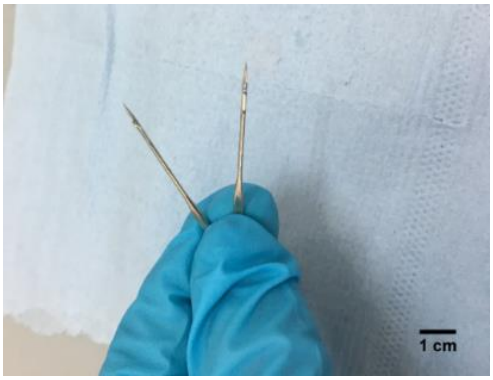

Figure 64. Needles used to transfer the layers to new cleaned glass substrates

The Kapton substrate was chosen due to its flexibility which allows an easy sliding of Kapton substrate underneath the floating stack and thus transferring the stack. Additionally, because of the SU-8 transparency, the sample was coated with platinum Pt as shown in Figure 65 b) (so that the layer can be seen easily when it is floating on the remover solution). Also, Pt has high stability and can be utilized as contact in solar cells [270]. Using the needles made the transfer of the stack complicated as the layer was

fragile and needs to be gently dealt with. Thus, to rectify this issue, a flexible kapton substrate was used instead by sliding it in the remover solution under the floating stack of layers, for easy transfer. Figure 65 shows the structure used before, during and after lift-off. To release the SU-8/Pt structure, this was carried out by using the Omnicoat developer and remover solution at room temperature (without heating up the solutions). This method was not successful as the releasing time was lengthy (i. e. more than 10 min). As ZnO NRs were to be grown on Omnicoat/SU-8, it was better to optimise a process with less lift-off step time.

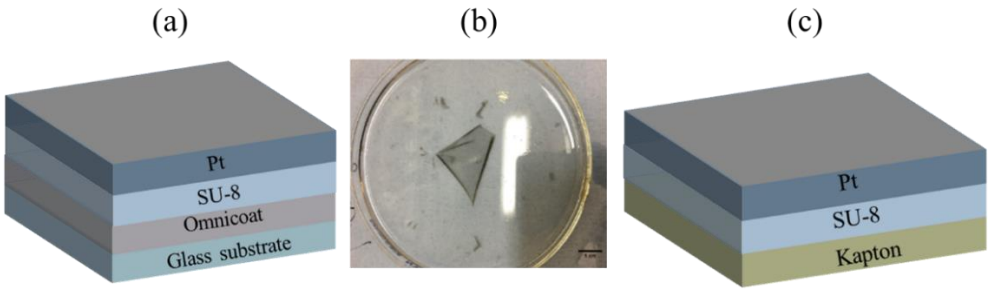

Figure 65.The Pt/SU-8 structure. a) Before lift-off (on glass), b) during lift-off (in the remover solution) and d) after lift-off (on flexible kapton substrate).

It should be noted that immersing the SU-8 for a longer time might lead the Omnicoat developer to attack the upper layer which could include the ZnO NRs at a later stage and this could deform the structure which is intended to be retained. This was clearly observed as shown in figure 66. When the sample was immersed in the remover solution, the ZnO NRs was attacked and this cause the structure to deform and damage. In order to solve this problem, various modifications were considered. Hence, Omnicoat developer and remover were placed on a hot plate at 50-80°C during this step. Typically, ultrasonic agitation is used to lift-off the structures, however, in this study there was no need to do that as the layers were released manually by shaking the floating samples in the developer and remover solutions without the help of agitation.

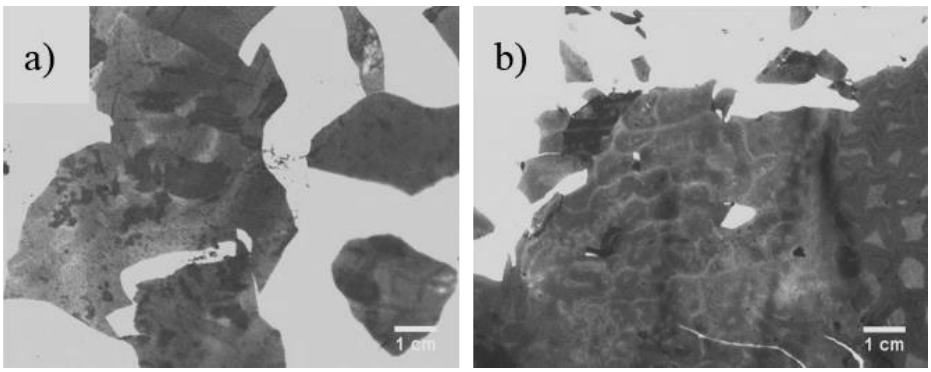

Figure 66. ZnO NRs deformation after long time lift-off process. a) And b) are for the same sample at different places.

Figure 67 shows examples of obtained lifted-off Pt coated SU-8 resit. First the process conditions recommended by the SU-8 supplier were followed to cure SU-8 by using 1 min for soft-baking at 95°C, 20 % UV-exposure dose for 20s, 1 min post-exposure-baking. In this case, the recommended recipe by the SU-8 supplier was not appropriate as the structure was deformed during the hydrothermal growth process and almost nothing lift on the glass substrate. 1 min is the recommended soft-baking (SB) time and 2min for post exposure baking (PEB) from MichroChem supplier. This baking time possibly might be good enough when using SU-8 in other SEMS applications. However, the requirements of the project presented here are different. Hence, finding the correct recipe was essential. The lifted-off structure was not strong enough for the specifications employed in this project where a number of layers were built up over the resist layer. The hydrothermal growth used in this project is set to 2 h, and during this duration the structure was damaged. The specified parameters provided by the supplier are limited, seeing as they were obtained following specific procedures. Thus, cannot be applied immediately in different environments as the released SU-8 layers were almost all damaged. Two important parameters had shown strengthen the SU-8 and made it strong enough to grow the NRs which are (SB) and (PEB). After a series of SU-8 processing by means of increasing the SB for 10min, PEB time From 1min to 5min, 10mins and 30min, better layers were lifted-off by improving their mechanical strength, as revealed in 67. An

improvement was observed on the structure after lift-off, once the soft baking and post exposure baking was increased. This can be clearly seen in Figure 67 c) and Figure 67 d).

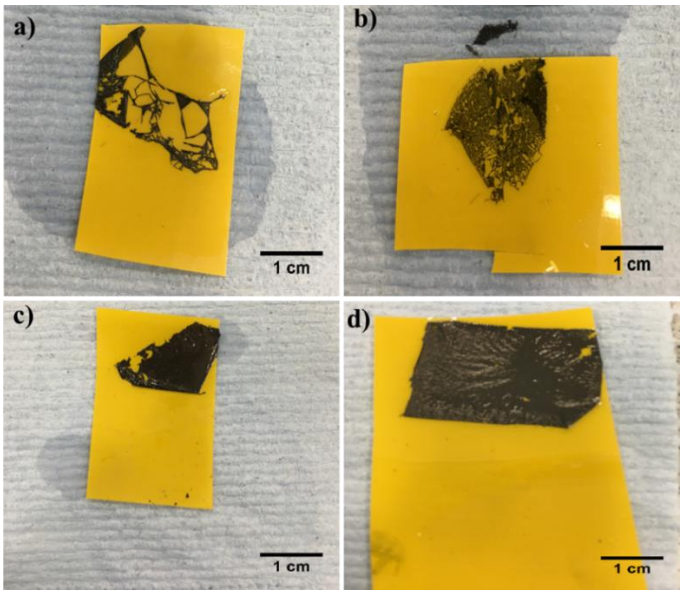

Figure 67. Released SU-8/Pt/kapton structures after using 10min soft baking and post exposure baking at different baking times. a) 1min post exposure baking, b) 5min post exposure baking, c) 10min post exposure baking and d) 30min post exposure baking.

Figure 67 clearly shows the SU-8 effect of soft baking and post exposure baking times. The resist layer became less sensitive to the remover/stripping chemical solution. The soft baking step evaporates the solvents and improves the resist adhesion to the coated substrate. The weak layers of Figure 67 a) and Figure 67 b) are due to the short baking time that does not allow the solvents to completely evaporate. This indicates why the former Figure 67 a) and Figure 76 b) are less strong than Figure 67 c) and Figure 67 d), given that the latter two had a longer baking time; thus, most of the solvent was evaporated. Also the former is not 100% cross-linked. Therefore, the polymer will dilute and dissolve in the remover solution. If the cross-linking process has worked, then a strong bond between polymer chains is achieved, Conversely, post exposure baking is the thermal energy assistance that enhances the resist polymerization after the resist was exposed to the light, as it helps in increasing the degree of resist cross-linking [127, 271].

These results indicate the effect of soft-baking and post-exposure-baking on the resit film. After being pre-baked, the photo-acid was produced when the resist was exposed to UV [272]. Increasing the time for post exposure baking causes the resist to polymerize as the acid catalyst is regenerated and hence, the cross-linking time. However, using 1min, particularly for soft-baking resulted in the solvents failing to be evaporated entirely.

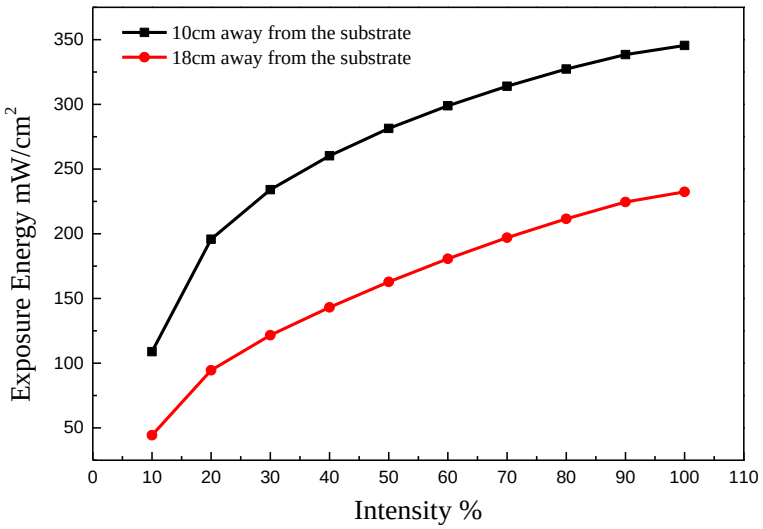

Figure. 68 Exposure energy vs Intensity.

To enhance the crosslinking, the photoresist in exposed to UV light. Different exposure does were tested first as shown in Figure 68. It presents the exposure energy (mW/cm^2) vs Intensity (%). A power meter was used for calibration in order to measure the exact energy dose used to expose the SU-8 resist layer. The highest distance between the source and the sample was approximately 18cm, although 10cm is used in the presented measurements to ensure the sample is covered by UV-light. The intensity was set at different values from 10-100%, whilst the exposure energy was measured using 5 s. These measurements were repeated three times to determine. In this study, in terms of exposure time, the following equation is used to determine the exposure time.

$$\text{Exposure time (s)} = \frac{\text{Exposure energy (mJ/cm}^2\text{)}}{\text{Light intensity (mW/cm}^2\text{)}} \qquad (19)$$

15 s was the starting exposing time (recommended by MichroChem). However, according to the specific requirements of the targeted application in this project, 15 s was not enough as the resulting film cannot be intact after the hydrothermal growth process. From SU-8 datasheet, the relative required exposure energy dose when the glass substrate is 1.5X. As the used SU-8 here is SU-8 2000, then the required exposure energy is 60-80mJ/cm^2. Hence, (60-80mJ/cm^2 * 1.5X) = (90-120mJ/cm^2). The data of exposure and resulted thicknesses are shown in the next section.

5.1.2.1 Effect of UV light intensity on SU-8 thickness and light transmittance

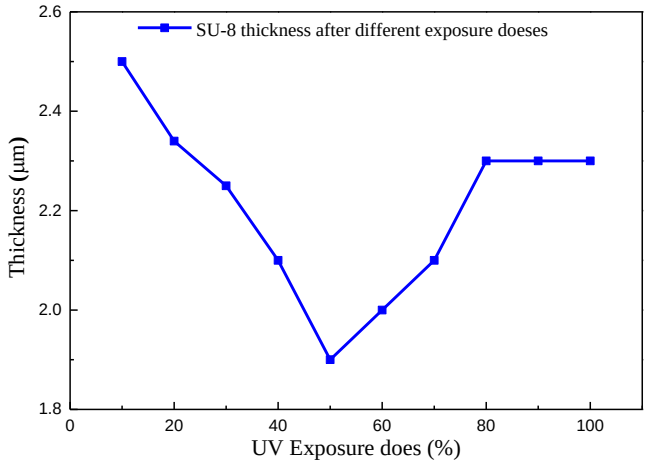

Figure 69. The effect of UV light intensity in % on SU-8 thickness.

The effect of the UV-exposure dose on the SU-8 thickness and transmittance have been studied and is shown in Figure 69 and Figure 70. The thickness measured by porifilometer ranged from 1.9µm to 2.6µm. From Figure 69 it can be concluded that, from 10-60% light intensity, the SU-8 thickness decreased as the UV-light intensity increased. However, the thickness started to increase when a light intensity was more than 70% is used. The thickness remains at one level (roughly 2.3µm) when the other is exposed at 80%, 90%. This could be due to the SU-8 saturation after 60% intensity which indicates that the photo-acid diffused in a shorter time compared to low doses. Photoacids are molecules

that become acidic when light is absorbed [273]. In simple words, any compound converted into a strong acid due to the action of light. This is due to two different reasons, either protons dissociation upon photoassociation (e.g. ring - closing) or strong acids formation after photodissociation [274]. During the exposure step, when photoresist is exposed with UV-light, a strong acid is generated. This will enhances the reset polymerization in the consequence post exposure baking step. Hence, as the target in this project the photoresist layer has to be maintained.

Different factors can contribute to reducing the thickness of SU-8 during its processing, such as UV absorption over the resist film, volume changing during polymerization, the chemical diffusing of the agents during cross-linking, beam reflectivity and divergence from the substrate [275].

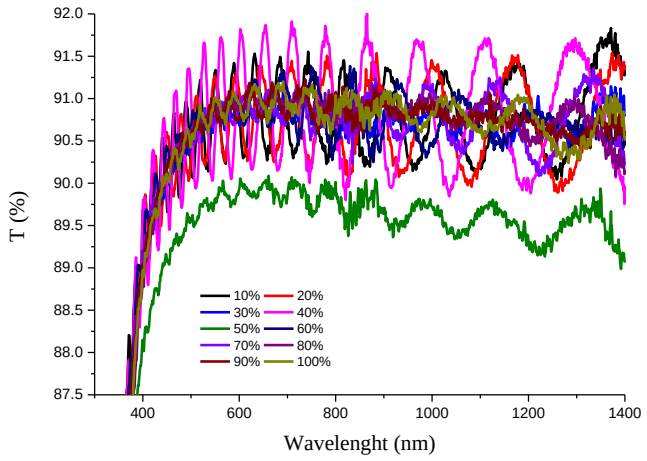

Figure 70. Ultraviolet (UV) light intensity in % on the light transmittance.

The transmittance spectra of the SU-8 exposed at different doses from 10% to 100% is shown in Figure 70. From the figure it can be seen that, the 10 different exposure doses showed high transmittance ranging from 90-91% over the spectral range. Only the sample exposed at 50% displayed the lowest transmittance. The oscillation are attributed to interface constructive and destructive interference. The resulted transmittance indicates

that the different exposure doses exhibited good transparency over the spectral range. Hence, making the resist a good material for several applications when the optical properties are highly important, such as [276]. In this project, the optical properties are highly important.

5.1.2.2 **Hydrothermal growth of ZnO NRs (wet and dry lift-off)**

In this section, the results of growing ZnO NRs on a support structural layer will be shown. Five different growth temperatures (T_{growth} = 40°C, 45°C, 60°C, 65°C and 85°C) were used to grow the NRs. This section will provide the resulting ZnO nanostructures grown on the Omnicoat/SU-8 structure as well as the results on lifting the structure off the initial substrate. The SU-8 layer soft baking and post exposure baking were 10min and 30min respectively. The influence on the performance of different solar cells will be reported. As a prelude to the NRs growth, the Omnicoat/SU-8 structure was coated with ZnO seed layer (by sputtering technique) in order to enhance the growth processes nucleation. The effect of hydrothermal growth conditions on Omnicoat/SU-8 structure and ZnO adhesion to the SU-8 was studied. This study addresses the fabrication of a controllable release/transfer of ZnO NRs where high growth temperatures represent a barrier to conducting direct growth on flexible substrates, for example in wearable electronics applications.

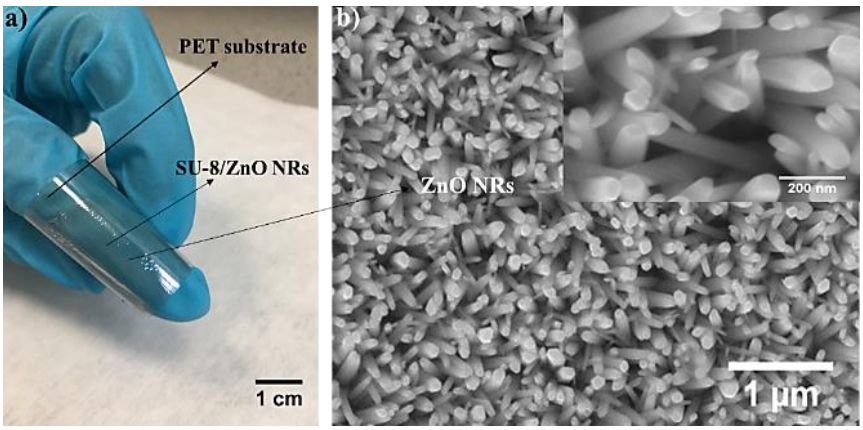

Figure 71. ZnO NRs/SU-8 (T_{growth} = 85 °C) on (a) bent PET substrate after lift-off bending and (b) the corresponding SEM images of the ZnO NRs (the inset is high SEM magnification).

The evolution of ZnO NRs with T_{growth} were characterised by scanning electron microscopy (SEM), X-ray diffraction (XRD) and UV-Vis spectrometry. The ZnO NRs/SU-8 structures were successfully released as shown in Figure 71 a) and transferred to flexible PET substrate. When conducting the ZnO NRs wet lift-off, it was found that the photoresist displayed delamination and shrinkage as in Figure 72. The photoresist shrinkage is dependent on several parameters, such as Young's modulus, density, inhibitor concentration, the number of photo-acid generators (PAG) of the photoresist, development rate and time, exposure dose, as well as the coefficient of thermal expansion. Keeping the mentioned parameters in mind, it is critical to consider each parameter individually in order to create a clear image of the phenomenon of shrinkage.

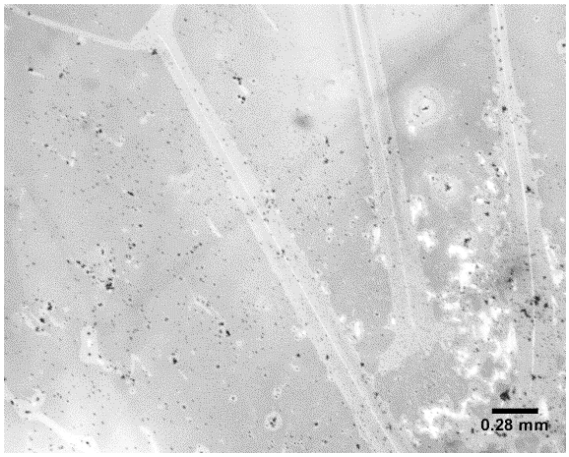

Figure 72. Omnicoat/SU-8/ZnO seed/ZnO NRs structure delamination after the hydrothermal growth process.

Both the photoresist and the coated substrate have a different thermal expansion coefficient. Thus, stress and cracks are resulted in particular thick resist layers. Similarly, the magnitude related to the expansion coefficient in the thin films is profoundly influenced by the effect of surface energy, particularly in the thin films of 100 nm thickness. The substrate is expanded due to heating which will cause stress and cracks. Submerging SU-8 into a solvent causes its polymer matrix to absorb the solvent molecules. Accordingly, this will make SU-8 to expand. The epoxies possess a high melting temperature and high glass transition temperature [277]. The glass transition temperature is a very significant parameter for epoxy resin and epoxy matrix composites as it determines the service condition for the use of the materials. A very low net built-in stress resulted when submerging SU-8 in water compared to submerging it in a solvent [278].

On the initial tensile stress, a compressive stress effect is superimposed. Thus, the highly cross-linked resists are more sensitive to the swelling that water causes. This is because in the polymer matrix, more hydroxyl groups are present and strong bonds can be formed by water molecules [279]. Therefore these residual stress are not linked to the thermal stress which make sense as it is not really operated at high growth temperatures. Processing conditions such as irradiation dose, temperature and time of curing are significant for the SU-8 properties to depend on [280]. The aforementioned cited parameters are directly controlling the degree of SU-8 cross-linking. Additionally, the glass transition temperature of the resist progresses as the SU-8 is cross-linking. When the resist is fully cross-linked, a higher glass transition temperature can be observed, which in turn results in higher stress, shrinkage, adhesion problems and cracks [281]. It is recognised that during the SU-8 baking process, intrinsic and residual stress are generally the outcome. Hence, overcoming this problematic effect is a challenge. The

intrinsic stress has a crucial role in the quality of the resulting structure. For thicker SU-8 structures, Chang et al. [282] suggest applying a constant rate by decreasing the post-exposure baking temperature 25-96 °C. External factors induce extrinsic stress. Likewise, from the interaction between the environmental subsequence's and the deposited material. It was assumed that the delamination is caused by the ZnO solution used in nanorods growth. However, further investigation has shown that when the Omnicoat/SU-8 structure with 1µm and 2µm of SU-8 thicknesses is employed in the wet solution deposition process (hydrothermal ZnO NRs growth), delamination will be the result and the structure will partly begin to be detached from the substrate. This was confirmed by floating Omnicoat/SU-8/glass on 40°C DI water. Microscopic images figure 73 show the delaminated structure after soaking the sample in 40°C DI water for 2 h. It was observed that whatever the solution used, the solution will penetrate under the structure, which therefore will cause it to delaminate.

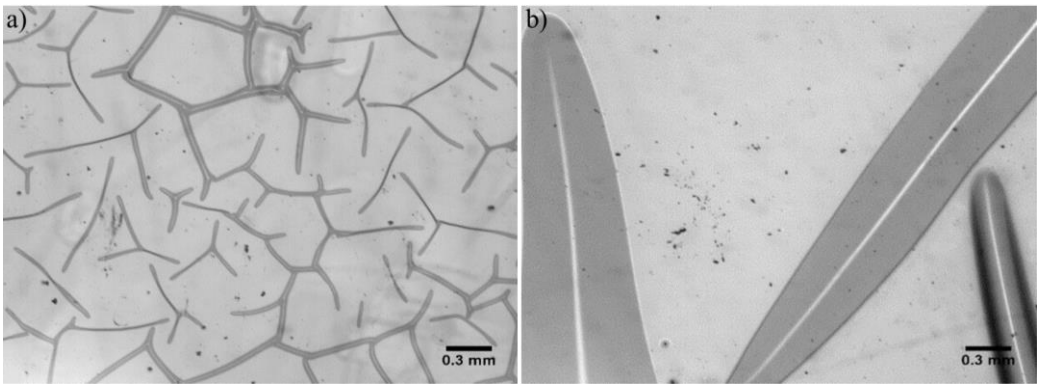

Figure 73. The Omnicoat/SU-8 structure delamination after 2 h soaking in 40°C DI water. a) Low magnification and b) high magnification.

From the figure, it can be seen that, the SU-8 started to shrink and delaminate from the substrate. The SU-8 delamination effect can be removed by adding an extra step in the SU-8 processing, referred to as the hard baking step (HB). Hard baking is an optional step in the SU-8 processing as it is responsible for hardening the SU-8 structure. Soonwan et

al. [283], stated that using maximum operating temperatures (such as 120°C) has a significant effect on obtaining constant material properties when these higher temperatures are applied. An additional thermal curing step can be added in this project to the process steps, so as to increase the SU-8 strength and to prevent the layers from peeling off the glass substrate during the hydrothermal growth. The aim was to reduce the delamination effect and shrinkage. However, after a quick test annealing the Omnicoat/SU-8 sample before growing the NRs, this step was excluded. It was excluded from the process steps because it caused the structure to be almost impossible to lift off. An alternative option was to explore the use of Polydimethylsiloxane (PDMS) as a flexible substrate for the NRs. As will be demonstrated in subsequent sections, the delamination and swelling effects were successfully removed by using the PDMS (dry lift-off) process. The swelling, delamination and micro-cracks in the SU-8 thin films may well occur due to the penetration of solvent molecules into the cross-linked part of the resist during exposure, produced by the reaction of acid catalysed cross-linking and hence, high elastic energy in the polymer layer with respect to the adhesion and strength of the material.

5.1.2.3 **UV-VIS spectrometry and haze**

The investigation of optical properties from ZnO NRs on the Omnicoat/SU-8/ZnO seed was performed using UV-VIS spectrometry. Light transmittance and scattered light were measured for all samples (before and after lift-off). Figure 74 indicates that the total transmitted light and total diffused light (scatter light) of the glass/Omnicoat/SU-8, glass/Omnicoat/SU-8/ZnO seed and ZnO NRs were grown on Omnicoat/SU-8/ZnO seed at T_{growth} = (40°C, 45°C, 60°C, 65°C, 85°C).

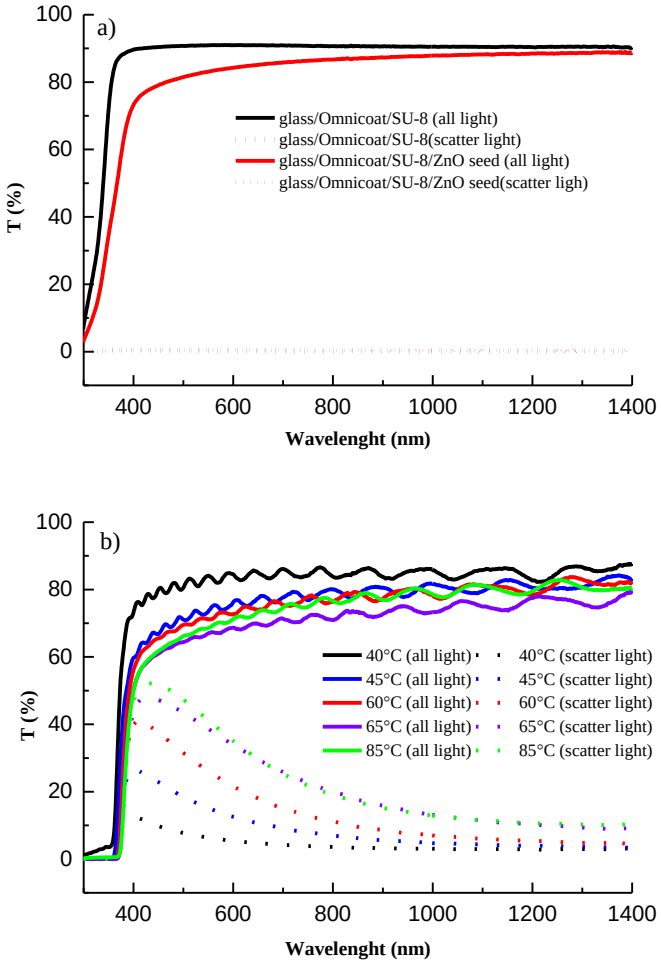

Figure 74. UV-VIS-NIR transmittance of a) glass/Omnicoat/SU-8 before and after ZnO seed deposition and b) ZnO NRs grown on glass/Omnicoat/SU-8 structure (before lift-off) using T_{growth} = (40°C- 85°C). Solid lines represent the total transmitted light and the dotted lines represent the diffused light.

It can be observed in Figure 74 that the five different T_{growth} exhibited total transmitted light ranging from 60-90%. The NRs grown at 40°C showed a higher transmittance at above 80%, whereas, surprisingly, 65°C displayed the lowest transmitted light at above 60% in the spectral range from 300nm–1400nm. Regarding 40°C, this is well understood due to the morphological structure of the ZnO NRs, as shown in Figure 75 (SEM morphology). The NRs grown a low T_{growth} 45°C and 45°C have a shape of more or less close to continuous film as the resulting average diameter was large. Polsongkram et al. showed that, when the increases, the NRs diameter diminishes [79]. Similar structure was

observed by Guo et al. [284] when they used range of T_{growth} = (40°C, 60°C, 80°C and 95°C) as shown in figure 75. Figure 75 h) showed almost continuous film. This is a clear indication of the ZnO NRs growth rate at low T_{growth} is slow.

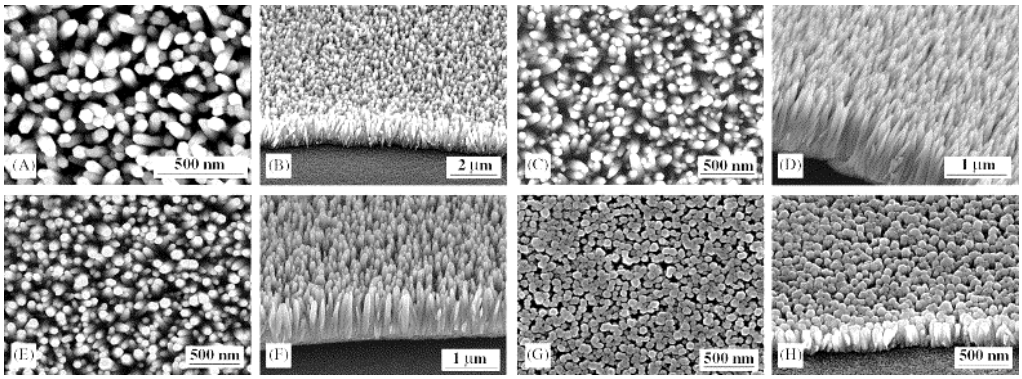

Figure 75. SEM images for ZnO NRs grown on ITO substrate at different temperatures 95°C-40 °C respectively for 4 hours. (A, C, E, G) is top-view and (B, D, F, H) represent view from 45° [284].

However, for 65°C, the lowest transmittance is due to the improvement in the morphology of the NRs where the NRs are sharp comparing to low T_{growth}, which was plainly seen in Figure 74. Increasing the T_{grwoth} enhances the growth rate to be faster [285]. The more scattered light the less transition occurs. The latter mentioned NRs grown at 65°C had different diameter. It is worth mentioning that, the higher the transmittance the lower the light scattering and vice versa. Hence, the high scattering would be suitable for harvesting. The other growth temperatures T_{growth} = (45°C, 60°C, and 85°C) presented there is a clear change in scattered light in at least the 400-900 nm region which is an ideally region for say an absorber of 1.5eV band gap energy.

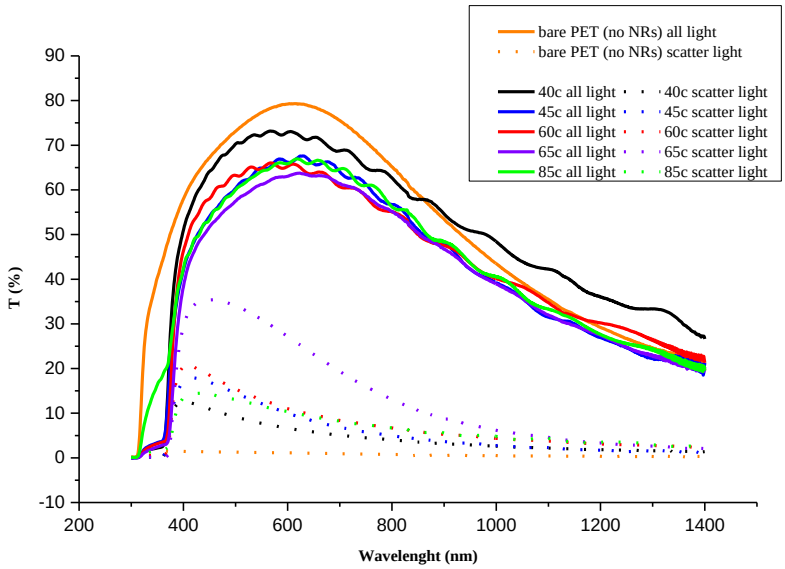

Figure 76. ZnO NRs/SU-8 structure on PET (after lift-off).

Figure 76 shows all transmitted and scattered light derived from the released ZnO NRs/SU-8 on the PET flexible substrate. The transmittance and scatter light for the bare PET substrate (no NRs added on) was measured as a reference. As shown, all transmitted and scattered light of the bare PET substrate and five T_{growth} samples show similar curves. Where the transmittance was higher in the short wavelength range (300-900nm) regions and drops at the reset spectral range. The light scattered at 400-800nm regions for the five T_{growth} samples. There was no scattering from the bare PET substrate, which exhibited almost a flat line. The drop in the long wavelength range (800-1400nm) region is attributed to the optical properties of the substrate, confirmed by the response of the bare PET.

It can be seen that all scattered peak are lower once transferred to PET. T_{growth} = 65°C scattered more light at approximately 35% in the short wavelength (300-800nm) spectral region compared to the remainder of the samples. From figure 76, it can be clearly seen that the values of all transmitted and scattered light dropped considerably after transferring the ZnO NRs to the PET substrate. This behaviour is completely understood due to the two different substrates used (glass as the initial substrate before lift-off) and

(and PET as the final substrate after lift-off) as well as he resulting ZnO NRs morphology at this T_{growth}. Therefore, for transmittance, the glass transparency will allow more light to pass through, which is not the case for the PET which is less transparent than the glass substrate. To further investigate the resulted all transmitted light and scattered light, haze ratio is calculated. The haze ratio is considered as the characteristic value of a substrate ability to scatter light to off - normal angles [246]. Transmission haze (H_T) which is the ratio of diffused light to total transmitted radiation ($H_T = T_{diff} / T_{tot}$), is usually used for estimating the light scattering effect [245]. The haze values of the ZnO NRs on the SU-8 resist were calculated, as shown in 87. The haze values were extracted using the wavelength range 400nm-1400nm.

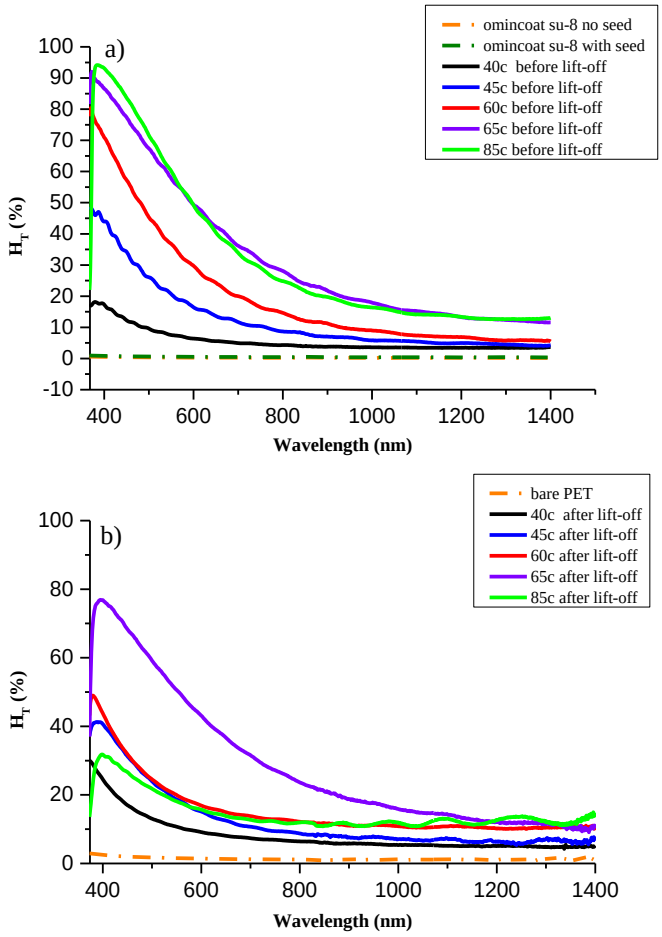

Figure 77. Transmittance haze spectra as a function of the wavelength for glass/Omnicaot/SU-8/ZnO nanorods under T_{growth} = 40°C, 45°C, 60°C, 65°C and 85°C a) (before lift-off) and b) after lift-off.

Nanostructures tend to increase haze as transmission decreases because tradeoff between these two properties tends to take place while bare PET has a transparency and haze of 88% and 1% at 550 nm, respectively [286]. From Figure 77 a) it can be seen that, Omnicaot/SU-8 with and without ZnO seed layer showed low haze values. Before lift-off showed H_T higher than that of after lift-off. This is due to the two different substrates used before and after lift-off (glass and PET respectively). Before lift-off, the H_T spectra of NRs grown at 85°C is the highest reaching about 95% at 400nm.Whereas NRs at 40°C showed the lowest value at about 17% at 385nm. After transferring the ZnO NRs to PET substrate, bare PET substrate showed low haze value. Also, it was found that, the highest value was observed for 65°C NRs and the lowest was for 40°C. Increasing the light scattering is connected to the ZnO film roughness and therefore, correlating that to the obtained morphology [239].

5.1.2.4 Scanning electron microscopy (SEM) and energy dispersive spectroscopy (EDS)

SEM images confirmed that the diameter of the formed ZnO NRs reduced from 100nm to 54nm, as the T_{growth} increased, while their density increased from 50/µm² to 102/µm². Furthermore, the shape of the NRs became sharper at the tip with increasing T_{growth}. This was accompanied by the crystal size variations from 46.9 nm to 70.3nm along (002) plane with increasing T_{growth}, displaying a preferred orientation along the c-axis. EDS was accomplished, as shown in Table 7.

Table 7. EDS results for ZnO NRs/SU-8

ZnO NRs/SU-8		
Atomic (%)		
Sample	**Zn**	**O**
40°C	88.6	11.4
45°C	78.3	21.7
60°C	79.9	20.1
65°C	76.5	23.5
85°C	77.8	22.2

From the resulting curves it is important to mention that the fluctuations in the optical measurements might be due to the delamination of the SU-8 film during the ZnO hydrothermal growth process. The delamination is principally caused by the Omnicoat layer, seeing as it tends to reduce the adhesion between the substrate and the SU-8 layer. The ZnO solution penetrated under the Omnicoat layer.

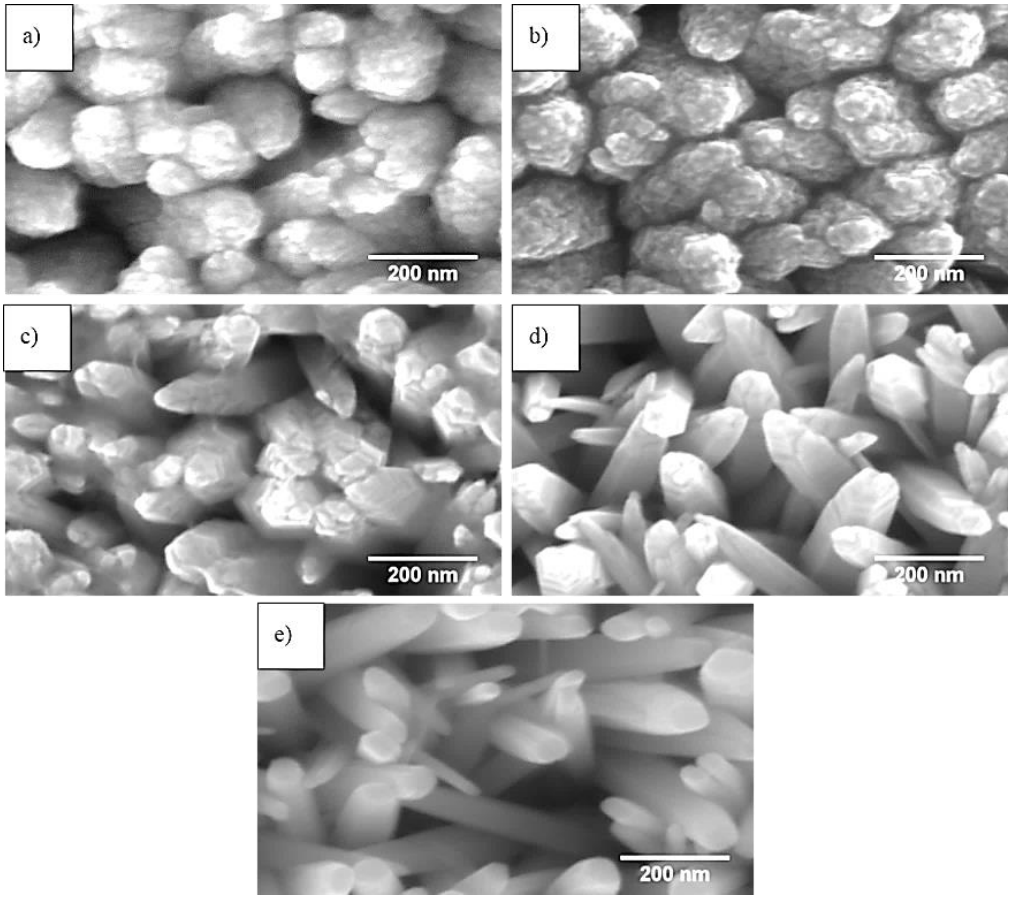

Figure 78. Scanning electron microscopy (SEM) images of the grown ZnO nanorods/SU-8 under five T_{growth}. a) 40°C, b) 45°C, c) 60°C, d) 65°C and e) 85°C.

5.1.2.5 XRD for ZnO nanorods/SU-8 under T_{growth} = 40°C, 45°C, 60°C, 65°C and 85°C

It was clearly observed that a wurtzite hexagonal structure was the outcome for all samples with diffraction intensity peak of (002). The results presented in this work can be indexed to the used standard spectrum in JCPDS (No. 36-1451). Figure 79 shows the XRD of the grown ZnO NRs using the mentioned different T_{growth}. It was established that the XRD patterns revealed the mentioned preferential orientation growth of (002) at (2θ = 34 °ɵ) in the c-axis respectively for the T_{growth} range. Three peaks were almost revealed and the XRD spectra demonstrated the peaks of (002), (004) and (103). This is an indication of the c-axis orientation perpendicular to the sample surface; therefore, a variation in structural parameters. The highest 002 intensity was observed for T_{growth} = 60°C.

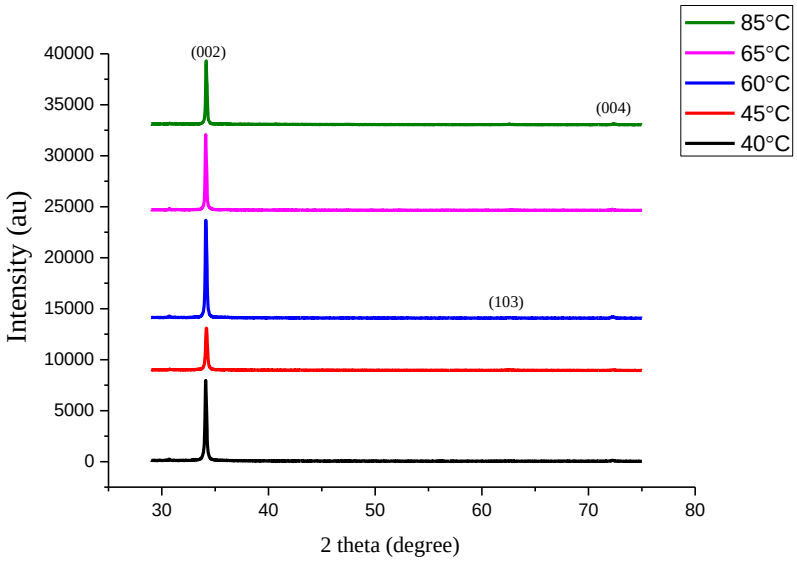

Figure 79. The XRD patterns of ZnO NRs grown on Omnicoat/SU-8 structure before lift-off using T_{growth} = 40°C, 45°C, 60°C, 65°C and 85°C.

5.1.3 **ZnO NRs/PDMS/glass (dry lift-off)**

As shown above, the ZnO NRs can be grown on an SU-8 layer. We termed this process (wet lift-off) due to the need to use chemical solutions, such as developer and remover to be able to release the resist layer from the initial substrate. To provide a comprehensive study relating to releasing ZnO NRs grown on a removable layer, another material PDMS was chosen to be a candidate for this purpose. PDMS can be easily peeled off from the substrate without using any chemical remover [287]. After using the dry lift-off process, a number of features are observed in this process in contrast to the wet lift-off. The dry lift-off process is time and cost-effective as no wet remover solutions are required. As a result, additional material or releasing methods are required in order to detach the fabricated/targeted structure. Hence, further cost reduction to produce the targeted structure can be easily achieved. This section will provide comprehensive details on the dry lift-off process and what could be different compared to the first method used; specifically, wet lift-off. PDMS can be firmly and easily attached to a glass substrate without the need for the addition of any other adhesives. That is due to the strong Van der Waals interactions between the glass substrate and PDMS [288].

5.1.3.1 **Scanning electron microscopy (SEM) and energy dispersive spectroscopy (EDS) for ZnO NRs**

The morphological investigation was performed by means of scanning electron microscopy (SEM). Figure 80 illustrates the SEM images of the ZnO NRs grown on the PDMS layer at five different T_{growth} = 40°C, 45°C, 60°C, 65°C and 85°C. It was determined that the T_{growth} has a significant effect on the morphology of the ZnO NRs. From the figure, it was observed that by increasing the T_{growth}, the diameter, the length of the NRs decreases. At low T_{growth}, the morphological shape and structure is highly dense.

This is due to the larger diameter of the NRs in comparison to the NRs when grown at higher T_{growth}.

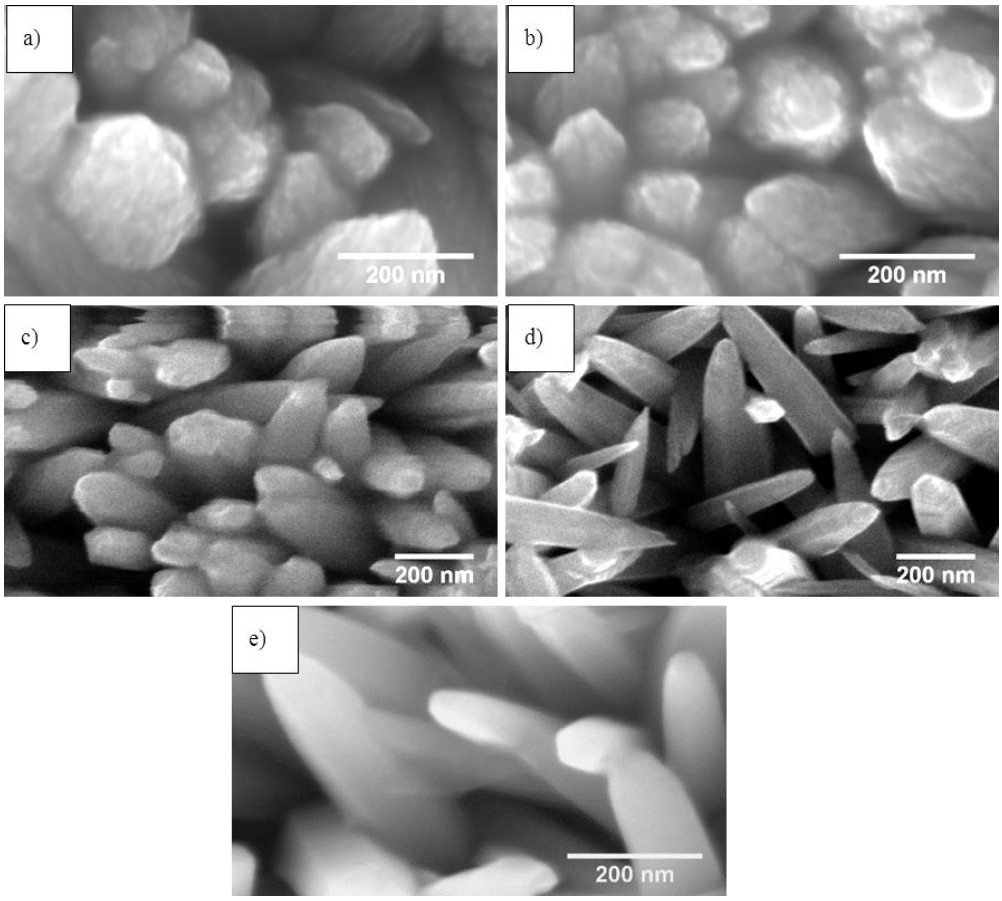

Figure 80. SEM images of ZnO NRs grown on PDMS using Tgrowth = 40°C, 45°C, 60°C, 65°C and 85°C.

Comparing to data shown in Figure 78, here when NRs grown on PDMS as shown in the figure 80, different diameter and length are obtained for the five different T_{growth} respectively. Increasing and decreasing the diameter will significantly affect the light scattering effect (which is the target in this project to be increased). Increased diameters mean that the spacing in between the NRs will be less; thus, the light scattering will be less, whereas NRs with a lesser diameter means more spacing in between and that more light can be scattered and trapped inside the used samples. This is a clear indication that the morphology of the NRs showed here are hugely dependent on the T_{growth}. EDS investigation was performed, as shown in Table 8.

Table 8. EDS results of ZnO NRs/PDMS

ZnO NRs/PDMS				
Atomic (%)				
Sample	**Zn**	**O**	**C**	**Si**
40°C	69.5	20.4	8.4	1.7
45°C	68.3	21.3	8.6	1.9
60°C	67.2	22.1	8.9	1.8
65°C	75.7	14.8	6.9	2.6
85°C	68.9	20.1	8.6	2.4

5.1.3.2 **UV-VIS spectrometry**

Figure 81 illustrates all the transmitted and scattered light of the ZnO NRs/PDMS on the glass substrate (before and after peel off) with variations in growth temperature using the range of T_{growth} = 40°C, 45°C, 60°C, 65°C and 85°C. These are different results comparing to ZnO NRs grown on SU-8. These optical characteristics were performed with the wavelength range of 300-1400nm. Generally, when introducing a nanostructure on any targeted structure, this will enhance the performance of the device (optically for example) [289]. The higher the all transmitted light, the lower the scattered light and vice versa. This can be distinctly perceived in the figure, where the lowest T_{growth} = 40°C revealed the highest all transmitted light and lowest scattered light values over the spectral range. In contrast, T_{growth} = 65°C was scattering more light.

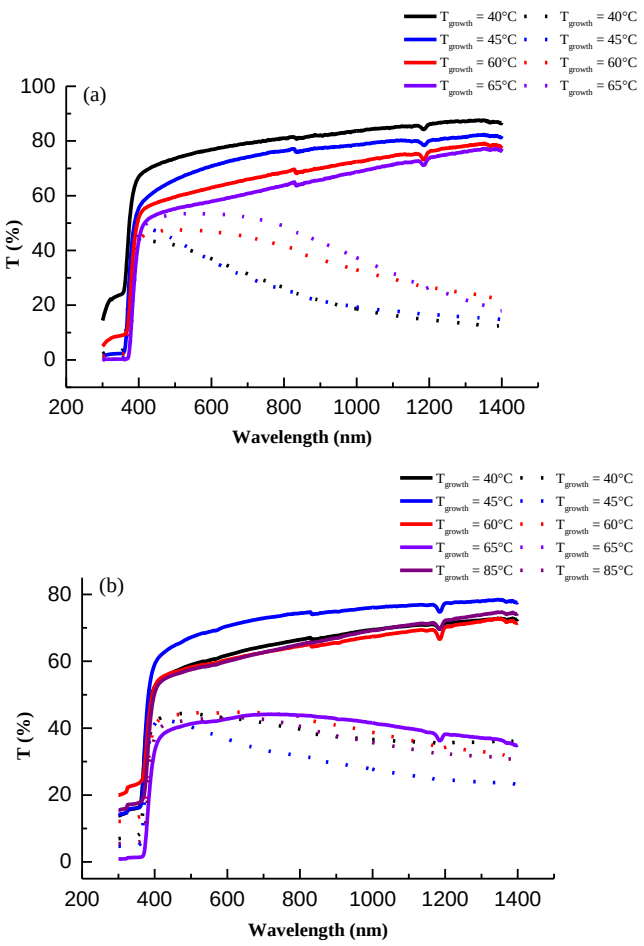

Figure 81. The transmittance spectra of a) ZnO/PDMS (before peel-off) and b) after peel off. Solid lines represent the total transmitted light and the dotted lines represent the diffused light.

The improvement in the light scattering was due to the drop in the all transmitted light, as well as the crystalline structure mentioned improving the NRs as the T_{growth} goes from 40°C to 65°C. The low (T_{growth} = 40°C and 45°C) displayed almost the same trend as the T_{growth} was just 5°C higher, whereas the high (T_{growth} = 60°C and 65°C) presented a similar trend with high light scattering and lower transmitted light. These variations due to the wavelength and intensity of scattered radiation have primarily clear dependence on the ZnO NRs diameter and length respectively [245].

5.1.3.3 **X-ray diffraction**

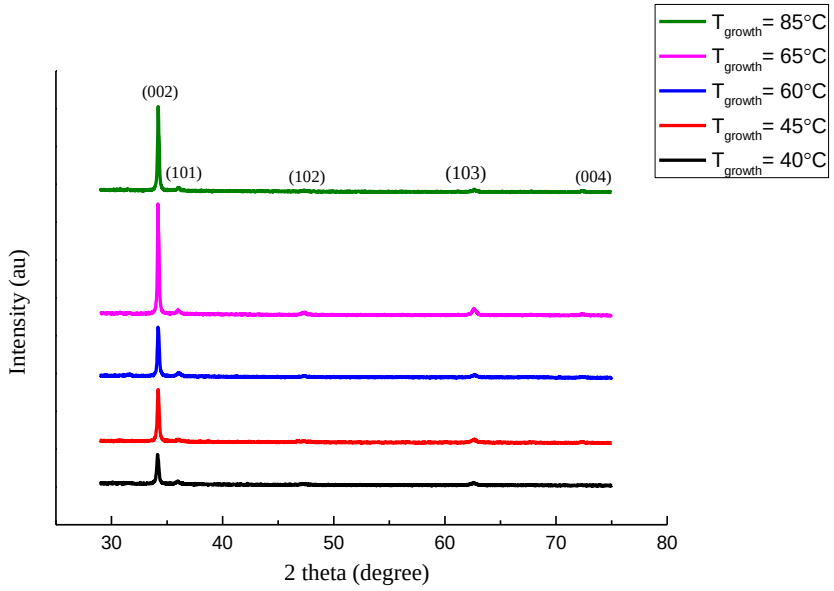

Figure 82. XRD patterns of ZnO NRs grown on PDMS using T_{growth} = 40°C, 45°C, 60°C, 65°C and 85°C.

The ZnO NRs/PDMS crystalline structure was further investigated by means of using XRD. As shown in Figure 82, a number of wurtzite characteristic peaks have been observed as (002), (101), (102), (103) and (004). However, the (002) diffraction peak exhibited the strongest intensity which reveals that the grown NRs have been preferably grown in the c-axis direction [290, 291]. From the figure, it can be seen that the T_{growth} = 65°C showed the highest (002) peak intensity, whereas the T_{growth} = 40°C demonstrated the lowest (002) peak intensity. It is completely understood that as the T_{growth} increases, the morphology of the NRs will improve. This was confirmed by the SEM images. The different NRs diameters when the T_{growth} = 40°C and T_{growth} increased to T_{growth} = 65°C are resulted. The clear morphology and characteristics of the NRs was observed after changing the T_{growth}. For the rest of the T_{growth}, the (002) intensity varies. Comparing to wet lift-off, ZnO NRs on PDMS showed more XRD peaks.

5.1.4 **Flower like nanostructure/diluted PDMS**

A flower like nanostructure was grown on diluted PDMS. Diluting PDMS was in order to reduce the PDMS thickness. Same growth process was followed at this method and as shown, the nanostructure is dense

5.1.4.1 **Scanning electron microscopy (SEM) and energy dispersive spectroscopy (EDS) for ZnO NRs**

The SEM images were taken for all samples and it was revealed that the resultant structure is a flower like structure. It is worth stating that the ZnO NRs have shifted to flower like due to the existence of toluene which is used to dilute the PDMS. This is confirmed by comparing these structures with the resultant structures when the PDMS was used with any further additions.

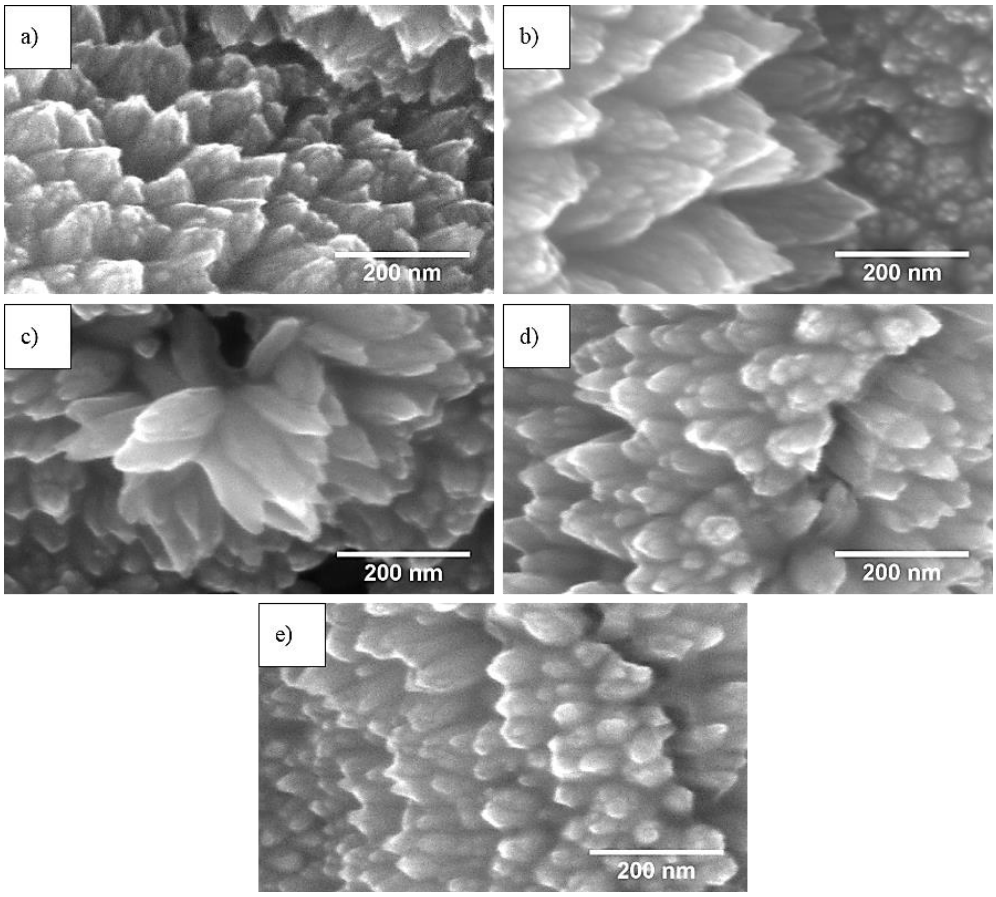

Figure 83. SEM images of ZnO flower-like grown on diluted PDMS using T_{growth} = 40°C, 45°C, 60°C, 65°C and 85°C.

It is extremely apparent that the flowers are heavily dense for all five samples and from the top-view, the nanorods are small in length. Different studies showed the growth of ZnO nanoflower using hydrothermal process using different substrate as stated in [292, 293]. However, in this project the nanoflower were grown on a flexible diluted PDMS substrate.

5.1.4.2 **X-ray diffraction**

To further investigate these structures, XRD was taken. The resulting patterns are shown in Figure 84. Just two peaks were observed (002) and (103). It interesting to mention that the higher T_{growth} shed less intensity than the remainder of the samples. This is because the growth process is saturated due to the fast growing mechanism. This indicates that the flower like has been formed in less time compared to the other T_{growth}. Similarly, EDS was performed, as shown in table 9 which showed different values. Comparing to figure 82, the resulted XRD peaks in Figure 84 showed two peaks (002) and (103).

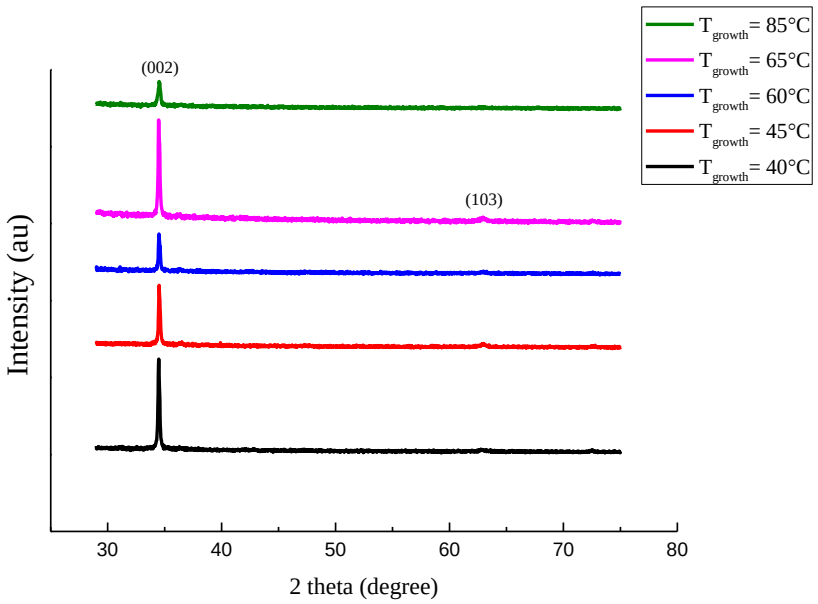

Figure 84. XRD patterns of ZnO flower like/diluted PDMS using Tgrowth = 40°C, 45°C, 60°C, 65°C and 85°C.

Table 9. EDS results for ZnO flower like/diluted PDMS

ZnO flower like/diluted PDMS				
	Atomic (%)			
Sample	**Zn**	**O**	**C**	**Si**
40°C	59.9	24.1	11.5	4.5
45°C	69.6	19.3	8.3	2.8
60°C	31	29.3	17.8	21.9
65°C	40.9	18.1	9.2	31.8
85°C	33.4	24.8	12.5	29.2

To additionally investigate the growth mechanism, the pH value, which was fixed at (10.3-10.4) was monitored at two different stages (before and after the growth), as shown in Figure 85. The pH value at lower T_{growth} dropped slightly from 10.4 to 9.8 and remained stable. Conversely, as the T_{growth} increases the pH decreases, which indicates the fast growth process which requires more of the used ammonia to be consumed.

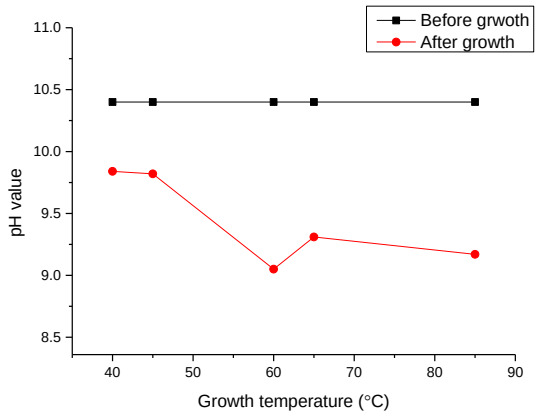

Figure 85. pH value before and after the flower like growth processes.

5.1.5 **Mounting the ZnO nanostructures on a complete**

5.1.6 **Solar cell for I-V and EQE measurements.**

The ability to capture the incident light photons represents the key characteristics of any photovoltaic device. The reflected light is uncaptured light. Hence, reducing this reflectance effect will strongly enhance the light capturing and therefore increase the functionality and efficiency of the device. With regards to solar-based cells, less is more. In other words, the less reflected sunlight from their surfaces the more energy generation can be achieved. Thus, fixing the reflectivity issue is by way of using the anti-reflective coated layers. In the solar cells fabrication field, anti-reflection (AR) schemes have been extensively used in order to enhance solar cell efficiency. However, the effectiveness of the AR coating is highly dependent on the incident angle and wavelength, whilst their high quality requires expensive chemical processes [288, 294]. Hence, introducing nanostructures can reduce this reflection effect as it can act as an anti-reflection layer. Given that ZnO is a material with 2.02 reflective index, the oxide nanostructure can act as an AR medium [295]. ZnO NRs have a significant impact on increasing the performance of different types of solar cell as it facilitates the infiltration of perovskite solar cells and it boosts the charge transport to be faster, as stated by Mahmood et al [296]. In this section, the lifted-off NRs structure have been employed to investigate their influence on the performance of different solar cells. Here, GaAs and CZTS solar cells (shown in Figure 86) were employed as a candidate devices investigate the effect of lifted-off NRs on the different solar cell performance and parameters.

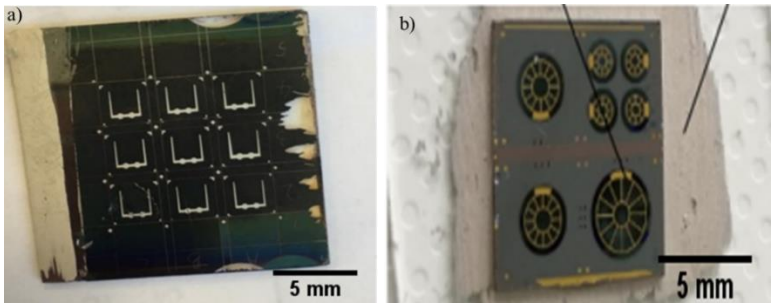

Figure 86. The two used solar cells. a) GaAs solar cell structure and b) CZTS solar cell structure.

Conversely, the ability of higher light scattering is represented to be another method in improving the efficiency of light harvesting. Therefore, the UV-VIS reflectance further investigated the used solar cells in two different cases (before and after NRs).

5.1.6.1 Reflectance measurements with and without NRs on solar cells

To measure the reflectance (R %) of the different solar cells applied, the light beam was directed to the centre of the cell, as shown in Figure 87. The figure presents the CZTS solar cell before the ZnO NRs to perform the R% measurements. It should be mentioned that the light beam position is the same with or without NRs.

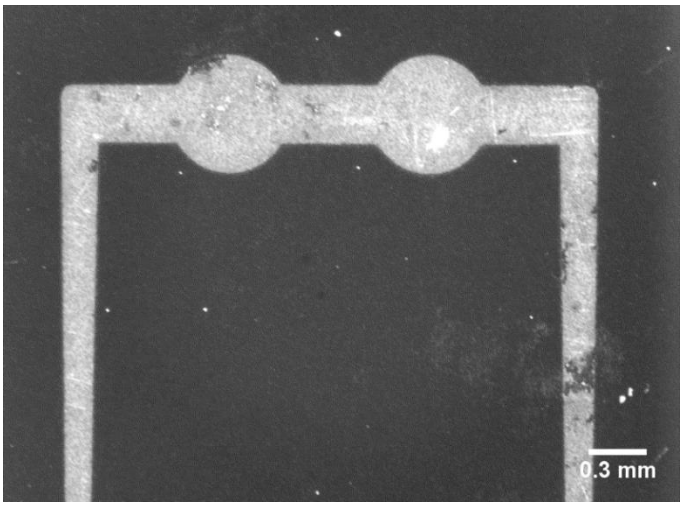

Figure 87. Reflectance measurement method for CZTS solar cell (before adding the ZnO NRs).

The initial investigation was performed using CZTS substrate configuration and GaAs substrate configuration. Figure 88. Here shows reflectance of both the devices measured (before and after the NRs addition) using the ZnO NRs/SU-8 (wet lift-off) and the ZnO NRs/PDMS (dry lift-off).

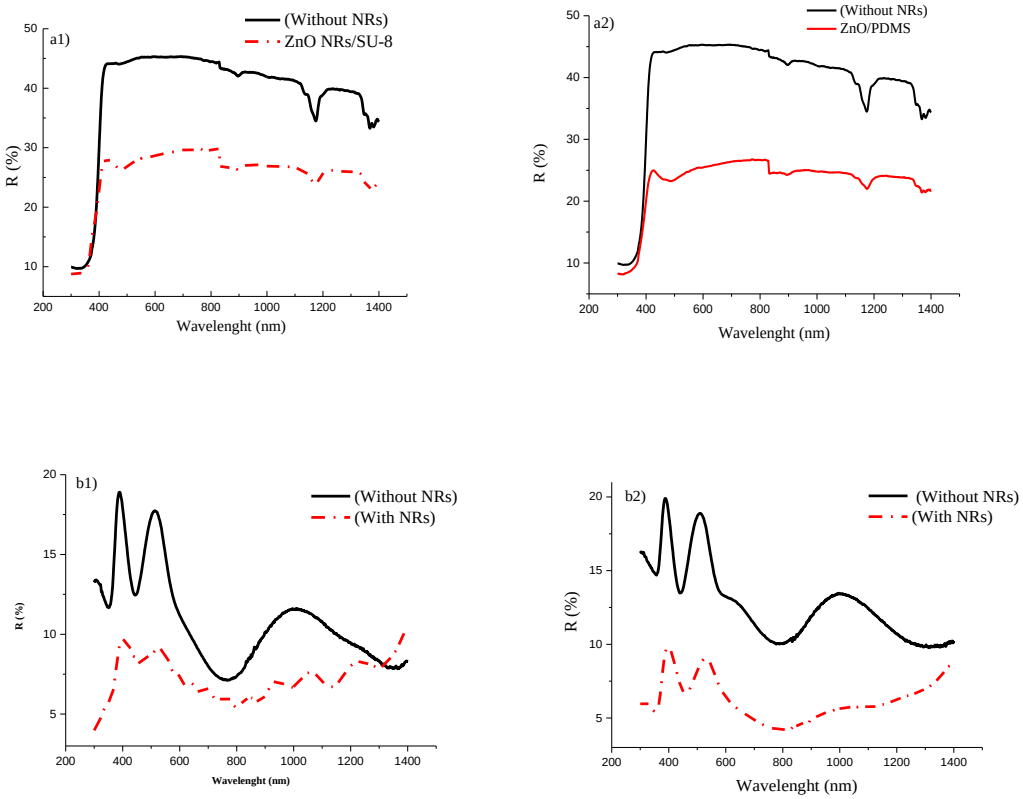

Figure 88 Reflectance spectra of a1), a2) for GaAs and b1), b2) for CZTS substrate configuration solar cell with and without ZnO NRs/SU-8 and ZnO NRs/PDMS respectively.

Figure 88 represents the reflectance spectra of two different (GaAs and CZTS) substrate configuration solar cells with and without ZnO NRs. Figure 88 a1) and Figure 88 a2) illustrate the influence of the ZnO NRs on the total reflection of the light. It can be clearly noticed that while the cell is without NRs, it reflected approximately 45% of the light over the wavelength spectra range (300-1400nm). After introducing ZnO NRs grown on both the SU-8 and PDMS, a significant decrease in the reflected light was observed. Less than 30% for the SU-8 and roughly 25% for PDMS respectively. For GaAs solar cells (tandem structures for example), this type of solar cell can generate more electrical power

under brighter conditions. Additionally, when the light occurs on the air/GaAs interface, a reflection will occur due to the different refractive indices [297]. Figures 95 b1) and b2) the (CZTS cell) oscillations were observed. The spectra demonstrated that the optical reflectance varies over the operational range. A 390-550nm range showed about 20% and 14-9% 600-1400nm. These resulting ripples in the CZTS spectra are due to the effects of optical interfaces [298]. These ripples are normally obtained for CZTS reflection, which is also reported in [299].

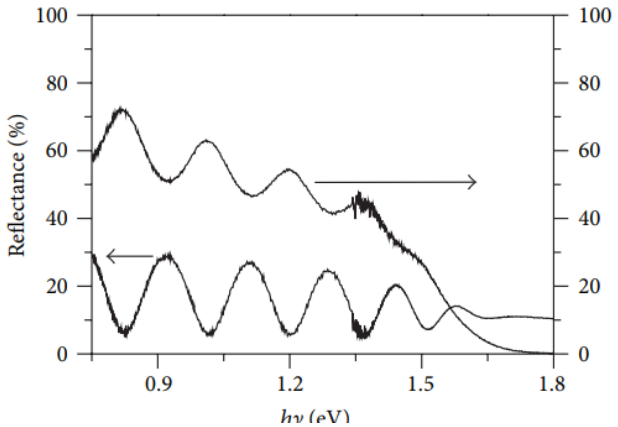

Figure 89. CZTS reflectance ripples reported by [299].

Both cases (two different cells) presented an agreement that ZnO NRs grown on PDMS provide more anti-reflection properties. This can be due to the alignment of the NRs as shown in the SEM images Figure 78 and Figure 80. The ZnO NRs on the PDMS demonstrated better alignment, which suggests that the optical light path was longer than the one related to the ZnO NRs on SU-8**.** This obvious reflection reduction in these cells is attributed to the increasing light scattering effect that is induced by the ZnO NRs. The existence of these NRs allowed the light to be trapped within the cell for longer and prevented it from reflecting back. Hence, reducing the light reflection can be explained by the factor of creating and introducing the ZnO NRs. Increasing the light optical path is documented when a textured structure film is used in solar cell fabrication [300], seeing as this structure will lead the light propagation to be randomized in different directions.

Thus, the result is a longer optical path of light and effective light trapping is achieved [301]. Light reflection from the front solar cell surface is represented to be the main barrier. The front surface of the GaAs solar cells reflects in the region of 33% of the light, which is due to the GaAs high refractive index.

GaAs solar cells have the ability to generate high currents and voltages. The theoretical power conversion efficiency of these cells is high, at about 33%, although this power conversion efficiency did not allow the performance of the GaAs solar cell to reach its peak level due to the relatively high refractive index (n=3.7) [302]. The reason for selecting ZnO as a candidate to reduce the reflectance and increase the light scattering effect is that ZnO appears to be ideal owing to its wide bandgap of 3.3 eV and low refractive index value, which makes the material transparent in the visible region of the light [302]. From the results shown in Figure 88, it can be observed that the performance of the GaAs solar cells have been notably improved due to the addition of lifted-off ZnO NRs on top of it. The light reflected from the bare solar cell (no NRs added) is delivering EQE values at approximately 39%. In contrast, the reflected light declined significantly after applying the ZnO NRs. The improvement is clearly observed in the solar cell characteristic properties; specifically in optical reflectance spectral response, external quantum efficiency (EQE and power conversion efficiency (η).

5.1.6.2 **GaAs solar cell with and without NRs (I-V characteristics)**

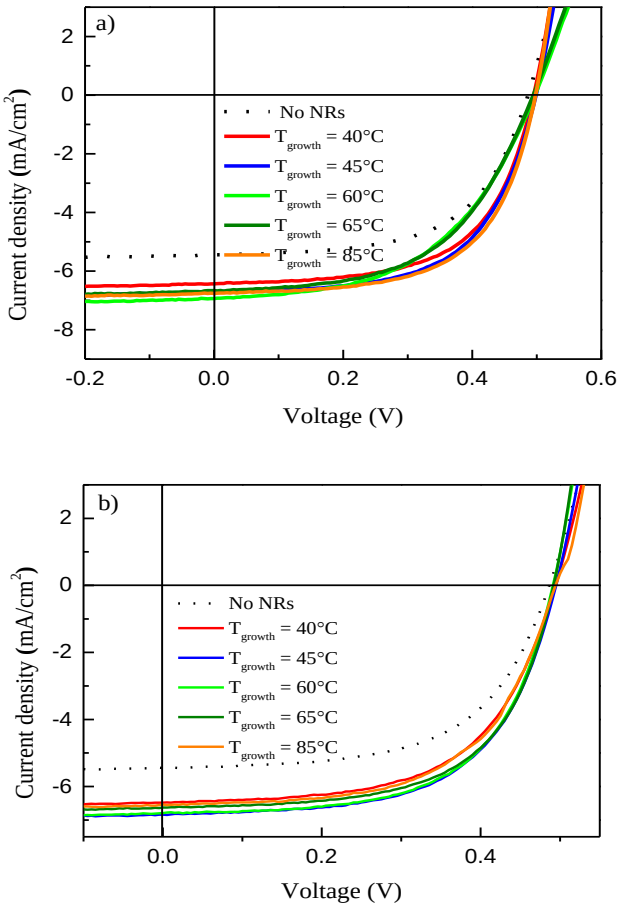

Figure 90. I-V characteristic for GaAs solar cell using two different ZnO nanostructures. a) ZnO NRs/SU-8 and b) ZnO NRs/PDMS.

The GaAs solar cell used here consists of QDs. These QDs tend to provide more contribution to the photocurrent by means of capturing the photons that comprise energies that are less than the energy bandgap of the used solar cell [303]. Current density of the used solar cell (which is GaAs in this case) are shown in Figure 90 before and after applying the lifted-off ZnO NRs on the mentioned GaAs solar cell. Both methods are applied here on the solar cell (wet and dry lift-off methods). The cells with seeded SU-8 and PDMS showed almost similar values as the bare cell (before NRs grown on). Figure 90 a) shows the effect of the ZnO NRs/SU-8 and Figure 90 b) presents the effect of the ZnO NRs/PDMS on the overall performance of the GaAs solar cell. It can be clearly noted that the device efficiency has increased from 1.56% to the highest values of 2.05% and

2.03% for wet and dry lift-off respectively. Different values which display remarkable solar cell improvement are obtained, as shown in Table 10. The initial short current density before NRs was roughly J_{sc} = 5.5 mA/cm^2. This value has increased to nearly J_{sc} = 6.7 mA/cm^2 and J_{sc} = 6.8 mA/cm^2 after applying ZnO NRs grown at different T_{growth}. The ZnO NRs/SU-8 and ZnO NRs/PDMS showed almost similar increased values of J_{sc}. T_{growth} = 60°C revealed the highest values at the two different methods. This can be attributed to the resulting ZnO NRs morphology which revealed various crystal sizes.

Table 10. GaAs solar cell performance with and without mounted ZnO NRs.

ZnO NRs/SU-8 structure		
T_{growth} (°C)	**η (%)**	**Improvement (%)**
No NRs	1.56	-
40°C	1.92	23
45°C	2.01	28.8
60°C	1.76	12.8
65°C	1.78	14.1
85°C	2.05	31.4
ZnO NRs/PDMS structure		
T_{growth} (°C)	**η (%)**	**Improvement (%)**
No NRs	1.56	-
40°C	1.88	20.5
45°C	2.03	30.1
60°C	2.02	29.4
65°C	1.99	27.6
85°C	1.90	21.8

Figure 91 a) illustrates the solar cell efficiency for all used different five T_{growth}. It can be seen that for both cases, when the T_{growth} increased from 40°C to 45°C, the η increased from (1.92% to 2.01%) and from (1.88% to 2.03%) respectively. Moreover, the η dropped when a higher T_{growth} was used except in T_{growth} = 85°C ZnO NRs/SU-8 which exhibited well aligned NRs in SEM morphology. The initial open circuit voltage V_{oc} remains constant and unchanged as stated in Table 11. Thus, the increased Jsc values are the primary reason for the increased efficiencies η=1.56% before NRs to η=2.05% and 2.03% after ZnO NRs/SU-8 and ZnO NRs/PDMS respectively, which is approximately a 31.4%

and 30.1% improvement, as can be observed in Table 10. Hence, Figure 91 b) shows how much improvement has been made in relation to the solar cell using the ZnO NRs technique. Therefore, an effective improvement has been successfully achieved by this technique.

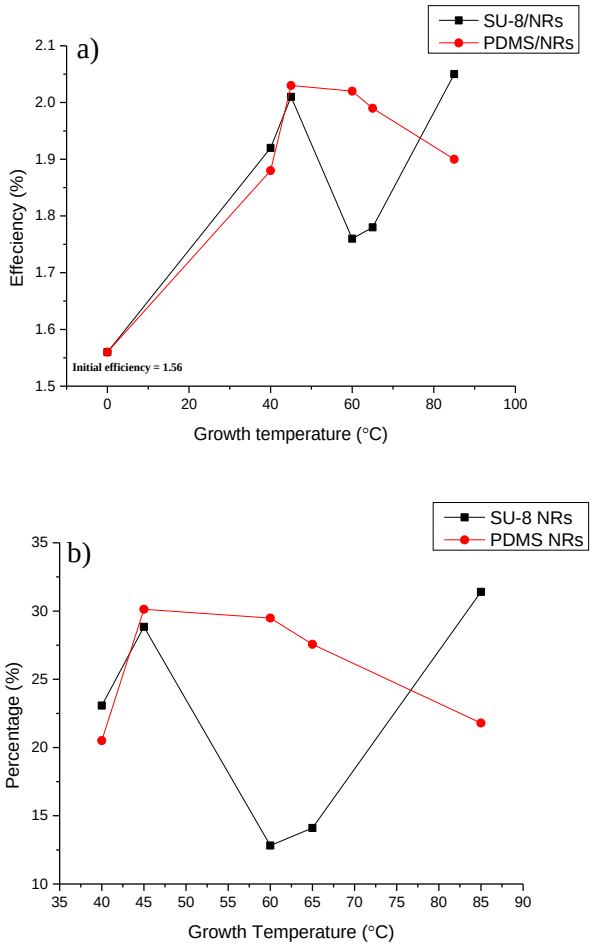

Figure 91. Improvement of GaAs solar cell performance after the addition of NRs. a) increased efficiency and b) increasing percentage.

Table 11. The extracted device parameters from I-V characteristics for GaAs solar cell with and without ZnO NRs as a function of T_{growth}.

ZnO NRs/SU-8 structure				
T_{growth} (°C)	**V_{oc} (mV)**	**J_{sc} (mA/cm^2)**	**FF**	**η (%)**
No NRs	400	5.5	71.5	1.56
40°C	400	6.4	74.7	1.92
45°C	400	6.7	74.6	2.01
60°C	400	6.9	63.6	1.76
65°C	400	6.7	66.4	1.78
85°C	400	6.8	75.7	2.05
ZnO NRs/PDMS structure				
T_{growth} (°C)	**V_{oc} (mV)**	**J_{sc} (mA/cm^2)**	**FF**	**η (%)**
No NRs	400	5.5	71.5	1.56
40°C	400	6.5	72.66	1.88
45°C	400	6.8	74.21	2.03
60°C	400	6.8	74.42	2.02
65°C	400	6.6	75.18	1.99
85°C	400	6.6	72.37	1.9

5.1.6.3 **GaAs solar cell with and without NRs (EQE)**

Measuring the EQE is necessary as this step helps in observing the behaviour of the solar cell at a specific wavelength range. QE has a strong dependence on the photo-generated current [304]. Figure 92 highlights the EQE curves of the GaAs solar cell before and after the addition of the ZnO NRs. Figure 92 a) represents the ZnO/NRs (wet lift-off) and Figure 92 b) represents the ZnO NRs/PDMS. The highest EQE value of the initial cell (prior to adding the ZnO NRs) was roughly 40%. However, a remarkable increase in the EQE values was obtained after the addition of the ZnO NRs. It demonstrates that for both cases, the EQE values give similar values. The EQE increased rapidly from the 410nm wavelength until about 650nm. Next, it remains in a relatively steady state high position until almost 890nm, before it drops back to 900nm. The maximum observed EQE values for wet and dry lift-off processes were approximately 50% and 48% respectively. The low EQE values can be a result of the material's band gap, as below the energy bandgap and longer wavelength, the light will not be absorbed [304]. The resulted peaks at about

923nm due to the quantum dots used during the solar cell fabrication. It can be concluded that the EQE work area of this solar cell before and after adding the ZnO NRs expands from 410nm until 890nm. Figure 92 and table 12 present the integrated and calculated Jsc from the EQE. The figure and table showed acceptable values of Jsc after being extracted from the measured EQE.

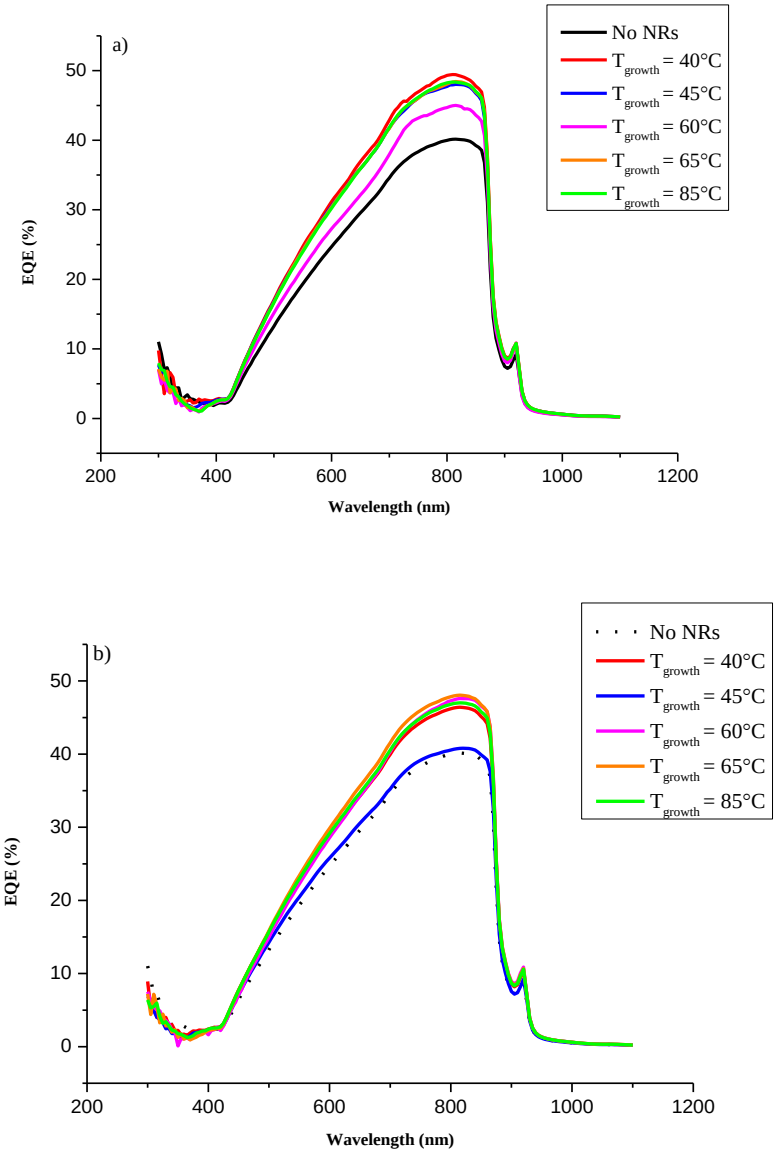

Figure 92. The external quantum efficiency (EQE) for GaAs solar cell with and without NRs using different Tgrowth. a) Using wet lift-off and b) using dry lift-off.

Table 12. Jsc values extracted from EQE.

ZnO NRs/SU-8 structure		
T_{growth} (°C)	**J_{sc} (mA/cm^2)**	**J_{sc} (mA/cm^2) from EQE**
No NRs	5.5	8.7
40°C	6.4	10.7
45°C	6.7	10.5
60°C	6.9	9.5
65°C	6.7	10.5
85°C	6.8	10.4
ZnO NRs/PDMS structure		
T_{growth} (°C)	**J_{sc} (mA/cm^2)**	**J_{sc} (mA/cm^2) from EQE**
No NRs	5.5	8.7
40°C	6.4	10
45°C	6.7	8.9
60°C	6.9	10
65°C	6.7	10.3
85°C	6.8	10

It is apparent from the presented result that the ZnO NRs are effective for increasing the EQE of the GaAs solar cell as judged from the performance enhancement of the solar cell. Increasing the EQE from 40% to approximately 49% in the spectral work area is remarkable. Hence, an increasing value of about 10%. Varying the T_{grwoth} revealed a significant effect, as seen in the figure. On the one hand, for wet lift-off a), the highest EQE achieved was when the T_{growth} = 40°C and the lowest value was at T_{grwoth} = 60°C. T_{grwoth} = (45°C, 65°C and 85°C) showed an almost similar trend. Conversely, for dry lift-off, lowest value was at T_{growth} = 45°C and the highest value was at T_{growth} = 65°C which was quit T_{grwoth} = (40°C, 60°C and 85°C). These variations in the EQE value are clearly due to the different resultant ZnO NRs morphologies. In principle, increasing the T_{growth} will cause the morphology of the NRs to change and the NRs will become sharper. In the SEM images, it was observed that low T_{growth} has resulted in NRs with diameters larger than the higher T_{growth}. This means that primarily, the larger the NRs diameter, the less spacing in between the NRs and vice versa. Larger diameter will provide less scattering.

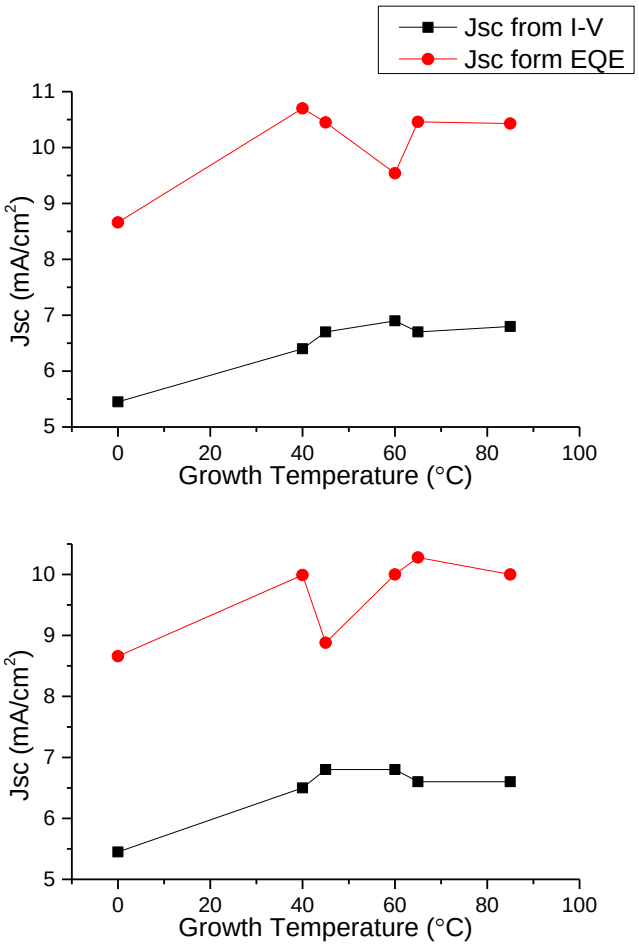

Figure 93. Integrated Jsc from EQE.

Smaller NRs diameter will enhance the light reflection more and hence, it will be trapped for a longer time in the solar cell. Surprisingly here, this was not the case for wet lift-off, seeing as the lowest T_{grwoth} = 40°C demonstrated better EQE, while for dry lift-off T_{grwoth} = 65°C showed the highest EQE values. A number of factors have to be considered in this case, besides the different ZnO NRs morphologies, the GaAs solar cell structure has to be considered too. In a thin film cell, normally the high QE value near the band gap edge specifies an increase in collection efficiency resulting from the carriers generated by the photon in the mentioned region. This is a clear agreement with the fact of average of the photons are being absorbed in the region close to the used p-n junction than the substrate cell.

5.1.6.4 **CZTS solar cell with and without NRs (IV)**

In the previous sections, the effect of the ZnO NRs grown on the SU-8 and PDMS on the performance of the GaAs was shown. In this section, a CZTS solar cell have been used to investigate the influence of these NRs. When mentioning CZTS solar cells, it is important to mention that the efficiency of these solar cells are low comparing CIGS solar cells reported in [305]. This is due to the CZTS thin film quality. Hence, further improvement can be reached and obtained regarding the CZTS by introducing nanostructures to facilitate the charge transport. Here, three different structures (ZnO NRs/SU-8, ZnO NRs/PDMS and flower like/diluted PDMS) were introduced and mounted on CZTS solar cells, and their influence investigated.

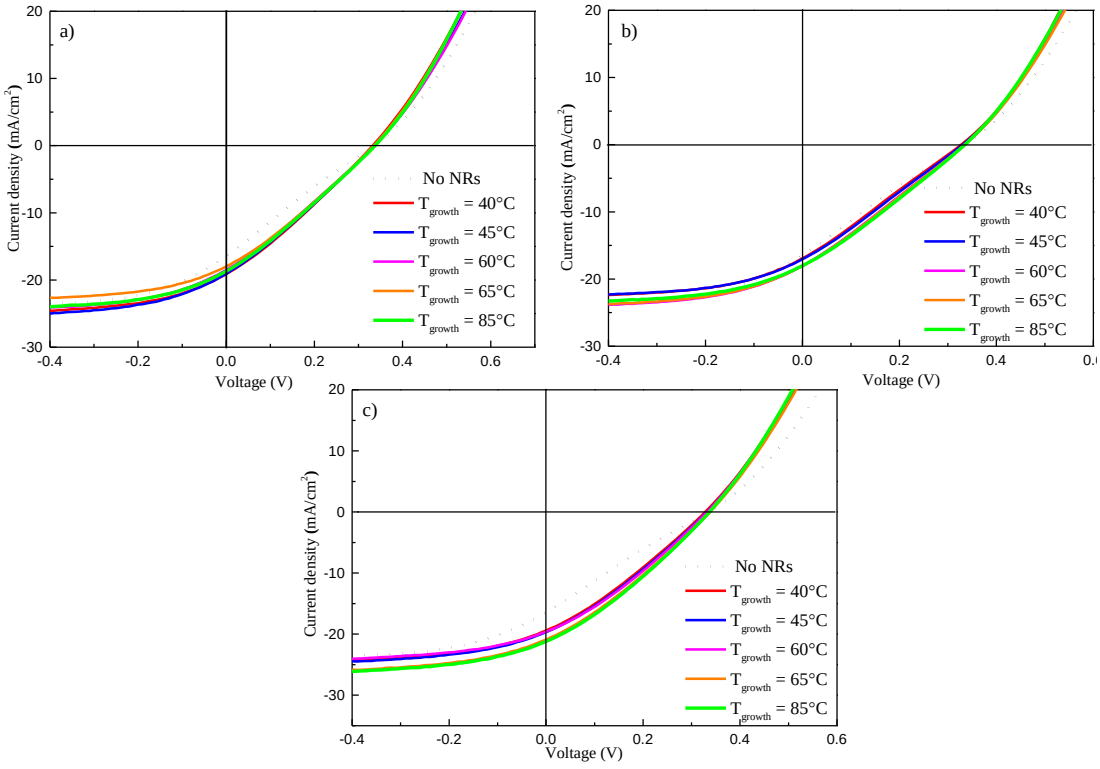

Figure 94. I-V characteristic for CZTS solar cell using three different ZnO nanostructures. a) ZnO NRs/SU-8, b) ZnO NRs/PDMS and c) flower like/diluted PDMS.

Current density vs voltage data of CZTS solar cells before and after placing the realised NRs are shown in Figure 94. Figure 94 a), represents the influence of the ZnO NRs/SU-8, Figure 94 b) signifies the influence of the ZnO NRs/PDMS and Figure 94 c) represents flower like/diluted PDMS. In relation to the bare CZTS cell, an efficiency of 1.3% was obtained and the corresponding V_{oc}=330, J_{sc}=16.4 and FF= 23.9%. After introducing NRs and flower like on the cell it was established that the five T_{growth} showed a variety of cell performance improvement as well as its photocurrent. This improvement is attributable to increasing the scattering light effect that the ZnO nanostructure causes. The significant improvement of the J_{sc} will enhance and generate much higher efficiencies [305]. This is plainly seen in Table 13. The V_{oc} values almost remained constant for all values.

Table 13. The extracted device parameters from I-V characteristics for CZTS solar cell with and without ZnO NRs as a function of T_{growth}.

ZnO NRs/SU-8 structure				
T_{growth} (°C)	**V_{oc} (mV)**	**J_{sc} (mA/cm^2)**	**FF (%)**	**η (%)**
No NRs	330	16.4	23.9	1.3
40°C	330	19.1	28.4	1.79
45°C	330	19.1	28.08	1.77
60°C	330	18.5	28.01	1.71
65°C	330	18	28.8	1.71
85°C	330	18.7	28.3	1.74
ZnO NRs/PDMS structure				
T_{growth} (°C)	**V_{oc} (mV)**	**J_{sc} (mA/cm^2)**	**FF (%)**	**η (%)**
No NRs	330	16.4	23.9	1.3
40°C	320	16.9	26.3	1.42
45°C	330	17.1	26.3	1.48
60°C	330	18	26.6	1.59
65°C	330	18	27	1.61
85°C	330	18	27.8	1.65
Flower like/Diluted PDMS structure				
T_{growth} (°C)	**V_{oc} (mV)**	**J_{sc} (mA/cm^2)**	**FF (%)**	**η (%)**
No NRs	330	16.4	23.9	1.3
40°C	320	19.4	19.4	1.87
45°C	330	19.7	29.7	1.93
60°C	330	19.6	30.4	1.97
65°C	330	21	30.3	2.09
85°C	330	21.2	30.7	2.15

From the above table, it can be concluded that the highest efficiency for n a), n b) and n c) was 1.79%, 1.65% and 2.15% respectively. The ZnO NRs/SU-8 displayed almost similar values as the T_{growth} increased. However, after introducing the ZnO NRs/PDMS, it was ascertained that the cell parameters were further improved with the different T_{growth}. Furthermore, the highest achieved efficiency in this study is 2.15% for flower like structure T_{growth} = 85°C. The resultant low fill factor can be due to the high series resistance originating from the back contact, which in turn should provide a good adhesion to obtain and serve an ohmic contact [306]. Practically, the FF is often lower as a result of parasitic resistive losses presence. Also, it is important to reduce the voltage to achieve high power-conversion efficiencies.

Table 14. Improvement in CZTS solar cell after the addition of ZnO nanostructures.

ZnO NRs/SU-8 structure		
T_{growth} (°C)	**η (%)**	**Improvement (%)**
No NRs	1.3	-
40°C	1.79	34.5
45°C	1.77	33.08
60°C	1.71	28.6
65°C	1.71	28.6
85°C	1.74	30.8
ZnO NRs/PDMS structure		
T_{growth} (°C)	**η (%)**	**Improvement (%)**
No NRs	1.3	-
40°C	1.42	6.8
45°C	1.48	11.2
60°C	1.59	19.5
65°C	1.61	21.05
85°C	1.65	24.06
Flower like/PDMS structure		
T_{growth} (°C)	**η (%)**	**Improvement (%)**
No NRs	1.3	-
40°C	1.87	40.6
45°C	1.93	45.1
60°C	1.97	48.1
65°C	2.09	57.1
85°C	2.15	61.7

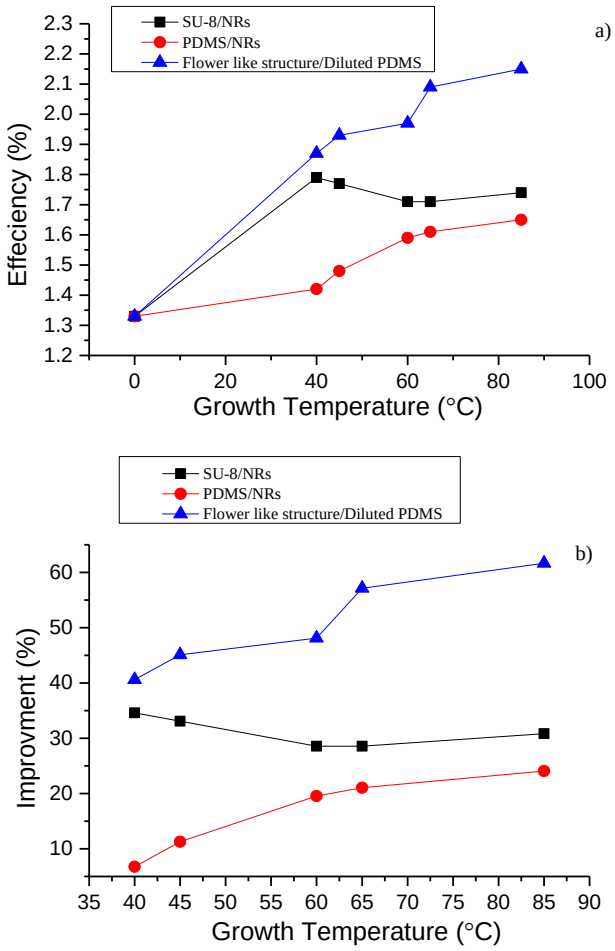

Figure 95. The effect of the three ZnO nanostructures on CZTS solar cell. a) Efficiency and b) resulted improvement in percentage.

Table 14 and Figure 95 exhibit the gradual improvement from the bare CZTS solar cell to the nanostructures/CZTS. Figure 95 a). It is apparent that when using the wet lift-off method (ZnO NRs/SU-8), the efficiency increased dramatically from 1.3% to 1.79%. However, the ZnO NRs/PDMS exhibited a trend in the device behaviour, where the efficiency increased from 1.3% for bare solar cell to 1.65% for T_{growth} = 85°C. Finally, a significant increase in device performance is shown when the flower like structure was placed on the solar cell. This structure demonstrated an efficiency increase from 1.3% to 2.15%. Figure 95 b), the highest device behaviour improvement for the ZnO NRs/SU-8, ZnO NRs/PDMS and flower like/diluted PDMS was obtained at 35%, 24% and 62% respectively. Figure 97 and Table 15 showed acceptable values of Jsc after being extracted from the measured EQE.

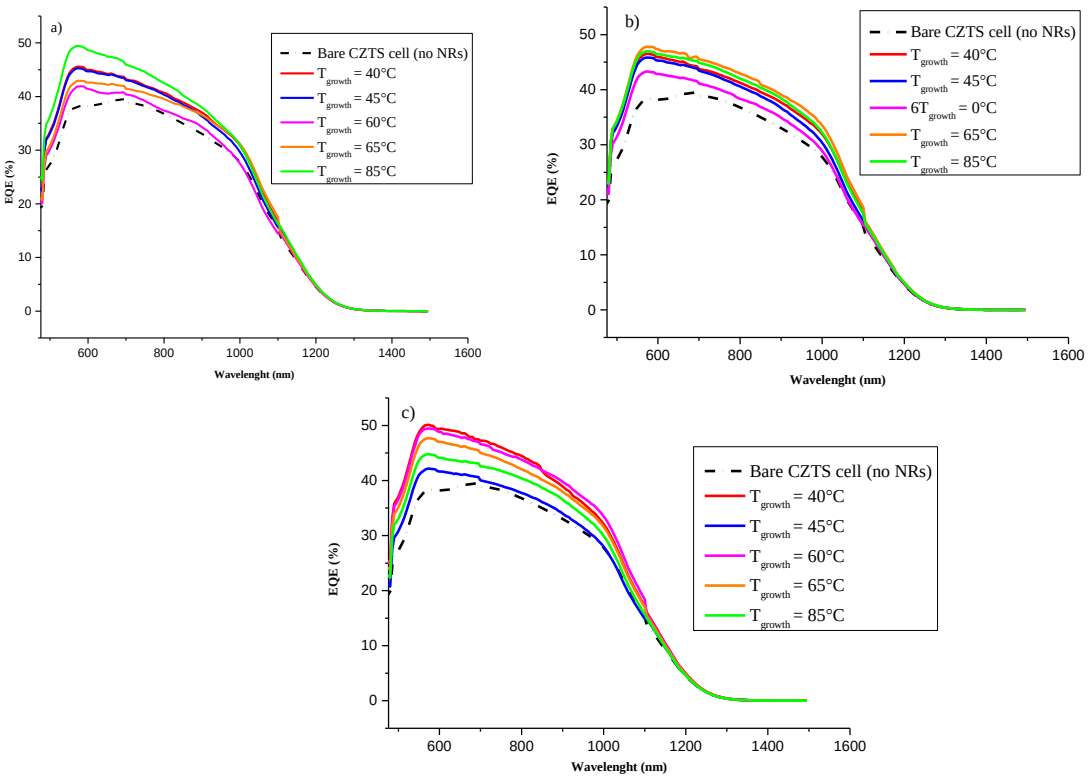

Figure. 96. The external quantum efficiency (EQE) for CZTS solar cell with and without NRs using different Tgrowth. a) ZnO NRs/SU-8, b) ZnO NRs/PDMS and c) flower like/diluted PDMS.

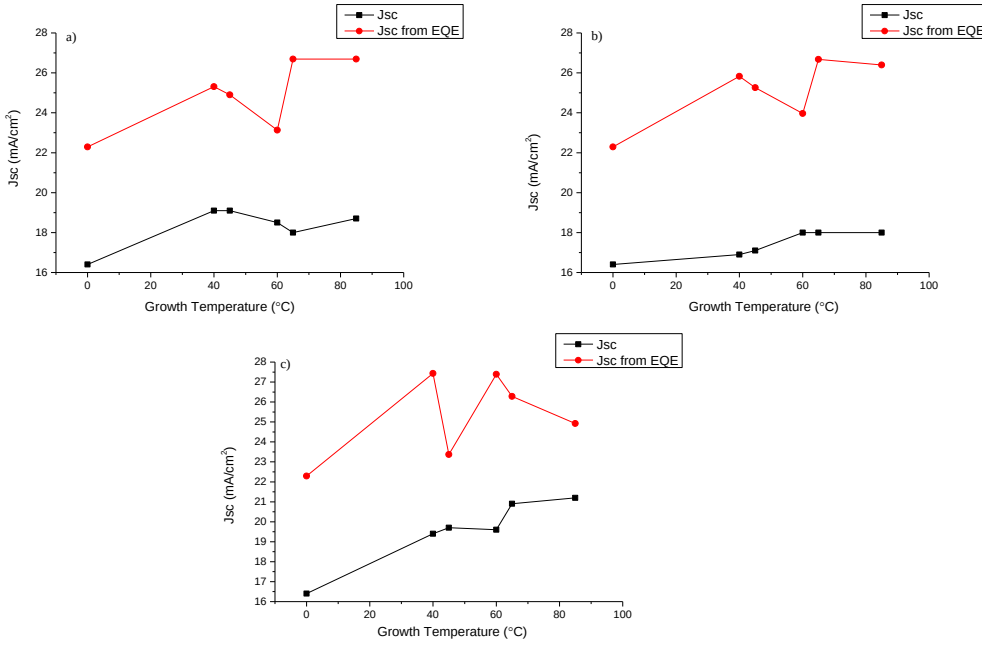

Figure 97. Jsc extracted form EQE for CZTS solar cell. a) ZnO NRs/SU-8, b) ZnO NRs/PDMS and c) flower like/diluted PDMS.

Table 15. Jsc extracted from EQE

ZnO NRs/SU-8 structure		
T_{growth} (°C)	**J_{sc} (mA/cm^2)**	**J_{sc} (mA/cm^2) from EQE**
No NRs	16.4	22.3
40°C	19.1	25.3
45°C	19.1	24.9
60°C	18.5	23.1
65°C	18.0	26.7
85°C	18.7	26.7
ZnO NRs/PDMS structure		
T_{growth} (°C)	**J_{sc} (mA/cm^2)**	**J_{sc} (mA/cm^2) from EQE**
No NRs	16.4	22.3
40°C	16.9	25.8
45°C	17.1	25.3
60°C	18	23.9
65°C	18	26.7
85°C	18	26.4
Flower like/PDMS structure		
T_{growth} (°C)	**J_{sc} (mA/cm^2)**	**J_{sc} (mA/cm^2) from EQE**
No NRs	16.4	22.3
40°C	19.4	27.4
45°C	19.7	23.4
60°C	19.6	27.4
65°C	21	26.3
85°C	21.2	24.9

The EQE spectra of the three mentioned nanostructures on the CZTS solar cell is shown in Figures 96 a), 96 b) and 96 c) respectively. It can be observed that the EQE has increased from 39% (bare CZTS cell) to roughly 50% (after the addition of nanostructures). The three methods showed less ideal EQE curves with regard to longer wavelengths. This was due to the recombination losses. In 96 a), NRs grown at 85°C exhibited the highest value of approximately 50% EQE. While, in Figure 96 b), the highest EQE was obtained for 65°C. Finally, for Figure 96 c), 40°C and 60°C revealed EQE of about 49%. The variations in EQE values are derived from the different nanostructures regarding length and diameter, as well as their density. The resultant step at approximately 475nm could be due to the artefact arising from the detector changes.

5.2 Conclusion

In this chapter, the release of the ZnO nanostructures has been successfully achieved by means of three diverse methods (ZnO NRs/SU-8, ZnO NRs/PDMS and ZnO flower-like/diluted PDMS). The morphology of the nanostructures exhibited different structures for each method. The presented experiments portray new approaches with regards to wet and dry releasing of ZnO NRs grown on releasable layers (SU-8 and PDMS). Therefore, releasing the structures (i.e. SU-8/ZnO NRs, PDMS/ZnO NRs and ZnO flower like/diluted PDMS) were successfully achieved, released from the glass substrate and transferred to a flexible Kapton and PET substrates as the initial step. The experiments showed that for wet lift-off, a direct SU-8 detaching from the initial glass substrate can be achieved through the use of the sacrificial layer (Omnicoat in this case, which will facilitate the SU-8 lift-off) that is coated between the substrate and the SU-8 layer. In addition, peeling the PDMS layer easily from its substrate can be achieved by direct peeling of the PDMS layer without the assistance of any remover solutions (in comparison to the wet lift off). For the wet lift-off, the NRs were successfully transferred to the PET substrate and form peel off the NRs were kept on PDMS which was used as a flexible substrate in this case. The main target of enhancing the performance of different solar cells was clearly seen by using the three methods. In comparison to the pure SU-8 photoresists, nanocomposite photoresist structures demonstrated fewer cracks and low stress as the nanocomposite type has more sensitivity. Elaborating this type of photoresist was a result of overcoming the stress, cracks, shrinkage and adhesion problems that the pure SU-8 produces. Different studies stated that the transparency of the composites remains and moreover, that it is maintained, has better sensitivity, lower thermal expansion and lower internal stress, whilst the improved adhesion and mechanical properties were shown [281, 307]. The findings obtained from this study offer a simple

method for lift-off ZnO NRs (and subsequent stack of layers) using low-cost facilities, at low growth temperatures. This will open a new path in decoupling the fabrication of functional structures and the use of temperature sensitive flexible substrates, such as wearable fabrics. Additionally, the demonstrated structure provides less fabrication materials/steps compared to other studies [308, 309].

Chapter 6 EXTREMELY THIN ABSORBER (ETA) SOLAR CELL

The ability to capture the incident light photons represents the key characteristics of any photovoltaic device. The reflected light is basically uncaptured light in which the device will not be able to capture it. Hence, reducing this reflectance effect will strongly enhance the light capturing and therefore increase the functionality and efficiency of the device. With regards to solar-based cells, less is more. In other words, the less reflected sunlight from their surfaces the more energy generation can be achieved. Thus, fixing the reflectivity issue is by way of using the anti-reflective coated layers. A combination of light trapping effects and developed areal density of any semiconductor junction (because of the enhanced NRs surface area) are expected to improve spectral and photocurrent response [ref]. Kartopu et al. [1] demonstrated study on CdTe –NRs based photovoltaic, other factors can affect the performance of the solar cells and furthermore, that it is not straightforward to depend on both factors mentioned above in regard to improving the fabricated solar cell performance, seeing as other reasons can contribute to that too, such as (technical issues associated with deposition uniformity and material properties) and as a consequence, a poor or even non-functional 1D PV device is the outcome [157]. Theoretically higher efficiencies can be provided by ETA cells than planar cells by using low quality absorbers, however, this can be obtained when a nanostructure morphology is applied and suitably controlled [310]. Basically, electrons and holes are generated when

illuminating ETA cells and would be separated through the respective interfaces faster than the recombination of the bulk. Careful selection of the material should be followed in order to provide and obtain suitable energy offsets for charge transfer. At the interfaces, transporting the separated charges to the opposite contact must be achieved faster than recombination [310].

The main target of using ultra-thin absorbers is to achieve high light scattering. In other words, increasing light diffusion L_{diff} in the bare absorber material (bare absorber is the absorber that does not include any nanostructure). An effective diffusion length can be obtained in relation to the light, which is considered one of the most significant characteristics of the nanocomposite [170]. On the one hand, in inorganic nanostructure solar cells, the correct combination of materials with different lengths and scales is required to achieve high photocurrent. These factors are for example ($L_{diff,}$ light drifting l_{drift}, local absorber layer thickness d_{local} etc). Conversely, the appropriate combination of device material is necessary to reduce losses in solar cell and photovoltage which can be as a result of the potential drop as well as recombination that occurs at the surface of the solar cell [170]. The thickness of the local absorber layer d_{local} must not be smaller than the tunnelling length d_{tunnel}. This is to reduce the effect of the shunts between the hole conductors and transparent electron [170].

In this chapter, the results of the fabricated ETA solar cells are reported**.** The cell structure was (ITO/ZnO seed/ZnO NRs/CdS/CZTS/P3HT/gold contact*).* A flat cell (no NRs included in the structure) was applied to act as a reference sample. In order to validate the seed layer thickness effect on the ZnO NRs, the ETA cells were fabricated with five different ZnO seed layers which has an impact of the resulted morphology. Figure 89 represents the ETA cell structure fabricated in this project. The annealing method (to anneal the ZnO NRs immediately after deposition and prior to the final ETA fabrication step) was analysed. NRs annealed using carbolite tube furnace.

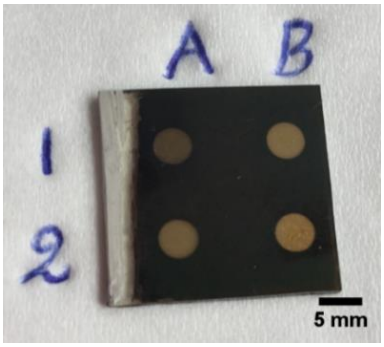

Figure 98 an example of the fabricated ETA cell structure (ITO/ZnO seed/ZnO NRs/CdS/CZTS/P3HT/gold contact).

Therefore, this chapter deals with full details with regard to the fabricated ETA cells. Starting from the ZnO hydrothermal growth and ending with the gold contact deposition as the final step in ETA solar cell fabrication. This solar cell is composed of direct ZnO growth on indium tin oxide (ITO) substrate, ZnO seed/ZnO NRs, /CdS/CZTS/P3HT and includes sputtered gold as the back contact. The NRs were characterised by SEM, XRD, and UV-VIS spectrometry. NRs annealing has been studied and its effect on the ETA cell performance was also investigated. The completed ETA solar cells were characterised by current-voltage (I-V) and external quantum efficiency (EQE). More details will be provided on the observations related to the materials and devices used will be reported in this chapter.

6.1 Results and Discussion

6.1.1 CdS deposition on non-annealed ZnO NRs

The ZnO NRs used in this process to fabricate the targeted ETA cells were grown using (T_{growth} = 65°C). These nanostructures will be annealed at a later stage prior to the deposition the following layers for a complete ETA solar cell. The target for growing ZnO NRs on ITO-coated glass is to form a 3D nanostructure scaffolding from the ZnO nanorod array, which would maintain electron collection from the absorber and transport through the high quality crystal structure within the NR. These structure form the basis to fabricate ETA solar cell devices. The NRs were not strong enough during the CdS deposition, therefore they were dissolved (more details on this will be provided in the next sections). Additionally, it was necessary to treat the NRs before any further depositions, so as to improve the structural properties of the NRs. The process of annealing is one of the most important methods that can have a major impact on ZnO nanostructure properties. The annealing process, on the other hand, can lead to remove surface defects and contamination as well as modify the surface absorption and desorption of oxygen molecules, thus improving the ZnO surface condition [311]. Panda reported that after annealing, the ZnO sensor device increased its sensitivity to UV light. The concentration of defects in ZnO NR arrays undergoes a considerable change through annealing. On the other hand, annealing, as a surface treatment process, can remove surface defects and contamination and modify oxygen molecules ' surface absorption and desorption, thereby improving oxygen molecules [312].

Post-annealing thermal treatment was carried out using tube furnaces. The NRs were annealed in at 400°C for 1 hour and the samples cooled to room temperature. The morphologies of the grown ZnO in addition to the ZnO NRs/CdS were investigated by

using scanning electron microscopy (SEM). ITO-coated glass was the superstrate used to grow both the structures mentioned (bare ZnO NRs and ZnO NRs/CdS). Superstrate term refers to a configuration of solar cells where the glass substrate is used not just as a supporting structure however also as an illumination window and as part of the encapsulation. The glass is "above" the actual solar cell during the operation. ZnO NRs shown in chapter 4 using zinc nitrate were used for CdS deposition.

6.1.1.1 Scanning electron microscopy (SEM) and Energy-dispersive X-ray spectroscopy (EDS)

The SEM images in figure 99 illustrate the morphological structure of non-annealed ZnO NRs coated with CdS. After CdS deposition by CBD, a deformation of the ZnO NRs was observed. When considering the complementary properties of ZnO and CdS, both materials have been coupled and used with each other as a hybrid nanostructure composite in order to exhibit the extended absorption of the solar spectrum besides improving the photogenerated electron-hole pairs separation. Owing to the high electron mobility of the ZnO, their 1D structure can be used in functioning as a highway with the aim of facilitating the transportation of separated photocarriers. Thus, depositing controllable qualities of CdS on 1D ZnO NRs is desirable due to the excellent photoconductivity, enlarged interface area and good electron mobility.

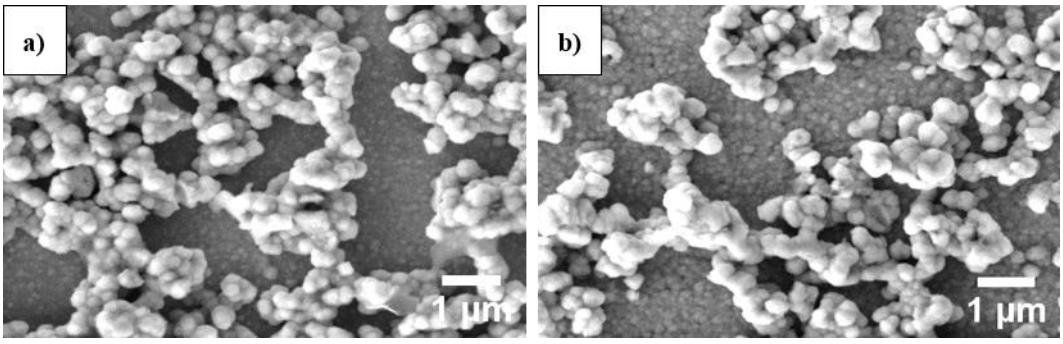

Figure 99. Top-view of SEM images of CdS deposited on ZnO NRs. a) 27nm seed sample and b) 130nm seed sample.

From Figure 99, it can be clearly noted that the NRs shape was not retained during the CdS deposition step. Hence, almost the entire structure was dissolved. This due to the ZnO NRs structure that might not be strong enough to be used for CdS deposition. The deformation of the NRs is significantly noticeable. Therefore, annealing can improve the ZnO crystal structure. Consequently, the crucial role that ZnO plays with regard to the ETA cell (i.e. spaced NR array as scaffolding) will not be provided due to its complete deformation. As for the ETA cells, the main role of the ZnO NRs is to provide an open structure which in turn will allow the precursors penetration during the absorber layer deposition step [313]. The absence of Zn is confirmed by chemical or elemental characterisation (EDS), as shown in Figure 100.

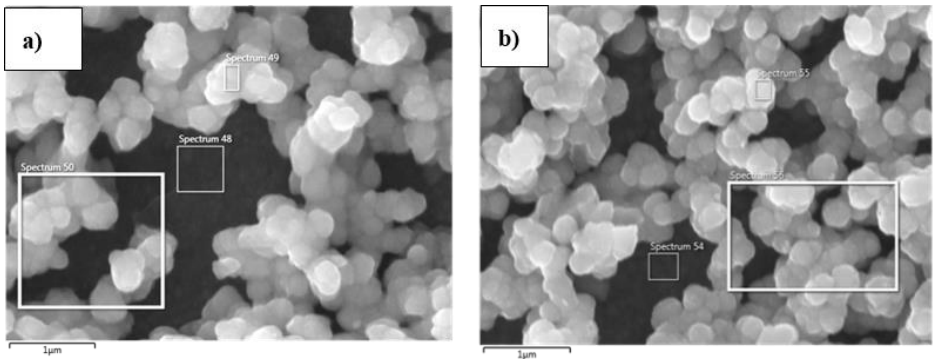

Figure 100. An example of the EDS analysis and the different scanned areas on ZnO NRs/CdS a) 27nm seed sample and b) 130nm seed sample.

As shown in the images, three different areas were scanned. These values are taken from the largest scanned area (squares shown). It was found that, the atomic percentage of Zn after CdS was significantly low for all samples approximately 0.1%. This can be clearly observed in the table presented here. O was almost the dominant element for each sample and Zn was almost not present. In terms of dense NRs, as the NRs density increases, the surface area will decrease. Thus, it will prevent the coated layer on the (nanorods NRs) from fully penetrating the entire ZnO films [314]. Table 16 presents the observed elemental values for the ZnO NRs/CdS sample.

Table 16. ZnO NRs/CdS elemental composition

Sample	Atomic (%)					
	Zn	**O**	**In**	**Sn**	**Cd**	**S**
T_{27nm}	0.1	43.1	14.9	2.9	18.3	20.8
T_{130nm}	0.1	26.9	13.5	2.3	26.9	30.5

6.1.2 **The annealed ZnO NRs**

After the evaluation of the first fabricated ETA cells, it was necessary to find a suitable annealing treatment for the ZnO NRs. In the first fabricated ETA cell, maintaining and retaining the NRs was obviously not successful when the samples were non-annealed. Therefore, in the following results section, more information and details will be provided on the annealing treatment. Here, the same steps were followed in growing the NRs to keep the investigation systematic. Morphological, elemental, structural and optical properties of the as grown and annealed NRs will be provided in the upcoming sections, besides the I-V and EQE characteristics for the ETA cells.

6.1.2.1 **Scanning electron microscopy (SEM)**

The ZnO NRs SEM micrograph for as grown and annealed NRs are shown in figure108. Highly densely backed NRs was observed. Annealing the NRs has almost no influence on the morphological structure of all the samples. This was what Pan et al also observed. They stated that the size and shape of the NRs was almost the same in both cases (before and after annealing) [315].

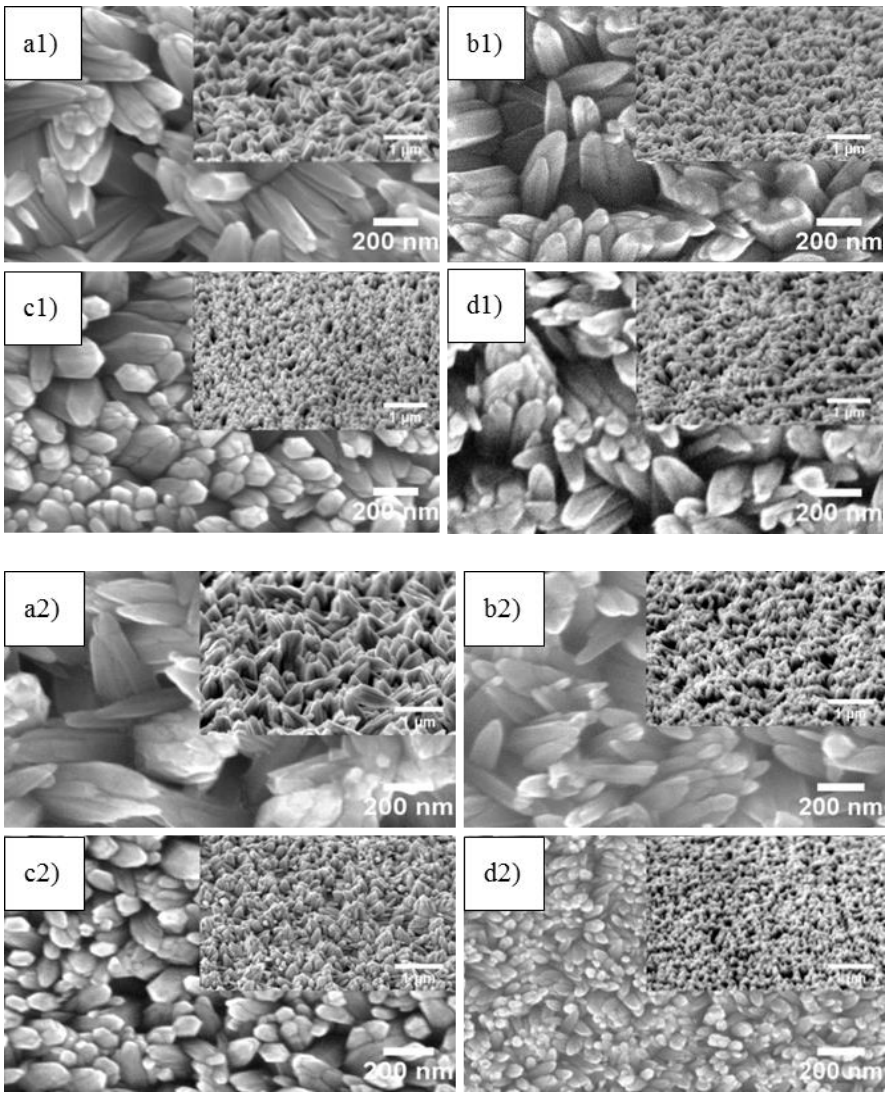

Figure 101. Top-view and tilted SEM images for ZnO NRs grown at 65C using four different seed thicknesses with 27nm, 63nm, 70nm and 130nm respectively. (a1-d1) before annealing and (a2-d2) after annealing.

6.1.2.2 **Energy-dispersive X-ray spectroscopy (EDS)**

EDS was also accomplished for as grown ZnO NRs. Figure 103 shows an example of the scanned areas on the as grown ZnO NRs. From Figure 103, the images resulting from the EDS denoted that for the as grown ZnO NRs for all samples, the structures are composed of Zn, O. The In and Sn are attributed to the used ITO-coated glass substrate. No other impurities were observed or found and the all presented samples were nearly pure.

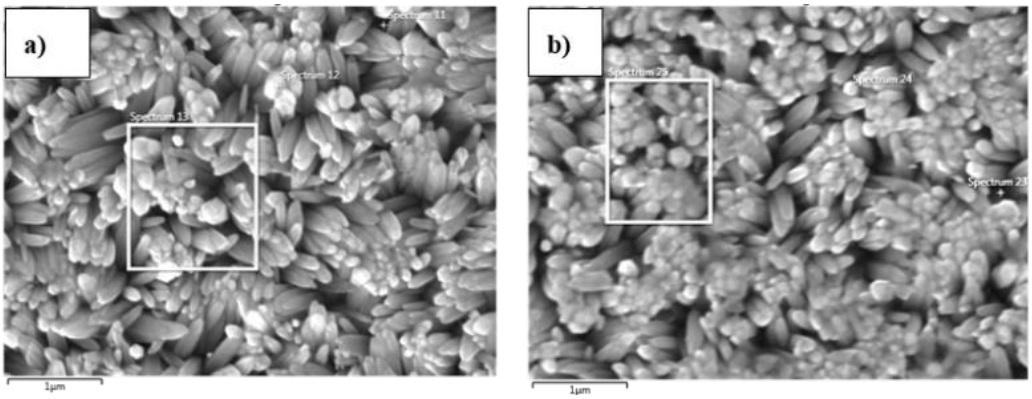

Figure 102. An example of the EDS analysis and the different scanned areas on a) 27nm seed and b) 70nm seed sample

All presented values were chosen from the largest scanned area on each sample (squares shown). As shown in Table 17, the obtained values of the elements are more or less the same with small differences which can be unpronounced.

Table 17. Chemical composition of as grown ZnO NRs obtained from EDS analysis

	Atomic (%)		
Sample (seed thickness nm)	**Zn**	**O**	**Zn/O (atm %)**
27nm	32.7	67.3	0.485
63nm	34.9	65.1	0.536
70nm	28.57	71.25	0.403
130nm	34.75	65.25	0.535

6.1.2.3 **X-ray diffraction analysis**

The XRD analysis was investigated for the grown NRs (before and after annealing). Figure 104 reveals the XRD patterns of the grown ZnO NRs using T_{growth} = 65ºC. a) Indicates the NRs before annealing (as deposited) and after annealing in at 400ºC for 1 hour. It can be seen that the resulting ZnO NRs structure on the ITO showed wurtzite-structured (hexagonal) ZnO and preferred growth along (002) direction. For both

processes (annealed and non-annealed NRs), the surface appears uniform and smooth with variations in the resulting high-density NRs.

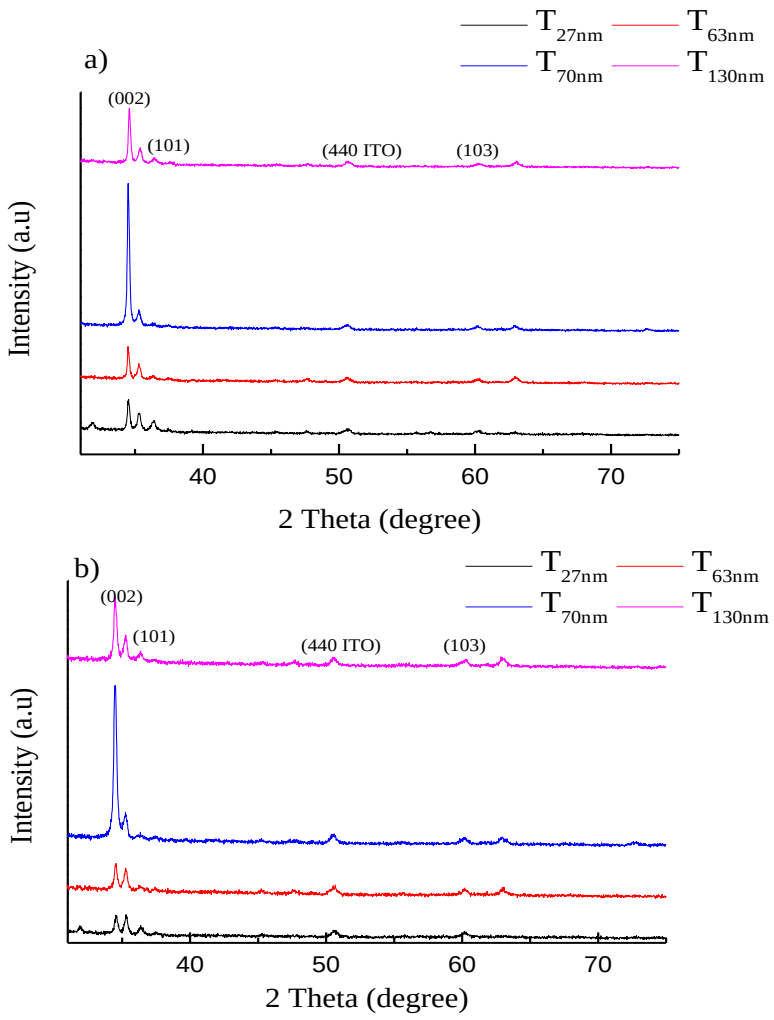

Figure 103 X-ray diffraction patterns of ZnO NRs grown at 65oC with various ZnO seed thicknesses. a) Before annealing and b) after annealing.

From figure it can be clearly seen that almost similar trend has been observed on the ZnO NRs before and after annealing. Some changes in the structural parameters of the as-deposited and post-annealed NRs. The effect of annealing on the NRs (002) intensity and 2θ is clearly seen. This is a result of changes in the crystal size which exhibited a different trend of crystal size values after annealing the NRs. These variations on the structural parameters on the ZnO NRs before and after annealing illustrates the strong and significant influence of the annealing treatment. It is known that, different annealing

temperatures are used to anneal the NRs structure, ranging from 300°C-500°C. It was found that 400°C is the optimum annealing temperature. Moreover point defects at the oxygen vacancies will be the result [311]. What is occurring exactly during the vacuum annealing is that. It can be summarised as follows [316]:

1. There is surface oxygen desorption as well as band bending to a lesser degree compared to the non-annealed samples.
2. Zn or impurities ions migration, which is a similar effect that is produced by oxygen annealing, although to a lesser extent.
3. After annealing in the vacuum, there is a significant reduction in the depletion layer and a flat band.

When using the method of annealing under protective vacuum or gas, no undesirable surface reaction or oxidation will occur which will cause the surface to be maintained. This is one of the positive features of this annealing method. A further advantage of annealing in a vacuum is that the process of heating and cooling can be controlled in a better way. This is an advantageous issue when considering the dimensions (like dimensional stability and shape of the targeted product). Moreover, after vacuum annealing, argon or overpressure nitrogen can be used in cooling. Hence, faster cooling can be obtained in contrast to annealing using argon.

6.1.2.4 **UV-VIS-NIR spectroscopy**

Optical transmittance of the grown ZnO NRs prepared on different seed layer thicknesses in the wavelength range 300-1400nm (before and after annealing) are shown in Figure 105. It is observed that by increasing the ZnO seed thickness, the spectral range 300-1400nm was more or less similar for all samples, thus almost no changes were observed for different seed layer. In terms of scattered light for both case before and after annealing, the thinnest seed thickness showed the highest scattered light. The rest of the samples

showed almost similar trend. This behaviour can be a result of the increased thickness of the seed layer, seeing as the seed layer has a strong influence on the resulting NRs morphology and the corresponding crystal size [199].

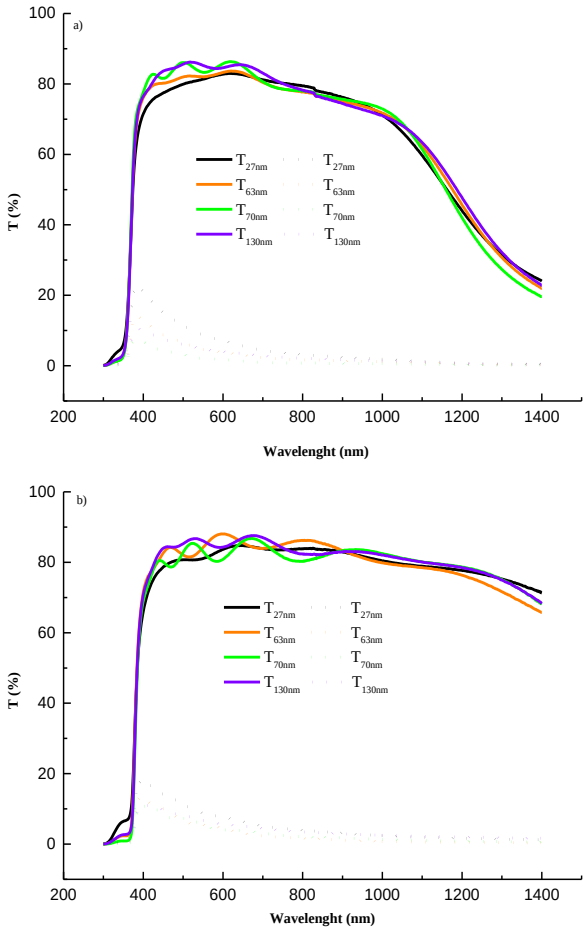

Figure 104. UV-VIS spectra of ZnO NRs grown at 65°C. a) As deposited NRs and b) after annealing the NRs.

Regarding the results presented, the significant effect on the annealing process can be clearly seen. For as deposited NRs (Figure 105 a), the transmitted light of the NRs was at approximately 90% in the range 400nm-1100nm, whereas the scattered light of the NRs was not as strong as it showed roughly 20% in the 400nm range. The different behaviour of the light in all the samples is due to the different seed thicknesses applied. The thinnest seed layer deposited at 5min demonstrated the highest scattering light and lowest transmittance. Almost the same trend was observed for the remainder of the samples. The

highest scattering can be attributed to morphology which revealed NRs with resulted diameter and spacing in which the scattering of the light was enhanced. The reduction in the transmittance of the other samples might be due to the reduction in the density of grain boundaries due to the grain growth, seeing that this effect leads to a reduction in the optical scattering of the light in the visible range.

After annealing, a significant improvement was obtained concerning the transmitted light in almost the full range, 400nm-1400nm. However, the more transmitted light, the less scattered light. This can be seen in the scatter light behaviour of the sample. As, prior to annealing the highest scattering was at around 20% and moreover, due to the annealing process, this range was dramatically reduced by almost to 15%. This reduction in scattered light can be as a consequence of the reduction in the particle size. Additionally, from the point view of the XRD and the calculated parameters, the crystal size of these sample are having different values. Hence, it can be seen that the thickest seed layer samples were showing the lowest scattered light. The thinnest sample (T_{27nm}) had the highest scattered light despite the bulk ZnO (34.375°) not being observed, which was considered as zero here.

6.1.2.5 CdS deposition on annealed ZnO NRs

6.1.2.6 Scanning electron microscopy (SEM) and Energy-dispersive X-ray spectroscopy (EDS)

After the investigation of ZnO NRs at two different cases (as grown and annealed) NRs, the subsequent step is to deposit CdS on the annealed NRs to study and address the effect of the annealing process on ZnO NRs. The morphological structure shown in Figure 106 is for the annealed ZnO NRs/CdS structure. Inset is tilted view. From the top view it can be seen that the NRs were partially retained and maintained compared to non-annealed NRs. The CdS layer was almost entirely covering the NRs. Hence, the SEM top-view and tilted SEM images showed that the CdS was deposited with a homogenous distribution on ZnO NRs. When CdS is deposited using the conventional electrodeposition method. The NRs array will be coated easily and quickly by the CdS layer, while at the same time it prevents any subsequent deposition on the bottom region. Besides, the NRs will function as a scaffold for enlarged interfaces to be provided with CdS nanocrystals on the bottom region.

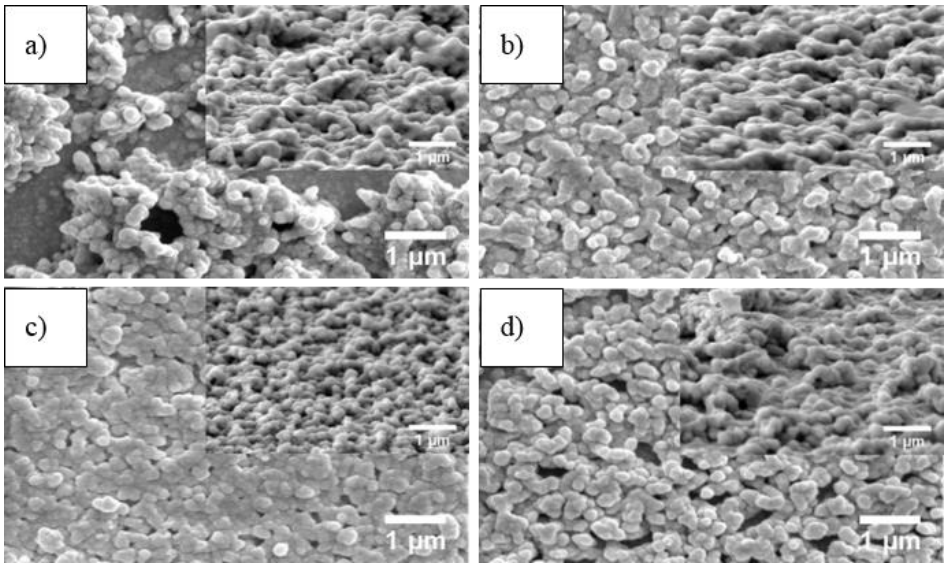

Figure 105. Top-view and tilted SEM images of CdS/ZnO NRs. a) 27nm seed sample, b) 63nm seed sample, c) 70nm seed sample and d) 130nm seed sample.

As shown in Figure 106 a), after depositing CdS, a densely backed structure was observed for all samples and the top SEM view showed full coverage of the CdS on ZnO NRs. Almost the same morphology was obtained for T_{27nm}, T_{63nm} and T_{130nm}, whereas the T_{70nm} sample exhibited different behaviour as it is close to a continuous film and the spacing in-between the NRs was significantly reduced. This is might possibly be due to the surface roughness. An example on ZnO NRs/CdS cross section is shown in Figure 107 .The deformation of the NRs can clearly be seen. Figure 107 b) showed full damage of the NRs. In relation to the EDS analysis, the images and Table 18 show the obtained atomic values of the existing elements on each sample.

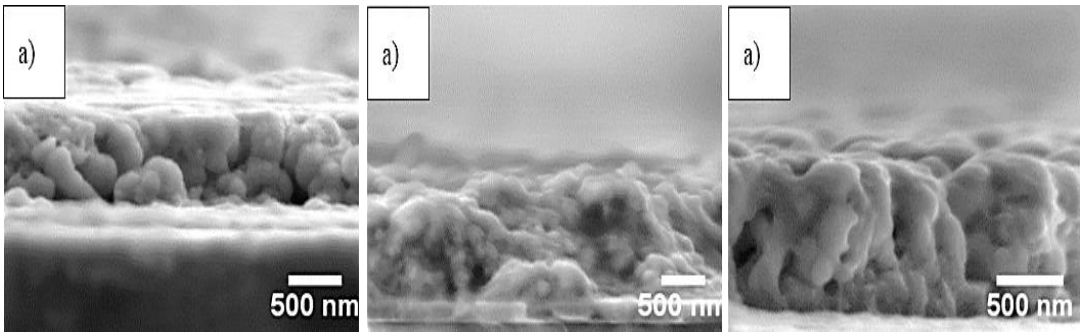

Figure 106. Examples of cross-section SEM images for CdS/ZnO a) 27nm seed sample, b) 63nm seed sample and c) 70nm seed sample.

It can be clearly seen that the NRs after CdS deposition were partially dissolved and remained partially intact after the CdS was deposited. This also confirmed the cross-sectional analysis of the CdS/NRs. In this case, it was ascertained that the NRs shape was not retained during the CDB process. Although the NRs were partially deformed, annealing NRs demonstrated better results on maintaining the shape and the NRs morphology. Hence, further investigation on annealing time and temperature should contribute to improving the stability of the structure during the CdS wet chemical process.

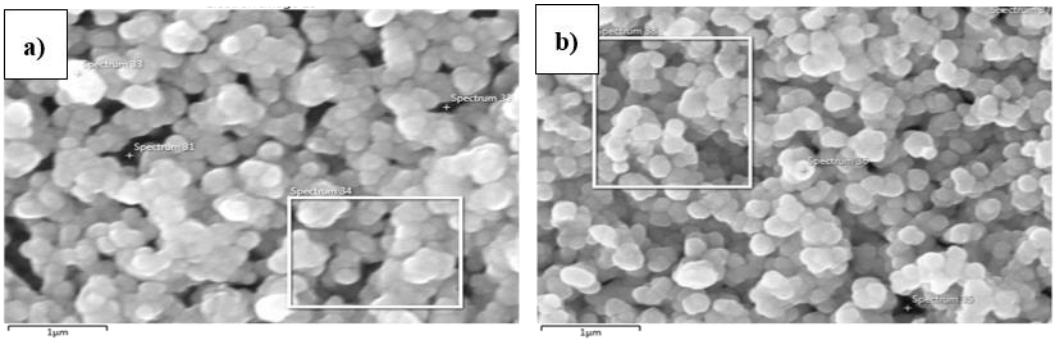

Figure 107. EDS obtained from ZnO NRs/CdS. A) 63nm seed sample and b) 130nm seed sample.

It was found that the Zn was almost low in all samples. The highest atomic percentage of Zn was roughly 10.15 for T_{27nm} seed thickness sample. The other samples showed virtually lower atomic values of ZnO after the CdS deposition. The squares shown in the above EDS images (for the T_{63nm} sample) and the other samples (which are not presented here) showed that the area had 0 Zn. This denotes that during the CBD deposition process, the ZnO NRs samples were not fully coated and covered with CdS.

Table 18. The percentage elemental composition of ZnO NRs/CdS

Sample	**Atomic (%)**			
	Zn	**O**	**Cd**	**S**
T_{27nm}	10.15	29.35	28.4	32.1
T_{63nm}	8	37.1	26	28.9
T_{70nm}	7.35	25.05	31.9	35.7
T_{130nm}	7.2	25.7	31.6	35.5

One of the advantages of ZnO is that it has higher carrier mobility. Thus, adding a layer of CdS with ZnO as a visible active layer will enhance the process of light absorption [317]. Cadmium sulphide (CdS) is an II–VI semiconductor type that comprises a 2.4 eV direct band gap as well as high absorbance in the violet to cyan region. This semiconductor is mentioned as one of the most appropriate visible sensitizers with ZnO [318], as both materials (CdS and ZnO) have the same structure and therefore, good

compatibility [318]. CdS is an excellent candidate to construct core/shell heterostructures including 1D core/shell with ZnO as the most promising materials for photocatalytic and photovoltaic applications [318].

6.1.3 **I-V characteristics**

Figure 109 shows the current density ZnO NRs ETA cell. Four Different solar cell devices were characterised, with ZnO seed thicknesses of T_{27nm}, T_{63nm}, T_{70nm} and T_{130nm} respectively. I-V measurements were carried out for the different fabricated ETA cells. A reference sample (with just ZnO seed layer and without ZnO NRs) was also fabricated. For the reference sample, no photo-generation was observed (not included in the figure). Although the NRs were not fully retained during the CdS deposition, the T_{27nm} ETA cells with partially dissolved NRs gave approximately (0.02%) efficiency η, (0.15 mA/cm^2) J_{sc} and (0.05 mV) V_{oc} and (27.46 %) FF for the T_{27nm} sample. For T_{130nm}, the extracted efficiency η was approximately 0.01% whereas FF exhibited value of (0.38 mA/cm^2) J_{sc} and (0.097 mV) V_{oc} and (25.61 %) FF. No photo-generation was absorbed for other samples. Therefore, recombination probability was significantly reduced [170].

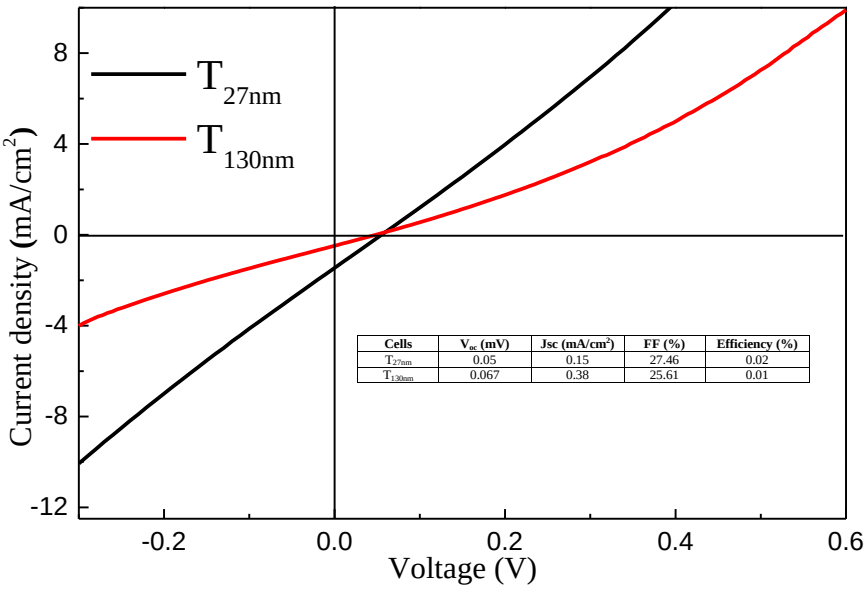

Figure 108.Current density vs voltage of the fabricated ETA solar cells.

These efficiency values are relatively low compared to what was reported in [157]. However, according to the EDS study, these low efficiencies are attributed to the Zn which was partially dissolved after CdS deposition. Positively, these low efficiencies are promising and further treatment of ZnO NRs will definitely improve the overall ETA cells. The optical and specifically, the structural properties of the ZnO NRs/CdS core/shell can be improved by pre-treating the as grown ZnO NRs. The ZnO NRs/CdS core shell appears to be a successful solution for the ETA cell due to its remarkable features and properties [319]. Moreover, the large series resistance has a remarkable effect on reducing the Jsc values. The power loses in the fabricated solar cells are caused by the shunt resistance, which occurred by providing an alternate current path to the light generated current. This diversion leads to a reduction in the current amount flowing in the cell junction, besides reducing the Voc and accordingly, the fill factor FF of the solar cell. These parameters are relatively low in contrast to the reported parameters by [314].

6.1.4 **EQE data and discussion**

Figure 110 shows the measured EQE for the fabricated cells. It can be seen that there is an increase in the EQE within the 350nm-500nm spectra region of the measured samples. Whereas no EQE was observed in the reference sample. The highest obtained EQE was roughly 20% in the 300nm-500nm spectra region for ETA cell grown in using the thinnest ZnO seed layer (which is T_{27nm} seed). This might be due to the J_{sc} and V_{oc} values obtained from these cells. It is worth mentioning that the light scattering effect might not be the principal factor that effects the performance of the solar cell, as the NRs were partially dissolved during the CdS deposition step, as previously confirmed by SEM images.

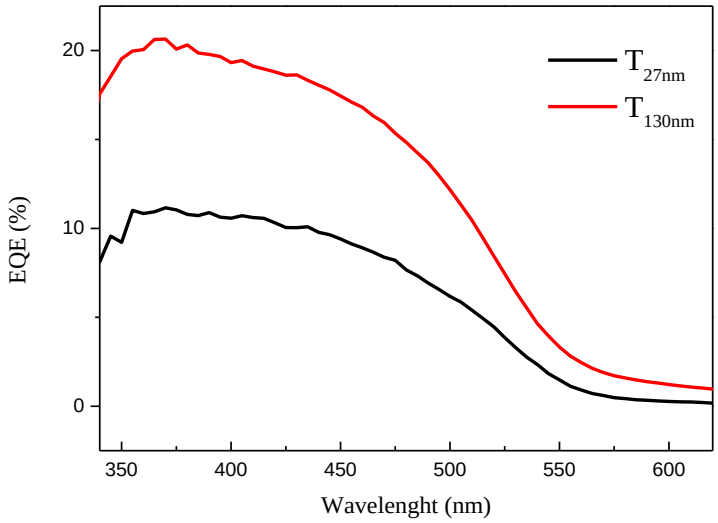

Figure 109. EQE for the fabricated ETA cells.

This might be partly because of the CZTS being too thin or having too much carrier recombination. EQE depends on the light absorption as well as the charge collection. After absorbing the photon and generating the electron-holes pair, a separation of these charges must take place and eventually must be collected at the junction of the used semiconductor. A good choice of solar cell material signifies that charge recombination can be avoided and thus, a drop in EQE.

6.2 **Conclusion**

In this investigation, a hydrothermal-gown ZnO NRs with the aim of fabricating ETA cells was presented. The NRs were grown using (T_{growth} = 65°C). The growth process that is used to create the NRs is a wet-chemical process. The effect of CBD deposition on annealed and non-annealed NRs was studied. Moreover, the effect of annealing the NRs at $T_{annealing}$ = 400°C for 1-hour was studied. Characterization and elaboration of ZnO NRs was performed. The grown NRs displayed an obvious hexagonal wurtzite structure and were grown preferentially along the *c*-axis (002), which clearly indicates that the NRs are

perpendicular to the used substrate. The SEM morphology revealed highly packed nanorods for almost all represented samples. The maximum power conversion achieved for ETA cells was roughly 0.02%. As shown in the morphology results, retaining the CdS layer during the CBD wet chemical process was a challenging point. Hence, further investigation and improvement needs to be followed to avoid this problem. Thus, further ambitions for developing possible functionalising ETA cell routes could possibly be by using the dry deposition technique to grow the CdS thin film instead of the CBD method.

Chapter 7 CONCLUSIONS AND FUTURE WORK

7.1 Thesis summary

There is still a lot of efforts about the feasibility and efficiency of using ZnO nanostructures solar cells as one of the leading energy sources in the real world on a large industrial scale. However, during this project, the experimental data of ZnO nanostructures have shown that, especially in the field of renewable energy, ZnO nanostructures have great possibilities in improving the overall device performance. In this project, confirmed that hydrothermal synthesis of the ZnO nanostructures used in enhancing the solar cell performance has many advantages including the use of inexpensive production costs, lower reaction temperatures, less rigorous conditions of synthesis and processes simplicity. This thesis investigates and details ZnO nanostructures for photovoltaic applications. Specifically, two aspects of the fabrication were studied to investigate the effect of these nanostructures on different types of solar cells. These were, i) grown ZnO NRs by using two zinc nitrate and zinc chloride salts to fabricate ETA solar cells, ii) growing ZnO NRs on Omnicaot/SU-8 structure and growing ZnO NRs and flower-like structure on PDMS which then to be released from the initial substrate and this process is known as lift-off process. Different five T_{growth} = (40°C, 45°C, 60°C, 65°C and 85°C) have been used in both mentioned aspects. In chapter 4,

ZnO NRs were successfully synthesised on ITO-coated substrate by hydrothermal method. Throughout the reaction, the NRs had hexagonal structure for all used samples with variation in the resulted length and diameter. The influence of zinc salt and growth temperature on optical, compositional and structural properties were systematically studied. By changing the zinc salt and increasing the T_{growth}, it was found that, for zinc nitrate, the NRs had an average lengths and diameters ranging at (0.233μm-1146μm) and (59nm-165nm) respectively. Whereas, by using zinc chloride, the average lengths and diameters were ranging at (0.237μm-1093μm) and (55nm-150nm) respectively. Hence, the NRs showed an improvement on the resulted morphology as the T_{growth} increases. Regarding the optical properties, the NRs were studied to transmit from 60% of light and to over 80% of light for zinc nitrate and zinc chloride in the spectrum range of 400nm-1400nm. These findings factors were found to have a strong influence on haze, energy bandgap and structural parameters of ZnO NRs. In chapter 5, lift-off, the experimental investigation was performed in order to determine the possibility of achieving enhancing the solar cell performance based on ZnO nanostructures by providing light scattering effect. This process allows one to grow nanostructure on releasable and fixable substrates on Omnicaot/SU-8 structure (wet lift-off) and on PDMS layer (dry peel-off). By varying the T_{growth} ZnO nanostructure with different morphologies were achieved. It is important to understand and investigate the influence of these different morphologies regarding their length, diameter and density on the overall solar cells. In this chapter, efficiency enhancement was demonstrated when using the released ZnO nanostructures and mounted on different solar cells were used. It was indicated that, the ZnO nanostructures could be utilized to harvest more light by trapping the light for longer in the solar cells which in turn will improve its functionality. Moreover, it is relatively simple process. Lifted-off/peeled-off ZnO nanostructures will further extend the range of applications as it can be applied on different applications. Both methods showed an enhancement of solar

cells functionality. Wet lift-off showed an increasing η from 1.56% to 2.05% when GaAs solar cell is used. Whereas the same solar cell showed an efficiency η increasing to about 2.03% when using dry peel-off nanostructures. CTZS solar cell showed an increase in η from 1.3% to (1.79%, 1.65% and 2.15) for ZnO NRs/SU-8, ZnO NRs/PDMS and flower-like/diluted PDMS respectively. Moreover, EQE characteristic had been significantly improved after mounting SU-8/ZnO NRs, PDMS/ZnO NRs and diluted PDMS/flower-like structure respectively. In chapter 6, the resulted fabricated ETA solar cells were shown. ZnO NRs grown at T_{growth} = 65°C were embedded into ETA solar cells and the performance were studied. During the ETA solar cell fabrication, the NRs were not retained when depositing CdS. Hence annealing treatment was followed to avoid such effect. It was found that, relatively annealing NRs conditions yielded to get 0.02% and 0.01% efficiencies. Additionally, EQE was showed to about 20% and 10%. Although it is not high value however, as starting point this method will pave the way to get higher solar cell performance in the future.

7.2 **Suggestions for Future Work**

There is still a lot of scepticism regarding the ability of controlling the growth process of ZnO NRs. However, throughout this project, the data showed that, in particular in the field of renewable energy, ZnO NRs have great potential. Further point has to be taken into consideration is to control the seed layer as it is the main base of the growth process. It was confirmed that the ZnO NRs hydrothermal growth used in this research has many advantages including the inexpensive production costs, simplicity of processes, use of lower reaction temperatures and less rigorous conditions of synthesis. One of the key aspects for the solar cell applications is NRs with controllable density and desirable crystal growth direction. Thus the process will be more controlled and the desired density

if NRs can be achieved. For ETA solar cells fabrication, an optimised ZnO NRs annealing process for ETA cell is required to retain the NRs during CdS deposition. Another point to consider is controlling the amount of ammonium used in fabricating ETA solar cells this will reduce the NRs deformation effect during CdS deposition. Successful growth of ZnO nanorods with controlled surface morphology can be achieved by choosing the correct concentration of zinc acetate precursor, appropriate surfactant, repetition of growth, variance in ammonia concentration. Regarding lift-off process, although the goals of releasing ZnO nanostructures from the initial substrate have been achieved, it is recommended that the following future work be carried out in order to extend the work reported in this thesis. For wet lift-off process, preventing the growth solution to penetrate between the sacrificial layer and the support structural layer.

References

[1] F. Hussin, G. Issabayeva, and M. K. Aroua, "Solar photovoltaic applications: opportunities and challenges," *Reviews in Chemical Engineering,* vol. 34, no. 4, pp. 503-528, 2018.

[2] X. Li, "Diversification and localization of energy systems for sustainable development and energy security," *Energy policy,* vol. 33, no. 17, pp. 2237-2243, 2005.

[3] N. Kannan and D. Vakeesan, "Solar energy for future world:-A review," *Renewable and Sustainable Energy Reviews,* vol. 62, pp. 1092-1105, 2016.

[4] N. S. Lewis, "Powering the planet," *MRS Bulletin,* vol. 32, no. 10, pp. 808-820, 2007.

[5] R. E. Smalley, "Future global energy prosperity: the terawatt challenge," *Bulletin,* vol. 30, no. 6, pp. 412-417, 2005.

[6] P. Hersch and K. Zweibel, "Basic photovoltaic principles and methods," Solar Energy Research Inst., Golden, CO (USA)1982.

[7] K. Mertens, *Photovoltaics: Fundamentals, Technology, and Practice*. John Wiley & Sons, 2018.

[8] C. S. Solanki, *Solar photovoltaics: fundamentals, technologies and applications*. PHI Learning Pvt. Ltd., 2015.

[9] M. A. De Brito, L. P. Sampaio, L. G. Junior, and C. A. Canesin, "Research on photovoltaics: review, trends and perspectives," in *Power Electronics Conference (COBEP), 2011 Brazilian*, 2011, pp. 531-537: IEEE.

[10] V. A. Coleman and C. Jagadish, "Chapter 1 - Basic Properties and Applications of ZnO," in *Zinc Oxide Bulk, Thin Films and Nanostructures*, C. Jagadish and S. Pearton, Eds. Oxford: Elsevier Science Ltd, 2006, pp. 1-20.

[11] N. M Osman, O. Khalifa, H. A Albushra, M. E Mofdal, N. H Talib, and A. Eassa, "Synthesis, structural and optical properties of ZnO Nano-rods used in Solar Cells fabrication," 2019.

[12] A. B. Djurišić, X. Liu, and Y. H. Leung, "Zinc oxide films and nanomaterials for photovoltaic applications," physica status solidi (RRL)–*Rapid Research Letters,* vol. 8, no. 2, pp. 123-132, 2014.

[13] A. Pomorska, K. Wolski, M. Wytrwal-Sarna, A. Bernasik, and S. Zapotoczny, "Polymer brushes grafted from nanostructured zinc oxide layers – Spatially controlled decoration of nanorods," *European Polymer Journal,* vol. 112, pp. 186-194, 2019/03/01/ 2019.

[14] B. Seipel, A. Nadarajah, B. Wutzke, and R. Könenkamp, "Electrodeposition of ZnO nanorods in the presence of metal ions," *Materials Letters,* vol. 63, no. 9-10, pp. 736-738, 2009.

[15] R. Yang, "Ultra-violet lithography of thick photoresist for the applications in BioMEMS and micro optics," 2006.

[16] I. Hwang , "Enhancement of light absorption in photovoltaic devices using textured polydimethylsiloxane stickers," *ACS applied materials & interfaces,* vol. 9, no. 25, pp. 21276-21282, 2017.

[17] J. Wang, C. Gao, Y. Zhang, and Y. Wan, "Preparation and in vitro characterization of BC/PVA hydrogel composite for its potential use as artificial cornea biomaterial," *Materials Science and Engineering: C,* vol. 30, no. 1, pp. 214-218, 2010.

[18] K. H. Tsui., "Low-Cost, Flexible, and Self-Cleaning 3D Nanocone Anti-Reflection Films for High-Efficiency Photovoltaics," *Advanced Materials,* vol. 26, no. 18, pp. 2805-2811, 2014.

[19] P. A. Owusu and S. Asumadu-Sarkodie, "A review of renewable energy sources, sustainability issues and climate change mitigation," *Cogent Engineering,* vol. 3, no. 1, p. 1167990, 2016.

[20] O. Morton, "Solar energy: A new day dawning?: Silicon Valley sunrise," ed: Nature Publishing Group, 2006.

[21] F. M. Guangul and G. T. Chala, "Solar energy as renewable energy source: SWOT analysis," in *2019 4th MEC International Conference on Big Data and Smart City (ICBDSC)*, 2019, pp. 1-5: IEEE.

[22] Z. Fan, "Three-dimensional nanopillar-array photovoltaics on low-cost and flexible substrates," *Nature materials,* vol. 8, no. 8, p. 648, 2009.

[23] D. Popp, I. Hascic, and N. Medhi, "Technology and the diffusion of renewable energy," *Energy Economics,* vol. 33, no. 4, pp. 648-662, 2011.

[24] M. B. Hayat, D. Ali, K. C. Monyake, L. Alagha, and N. Ahmed, "Solar energy—A look into power generation, challenges, and a solar-powered future," *International Journal of Energy Research,* vol. 43, no. 3, pp. 1049-1067, 2019.

[25] C. J. Barnhart, M. Dale, A. R. Brandt, and S. M. Benson, "The energetic implications of curtailing versus storing solar-and wind-generated electricity," *Energy & Environmental Science,* vol. 6, no. 10, pp. 2804-2810, 2013.

[26] C. A. Wolden, "Photovoltaic manufacturing: Present status, future prospects, and research needs," *Journal of Vacuum Science & Technology A: Vacuum, Surfaces, and Films,* vol. 29, no. 3, p. 030801, 2011.

[27] L. A. H. Munoz, J. C. C. M. Huijben, B. Verhees, and G. P. J. Verbong, "The power of grid parity: A discursive approach," *Technological Forecasting and Social Change,* vol. 87, pp. 179-190, 2014.

[28] T. Markvart and L. Castañer, "Principles of solar cell operation," in *McEvoy's Handbook of Photovoltaics*: Elsevier, 2018, pp. 3-28.

[29] L. Spangler, "Zinc Oxide Nanostructured Extremely Thin Absorber Solar Cells," Drexel University, 2013.

[30] H. Morkoç and Ü. Özgür, "General Properties of ZnO," in *Zinc Oxide*: Wiley-VCH Verlag GmbH & Co. KGaA, 2009, pp. 1-76.

[31] Ü. Özgür, "A comprehensive review of ZnO materials and devices," *Journal of Applied Physics,* vol. 98, no. 4, p. 041301, 2005.

[32] A. Abdulrahman, S. Ahmed, N. Ahmed, and M. Almessiere, "DIFFERENT SUBSTRATES EFFECTS ON THE TOPOGRAPHY AND THE STRUCTURE OF THE ZnO NANORODS GROWN BY CHEMICAL BATH DEPOSITION

METHOD," *Digest Journal of Nanomaterials and Biostructures,* vol. 11, no. 3, pp. 1007-1016, 2016.

[33] Z. L. Wang, "Nanostructures of zinc oxide," *Materials Today,* vol. 7, no. 6, pp. 26-33, 2004/06/01/ 2004.

[34] H. Morkoç and Ü. Özgür, *Zinc oxide: fundamentals, materials and device technology*. John Wiley & Sons, 2008.

[35] Ü. Özgür *et al.*, "A comprehensive review of ZnO materials and devices," *Journal of applied physics,* vol. 98, no. 4, p. 11, 2005.

[36] S. Xu and Z. L. Wang, "One-dimensional ZnO nanostructures: solution growth and functional properties," *Nano Research,* vol. 4, no. 11, pp. 1013-1098, 2011.

[37] F. C. Porter, *Zinc handbook: properties, processing, and use in design*. CRC Press, 1991.

[38] R. Riedel and I.-W. Chen, *Ceramics Science and Technology, Volume 4: Applications*. John Wiley & Sons, 2013.

[39] M. I. Khalil, M. M. Al-Qunaibit, A. M. Al-zahem, and J. P. Labis, "Synthesis and characterization of ZnO nanoparticles by thermal decomposition of a curcumin zinc complex," *Arabian Journal of Chemistry,* vol. 7, no. 6, pp. 1178-1184, 2014/12/01/ 2014.

[40] L. Sang, M. Liao, and M. Sumiya, "A Comprehensive Review of Semiconductor Ultraviolet Photodetectors: From Thin Film to One-Dimensional Nanostructures," *Sensors,* vol. 13, no. 8, p. 10482, 2013.

[41] A. Janotti and C. G. Van de Walle, "Fundamentals of zinc oxide as a semiconductor," *Reports on Progress in Physics,* vol. 72, no. 12, p. 126501, 2009.

[42] A. B. Djurišić and Y. H. Leung, "Optical Properties of ZnO Nanostructures," *Small,* vol. 2, no. 8-9, pp. 944-961, 2006.

[43] M. Ghosh, "Effect of size and aspect ratio on structural parameters and evidence of shape transition in zinc oxide nanostructures," *Journal of Physics and Chemistry of Solids,* vol. 75, no. 4, pp. 543-549, 2014/04/01/ 2014.

[44] D. Zappa, "Metal oxide nanostructures: preparation, characterization and functional applications as chemical sensors," *Beilstein journal of nanotechnology,* vol. 8, pp. 1205-1217Accessed on: 2017. doi: 10.3762/bjnano.8.122 Available

[45] Z. L. Wang, "Zinc oxide nanostructures: growth, properties and applications," *Journal of physics: condensed matter,* vol. 16, no. 25, p. R829, 2004.

[46] T. Soga, *Nanostructured materials for solar energy conversion*. Elsevier, 2006.

[47] Z. Fan and J. G. Lu, "Zinc oxide nanostructures: synthesis and properties," *Journal of nanoscience and nanotechnology,* vol. 5, no. 10, pp. 1561-1573, 2005.

[48] M. Caglar, S. Ilican, Y. Caglar, and F. Yakuphanoglu, "Electrical conductivity and optical properties of ZnO nanostructured thin film," *Applied Surface Science,* vol. 255, no. 8, pp. 4491-4496, 2009.

[49] P. R. Talakonda, "Excitation-Intensity (EI) Effect on Photoluminescence of ZnO Materials with Various Morphologies," *Luminescence: An Outlook on the Phenomena and their Applications,* p. 91, 2016.

[50] W. Bousslama, "Structural and luminescence properties of highly crystalline ZnO nanoparticles prepared by sol–gel method," *Japanese Journal of Applied Physics,* vol. 51, no. 4S, p. 04DG13, 2012.

[51] D. Zaouk, Y. Zaatar, R. Asmar, and J. Jabbour, "Piezoelectric zinc oxide by electrostatic spray pyrolysis," *Microelectronics journal,* vol. 37, no. 11, pp. 1276-1279, 2006.

[52] S. Sakohara, M. Ishida, and M. A. Anderson, "Visible luminescence and surface properties of nanosized ZnO colloids prepared by hydrolyzing zinc acetate," *The Journal of Physical Chemistry B,* vol. 102, no. 50, pp. 10169-10175, 1998.

[53] A. Tabib, "Structural and optical properties of Na doped ZnO nanocrystals: application to solar photocatalysis," *Applied Surface Science,* vol. 396, pp. 1528-1538, 2017.

[54] M. Rusop, "Effect of film thickness on structural, electrical, and optical properties of sol-gel deposited layer-by-layer ZnO nanoparticles," *Transactions on Electrical and Electronic Materials,* vol. 13, no. 2, pp. 102-105, 2012.

[55] A. Uthirakumar, "Fabrication of ZnO Based Dye Sensitized Solar Cells," in *Solar Cells-Dye-Sensitized Devices*: InTech, 2011.

[56] C. H. Swartz, "Transport and surface conductivity in ZnO," *Journal of Materials Research,* vol. 27, no. 17, pp. 2205-2213, 2012.

[57] D. C. Look, "Recent advances in ZnO materials and devices," *Materials Science and Engineering: B,* vol. 80, no. 1, pp. 383-387, 2001.

[58] T. Aoki, Y. Hatanaka, and D. C. Look, "ZnO diode fabricated by excimer-laser doping," *Applied Physics Letters,* vol. 76, no. 22, pp. 3257-3258, 2000.

[59] Y. Liu, "Ultraviolet detectors based on epitaxial ZnO films grown by MOCVD," *Journal of Electronic Materials,* vol. 29, no. 1, pp. 69-74, 2000.

[60] Z. L. Wang, "ZnO nanowire and nanobelt platform for nanotechnology," *Materials Science and Engineering: R: Reports,* vol. 64, no. 3, pp. 33-71, 2009.

[61] S. Baruah and J. Dutta, "Hydrothermal growth of ZnO nanostructures," *Science and Technology of Advanced Materials,* vol. 10, no. 1, p. 013001, 2009.

[62] E. Muchuweni, T. S. Sathiaraj, and H. Nyakotyo, "Synthesis and characterization of zinc oxide thin films for optoelectronic applications," *Heliyon,* vol. 3, no. 4, p. e00285, 2017.

[63] S. Iijima, "Helical microtubules of graphitic carbon," *nature,* vol. 354, no. 6348, pp. 56-58, 1991.

[64] M. H. Huang, Y. Wu, H. Feick, N. Tran, E. Weber, and P. Yang, "Catalytic growth of zinc oxide nanowires by vapor transport," *Advanced Materials,* vol. 13, no. 2, pp. 113-116, 2001.

[65] M. H. Huang, "Room-temperature ultraviolet nanowire nanolasers," *science,* vol. 292, no. 5523, pp. 1897-1899, 2001.

[66] G. Gu, "Growth and electrical transport of germanium nanowires," *Journal of Applied Physics,* vol. 90, no. 11, pp. 5747-5751, 2001.

[67] Z. Bai, "Nano-scale GeO 2 wires synthesized by physical evaporation," *Chemical Physics Letters,* vol. 303, no. 3, pp. 311-314, 1999.

[68] Y. Cui, L. J. Lauhon, M. S. Gudiksen, J. Wang, and C. M. Lieber, "Diameter-controlled synthesis of single-crystal silicon nanowires," *Applied Physics Letters,* vol. 78, no. 15, pp. 2214-2216, 2001.

[69] X. Duan, Y. Huang, Y. Cui, J. Wang, and C. M. Lieber, "Indium phosphide nanowires as building blocks for nanoscale electronic and optoelectronic devices," *Nature,* vol. 409, no. 6816, pp. 66-69, 2001.

[70] K. Gautam, I. Singh, P. Bhatnagar, and K. R. Peta, "The effect of growth temperature of seed layer on the structural and optical properties of ZnO nanorods," *Superlattices and Microstructures,* vol. 93, pp. 101-108, 2016.

[71] G.-C. Yi, C. Wang, and W. I. Park, "ZnO nanorods: synthesis, characterization and applications," *Semiconductor Science and Technology,* vol. 20, no. 4, p. S22, 2005.

[72] R. Idiawati, N. Mufti, A. Taufiq, H. Wisodo, I. Laila, and A. Fuad, "Effect of Growth Time on the Characteristics of ZnO Nanorods," in *IOP Conference Series: Materials Science and Engineering*, 2017, vol. 202, no. 1, p. 012050: IOP Publishing.

[73] T.-J. Kuo, C.-N. Lin, C.-L. Kuo, and M. H. Huang, "Growth of ultralong ZnO nanowires on silicon substrates by vapor transport and their use as recyclable photocatalysts," *Chemistry of Materials,* vol. 19, no. 21, pp. 5143-5147, 2007.

[74] R. Kumar, G. Kumar, O. Al-Dossary, and A. Umar, "ZnO nanostructured thin films: depositions, properties and applications—a review," *Materials Express,* vol. 5, no. 1, pp. 3-23, 2015.

[75] Z. Yuan, J. Yu, and Y. Jiang, "Growth of diameter-controlled ZnO nanorod arrays by hydrothermal technique for polymer solar cell application," *Energy Procedia,* vol. 12, pp. 502-507, 2011.

[76] P. De Rango, "Texturing of magnetic materials at high temperature by solidification in a magnetic field," *Nature,* vol. 349, no. 6312, p. 770, 1991.

[77] X. Y. Kong and Z. L. Wang, "Spontaneous polarization-induced nanohelixes, nanosprings, and nanorings of piezoelectric nanobelts," *Nano Letters,* vol. 3, no. 12, pp. 1625-1631, 2003.

[78] H. Dang, J. Wang, and S. Fan, "The synthesis of metal oxide nanowires by directly heating metal samples in appropriate oxygen atmospheres," *Nanotechnology,* vol. 14, no. 7, p. 738, 2003.

[79] D. Polsongkram, "Effect of synthesis conditions on the growth of ZnO nanorods via hydrothermal method," *Physica B: Condensed Matter,* vol. 403, no. 19, pp. 3713-3717, 2008.

[80] A. Moezzi, A. M. McDonagh, and M. B. Cortie, "Zinc oxide particles: Synthesis, properties and applications," *Chemical Engineering Journal,* vol. 185, pp. 1-22, 2012.

[81] L. Spanhel, "Colloidal ZnO nanostructures and functional coatings: a survey," *Journal of sol-gel science and technology,* vol. 39, no. 1, pp. 7-24, 2006.

[82] S. Shingubara, "Fabrication of nanomaterials using porous alumina templates," *Journal of Nanoparticle Research,* vol. 5, no. 1, pp. 17-30, 2003.

[83] R. Ayouchi, F. Martin, D. Leinen, and J. Ramos-Barrado, "Growth of pure ZnO thin films prepared by chemical spray pyrolysis on silicon," *Journal of Crystal Growth,* vol. 247, no. 3, pp. 497-504, 2003.

[84] J.-H. Lee, C. Leu, Y.-W. Chung, and M.-H. Hon, "Fabrication of ordered ZnO hierarchical structures controlled via surface charge in the electrophoretic deposition process," *Nanotechnology,* vol. 17, no. 17, p. 4445, 2006.

[85] T. Yasuda and Y. Segawa, "Zinc oxide thin films synthesized by metal organic chemical reactions," *physica status solidi (b),* vol. 241, no. 3, pp. 676-679, 2004.

[86] Z. W. Pan, Z. R. Dai, and Z. L. Wang, "Nanobelts of semiconducting oxides," *Science,* vol. 291, no. 5510, pp. 1947-1949, 2001.

[87] L. Miao, "Synthesis, microstructure and photoluminescence of well-aligned ZnO nanorods on Si substrate," *Science and Technology of Advanced Materials,* vol. 8, no. 6, pp. 443-447, 2007.

[88] C. Tang, S. Fan, M. L. De La Chapelle, and P. Li, "Silica-assisted catalytic growth of oxide and nitride nanowires," *Chemical Physics Letters,* vol. 333, no. 1, pp. 12-15, 2001.

[89] Y. Satoh, S. Ohshio, and H. Saitoh, "Photoluminescence spectroscopy of highly oriented Y 2 O 3: Tb crystalline whiskers," *Science and Technology of Advanced Materials,* vol. 6, no. 2, pp. 215-218, 2005.

[90] S. Dalal, D. Baptista, K. Teo, R. Lacerda, D. Jefferson, and W. Milne, "Controllable growth of vertically aligned zinc oxide nanowires using vapour deposition," *Nanotechnology,* vol. 17, no. 19, p. 4811, 2006.

[91] G. F. Brown and J. Wu, "Third generation photovoltaics," *Laser & Photonics Reviews,* vol. 3, no. 4, pp. 394-405, 2009.

[92] A. A. F. Husain, W. Z. W. Hasan, S. Shafie, M. N. Hamidon, and S. S. Pandey, "A review of transparent solar photovoltaic technologies," *Renewable and Sustainable Energy Reviews,* vol. 94, pp. 779-791, 2018.

[93] S. Almosni, "Material challenges for solar cells in the twenty-first century: directions in emerging technologies," *Science and Technology of advanced MaTerialS,* vol. 19, no. 1, pp. 336-369, 2018.

[94] E. Płaczek-Popko, "Top PV market solar cells 2016," *Opto-Electronics Review,* 2017.

[95] M. T. Kibria, A. Ahammed, S. Sony, F. Hossain, and S. Islam, "A Review: Comparative studies on different generation solar cells technology," in *Proc. of 5th International Conference on Environmental Aspects of Bangladesh,* 2014.

[96] L. M. Fraas and L. D. Partain, *Solar cells and their applications*. John Wiley & Sons, 2010.

[97] C. U. Kim, "Optimization of device design for low cost and high efficiency planar monolithic perovskite/silicon tandem solar cells," *Nano Energy,* vol. 60, pp. 213-221, 2019/06/01/ 2019.

[98] P. Choubey, A. Oudhia, and R. Dewangan, "A review: Solar cell current scenario and future trends," *Recent Research in Science and Technology,* vol. 4, no. 8, 2012.

[99] F. Milési, "Homojunction silicon solar cells doping by ion implantation," *Nuclear Instruments and Methods in Physics Research Section B: Beam Interactions with Materials and Atoms,* vol. 409, pp. 53-59, 2017.

[100] Z.-L. Huang, C.-M. Chen, Z.-K. Lin, and S.-H. Yang, "Efficiency enhancement of regular-type perovskite solar cells based on Al-doped ZnO nanorods as electron transporting layers," *Superlattices and Microstructures,* vol. 102, pp. 94-102, 2017.

[101] M. Shur, *Physics of semiconductor devices*. Prentice-Hall, Inc., 1990.

[102] D.-Y. Son, J.-H. Im, H.-S. Kim, and N.-G. Park, "11% Efficient Perovskite Solar Cell Based on ZnO Nanorods: An Effective Charge Collection System," *The Journal of Physical Chemistry C,* vol. 118, no. 30, pp. 16567-16573, 2014.

[103] J. W. Orton, *The story of semiconductors*. Oxford University Press, 2004.

[104] G. Busch, "Early history of the physics and chemistry of semiconductors-from doubts to fact in a hundred years," *European Journal of Physics,* vol. 10, no. 4, p. 254, 1989.

[105] L. Łukasiak and A. Jakubowski, "History of semiconductors," *Journal of Telecommunications and information technology,* pp. 3-9, 2010.

[106] D. Ferry, R. Akis, M. Gilbert, A. Cummings, and S. Ramey, "Semiconductor device scaling: Physics, transport, and the role of nanowires," *International Journal of High Speed Electronics and Systems,* vol. 17, no. 03, pp. 445-456, 2007.

[107] F. Capasso, "Band-gap engineering: from physics and materials to new semiconductor devices," *Science,* vol. 235, pp. 172-177, 1987.

[108] H. Kroemer, "Quasi-electric and quasi-magnetic fields in nonuniform semiconductors," *RCA Review,* vol. 18, no. 3, pp. 332-342, 1957.

[109] D. A. Neaman, *Semiconductor physics and devices*. Irwin Chicago, 1992.

[110] J. Nelson, *The physics of solar cells*. World Scientific Publishing Co Inc, 2003.

[111] E. L. Wolf, *Nanophysics of solar and renewable energy*. John Wiley & Sons, 2012.

[112] G. Han, S. Zhang, P. P. Boix, L. H. Wong, L. Sun, and S.-Y. Lien, "Towards high efficiency thin film solar cells," *Progress in Materials Science,* 2017.

[113] W. Shockley, "The Theory of p-n Junctions in Semiconductors and p-n Junction Transistors," *Bell Labs Technical Journal,* vol. 28, no. 3, pp. 435-489, 1949.

[114] Z. A. Smith and K. D. Taylor, *Renewable and alternative energy resources: a reference handbook*. ABC-CLIO, 2008.

[115] L. C. Andreani, A. Bozzola, P. Kowalczewski, M. Liscidini, and L. Redorici, "Silicon solar cells: toward the efficiency limits," *Advances in Physics: X,* vol. 4, no. 1, p. 1548305, 2019.

[116] M. M. Cawte, X. Yu, B. P. Anderson, and A. Bradley, "Snell's Law for a vortex dipole in a Bose-Einstein condensate," 2019.

[117] C.-F. Lin, H.-J. Syu, T. Subramani, and H.-C. Lee, "Improved power conversion efficiency of solar cells," in *Proc. SPIE,* 2014.

[118] K. Junlapong, S. Suwanboon, and C. Khaokong, "Effects of zinc oxide particle shape on properties of a prevulcanized latex," *Iranian Polymer Journal,* vol. 28, no. 4, pp. 325-335, 2019.

[119] D. R. Lafreniere, "Silicone and adhesive removal composition," ed: Google Patents, 1999.

[120] E. Kuramochi, "Manipulating and trapping light with photonic crystals from fundamental studies to practical applications," *Journal of Materials Chemistry C,* vol. 4, no. 47, pp. 11032-11049, 2016.

[121] S. Buddhiraju and S. Fan, "Theory of solar cell light trapping through a nonequilibrium Green's function formulation of Maxwell's equations," *Physical Review B,* vol. 96, no. 3, p. 035304, 2017.

[122] M. A. Green, "Limits on the open-circuit voltage and efficiency of silicon solar cells imposed by intrinsic Auger processes," *IEEE Transactions on electron devices,* vol. 31, no. 5, pp. 671-678, 1984.

[123] J. Kane, "Spectroscopy Applications for Plasma Monitoring: Exploring the use of optical emission spectroscopy as a form of plasma monitoring during the manufacturing of electronics," *PhotonicsViews,* vol. 16, no. 3, pp. 64-67, 2019.

[124] A. SOYANO, "Application of polymers to photoresist materials," *Nippon Gomu Kyokaishi,* vol. 85, no. 2, pp. 33-39, 2012.

[125] X. Hu, "Photolithography technology in electronic fabrication," in *2015 International Power, Electronics and Materials Engineering Conference*, 2015: Atlantis Press.

[126] P. Wang, K. Tanaka, S. Sugiyama, X. Dai, and X. Zhao, "Wet releasing and stripping SU-8 structures with a nanoscale sacrificial layer," *Microelectronic Engineering,* vol. 86, no. 11, pp. 2232-2235, 2009.

[127] T. A. Anhoj, A. M. Jorgensen, D. A. Zauner, and J. Hübner, "The effect of soft bake temperature on the polymerization of SU-8 photoresist," *Journal of Micromechanics and Microengineering,* vol. 16, no. 9, p. 1819, 2006.

[128] H. Lorenz, M. Despont, N. Fahrni, N. LaBianca, P. Renaud, and P. Vettiger, "SU-8: a low-cost negative resist for MEMS," *Journal of Micromechanics and Microengineering,* vol. 7, no. 3, p. 121, 1997.

[129] R. Martinez-Duarte, "SU-8 Photolithography as a Toolbox for Carbon MEMS," *Micromachines,* vol. 5, no. 3, pp. 766-782, 2014.

[130] R. Martinez-Duarte and M. Madou, "SU-8 photolithography and its impact on microfluidics," *Microfluidics and Nanofluidics Handbook,* pp. 231-268, 2011.

[131] B. J. Kim and E. Meng, "Review of polymer MEMS micromachining," *Journal of Micromechanics and Microengineering,* vol. 26, no. 1, p. 013001, 2015.

[132] S. Arscott, "SU-8 as a material for lab-on-a-chip-based mass spectrometry," *Lab on a Chip,* vol. 14, no. 19, pp. 3668-3689, 2014.

[133] A. J. Dy, A. Cosmanescu, J. Sluka, J. A. Glazier, D. Stupack, and D. Amarie, "Fabricating microfluidic valve master molds in SU-8 photoresist," *Journal of Micromechanics and Microengineering,* vol. 24, no. 5, p. 057001, 2014.

[134] M. B. Chan-Park, J. Zhang, Y. Yan, and C. Yue, "Fabrication of large SU-8 mold with high aspect ratio microchannels by UV exposure dose reduction," *Sensors and Actuators B: Chemical,* vol. 101, no. 1, pp. 175-182, 2004.

[135] V. Linder, B. D. Gates, D. Ryan, B. A. Parviz, and G. M. Whitesides, "Water-Soluble Sacrificial Layers for Surface Micromachining," *small*, vol. 1, no. 7, pp. 730-736, 2005.

[136] C. Luo, "Releasing SU-8 structures using polystyrene as a sacrificial material," *Sensors and Actuators A: Physical*, vol. 114, no. 1, pp. 123-128, 2004.

[137] C. Chung and M. Allen, "Uncrosslinked SU-8 as a sacrificial material," *Journal of Micromechanics and Microengineering*, vol. 15, no. 1, p. N1, 2004.

[138] U. Ali, K. J. B. A. Karim, and N. A. Buang, "A review of the properties and applications of poly (methyl methacrylate)(PMMA)," *Polymer Reviews*, vol. 55, no. 4, pp. 678-705, 2015.

[139] K. Darowicki, M. Szociński, K. Schaefer, and D. J. Mills, "The influence of UV light on performance of poly (methyl methacrylate) in regard to dye-sensitised solar cells," *ECS Transactions*, vol. 24, no. 1, pp. 127-136, 2010.

[140] R. T. Howe, "Surface micromachining for microsensors and microactuators," *Journal of Vacuum Science & Technology B: Microelectronics Processing and Phenomena*, vol. 6, no. 6, pp. 1809-1813, 1988.

[141] M. J. Madou, *Fundamentals of microfabrication: the science of miniaturization*. CRC press, 2002.

[142] S. Vlassov, "ADHESION AND MECHANICAL PROPERTIES OF PDMS-BASED MATERIALS PROBED WITH AFM: A REVIEW," *Reviews on Advanced Materials Science*, vol. 56, no. 1, 2018.

[143] S. K. Sia and G. M. Whitesides, "Microfluidic devices fabricated in poly (dimethylsiloxane) for biological studies," *Electrophoresis*, vol. 24, no. 21, pp. 3563-3576, 2003.

[144] A. Mata, A. J. Fleischman, and S. Roy, "Characterization of polydimethylsiloxane (PDMS) properties for biomedical micro/nanosystems," *Biomedical microdevices*, vol. 7, no. 4, pp. 281-293, 2005.

[145] M. Matthiae and A. Kristensen, "Hyperspectral spatially offset Raman spectroscopy in a microfluidic channel," *Optics express*, vol. 27, no. 3, pp. 3782-3790, 2019.

[146] A. Auner, K. M. Tasneem, D. A. Markov, L. J. McCawley, and M. S. Hutson, "Chemical-PDMS Binding Kinetics and Implications for Bioavailability in Microfluidic Devices," *Lab on a Chip*, 2019.

[147] J. Gallardo-Gonzalez, "A fully integrated passive microfluidic Lab-on-a-Chip for real-time electrochemical detection of ammonium: Sewage applications," *Science of the Total Environment*, vol. 653, pp. 1223-1230, 2019.

[148] F. Hamouda, "Nanoholes by soft UV nanoimprint lithography applied to study of membrane proteins," *Microelectronic Engineering*, vol. 86, no. 4-6, pp. 583-585, 2009.

[149] J. Lee, S. Park, K. Choi, and G. Kim, "Nano-scale patterning using the roll typed UV-nanoimprint lithography tool," *Microelectronic Engineering*, vol. 85, no. 5-6, pp. 861-865, 2008.

[150] J. Lindsay, "Growth of ZnO nanorod arrays on flexible PDMS substrates," *Products Finishing(Cincinnati)*, vol. 76, no. 6, pp. 14-14, 2012.

[151] J. Liu, N. Motta, and S. Lee, "Ultraviolet photodetection of flexible ZnO nanowire sheets in polydimethylsiloxane polymer," *Beilstein journal of nanotechnology*, vol. 3, no. 1, pp. 353-359, 2012.

[152] Y. Chen, X. Guo, W. H. Tse, T.-K. Sham, and J. Zhang, "Magnetic anisotropy induced in NiCo granular nanostructures by ZnO nanorods deposited on a polymer substrate," *RSC Advances*, vol. 4, no. 89, pp. 47987-47991, 2014.

[153] F. Di Giacomo, A. Fakharuddin, R. Jose, and T. M. Brown, "Progress, challenges and perspectives in flexible perovskite solar cells," *Energy & Environmental Science*, vol. 9, no. 10, pp. 3007-3035, 2016.

[154] J. Briscoe and S. Dunn, "Extremely thin absorber solar cells based on nanostructured semiconductors," *Materials Science and Technology*, vol. 27, no. 12, pp. 1741-1756, 2011.

[155] R. Könenkamp, L. Dloczik, K. Ernst, and C. Olesch, "Nano-structures for solar cells with extremely thin absorbers," *Physica E: Low-dimensional Systems and Nanostructures*, vol. 14, no. 1, pp. 219-223, 2002.

[156] M. V. Santhosh, C. Sudha Kartha, K. Rajeev Kumar, and K. P. Vijayakumar, "Thin film solar cells with extremely thin absorber layer having multiple absorption bands: A novel attempt," *Solar Energy*, vol. 122, pp. 712-717, 2015.

[157] G. Kartopu, "Photovoltaic performance of CdS/CdTe junctions on ZnO nanorod arrays," *Solar Energy Materials and Solar Cells*, vol. 176, pp. 100-108, 2018.

[158] Q. Guo, H. W. Hillhouse, and R. Agrawal, "Synthesis of Cu2ZnSnS4 Nanocrystal Ink and Its Use for Solar Cells," *Journal of the American Chemical Society*, vol. 131, no. 33, pp. 11672-11673, 2009.

[159] C. Yan, "Cu 2 ZnSnS 4 solar cells with over 10% power conversion efficiency enabled by heterojunction heat treatment," *Nature Energy*, vol. 3, no. 9, p. 764, 2018.

[160] M.-H. Li, J.-H. Yum, S.-J. Moon, and P. Chen, "Inorganic p-type semiconductors: their applications and progress in dye-sensitized solar cells and perovskite solar cells," *Energies*, vol. 9, no. 5, p. 331, 2016.

[161] S. Siebentritt, K. Ernst, C. Fischer, R. Könenkamp, and M. Lux-Steiner, "CdTe and CdS as extremely thin absorber materials in an η-solar cell," in *Proc. 14 th European Photovolt. Sol. Energ. Conf*, 1997.

[162] A. Wahi, R. Engelhardt, P. Hoyer, and R. Könenkamp, "Interface characterisation of amorphous silicon on titaniumdioxide: towards a solid-state sensitizer cell," in *Proc. 11th Photovoltaic Solar Energy Conference (Montreux, 1992), pp. 714À717*, 1992.

[163] C. Lévy-Clément, R. Tena-Zaera, M. A. Ryan, A. Katty, and G. Hodes, "CdSe-sensitized p-CuSCN/nanowire n-ZnO heterojunctions," *Advanced Materials*, vol. 17, no. 12, pp. 1512-1515, 2005.

[164] I. Kaiser, "The eta-solar cell with CuInS2: A photovoltaic cell concept using an extremely thin absorber (eta)," *Solar Energy Materials and Solar Cells*, vol. 67, no. 1-4, pp. 89-96, 2001.

[165] K. Ernst, "Contacts to a solar cell with extremely thin CdTe absorber," *Thin Solid Films*, vol. 387, no. 1-2, pp. 26-28, 2001.

[166] I. Mora-Sero, S. Gimenez, F. Fabregat-Santiago, E. Azaceta, R. Tena-Zaera, and J. Bisquert, "Modeling and characterization of extremely thin absorber (eta) solar cells based on ZnO nanowires," *Physical Chemistry Chemical Physics,* vol. 13, no. 15, pp. 7162-7169, 2011.

[167] L. Isac, I. Popovici, A. Enesca, and A. Duta, "Copper sulfide (CuxS) thin films as possible p-type absorbers in 3D solar cells," *Energy Procedia,* vol. 2, no. 1, pp. 71-78, 2010.

[168] G. Hodes, "Comparison of dye-and semiconductor-sensitized porous nanocrystalline liquid junction solar cells," *The Journal of Physical Chemistry C,* vol. 112, no. 46, pp. 17778-17787, 2008.

[169] G. Hodes and D. Cahen, "All-solid-state, semiconductor-sensitized nanoporous solar cells," *Accounts of chemical research,* vol. 45, no. 5, pp. 705-713, 2012.

[170] T. Dittrich, A. Belaidi, and A. Ennaoui, "Concepts of inorganic solid-state nanostructured solar cells," *Solar Energy Materials and Solar Cells,* vol. 95, no. 6, pp. 1527-1536, 2011.

[171] I. Mora-Seró and J. Bisquert, "Breakthroughs in the development of semiconductor-sensitized solar cells," *The journal of physical chemistry letters,* vol. 1, no. 20, pp. 3046-3052, 2010.

[172] A. Goossens and J. Hofhuis, "Spray-deposited CuInS2 solar cells," *Nanotechnology,* vol. 19, no. 42, p. 424018, 2008.

[173] R. Scheer, R. Klenk, J. Klaer, and I. Luck, "CuInS2 based thin film photovoltaics," *Solar Energy,* vol. 77, no. 6, pp. 777-784, 2004.

[174] K. Ernst, A. Belaidi, and R. Könenkamp, "Solar cell with extremely thin absorber on highly structured substrate," *Semiconductor science and technology,* vol. 18, no. 6, p. 475, 2003.

[175] O. Niitsoo, S. K. Sarkar, C. Pejoux, S. Rühle, D. Cahen, and G. Hodes, "Chemical bath deposited CdS/CdSe-sensitized porous TiO2 solar cells," *Journal of Photochemistry and Photobiology A: Chemistry,* vol. 181, no. 2-3, pp. 306-313, 2006.

[176] K. Taretto and U. Rau, "Modeling extremely thin absorber solar cells for optimized design," *Progress in Photovoltaics: Research and Applications,* vol. 12, no. 8, pp. 573-591, 2004.

[177] W. Metzger, "Recombination kinetics and stability in polycrystalline Cu (In, Ga) Se2 solar cells," *Thin Solid Films,* vol. 517, no. 7, pp. 2360-2364, 2009.

[178] G. Larramona, "Nanostructured photovoltaic cell of the type titanium dioxide, cadmium sulfide thin coating, and copper thiocyanate showing high quantum efficiency," *Chemistry of materials,* vol. 18, no. 6, pp. 1688-1696, 2006.

[179] C. Herzog, A. Belaidi, A. Ogacho, and T. Dittrich, "Inorganic solid state solar cell with ultra-thin nanocomposite absorber based on nanoporous TiO 2 and In 2 S 3," *Energy & Environmental Science,* vol. 2, no. 9, pp. 962-964, 2009.

[180] S. H. Im, "Toward interaction of sensitizer and functional moieties in hole-transporting materials for efficient semiconductor-sensitized solar cells," *Nano letters,* vol. 11, no. 11, pp. 4789-4793, 2011.

[181] P. P. Boix, "From flat to nanostructured photovoltaics: balance between thickness of the absorber and charge screening in sensitized solar cells," *ACS nano,* vol. 6, no. 1, pp. 873-880, 2011.

[182] K. Ito and T. Nakazawa, "Electrical and optical properties of stannite-type quaternary semiconductor thin films," *Japanese Journal of Applied Physics,* vol. 27, no. 11R, p. 2094, 1988.

[183] A. Cazzaniga, "Ultra-thin Cu2ZnSnS4 solar cell by pulsed laser deposition," *Solar Energy Materials and Solar Cells,* vol. 166, pp. 91-99, 2017.

[184] R. Nitsche, D. F. Sargent, and P. Wild, "Crystal growth of quaternary 122464 chalcogenides by iodine vapor transport," *Journal of Crystal Growth,* vol. 1, no. 1, pp. 52-53, 1967.

[185] R. Nitsche, D. Sargent, and P. Wild, "Crystal growth of quaternary 122464 chalcogenides by iodine vapor transport," *Journal of Crystal Growth,* vol. 1, no. 1, pp. 52-53, 1967.

[186] K. Ito and T. Nakazawa, "Electrical and Optical Properties of Stannite-Type Quaternary Semiconductor Thin Films," *Japanese Journal of Applied Physics,* vol. 27, no. Part 1, No. 11, pp. 2094-2097, 1988.

[187] T. M. Friedlmeier, N. Wieser, T. Walter, H. Dittrich, and H. Schock, "Heterojunctions based on Cu2ZnSnS4 and Cu2ZnSnSe4 thin films," in *Proceedings of the 14th European Conference of Photovoltaic Science and Engineering and Exhibition*, 1997, vol. 1242.

[188] H. Katagiri, "Development of CZTS-based thin film solar cells," *Thin Solid Films,* vol. 517, no. 7, pp. 2455-2460, 2009/02/02/ 2009.

[189] N. Momose, "Cu2ZnSnS4 thin film solar cells utilizing sulfurization of metallic precursor prepared by simultaneous sputtering of metal targets," *Japanese Journal of Applied Physics,* vol. 50, no. 1S2, p. 01BG09, 2011.

[190] L. Atourki, "Pulse Electrodepositin of ZnO for Thin Absorber Solar Cells," *Energy Procedia,* vol. 50, pp. 376-382, 2014.

[191] M. Jiang and X. Yan, "Cu2ZnSnS4 thin film solar cells: present status and future prospects," in *Solar Cells-Research and Application Perspectives*: IntechOpen, 2013.

[192] Y. Qu, G. Zoppi, R. W. Miles, and N. S. Beattie, "Influence of reaction conditions on the properties of solution-processed Cu2ZnSnS4 nanocrystals," *Materials Research Express,* vol. 1, no. 4, p. 045040, 2014.

[193] G. Korotcenkov, *The Future of Semiconductor Oxides in Next-Generation Solar Cells*. Elsevier, 2017.

[194] N. Saidin, T. Choo, and K. Kok, "Hydrothermal growth of ZnO: a substrate-dependent study on nanostructures formation," in *IOP Conference Series: Materials Science and Engineering*, 2018, vol. 298, no. 1, p. 012016: IOP Publishing.

[195] A. Zainelabdin, "CuO/ZnO nanocorals synthesis via hydrothermal technique: growth mechanism and their application as humidity sensor," *Journal of Materials Chemistry,* vol. 22, no. 23, pp. 11583-11590, 2012.

[196] Y. Zhang, M. K. Ram, E. K. Stefanakos, and D. Y. Goswami, "Synthesis, characterization, and applications of ZnO nanowires," *Journal of Nanomaterials*, vol. 2012, p. 20, 2012.

[197] J.-S. Huang and C.-F. Lin, "Influences of ZnO sol-gel thin film characteristics on ZnO nanowire arrays prepared at low temperature using all solution-based processing," *Journal of Applied Physics*, vol. 103, no. 1, p. 014304, 2008.

[198] M. Sun, Q.-F. Zhang, and J.-L. Wu, "Electrical and electroluminescence properties of As-doped p-type ZnO nanorod arrays," *Journal of Physics D: Applied Physics*, vol. 40, no. 12, p. 3798, 2007.

[199] J. Song and S. Lim, "Effect of seed layer on the growth of ZnO nanorods," *The Journal of Physical Chemistry C*, vol. 111, no. 2, pp. 596-600, 2007.

[200] D. Köhl, G. Natarajan, and M. Wuttig, "Structure control of sputtered zinc oxide films by utilizing zinc oxide seed layers tailored by ion beam assisted sputtering," *Journal of Physics D: Applied Physics*, vol. 45, no. 24, p. 245302, 2012.

[201] S. Sen, D. Leary, and C. Bauer, "Characterization of rf-sputtered ZnO thin films by X-ray diffraction and scanning electron microscopy," *Thin Solid Films*, vol. 94, no. 1, pp. 7-14, 1982.

[202] G. Rughoobur, "Seed layer controlled deposition of ZnO films with a tilted c-axis for shear mode resonators," in *European Frequency and Time Forum (EFTF), 2014*, 2014, pp. 297-300: IEEE.

[203] M. N. Rezaie, N. Manavizadeh, F. D. Nayeri, M. M. Bidgoli, E. Nadimi, and F. A. Boroumand, "Effect of seed layers on low-temperature, chemical bath deposited ZnO nanorods-based near UV-OLED performance," *Ceramics International*, vol. 44, no. 5, pp. 4937-4945, 2018.

[204] S.-W. Chen and J.-M. Wu, "Nucleation mechanisms and their influences on characteristics of ZnO nanorod arrays prepared by a hydrothermal method," *Acta Materialia*, vol. 59, no. 2, pp. 841-847, 2011.

[205] P. Novák, J. Briscoe, T. Kozák, M. Kormunda, M. Netrvalová, and Š. Bachratá, "Optimization of sputtered ZnO transparent conductive seed layer for flexible ZnO-nanorod-based devices," *Thin Solid Films*, vol. 634, pp. 169-174, 2017.

[206] L. Whittaker-Brooks, J. M. Mativetsky, A. Woll, D. Smilgies, and Y.-L. Loo, "Sputtered ZnO seed layer enhances photovoltaic behavior in hybrid ZnO/P3HT solar cells," *Organic Electronics*, vol. 14, no. 12, pp. 3477-3483, 2013.

[207] L.-W. Ji, S.-M. Peng, J.-S. Wu, W.-S. Shih, C.-Z. Wu, and I.-T. Tang, "Effect of seed layer on the growth of well-aligned ZnO nanowires," *Journal of Physics and Chemistry of Solids*, vol. 70, no. 10, pp. 1359-1362, 2009.

[208] H. Sun., "Room-temperature preparation of ZnO nanosheets grown on Si substrates by a seed-layer assisted solution route," *Nanotechnology*, vol. 19, no. 12, p. 125603, 2008.

[209] G. A. Kumar, M. V. R. Reddy, and R. Katta Narasimha, "Structural and Optical properties of ZnO thin films grown on various substrates by RF magnetron sputtering," *IOP Conference Series: Materials Science and Engineering*, vol. 73, no. 1, p. 012133, 2015.

[210] R. S. Tondare, B. W. Shivaraj, H. N. Narasimhamurthy, M. Krishna, and T. K. Subramanyam, "Effect of deposition time on structural, electrical and optical

properties of Aluminium doped ZnO thin films by RF magnetron sputtering," *Materials Today: Proceedings,* vol. 5, no. 1, Part 3, pp. 2710-2715, 2018.

[211] H. Ghayour, H. Rezaie, S. Mirdamadi, and A. Nourbakhsh, "The effect of seed layer thickness on alignment and morphology of ZnO nanorods," *Vacuum,* vol. 86, no. 1, pp. 101-105, 2011.

[212] M.-S. Kim, K.-G. Yim, J.-S. Son, and J.-Y. Leem, "Effects of Al concentration on structural and optical properties of Al-doped ZnO thin films," *Bulletin of the Korean Chemical Society,* vol. 33, no. 4, pp. 1235-1241, 2012.

[213] L. Campo, "The effect of a sputtered Al-doped ZnO seed layer on the morphological, structural and optical properties of electrochemically grown ZnO nanorod arrays," *Journal of The Electrochemical Society,* vol. 163, no. 8, pp. D392-D400, 2016.

[214] X. Ren, "Superior texture-controlled ZnO thin film using electrochemical deposition," *Solar Energy,* vol. 125, pp. 192-197, 2016.

[215] M. Zhao, "Influence of water content in mixed solvent on surface morphology, wettability, and photoconductivity of ZnO thin films," *Nanoscale research letters,* vol. 9, no. 1, p. 485, 2014.

[216] K. Chongsri, K. Boonyarattanakalin, and W. Pecharapa, "Investigation on influence of seeding layer on morphological properties of ZnO-based nanostructure prepared by hydrothermal process," *Materials Today: Proceedings,* vol. 5, no. 6, pp. 14110-14115, 2018.

[217] L. Demianets, D. Kostomarov, I. Kuz'mina, and S. Pushko, "Mechanism of growth of ZnO single crystals from hydrothermal alkali solutions," *Crystallography Reports,* vol. 47, no. 1, pp. S86-S98, 2002.

[218] M. Kreye, B. Postels, H. H. Wehmann, D. Fuhrmann, A. Hangleiter, and A. Waag, "Aqueous chemical growth and patterning of ZnO nanopillars on different substrate materials," *physica status solidi c,* vol. 3, no. 4, pp. 992-996, 2006.

[219] L. Vayssieres, "Growth of arrayed nanorods and nanowires of ZnO from aqueous solutions," *Advanced Materials,* vol. 15, no. 5, pp. 464-466, 2003.

[220] S. Li, "Low-temperature hydrothermal growth of oriented [0001] ZnO film," *Materials Letters,* vol. 61, no. 1, pp. 30-33, 2007.

[221] S. Shaziman, A. S. Ismail, M. H. Mamat, and A. S. Zoolfakar, "Influence of Growth Time and Temperature on the Morphology of ZnO Nanorods via Hydrothermal," in *IOP Conference Series: Materials Science and Engineering*, 2015, vol. 99, no. 1, p. 012016: IOP Publishing.

[222] S. Guillemin, V. Consonni, E. Appert, E. Puyoo, L. Rapenne, and H. Roussel, "Critical nucleation effects on the structural relationship between ZnO seed layer and nanowires," *The Journal of Physical Chemistry C,* vol. 116, no. 47, pp. 25106-25111, 2012.

[223] Y. Dou, F. Wu, C. Mao, L. Fang, S. Guo, and M. Zhou, "Enhanced photovoltaic performance of ZnO nanorod-based dye-sensitized solar cells by using Ga doped ZnO seed layer," *Journal of Alloys and Compounds,* vol. 633, pp. 408-414, 2015.

[224] J. Elias, R. Tena-Zaera, and C. Lévy-Clément, "Electrodeposition of ZnO nanowires with controlled dimensions for photovoltaic applications: Role of buffer layer," *Thin Solid Films,* vol. 515, no. 24, pp. 8553-8557, 2007.

[225] S. Pokai, "Influence of seed layer thickness on well-aligned ZnO nanorods via hydrothermal method," *Materials Today: Proceedings,* vol. 4, no. 5, pp. 6336-6341, 2017.

[226] S.-J. Kim, "Novel fabrication of various size ZnO nanorods using hydrothermal method," *Microelectronic Engineering,* vol. 87, no. 5-8, pp. 1534-1536, 2010.

[227] K. N. Abbas, N. Bidin, R. S. Sabry, H. J. Al-Asedy, M. A. Al-Azawi, and S. Islam, "Structures and emission features of high-density ZnO micro/nanostructure grown by an easy hydrothermal method," *Materials Chemistry and Physics,* vol. 182, pp. 298-307, 2016.

[228] J. Joo, B. Y. Chow, M. Prakash, E. S. Boyden, and J. M. Jacobson, "Face-selective electrostatic control of hydrothermal zinc oxide nanowire synthesis," *Nature materials,* vol. 10, no. 8, p. 596, 2011.

[229] H.-S. Hong and G.-S. Chung, "Controllable growth of oriented ZnO nanorods using Ga-doped seed layers and surface acoustic wave humidity sensor," *Sensors and Actuators B: Chemical,* vol. 195, pp. 446-451, 2014.

[230] M. Poornajar, P. Marashi, D. H. Fatmehsari, and M. K. Esfahani, "Synthesis of ZnO nanorods via chemical bath deposition method: The effects of physicochemical factors," *Ceramics International,* vol. 42, no. 1, pp. 173-184, 2016.

[231] K. Gautam, I. Singh, V. S. Nirwal, J. Singh, K. R. Peta, and P. Bhatnagar, "Effect of lattice strain on structural and optical properties of ZnO nanorods grown by hydrothermal method," in *AIP Conference Proceedings*, 2016, vol. 1728, no. 1, p. 020511: AIP Publishing.

[232] K. Gautam, "Effect of lattice strain on structural and optical properties of ZnO nanorods grown by hydrothermal method," in *AIP Conference Proceedings*, 2016, vol. 1728, no. 1, p. 020511: AIP Publishing.

[233] N. Ekthammathat, T. Thongtem, A. Phuruangrat, and S. Thongtem, "Photoluminescence of hexagonal ZnO nanorods hydrothermally grown on Zn foils in KOH solutions with different values of basicity," *Journal of Nanomaterials,* vol. 2013, p. 2, 2013.

[234] Y. Wang, W. Tang, and L. Zhang, "Crystalline size effects on texture coefficient, electrical and optical properties of sputter-deposited Ga-doped ZnO thin films," *Journal of Materials Science & Technology,* vol. 31, no. 2, pp. 175-181, 2015.

[235] A. Singh and H. Vishwakarma, "Study of structural, morphological, optical and electroluminescent properties of undoped ZnO nanorods grown by a simple chemical precipitation," *Materials Science-Poland,* vol. 33, no. 4, pp. 751-759, 2015.

[236] G. Zoppi, K. Durose, S. Irvine, and V. Barrioz, "Grain and crystal texture properties of absorber layers in MOCVD-grown CdTe/CdS solar cells," *Semiconductor science and technology,* vol. 21, no. 6, p. 763, 2006.

[237] P. D. File, "Joint committee on powder diffraction standards," *ASTM, Philadelphia, Pa,* pp. 9-185, 1967.

[238] H. Schulz and K. Thiemann, "Structure parameters and polarity of the wurtzite type compounds Sic—2H and ZnO," *Solid State Communications,* vol. 32, no. 9, pp. 783-785, 1979.

[239] W. Riedel, Y. Tang, W. Ohm, J. Chen, M. C. Lux-Steiner, and S. Gledhill, "Effect of initial galvanic nucleation on morphological and optical properties of ZnO nanorod arrays," *Thin Solid Films,* vol. 574, pp. 177-183, 2015.

[240] T. H. Meen, W. Water, Y. S. Chen, W. R. Chen, L. W. Ji, and C. J. Huang, "Growth Of ZnO Nanorods by Hydrotherothermal Method Under Different Temperatures," in *2007 IEEE Conference on Electron Devices and Solid-State Circuits*, 2007, pp. 617-620.

[241] R. Tena-Zaera, J. Elias, and C. Lévy-Clément, "ZnO nanowire arrays: optical scattering and sensitization to solar light," *Applied Physics Letters,* vol. 93, no. 23, p. 233119, 2008.

[242] M. R. Khajavi, D. J. Blackwood, G. Cabanero, and R. Tena-Zaera, "New insight into growth mechanism of ZnO nanowires electrodeposited from nitrate-based solutions," *Electrochimica Acta,* vol. 69, pp. 181-189, 5/1/ 2012.

[243] Z. Jehl, J. Rousset, F. Donsanti, G. Renou, N. Naghavi, and D. Lincot, "Electrodeposition of ZnO nanorod arrays on ZnO substrate with tunable orientation and optical properties," *Nanotechnology,* vol. 21, no. 39, p. 395603, 2010.

[244] Z. Yu, A. Raman, and S. Fan, "Fundamental limit of nanophotonic light trapping in solar cells," *Proceedings of the National Academy of Sciences,* vol. 107, no. 41, pp. 17491-17496, 2010.

[245] V. Strano, "Low-cost high-haze films based on ZnO nanorods for light scattering in thin c-Si solar cells," *Applied Physics Letters,* vol. 106, no. 1, p. 013901, 2015.

[246] S. Q. Hussain, "Uniform 3D hydrothermally deposited zinc oxide nanorods with high haze ratio," *Materials Science in Semiconductor Processing,* vol. 37, pp. 99-104, 2015.

[247] T. Shinagawa, K. Shibata, O. Shimomura, M. Chigane, R. Nomura, and M. Izaki, "Solution-processed high-haze ZnO pyramidal textures directly grown on a TCO substrate and the light-trapping effect in Cu 2 O solar cells," *Journal of Materials Chemistry C,* vol. 2, no. 16, pp. 2908-2917, 2014.

[248] R.-E. Nowak, M. Vehse, O. Sergeev, K. von Maydell, and C. Agert, "ZnO nanorod arrays as light trapping structures in amorphous silicon thin-film solar cells," *Solar Energy Materials and Solar Cells,* vol. 125, pp. 305-309, 2014/06/01/ 2014.

[249] A. Sáenz-Trevizo, P. Amézaga-Madrid, P. Pizá-Ruiz, W. Antúnez-Flores, and M. Miki-Yoshida, "Optical Band Gap Estimation of ZnO Nanorods," *Materials Research,* no. AHEAD, pp. 0-0, 2016.

[250] R. Rusdi, A. A. Rahman, N. S. Mohamed, N. Kamarudin, and N. Kamarulzaman, "Preparation and band gap energies of ZnO nanotubes, nanorods and spherical nanostructures," *Powder Technology,* vol. 210, no. 1, pp. 18-22, 6/10/ 2011.

[251] Y. Yao, J. Taylor, L. Cirullo, R. Leguarda, B. Sheeran, and X. Ning, "Ultra-Thin, Ultra-Lightweight, and Multifunctional Skin for Highly Deformable Structures," in *AIAA Scitech 2019 Forum*, 2019, p. 2028.

[252] S. Surendran, S. Shanmugapriya, S. Shanmugam, L. Vasylechko, and R. Kalai Selvan, "Interweaved Nickel Phosphide Sponge as an Electrode for Flexible Supercapattery and Water Splitting Applications," *ACS Applied Energy Materials*, vol. 1, no. 1, pp. 78-92, 2018.

[253] G. Abadias, "Stress in thin films and coatings: Current status, challenges, and prospects," *Journal of Vacuum Science & Technology A: Vacuum, Surfaces, and Films*, vol. 36, no. 2, p. 020801, 2018.

[254] J. Alfonso, E. Greaves, B. Lavelle, and L. Sajo-Bohus, "Effect of sputtering pressure on residual stress in Ni films using energy-dispersive x-ray diffraction," *Journal of Vacuum Science & Technology A: Vacuum, Surfaces, and Films*, vol. 21, no. 4, pp. 846-850, 2003.

[255] K. Röll, "Analysis of stress and strain distribution in thin films and substrates," *Journal of Applied Physics*, vol. 47, no. 7, pp. 3224-3229, 1976.

[256] J. A. Thornton and D. Hoffman, "Stress-related effects in thin films," *Thin solid films*, vol. 171, no. 1, pp. 5-31, 1989.

[257] S. Lovell and E. Rollinson, "Density of thin films of vacuum evaporated metals," *Nature*, vol. 218, no. 5147, p. 1179, 1968.

[258] H.-F. Xiang, Z.-X. Xu, V. Roy, C.-M. Che, and P. Lai, "Method for measurement of the density of thin films of small organic molecules," *Review of scientific instruments*, vol. 78, no. 3, p. 034104, 2007.

[259] A. S. Alagoz, J.-D. Kamminga, S. Y. Grachev, T.-M. Lu, and T. Karabacak, "Residual stress reduction in sputter deposited thin films by density modulation," *MRS Online Proceedings Library Archive*, vol. 1224, 2009.

[260] J. F. Freedman, "Residual stress in single-crystal nickel films," *IBM Journal of Research and Development*, vol. 6, no. 4, pp. 449-455, 1962.

[261] J. Hammacher, A. Fuelle, J. Flaemig, J. Saupe, B. Loechel, and J. Grimm, "Stress engineering and mechanical properties of SU-8-layers for mechanical applications," *Microsystem Technologies*, vol. 14, no. 9-11, pp. 1515-1523, 2008.

[262] J. A. Thornton, "The microstructure of sputter-deposited coatings," *Journal of Vacuum Science & Technology A: Vacuum, Surfaces, and Films*, vol. 4, no. 6, pp. 3059-3065, 1986.

[263] H. Windischmann, "Intrinsic stress in sputter-deposited thin films," *Critical Reviews in Solid State and Material Sciences*, vol. 17, no. 6, pp. 547-596, 1992.

[264] J. Hinze and K. Ellmer, "In situ measurement of mechanical stress in polycrystalline zinc-oxide thin films prepared by magnetron sputtering," *Journal of Applied Physics*, vol. 88, no. 5, pp. 2443-2450, 2000.

[265] R. K. Sendi and S. Mahmud, "Stress control in ZnO nanoparticle-based discs via high-oxygen thermal annealing at various temperatures," *Journal of Physical Science*, vol. 24, no. 1, p. 1, 2013.

[266] A. , R. Pelzer, G. Khatibi, and J. Steinbrenner, "Thickness dependency of adhesion properties of TiW thin films," in *2014 IEEE 16th Electronics Packaging Technology Conference (EPTC)*, 2014, pp. 192-195: IEEE.

[267] D.-C. Baek, S.-Y. Kim, and S.-B. Lee, "Mechanical behavior of metallic thin film on polyimide substrate," in *Fracture of Nano and Engineering Materials and Structures*: Springer, 2006, pp. 721-722.

[268] M. Her, R. Beams, and L. Novotny, "Graphene transfer with reduced residue," *Physics Letters A*, vol. 377, no. 21–22, pp. 1455-1458, 2013.

[269] P. Carlberg, M. Graczyk, E. L. Sarwe, I. Maximov, M. Beck, and L. Montelius, "Lift-off process for nanoimprint lithography," *Microelectronic Engineering*, vol. 67-68, pp. 203-207, 2003/06/01/ 2003.

[270] F. Behrouznejad, S. Shahbazi, N. Taghavinia, H.-P. Wu, and E. W.-G. Diau, "A study on utilizing different metals as the back contact of CH 3 NH 3 PbI 3 perovskite solar cells," *Journal of Materials Chemistry A*, vol. 4, no. 35, pp. 13488-13498, 2016.

[271] A. del Campo and C. Greiner, "SU-8: a photoresist for high-aspect-ratio and 3D submicron lithography," *Journal of micromechanics and microengineering*, vol. 17, no. 6, p. R81, 2007.

[272] J. Melai, C. Salm, S. Smits, V. M. B. Carballo, J. Schmitz, and B. Hageluken, "Considerations on using SU-8 as a construction material for high aspect ratio structures," in *10th annual workshop on semiconductor advances for future electronics and sensors (SAFE)*, 2007, pp. 29-534.

[273] S. Haghighat, S. Ostresh, and J. M. Dawlaty, "Controlling proton conductivity with light: a scheme based on photoacid doping of materials," *The Journal of Physical Chemistry B*, vol. 120, no. 5, pp. 1002-1007, 2016.

[274] M. J. Moghaddam, Y. Inaki, and K. Takemoto, "Photolysis of Polyamides Containing Thymine Photodimer Units in the Main Chain and Application to Deep-UV Positive Type Photoresists," *Polymer Journal*, vol. 22, no. 6, p. 468, 1990.

[275] Z. G. Ling, K. Lian, and L. Jian, "Improved patterning quality of SU-8 microstructures by optimizing the exposure parameters," in *Advances in Resist Technology and Processing XVII*, 2000, vol. 3999, pp. 1019-1028: International Society for Optics and Photonics.

[276] J. Lee, K.-H. Choi, and K. Yoo, "Innovative SU-8 lithography techniques and their applications," *Micromachines*, vol. 6, no. 1, pp. 1-18, 2015.

[277] K. Wouters and R. Puers, "Accurate measurement of the steady-state swelling behavior of SU-8 negative photo resist," *Procedia Chemistry*, vol. 1, no. 1, pp. 60-63, 2009.

[278] K. Wouters and R. Puers, "Diffusing and swelling in SU-8: insight in material properties and processing," *Journal of Micromechanics and Microengineering*, vol. 20, no. 9, p. 095013, 2010.

[279] S. Schmid, S. Kühne, and C. Hierold, "Influence of air humidity on polymeric microresonators," *Journal of micromechanics and microengineering*, vol. 19, no. 6, p. 065018, 2009.

[280] R. Feng and R. J. Farris, "Influence of processing conditions on the thermal and mechanical properties of SU8 negative photoresist coatings," *Journal of Micromechanics and Microengineering,* vol. 13, no. 1, p. 80, 2002.

[281] S. Jiguet, A. Bertsch, M. Judelewicz, H. Hofmann, and P. Renaud, "SU-8 nanocomposite photoresist with low stress properties for microfabrication applications," *Microelectronic engineering,* vol. 83, no. 10, pp. 1966-1970, 2006.

[282] H.-K. Chang and Y.-K. Kim, "UV-LIGA process for high aspect ratio structure using stress barrier and C-shaped etch hole," *Sensors and Actuators A: Physical,* vol. 84, no. 3, pp. 342-350, 2000.

[283] S. Chung and S. Park, "Effects of temperature on mechanical properties of SU-8 photoresist material," *Journal of Mechanical Science and Technology,* vol. 27, no. 9, pp. 2701-2707, 2013.

[284] M. Guo, P. Diao, X. Wang, and S. Cai, "The effect of hydrothermal growth temperature on preparation and photoelectrochemical performance of ZnO nanorod array films," *Journal of Solid State Chemistry,* vol. 178, no. 10, pp. 3210-3215

[285] Z. Qin, Q. Liao, Y. Huang, L. Tang, X. Zhang, and Y. Zhang, "Effect of hydrothermal reaction temperature on growth, photoluminescence and photoelectrochemical properties of ZnO nanorod arrays," *Materials Chemistry and Physics,* vol. 123, no. 2, pp. 811-815

[286] S. Haghanifar, "Flexible nanograss with highest combination of transparency and haze for optoelectronic plastic substrates," *Nanotechnology,* vol. 29, no. 42, p. 42LT01, 2018.

[287] H. Lee, D. Koh, L. Xu, S. Row, S. T. Andreadis, and K. W. Oh, "A simple method for fabrication of microstructures using a PDMS stamp," *Micromachines,* vol. 7, no. 10, p. 173, 2016.

[288] Z. Fan and Q. Lin, "Reducing reflection losses in solar cells," ed.

[289] N. Mufti, I. K. Laila, R. Idiawati, A. Fuad, A. Hidayat, and A. Taufiq, "The Effect of Growth Temperature on The Characteristics Of ZnO Nanorods And Its Optical Properties," in *Journal of Physics: Conference Series*, 2018, vol. 1057, no. 1, p. 012005: IOP Publishing.

[290] R. S. Kumar, R. Sathyamoorthy, P. Matheswaran, P. Sudhagar, and Y. S. Kang, "Growth of novel ZnO nanostructures by soft chemical routes," *Journal of Alloys and Compounds,* vol. 506, no. 1, pp. 351-355, 2010.

[291] D. Bhat, "Facile synthesis of ZnO nanorods by microwave irradiation of zinc–hydrazine hydrate complex," *Nanoscale Research Letters,* vol. 3, no. 1, p. 31, 2008.

[292] K. Eswar., "Hydrothermal growth of flower-like ZnO nanostructures on porous silicon substrate," *Journal of Molecular Structure,* vol. 1074, pp. 140-143, 2014.

[293] Y.-J. Kim, A. Yoon, M. Kim, G.-C. Yi, and C. Liu, "Hydrothermally grown ZnO nanostructures on few-layer graphene sheets," *Nanotechnology,* vol. 22, no. 24, p. 245603, 2011.

[294] C. Huang, K. Sun, and W.-L. Chang, "Efficiency enhancement of silicon solar cells using a nano-scale honeycomb broadband anti-reflection structure," *Optics express,* vol. 20, no. 101, pp. A85-A93, 2012.

[295] L.-K. Yeh, W.-C. Tian, K.-Y. Lai, and J.-H. He, "Exceptionally omnidirectional broadband light harvesting scheme for multi-junction concentrator solar cells achieved via ZnO nanoneedles," *Scientific reports,* vol. 6, p. 39134, 2016.

[296] K. Mahmood, M. Hameed, F. Rehman, A. Khalid, M. Imran, and M. T. Mehran, "A multifunctional blade-coated ZnO seed layer for high-efficiency perovskite solar cells," *Applied Physics A,* vol. 125, no. 2, p. 83, 2019.

[297] K.-S. Han, J.-H. Shin, W.-Y. Yoon, and H. Lee, "Enhanced performance of solar cells with anti-reflection layer fabricated by nano-imprint lithography," *Solar Energy Materials and Solar Cells,* vol. 95, no. 1, pp. 288-291

[298] K. Diwate, "Synthesis and characterization of chemical spray pyrolysed CZTS thin films for solar cell applications," *Energy Procedia,* vol. 110, pp. 180-187, 2017.

[299] M. Xie., "Preparation and characterization of Cu2ZnSnS4 thin films and solar cells fabricated from quaternary Cu-Zn-Sn-S target," *International Journal of Photoenergy,* vol. 2013, 2013.

[300] J. A. Selvan, A. E. Delahoy, S. Guo, and Y.-M. Li, "A new light trapping TCO for nc-Si: H solar cells," *Solar energy materials and solar cells,* vol. 90, no. 18-19, pp. 3371-3376, 2006.

[301] V. Bhavanasi, C. B. Singh, D. Datta, V. Singh, K. Shahi, and S. Kumar, "Structural, optical and light scattering properties of post etched RF sputtered ZnO:Al thin films deposited at various substrate temperature," *Optical Materials,* vol. 35, no. 7, pp. 1352-1359

[302] Y. F. Makableh, R. Vasan, J. C. Sarker, A. I. Nusir, S. Seal, and M. O. Manasreh, "Enhancement of GaAs solar cell performance by using a ZnO sol–gel anti-reflection coating," *Solar Energy Materials and Solar Cells,* vol. 123, pp. 178-182, 2014/04/01/ 2014.

[303] N. S. Beattie, G. Zoppi, I. Farrer, P. See, R. W. Miles, and D. A. Ritchie, "Investigation of quantum dot solar cell device performance," *MRS Online Proceedings Library Archive,* vol. 1551, pp. 137-142, 2013.

[304] W. Ananda, "External quantum efficiency measurement of solar cell," in *Quality in Research (QiR): International Symposium on Electrical and Computer Engineering, 2017 15th International Conference on*, 2017, pp. 450-456: IEEE.

[305] M. Jiang, J. Wu, G. Di, and G. Li, "Nanostructured solar cell based on solution processed Cu2ZnSnS4 nanoparticles and vertically aligned ZnO nanorod array," *physica status solidi (RRL)–Rapid Research Letters,* vol. 8, no. 12, pp. 971-975, 2014.

[306] S. Ahmed, K. B. Reuter, O. Gunawan, L. Guo, L. T. Romankiw, and H. Deligianni, "A high efficiency electrodeposited Cu2ZnSnS4 solar cell," *Advanced Energy Materials,* vol. 2, no. 2, pp. 253-259, 2012.

[307] M. Mauger, A. Dubault, and J. Halary, "Synthesis and physico-chemical characterization of networks based on methacryloxypropyl-grafted nano-silica and methyl methacrylate," *Polymer international,* vol. 53, no. 4, pp. 378-385, 2004.

[308] H.-I. Lin, R.-H. Horng, K.-C. Shen, and D.-S. Wuu, "ZnO nanowires embedded in epoxy resin separating from the substrate for wearable electronics

applications," *IEEE Transactions on Nanotechnology,* vol. 13, no. 3, pp. 458-463, 2014.

[309] R.-H. Horng, H.-I. Lin, and D.-S. Wuu, "ZnO nanowires lift-off from silicon substrate embedded in flexible films," in *Nanoelectronics Conference (INEC), 2013 IEEE 5th International*, 2013, pp. 1-3: IEEE.

[310] H. Majidi, M. E. Edley, L. C. Spangler, and J. B. Baxter, "Tailoring Absorber Thickness and the Absorber-Scaffold Interface in CdSe-Coated ZnO Nanowire Extremely Thin Absorber Solar Cells," *Electrochimica Acta,* vol. 145, pp. 291-299

[311] A. Khayatian, M. A. Kashi, R. Azimirad, S. Safa, and S. F. A. Akhtarian, "Effect of annealing process in tuning of defects in ZnO nanorods and their application in UV photodetectors," *Optik,* vol. 127, no. 11, pp. 4675-4681

[312] M. H. Mamat, "Effects of annealing environments on the solution-grown, aligned aluminium-doped zinc oxide nanorod-array-based ultraviolet photoconductive sensor," *Journal of Nanomaterials,* vol. 2012, p. 8, 2012.

[313] Z. Liu, Z. Liu, Y. Li, K. Guo, and J. Han, "Fabrication of ETA cells based on ZnO/CuInS2 core/shell heterostructure," *Materials Technology,* vol. 31, no. 3, pp. 134-138, 2016.

[314] F. Mahmoud and N. Ahmed, "Elaboration of ZnO nanowires by solution based method; characterization and solar cell applications," 2018.

[315] A. Pan, "Surface crystallization effects on the optical and electric properties of CdS nanorods," *Nanotechnology,* vol. 16, no. 10, p. 2402, 2005.

[316] D. Wang, "Effects of postgrowth annealing treatment on the photoluminescence of zinc oxide nanorods," *Journal of Applied Physics,* vol. 99, no. 11, p. 113509, 2006.

[317] A. Rokade, "Electrochemical Synthesis of Core-shell ZnO/CdS Nanostructure for Photocatalytic Water Splitting Application," *Energy Procedia,* vol. 110, pp. 121-127

[318] X. Yang, "Extended photoresponse of ZnO/CdS core/shell nanorods to solar radiation and related mechanisms," *Solar Energy Materials and Solar Cells,* vol. 137, pp. 169-174

[319] R. Salazar, A. Delamoreanu, C. Levy-Clement, and V. Ivanova, "ZnO/CdTe and ZnO/CdS core-shell nanowire arrays for extremely thin absorber solar cells," *Energy Procedia,* vol. 10, pp. 122-127, 2011.